Disclaimer

This course material may contain copyrighted material the use of which has not been specifically authorized or licensed by the copyright owner. This material is used here for teaching purposes constituting a fair use as provided by Swiss copyright law (URG Art. 19 Abs. 1 lit. B).

The content of this presentation is meant for use as part of the course «Thin Films and Small Scale Mechanics» offered at Empa Thun. It is intended solely for the use of the registered course participants. Distribution to individuals who are not registered course participants is prohibited. If you are not a registered course participant, you are hereby notified that any review, dissemination, distribution, duplication or other use is strictly forbidden.

Testing methods

- Single cantilever bending

Jaya et al., J. Mater. Res., 2014

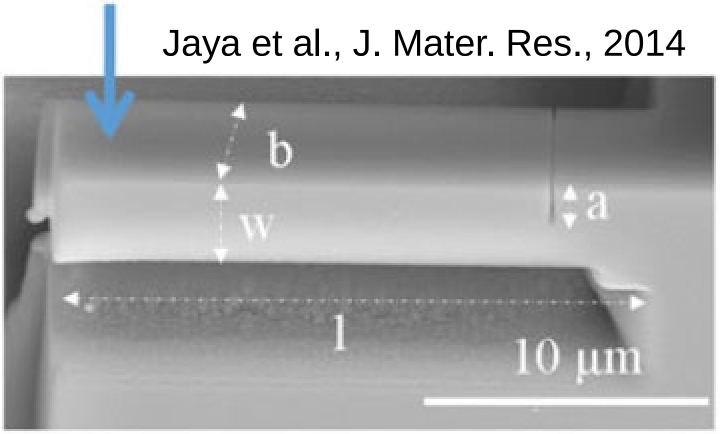

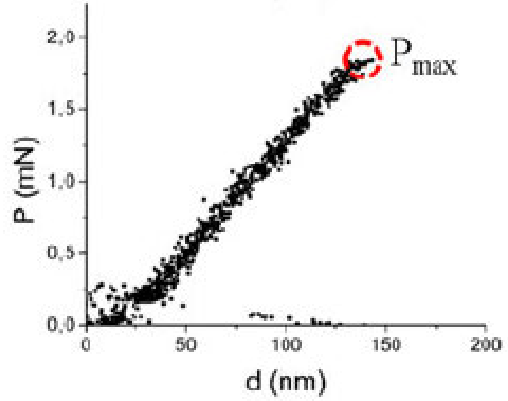

Linear Elastic Fracture Mechanics (LEFM)

$$K_I = \frac{P_{max}l}{bw^{3/2}} f\left(\frac{a}{W}\right)$$

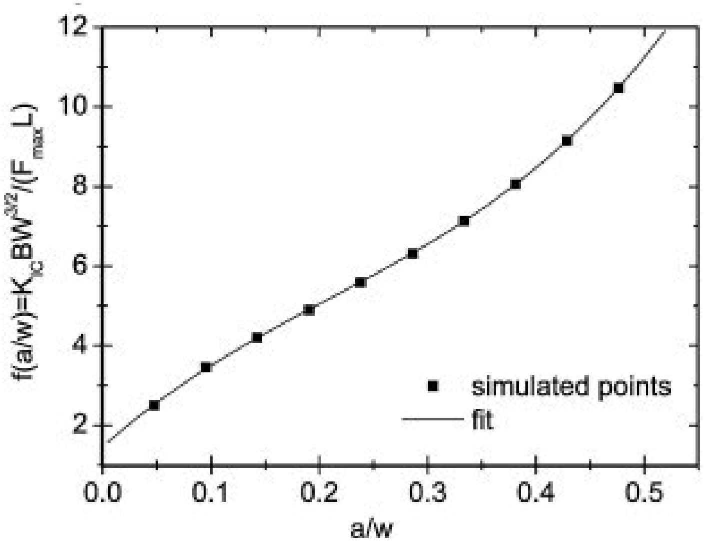

$$f\left(\frac{a}{w}\right) = 1.46 + 24.36\left(\frac{a}{w}\right) - 47.21\left(\frac{a}{w}\right)^2 + 75.18\left(\frac{a}{w}\right)^3$$

Geometry factor function

Matoy et al., Thin Solid Film, 2009

Testing methods

- Single cantilever bending

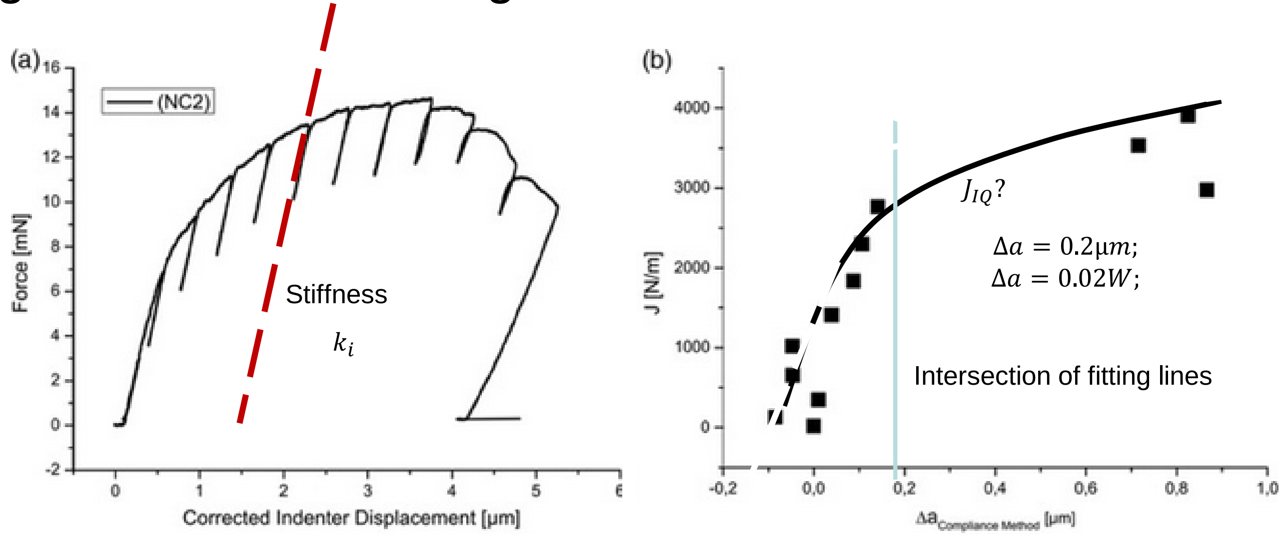

Stiffness

k_i

J_{IQ}?

$\Delta a = 0.2\mu m;$
$\Delta a = 0.02W;$

Intersection of fitting lines

Wurster et al., Philosophical Magazine, 2012

$$J = J_{el(i)} + J_{pl(i)}$$

$$J_i = \frac{\left(K_{(i)}\right)^2 (1-\nu^2)}{E} + \frac{\eta A_{Pl}(i)}{B(W-a_0)}$$

$$a_i = W - \sqrt[3]{\frac{4k_iL^3}{BE}}$$

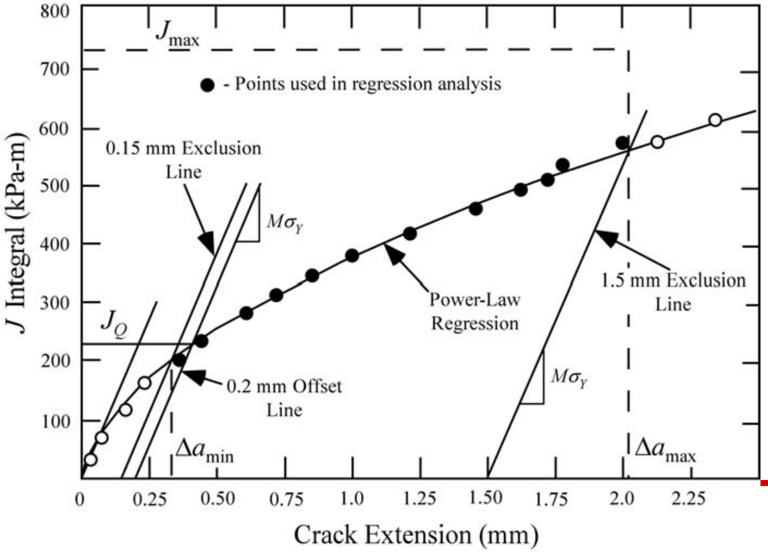

Testing methods

- Single cantilever bending - Temperature

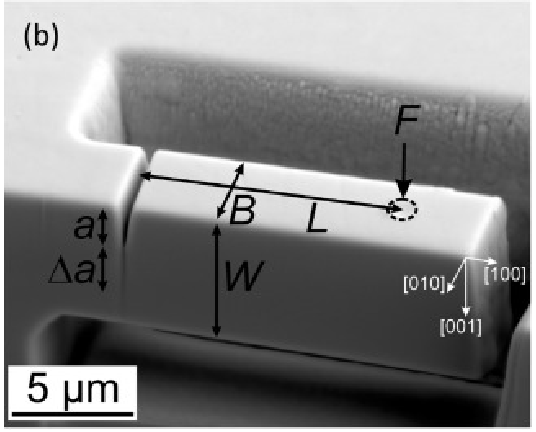

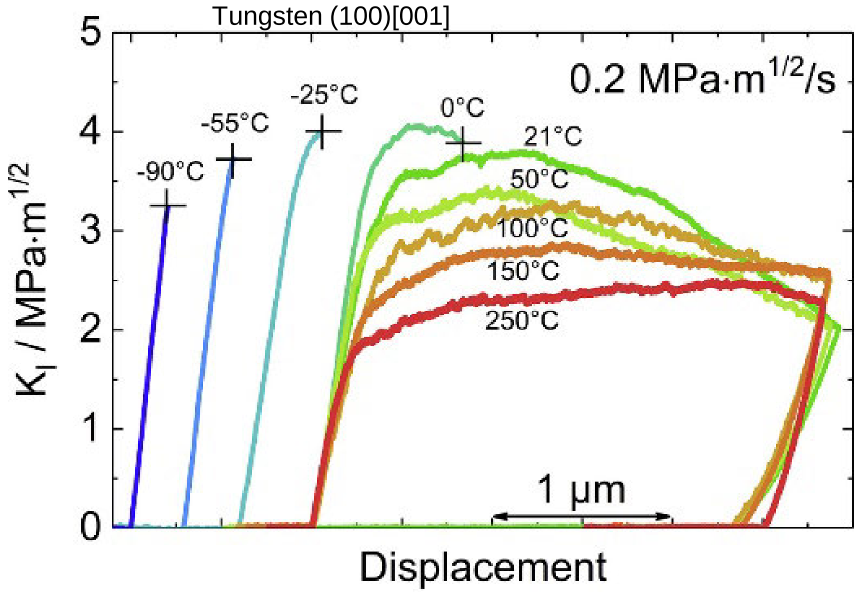

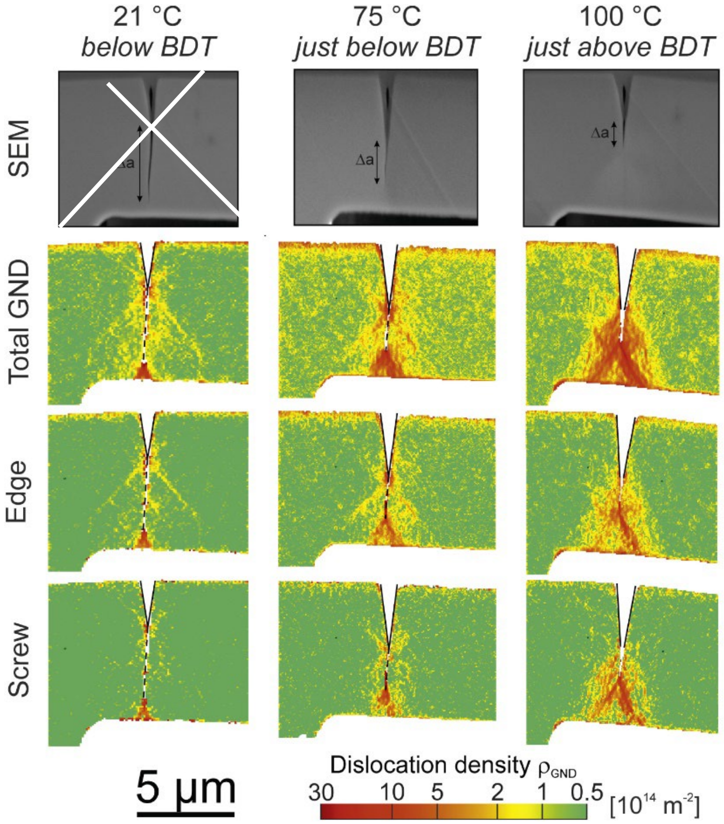

Edge dislocation caused slip trace at low T;

Ast et al., Material & Design, 2018

Testing methods

- Single cantilever bending-Size effect

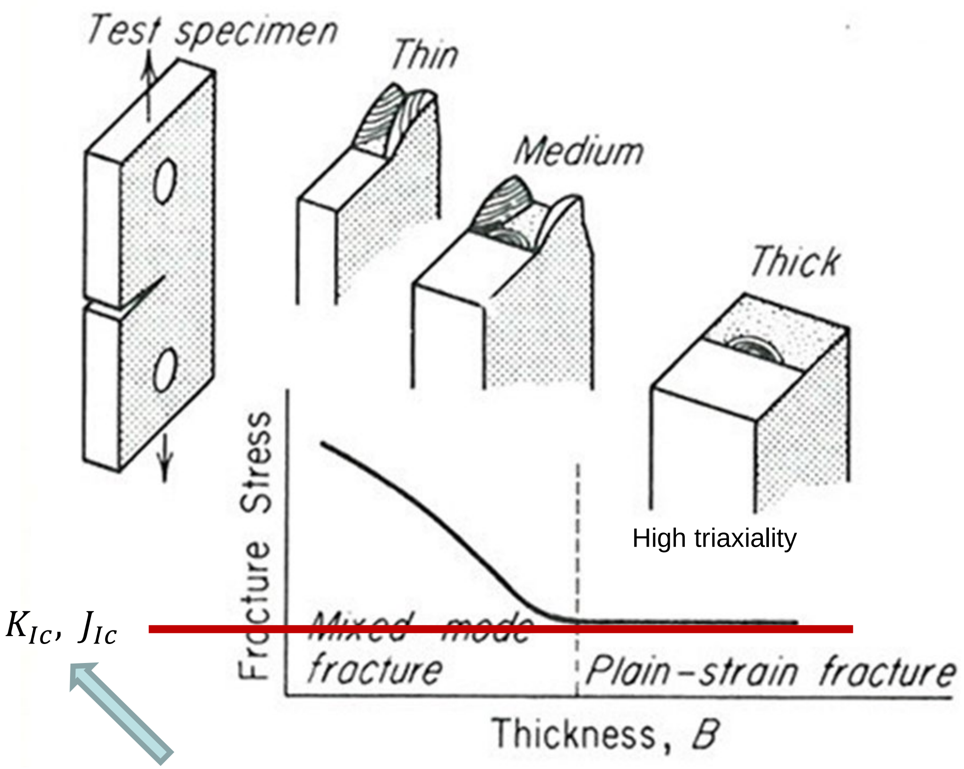

Geometry independent material property

Plastic zone size (Irwin):

Plane stress: $$r_y = \frac{1}{2\pi}\left(\frac{K_I}{\sigma_{YS}}\right)^2$$

Plane strain: $$r_y = \frac{1}{6\pi}\left(\frac{K_I}{\sigma_{YS}}\right)^2$$

1/3 in size!

ASTM E399 LEFM:

$$B, a \geq 2.5\left(\frac{K_Q}{\sigma_{YS}}\right)^2 \quad \gg r_y$$

ASTM E1820 EPFM:

$$B, b_0 \geq \frac{25 J_Q}{\sigma_Y}$$

Quelle: Mechanical Metallurgy, G.E. Dieter, Mac Graw-Hill, 1988

Testing methods

- Single cantilever bending-Size effect

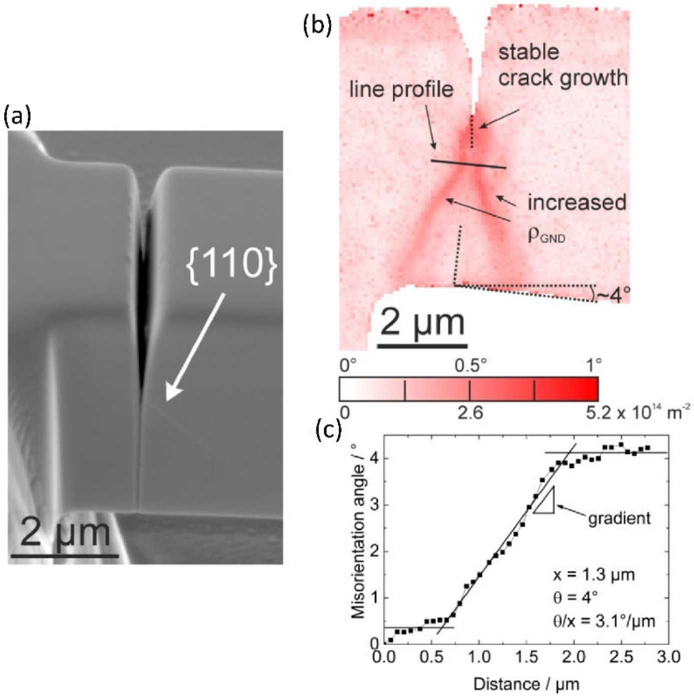

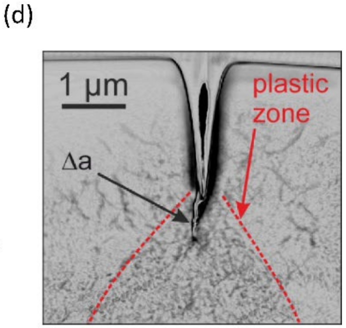

2) Characteristic Microstructure

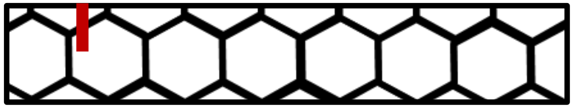

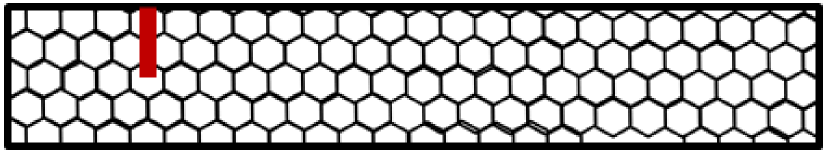

Plastic zone size already comparable to sample dimension!!!

1) Stress state caused dimension dependence

Ast et al., Acta Materialia, 2017

Testing methods

- Single cantilever bending-Size effect

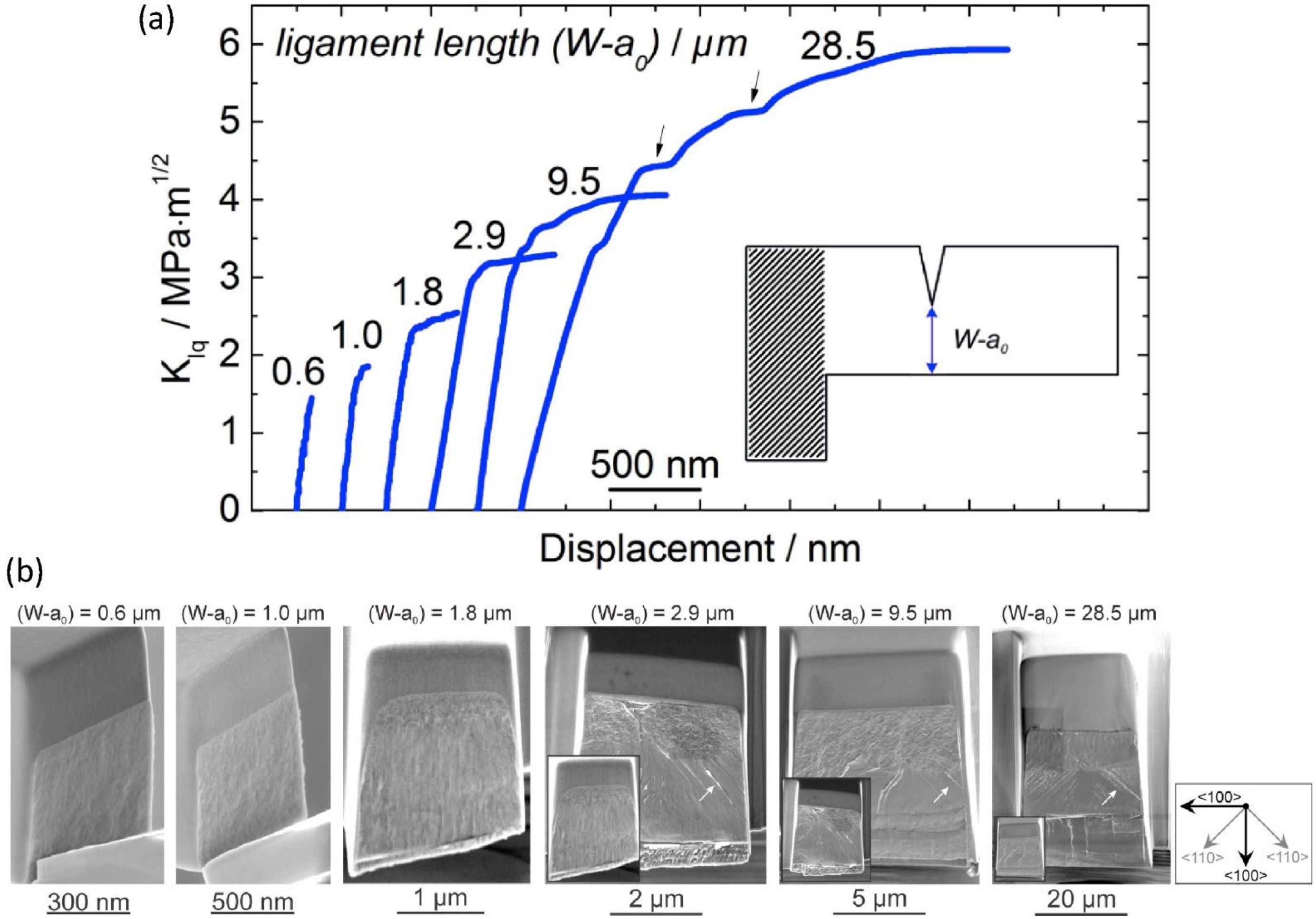

3) Dislocation availability caused dimension dependence

Ast et al., Acta Materialia, 2017

Testing methods

- Single cantilever bending-damage sensitive phase

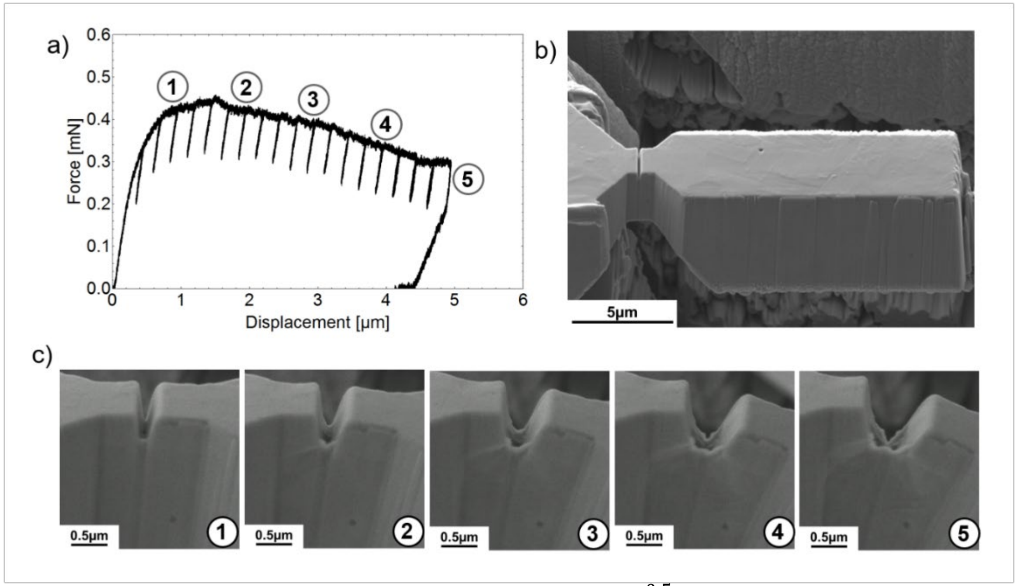

$K_{IQ} \sim 10\ MPa.m^{0.5}$

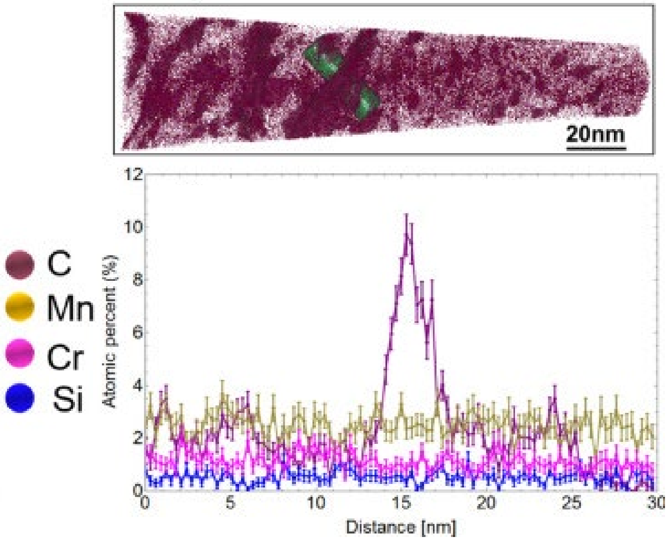

Martensite sensitive to damage initiation;
But not cause catastrophic fracture.

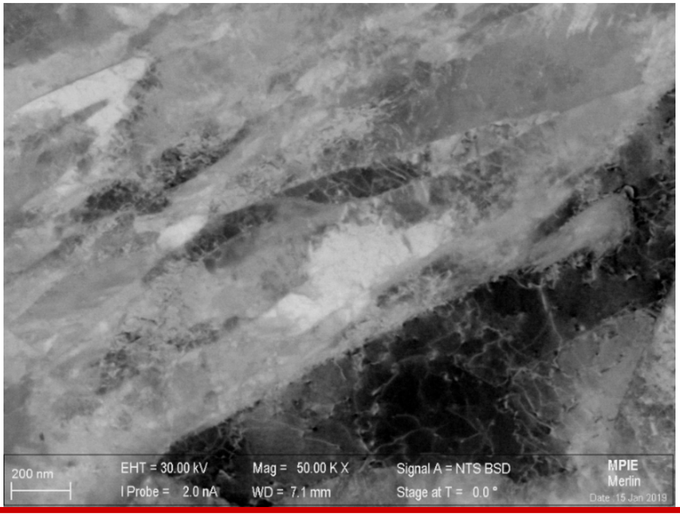

Tian, C., & Kirchlechner, C. JMR, 2021.

Tian, C. et al. Acta Materialia 2020

Testing methods

➢ Double cantilever beam

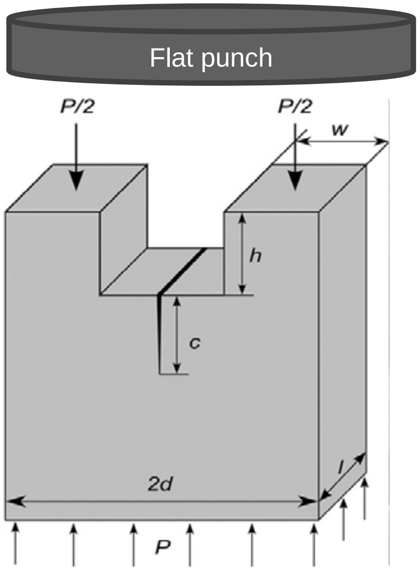

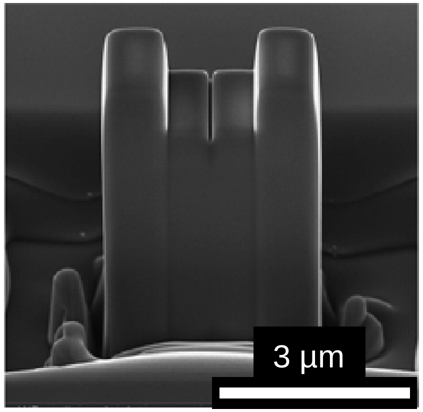

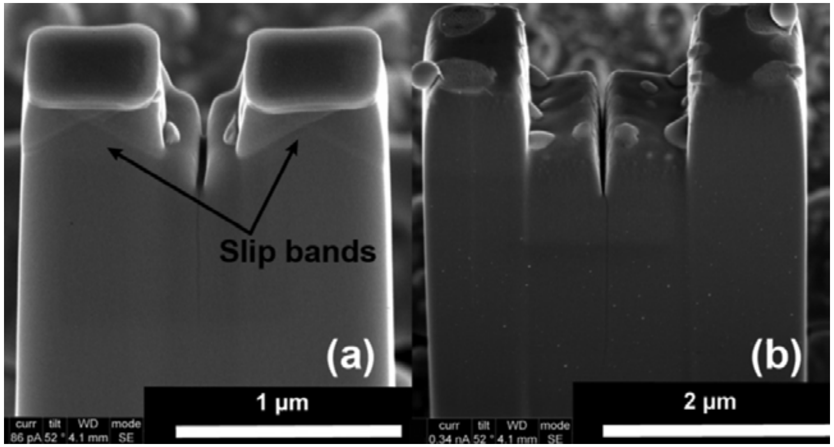

Liu, S., et al. Applied Physics Letters, 2013

$$K_{IC} = \sqrt{3}\frac{(e - \mu h)}{bd^{3/2}}P_C$$

Pros:
1) Less FIB time
2) More stable crack propagation
3) Free of residual stress

Cons:
1) Friction coefficient between tip and test sample required
2) Currently only applicable to brittle materials
3) Success rate low

Testing methods

➢ Double cantilever beam

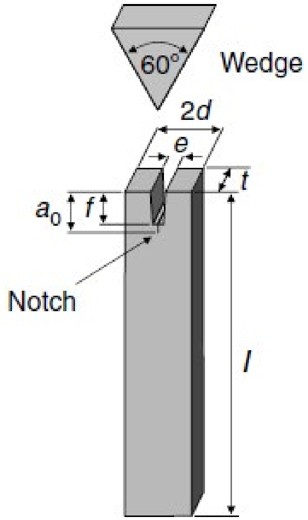

SiC

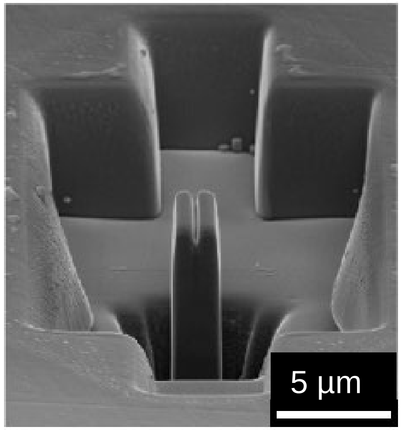

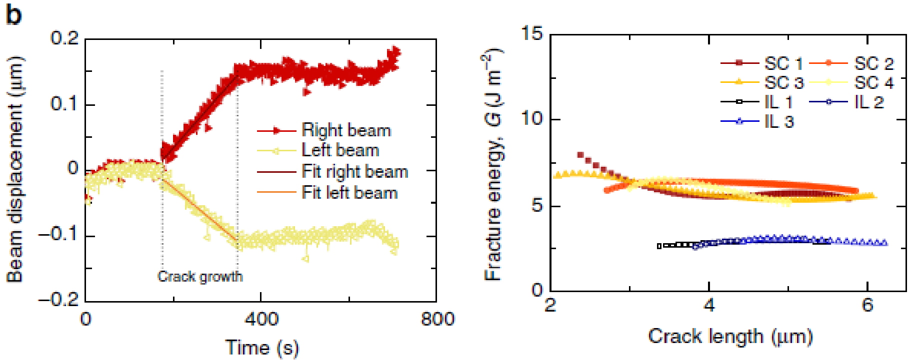

$$G = \frac{3Ed^3\delta^2}{8a^4}\left[1 + (1+\nu)(d/a)^2\right]$$

Pros:

1) No need to consider friction
2) Observation of stable crack propagation
3) Interfacial toughness measurement

Cons:

1) Tracking the beam displacement δ
2) Alignment issue with wedge

Sernicola, Giorgio, et al. Nature communications, 2017

Testing methods

➢ FIB influence

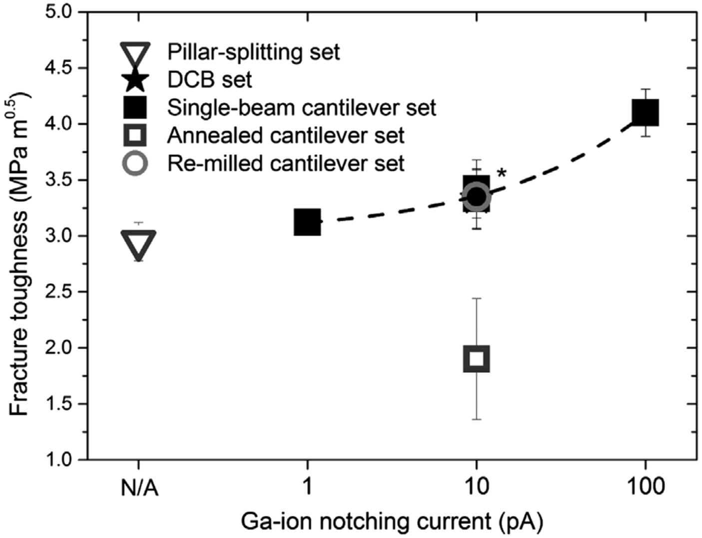

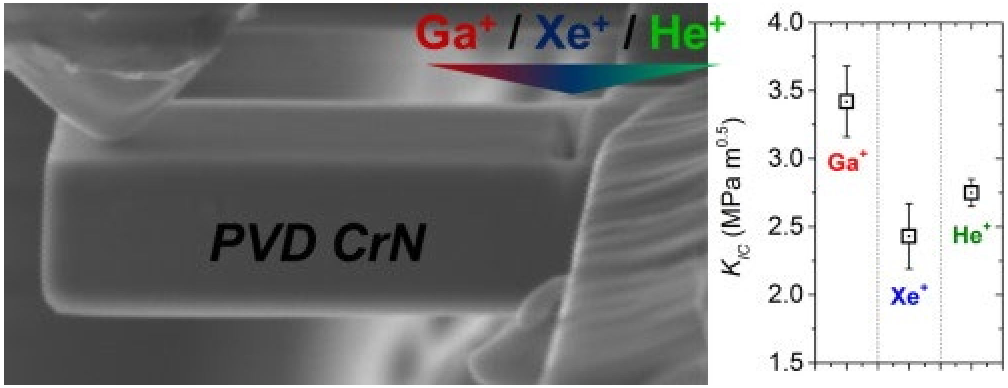

- Apparent fracture toughness depends on
  - Ion species (implantation depth, ion damage cascade)
  - Ion current during notching (damage, notch root radius)

J.P. Best et al., Phil. Mag. 2016 J.P. Best et al., Scripta Materialia, 2016

Testing methods

➢ Nanoindentation

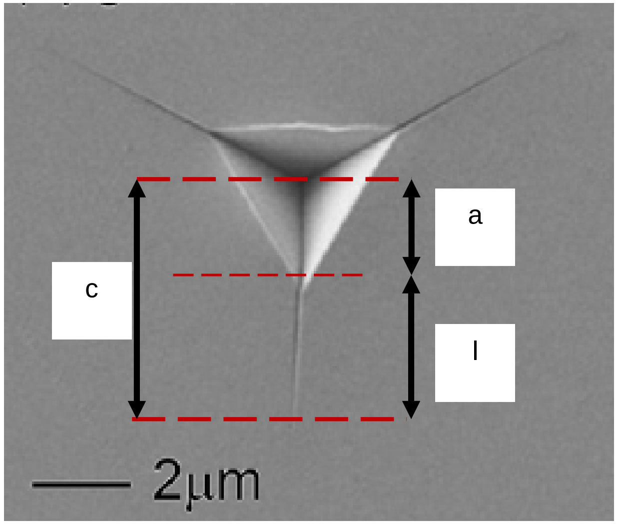

Crack on soda-lime glass

Cuadrado, N., et al. Journal of the European Ceramic Society 2015.

$$K_c = \alpha \cdot \sqrt{\frac{E}{H}} \cdot \frac{P_{max}}{c^{3/2}}$$

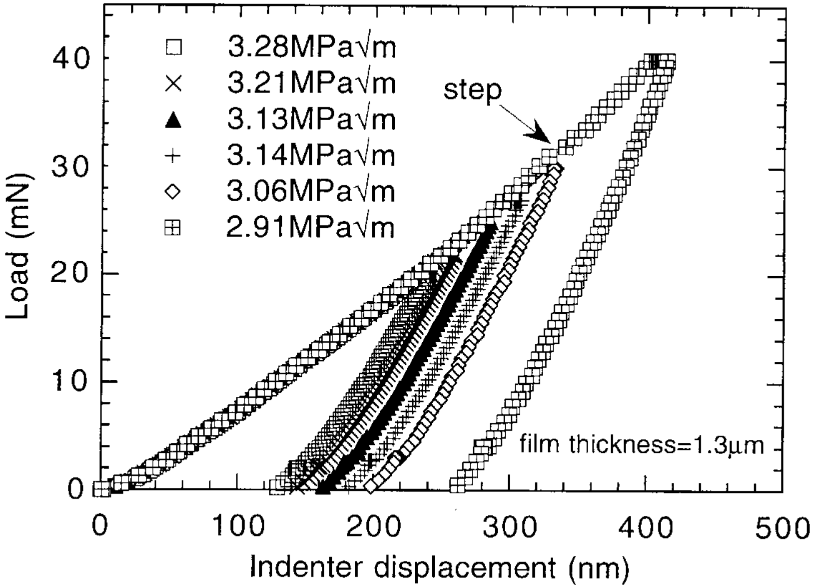

Scharf et al., Journal of Vacuum Science & Technology A: Vacuum, Surfaces, and Films (1997).

Pros:

1) No FIB induced damage
2) Simplicity

Cons:

1) Residual stress/substrate effect
2) Only applicable to brittle materials
3) Need special crack system

Testing methods

- Nanoindentation

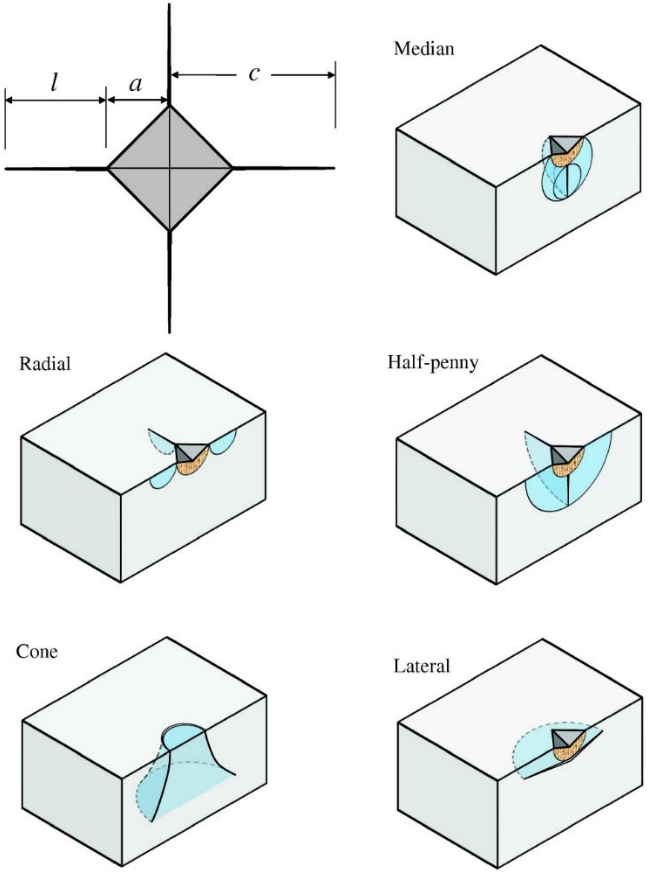

Lee et al. Acta Materialia, 2012

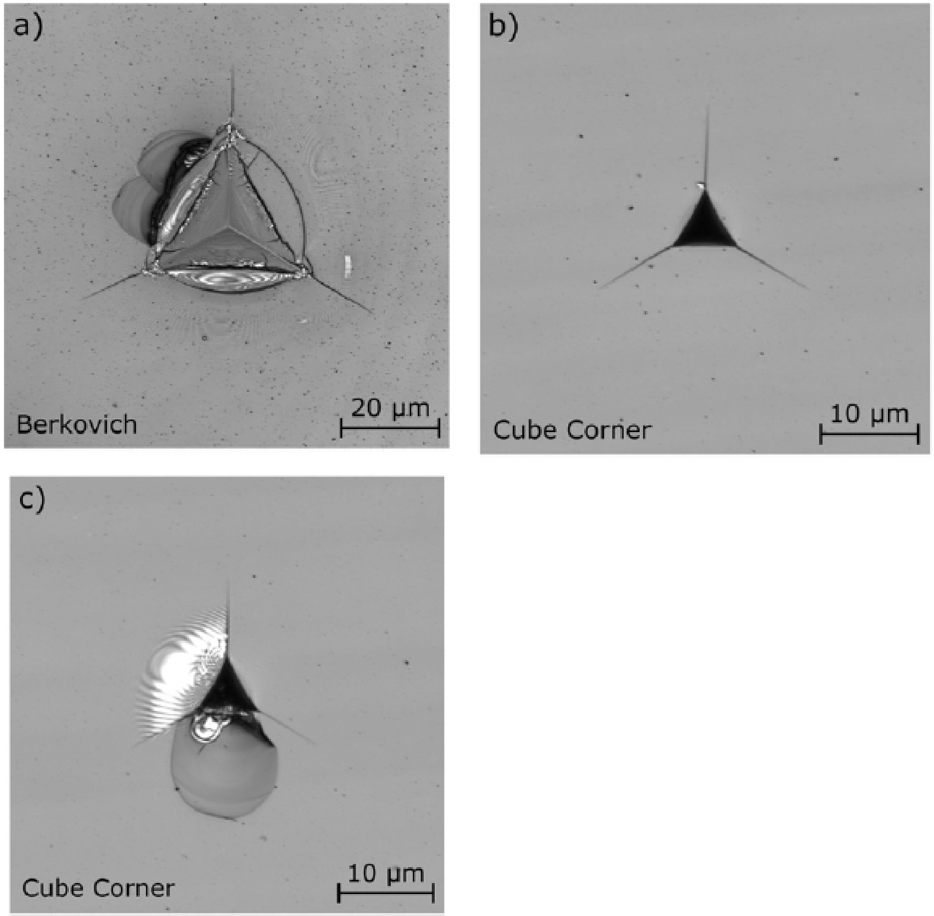

Bruns et al. Materials and Design, 2020

Testing methods

➢ Pillar splitting

(a)

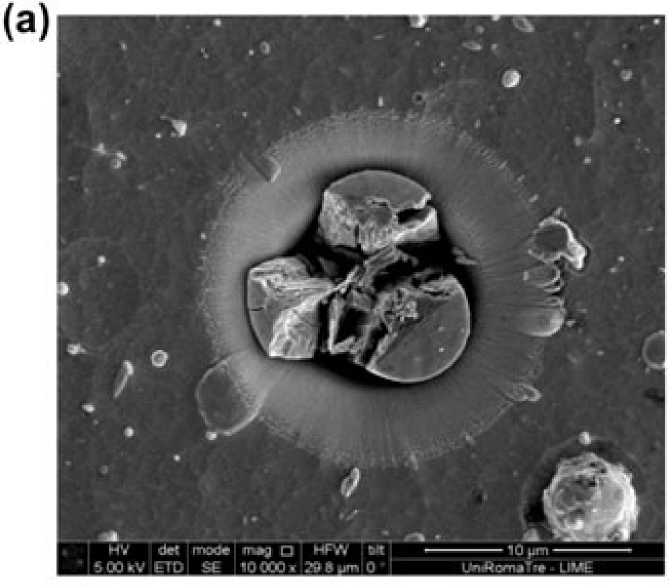

(b)

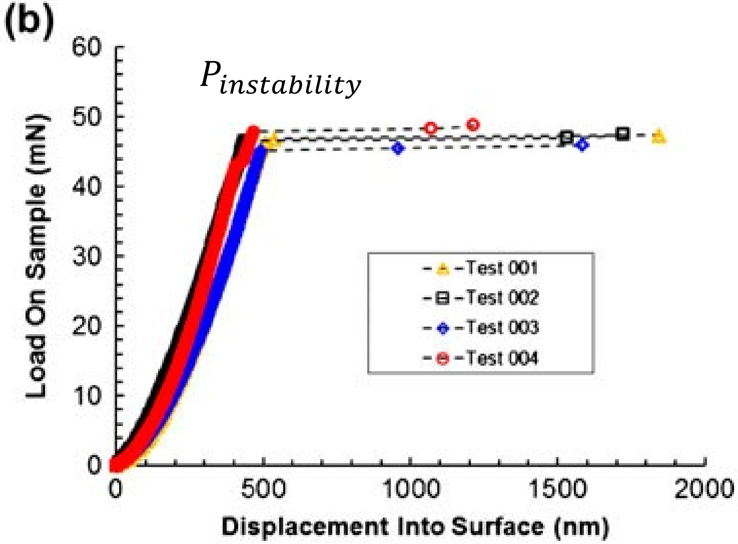

$$K_c = \gamma . \frac{P_c}{R^{3/2}}$$

$$Aspect\ ratio: \ \frac{z}{D} \geq 1$$

Pros:
1) Less FIB induced damage
2) No measurement of crack length
3) No substrate/residual stress influence

Cons:
1) Alignment when doing indentation
2) Cohesive zone FEM for evaluation γ
3) Only applicable to brittle materials

CrN hard coating film. Sebastiani et al., Philosophical Magzine, 2015

Testing methods

- Pillar splitting

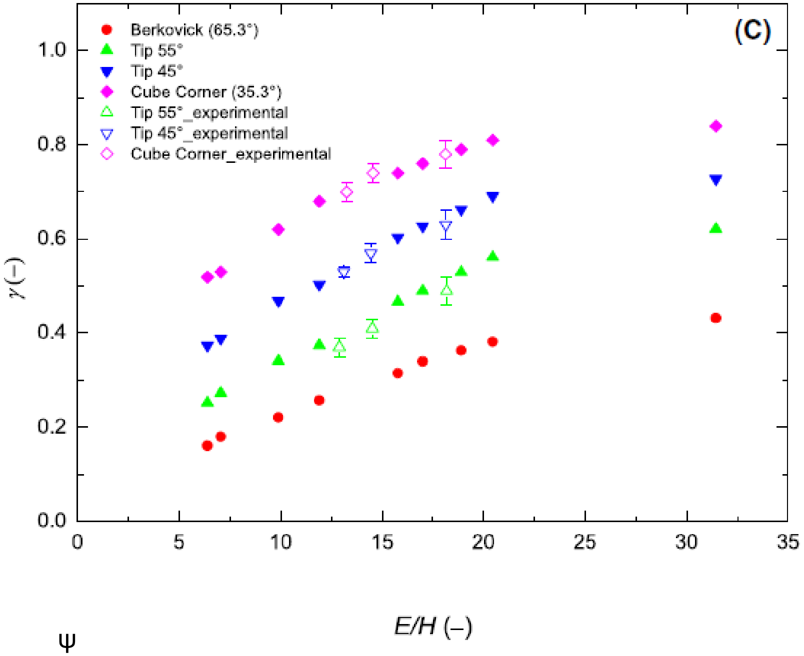

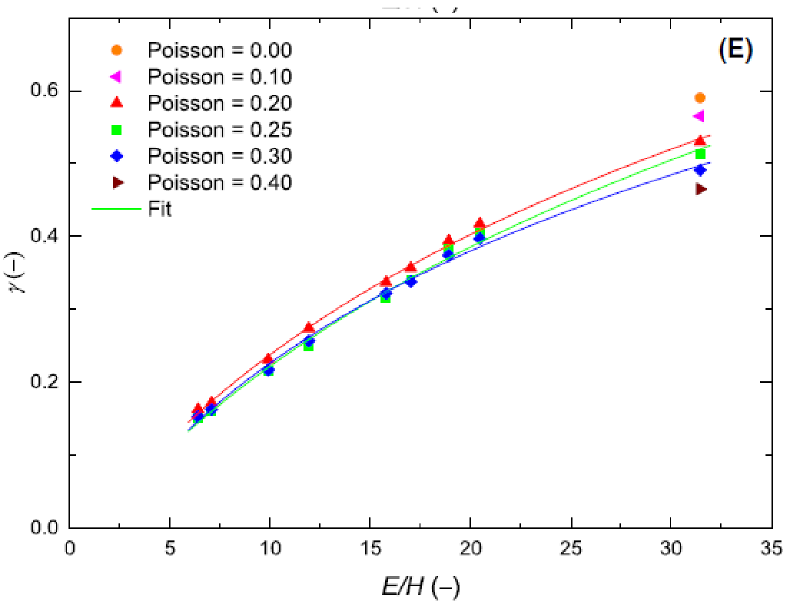

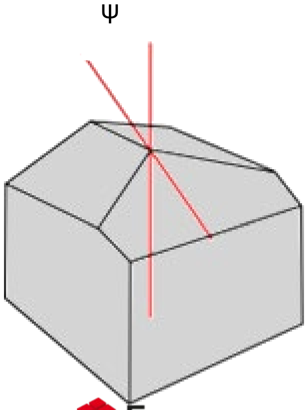

Ψ=65.3°: Berkovich tip

Ψ=35.3°: Cube corner tip

1) γ increases with the E/H ratio;
2) γ decreases with indenter angle;
3) Poisson's ratio has little influence on γ.

Ghidelli et al., Journal of the American ceramic 2017.

Testing methods

- Pillar splitting

J.P. Best et al. Scripta Materialia, 2019

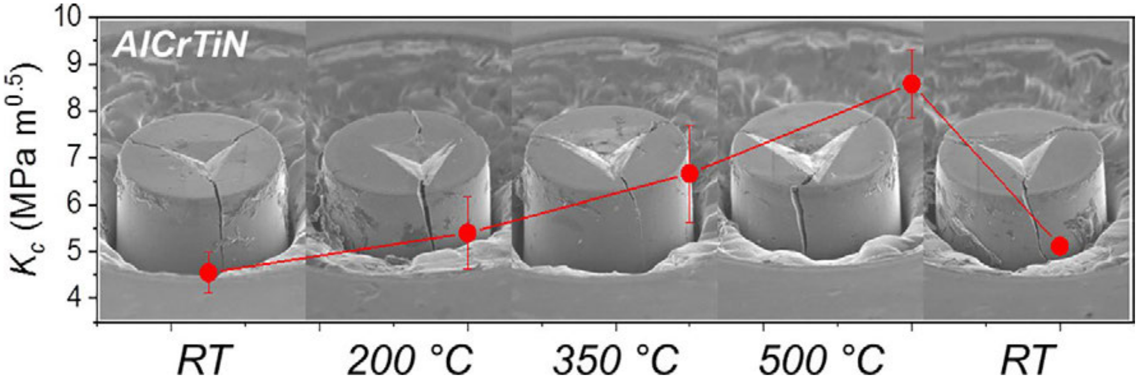

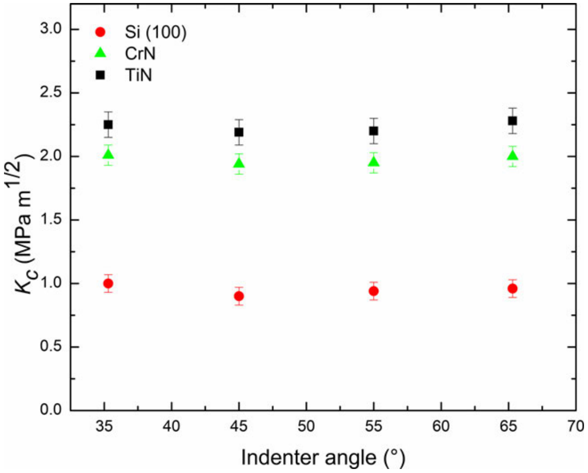

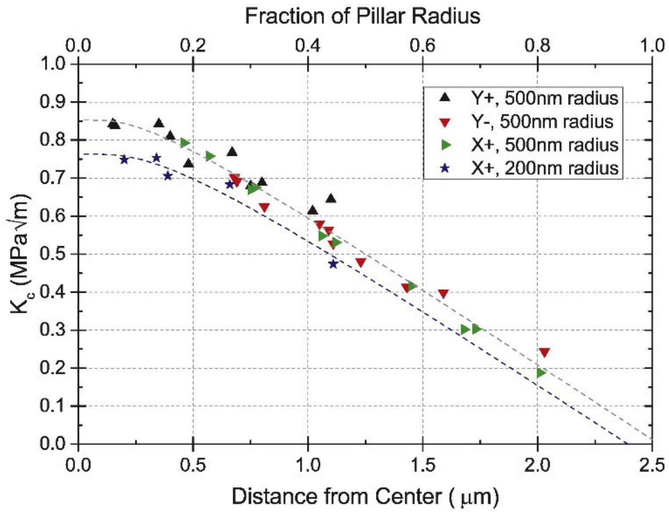

Ghidelli et al., J Am Cer Soc, 2017.

Lauener et al., Mat. & Des., 2018

Summary and comparison

Testing methods	Input parameter	Indenter type	Stable crack growth	Free of residual stress	Interface	Tolerance to misalignment	FIB influence
Single cantilever	P_{max}, a	Wedge/Cone	×	√	√	√	×
Double cantilever	P_{max}, μ	Flat punch	√	√	~	×	×
Naoindentation	P_{max}, a	Berkovich/cube	×	×	×	~	√
Pillar splitting	P_{max}, γ	Berkovich/cube	×	√	×	×	×

Mode-dependent fracture toughness testing at the micro-scale

Motivation: Cleavage of GaAs

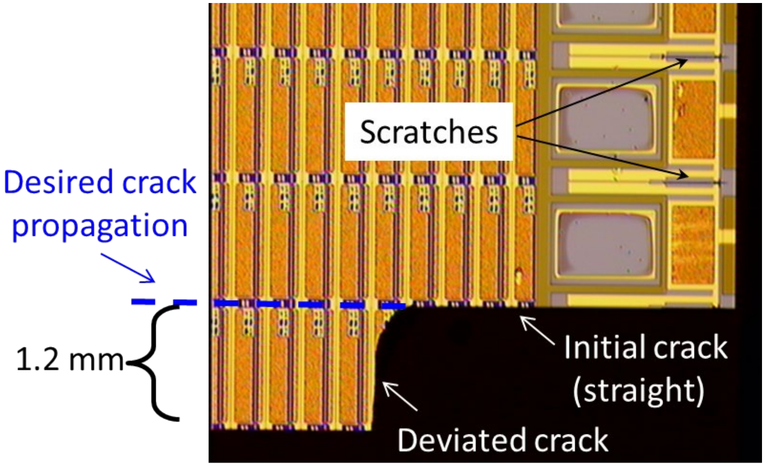

II-VI LASER ENTERPRISE

Change from mode I (start) to mode III (end)

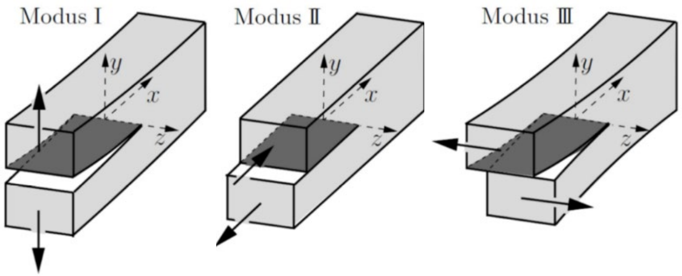

Different fracture modes

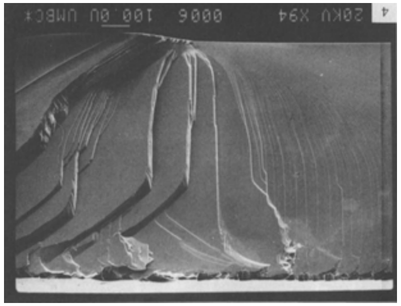

Belsinger et al., Eng. Fract. Mech., 1994
River-lines on GaAs fracture surface

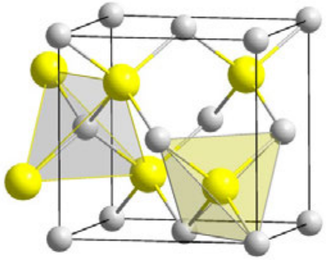

GaAs:
"ZnS" sphalerite structure
{110}-cleavage planes
K_{Ic} = 0.31 … 0.46 $MPam^{0.5}$

Empa
Materials Science and Technology

Macroscopic mode-dependent testing

Mixed mode study

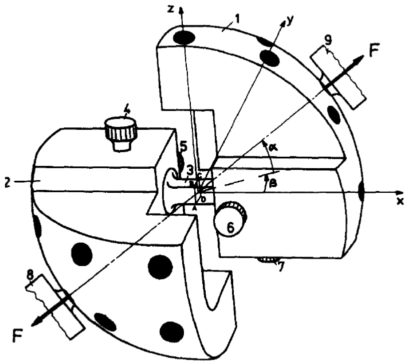

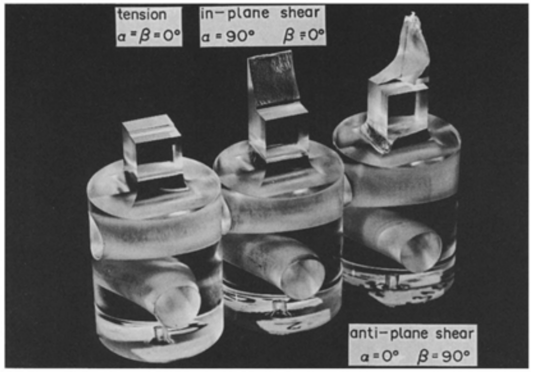

Richard and Kuna, Eng. Fract. Mech., 1990
All fracture-mode specimen

Mode I and III study

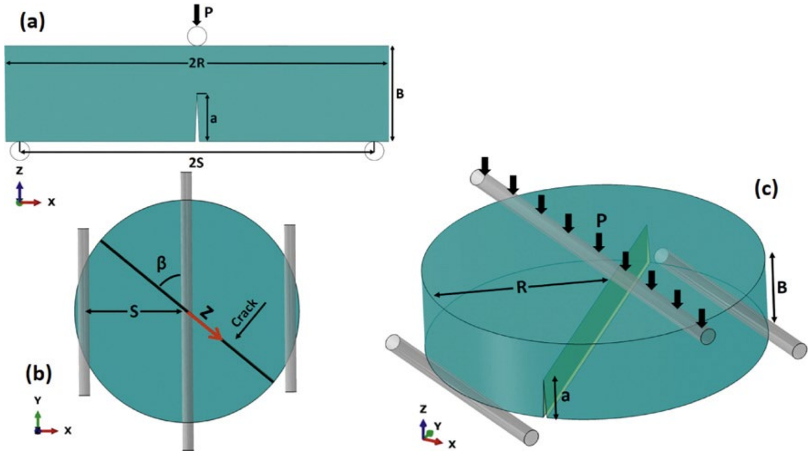

PMMA specimen subjected to pure mode I

asphalt specimen subjected to pure mode III

Aliha et al., Materials and Design, 2015
Edge Notched Disc Bend (ENDB) specimen for mode III

Maximum tangential stress criterion

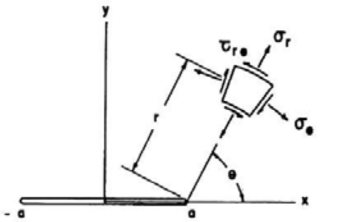

Fig. 1 Stress components near the crack tip in cylindrical coordinates

Mode I

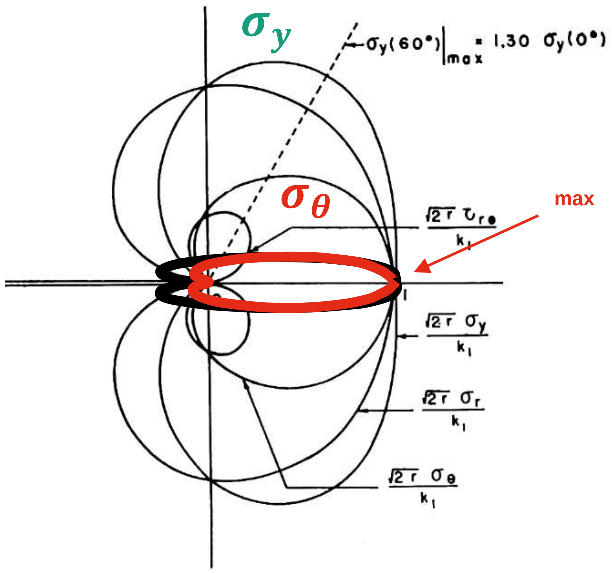

Fig. 2 Polar plot of stresses near the crack tip for symmetric case ($k_2 = 0$)

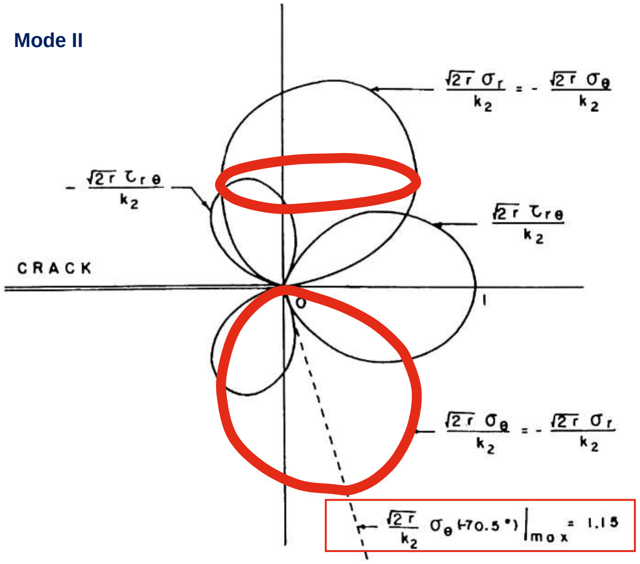

Fig. 3 Polar plot of stresses near the crack tip for skew-symmetric case

Erdogan and Sih, Journal of Basic Engineering, 1963

- Crack extension in a large plate subjected to general plane loading
- **Skew-symm. plane loading** leads to crack deflection under **~70°**, crack growth not in inital plane

Empa
Materials Science and Technology

Mode I / K_I - FE model

Ideal case

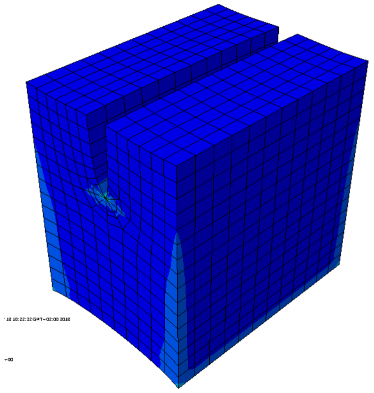

microcantilever

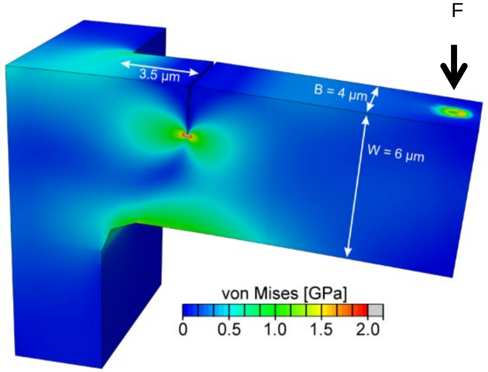

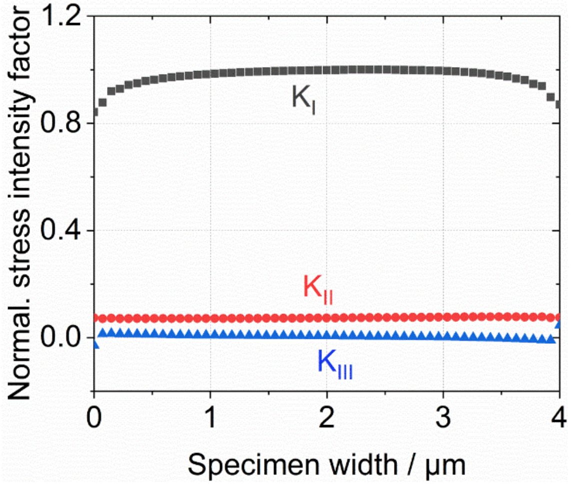

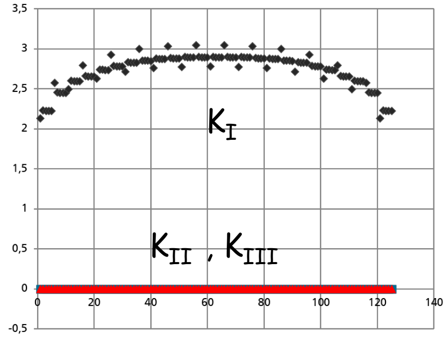

- For: $0.2 < a/W < 0.5$
- $L > 3 (W-a)$

$$K_I = \frac{F\ L}{B\ W^{3/2}} f_{KI}(a/W)$$

- K_I 10 times higher than K_{II} and K_{III}
- K_I, K_{II} and K_{III} nearly constant along the sample width B
- Slightly influenced by free surfaces

Ast & Schwiedrzik et al., Materials and Design, 2018

Mode I / K_I - FE model

Ideal case

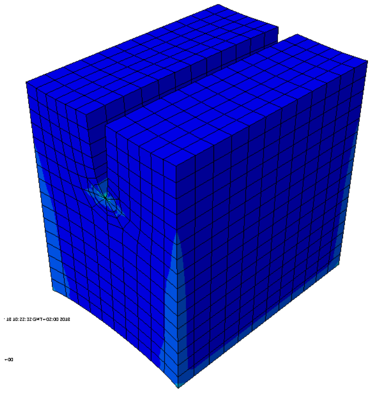

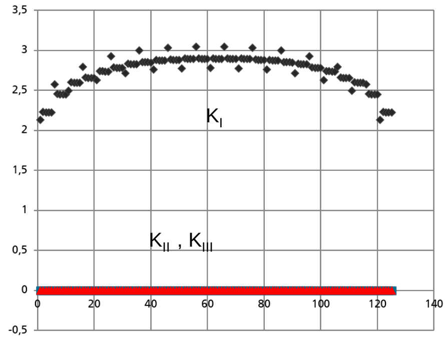

μ-SENT geometry

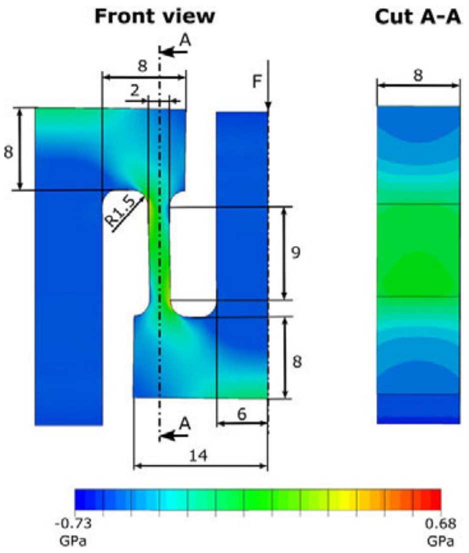

$$f(a/W) = 2.485\left(\frac{a}{W}\right)^2 + 2.721\left(\frac{a}{W}\right) + 0.401$$

$$K_I = \frac{F\,L}{B\,W^{3/2}} f_{KI}(a/W)$$

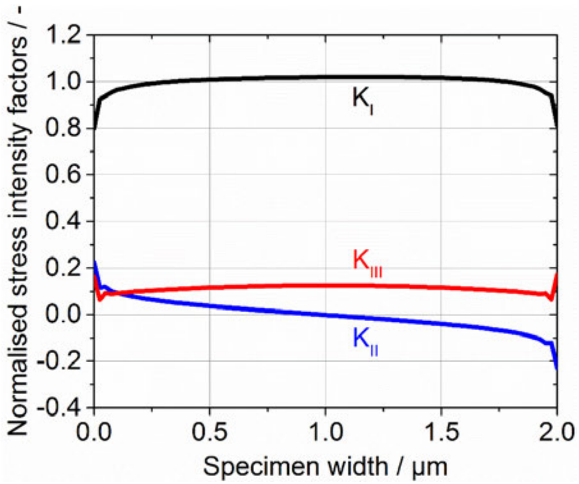

- Notched with a/W = 0.25
- Pure-tensile stress field at notch tip
- Low geometry factor and similar to SENT for small a/W ratios

Schwiedrzik et al., Fatigue Fract. Eng. Mater. Struct., 2017

Mode II / K_{II} – FE model

Ideal case

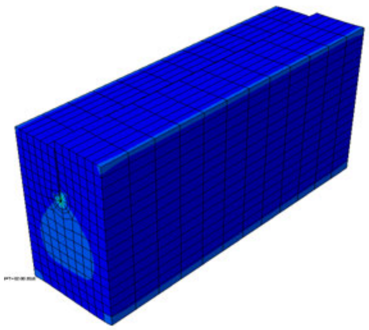

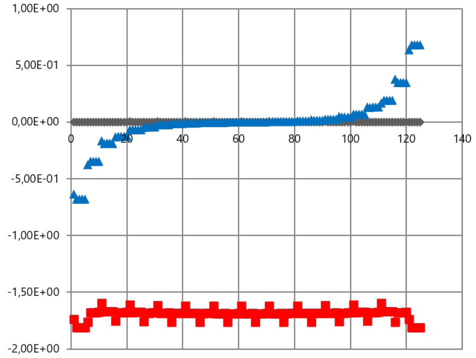

Symm. in-plane shear sample

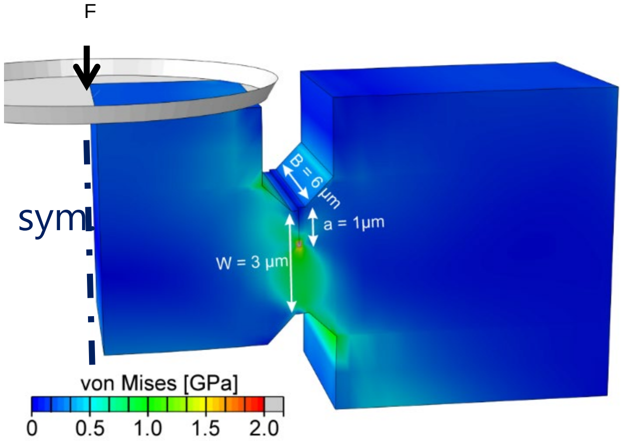

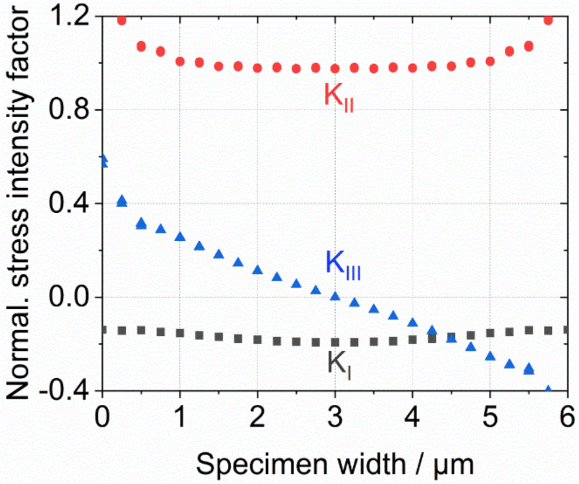

- For: 0.2<a/W<0.5

$$f(a/W)=4.14(a/W)+0.87$$

$$K_{II} = \frac{F}{2B\sqrt{W}} f_{KII}(a/W)$$

- K_{II} predominant
- K_I negligible, slightly negative because of compressive stresses
- K_{III} = 0 (average), due to Poisson ratio still present

Ast & Schwiedrzik et al., Materials and Design, 2018

Mode III / K_{III} - FE model

Ideal case

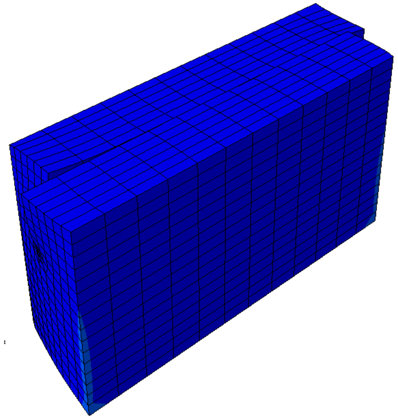

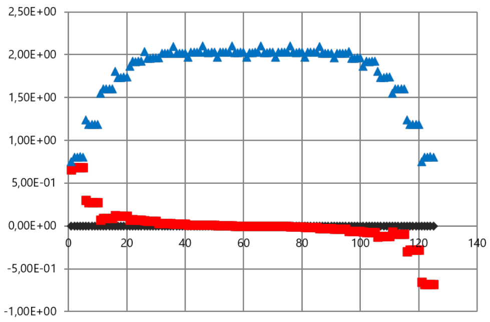

Symm. out-of-plane shear sample

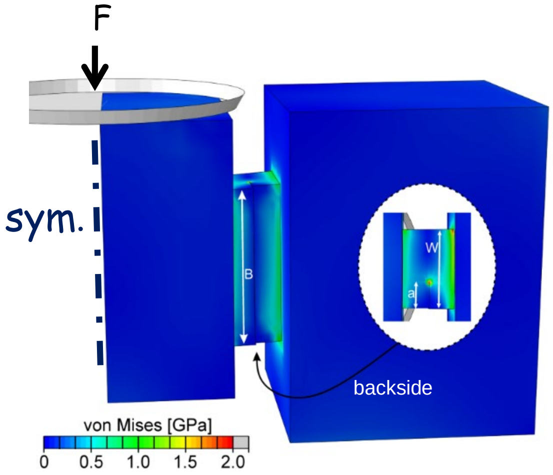

- For $0.2 < a/W < 0.5$

$$f(a/W) = 4.13(a/W) + 1.15$$

$$K_{III} = \frac{F}{2B\sqrt{W}} f_{KIII}(a/W)$$

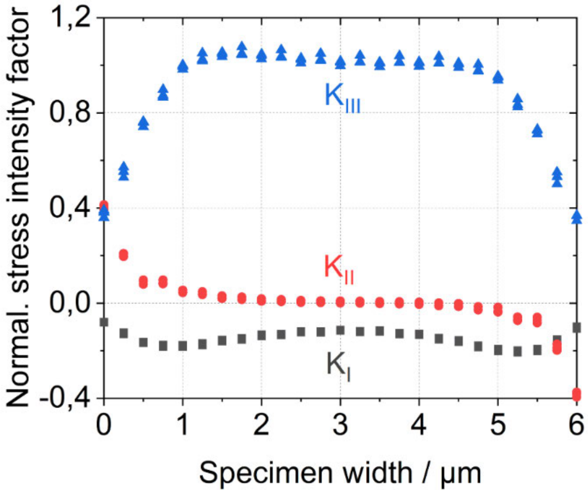

- K_{III} predominant
- K_I negligible, slightly negative because of compressive stresses
- K_{II} = 0 (average)

Ast & Schwiedrzik et al., Materials and Design, 2018

Mode I fracture testing

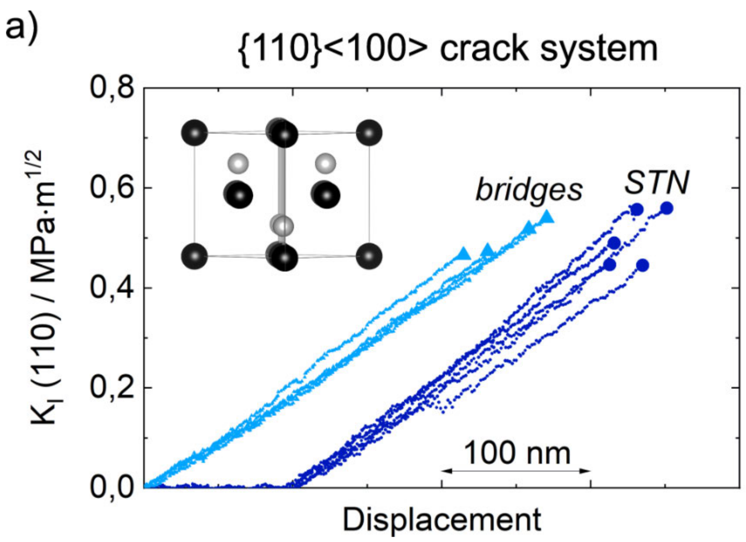

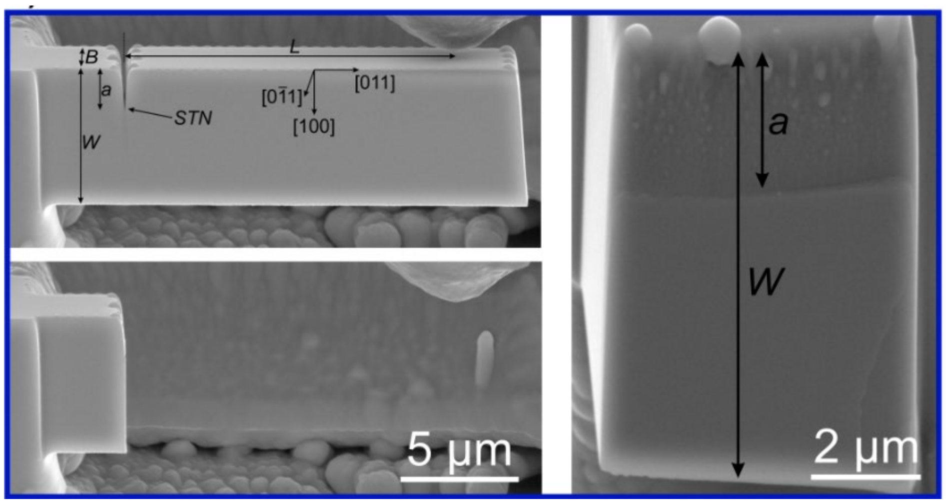

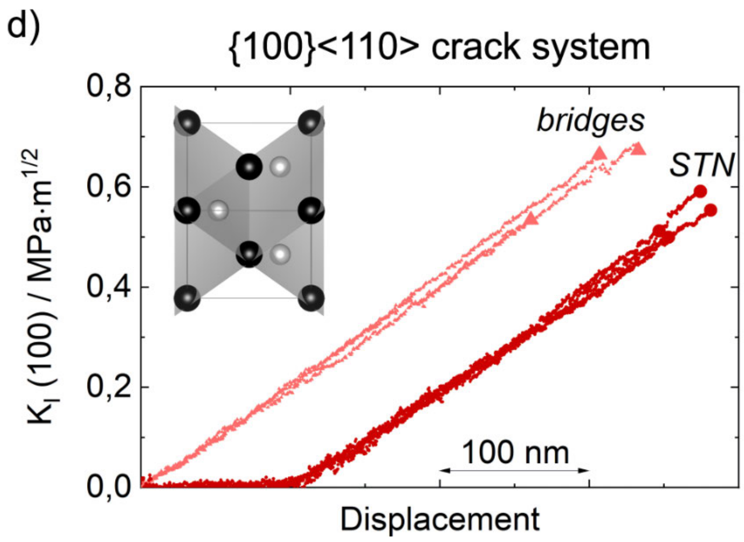

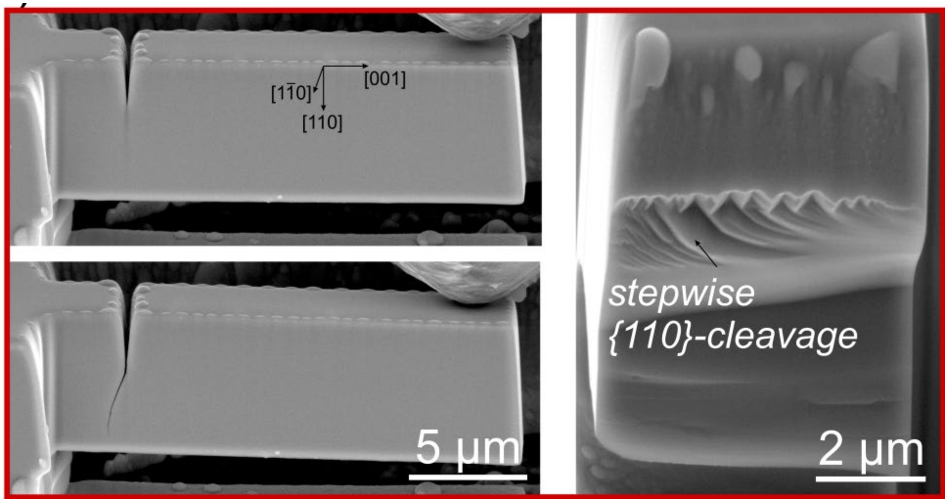

Mode II fracture testing

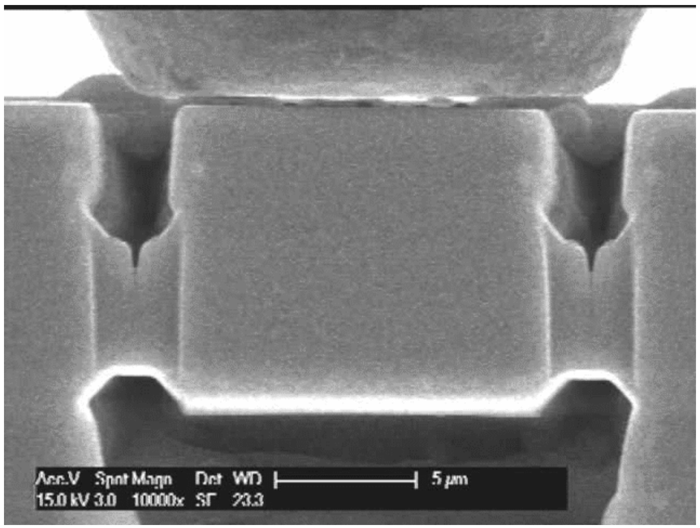

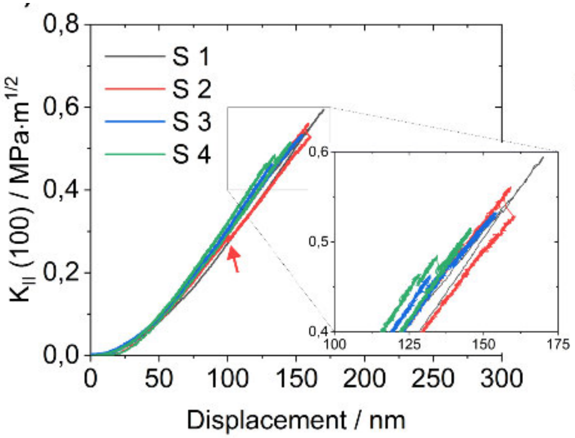

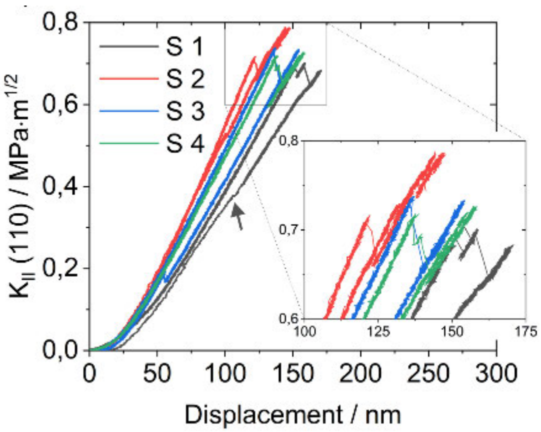

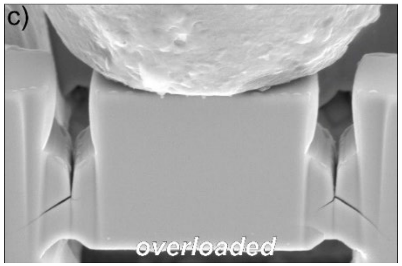

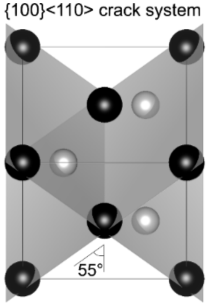

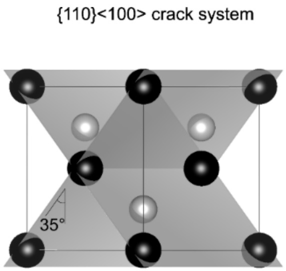

- Inclined {110} planes in both cases
- Sliding does not occur in a homogeneous crystal
- The angle between notch direction and crack propagation direction for:
  - {110}⟨100⟩: 45° → "tougher"
  - {100}⟨110⟩: 60° → closer to MTSC

Mode III fracture testing

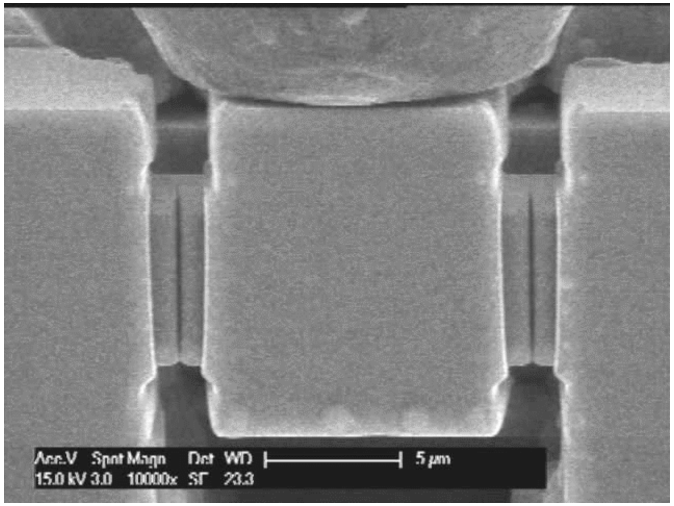

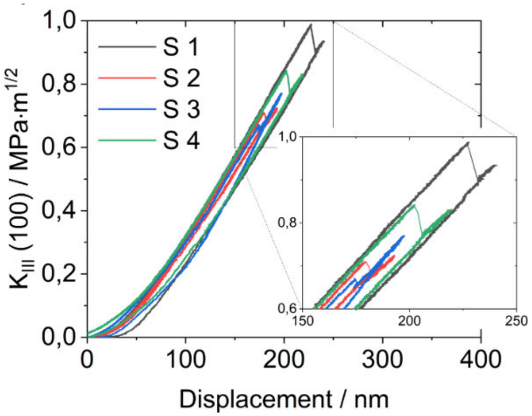

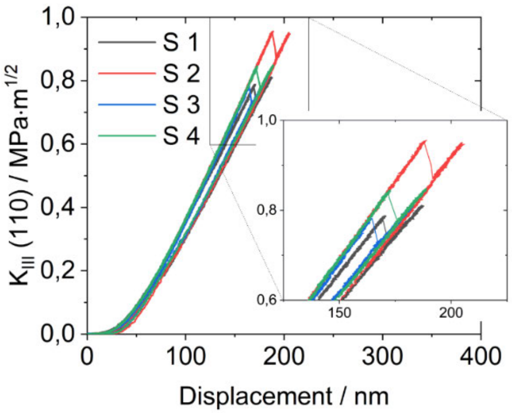

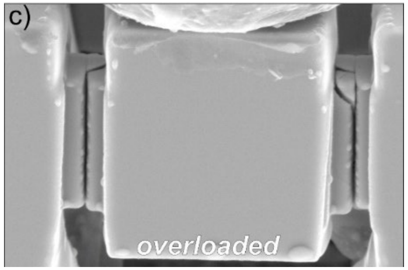

{110}<100> crack system

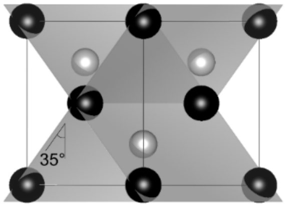

- Inclined {110} planes in both cases
- Sliding does not occur
- Complex fracture pattern
- Again: {110}⟨100⟩ slightly tougher than {100}⟨110⟩ crack system

Overview – fracture toughness

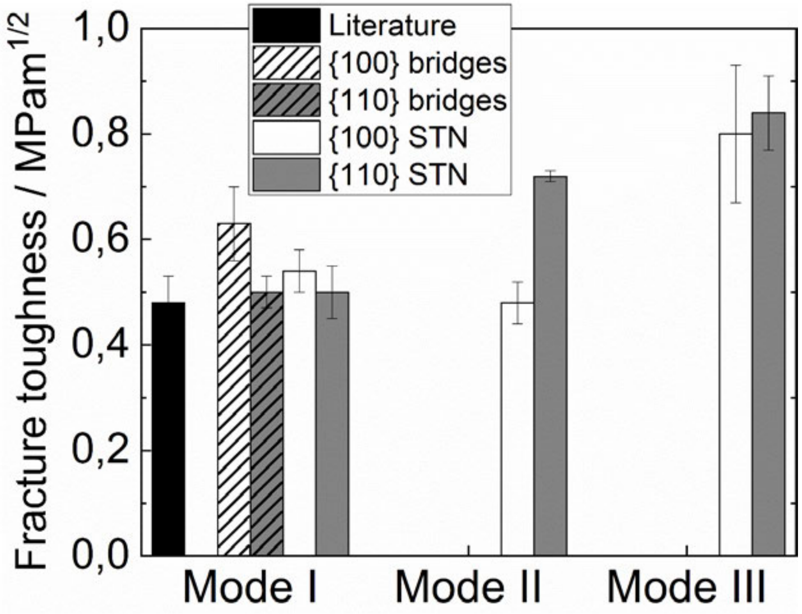

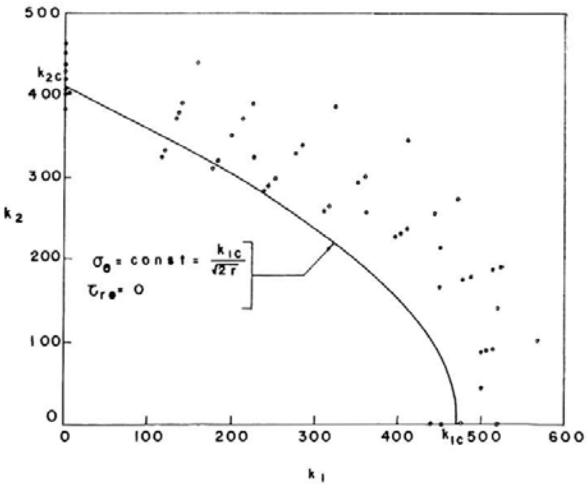

Erdogan and Sih, Journal of Basic Engineering, 1963
KI versus KII at the beginning of crack extension in a cracked plate under plane loading

- Literature data: Double-cantilever beams (DCB) and indentation fracture match results of this study
- Mode I lower bound, mode II and mode III higher

Summary and Conclusions : GaAs single crystals

- New micro-scale specimens for pure mode II and pure mode III fracture experiments were designed and characterized by FE modeling.
- Mode I, II and III fracture testing of anisotropic single crystal GaAs was performed focusing on crack systems {100}<110> and {110}<100>.
- Critical stress intensity factors of GaAs were determined for mode I, II and III loading and fracture patterns were analyzed.
- Mode I: Careful when studying anisotropic material and when applying the bridge notch (can influence fracture toughness)
- Mode II and III results confirm macroscopic studies and GaAs shows fracture anisotropy because of the preferred {110} cleavage planes

Ast, Schwiedrzik et al., Materials and Design 193 (2020)

Willkommen
Welcome
Bienvenue

Empa
Materials Science and Technology

Studying interface fracture in ceramic matrix composites

Ceramic matrix composites

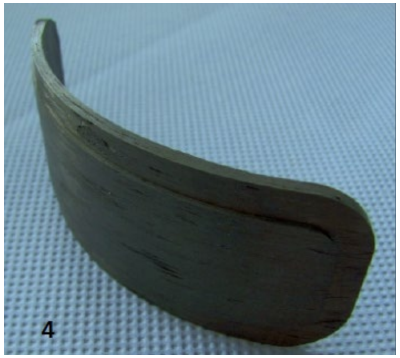

Curved tile made of SiC/SiC

SiC pipe reinforced with SiC/SiC

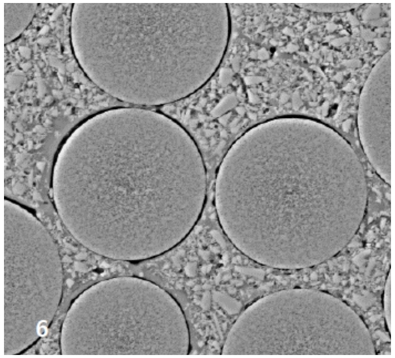

SEM image of microstructure

- Good high temperature mechanical properties, improved fracture and damage tolerance, good corrosion resistance in air and fuel gas atmosphere
- Complex shaping and geometries possible (large and thin walled components)
- Applications: Aero-engines, nuclear technology (radiation tolerance)
- SiC fibers surrounded by a SiC matrix with a Pyrolytic carbon (PyC) interphase
- Knowledge of interface toughness necessary to allow proper design of components

Failure along PyC interphase: Push-out test

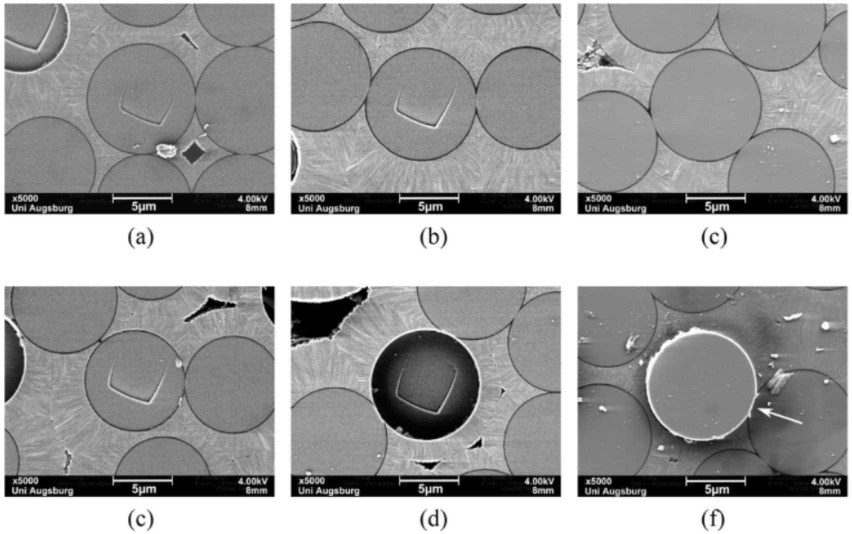

(a) (b) (c)

(c) (d) (f)

Mueller et al., J. Eur. Ceram. Soc., 2013

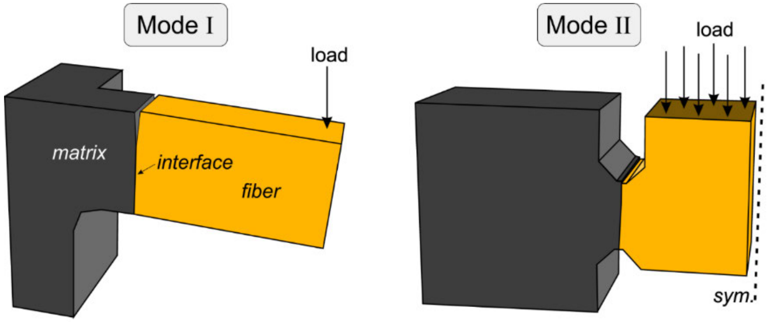

Ast, Schwiedrzik et al, Mat. & Des., 2020

- State of the art: Fiber push-out tests using a flat punch indenter
- Assumptions concerning stress distribution and crack growth along interface
- Can novel micromechanical specimens measure local fracture toughness more accurately?

Micromechanical sample development

- Parametric finite element simulations were performed varying notch depth, interphase thickness, and interphase stiffness
- Analysis of KI,II,III distributions at the notch root show that one mode is dominating in each specimen geometry
- The geometry factor was determined and normalized by the varied parameters to allow quantitative analysis of the experimental force measurements

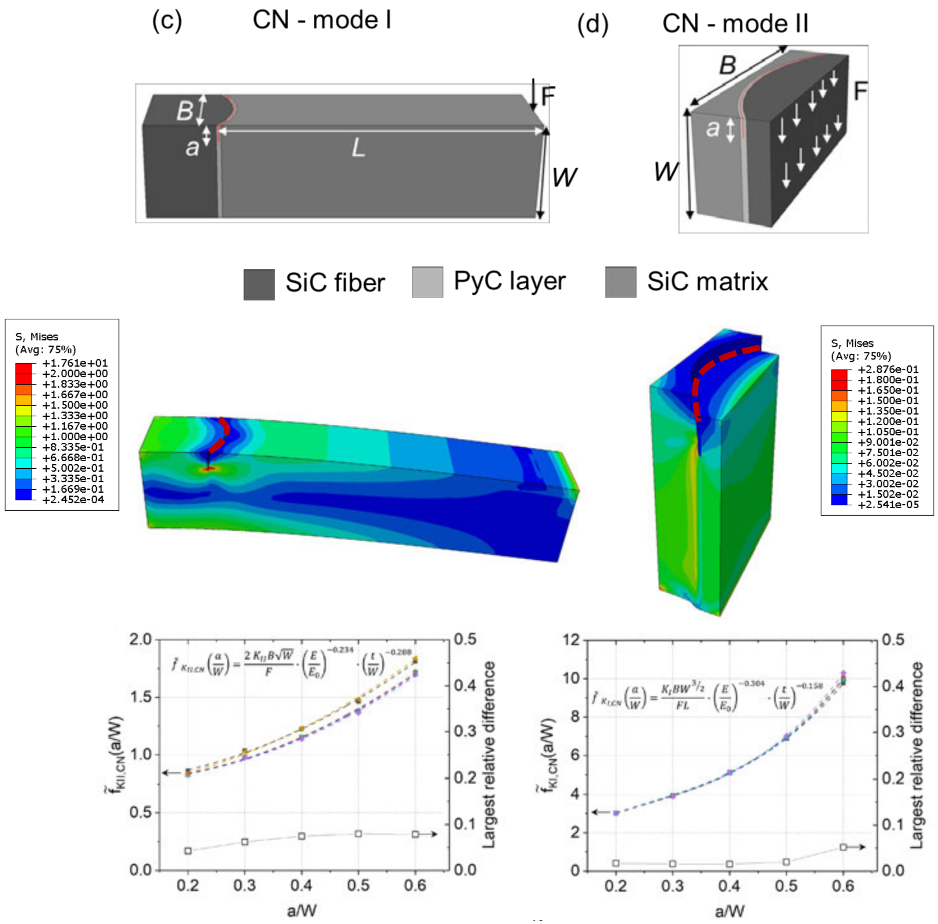

Ast & Tian et al., Acta Materialia, 2023

Empa
Materials Science and Technology

Micromechanical sample preparation

- Ps laser ablation of large areas to create edge near visible SiC fibers in correct orientation
- FIB milling from top and side to create freestanding cantilevers at a fiber-matrix interface
- Optimization of FIB settings at low currents to generate sharp and reproducible notches with known depth
- Cutting of curved notches along the PyC interphase

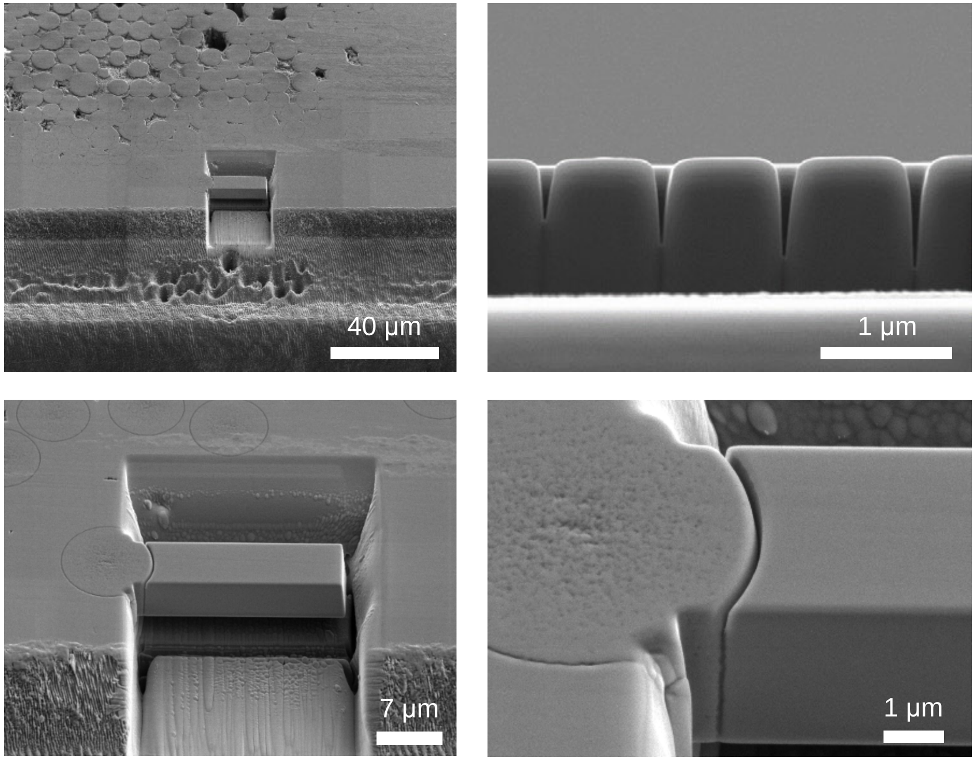

Experimental setup

- Preparation of notched and unnotched specimens loaded in bending and shear
- Testing inside a SEM using an in situ micromechanical tester
- Simultaneous measurement of force and displacement allows fracture mechanical analysis

FIB/SEM Crossbeam Auriga

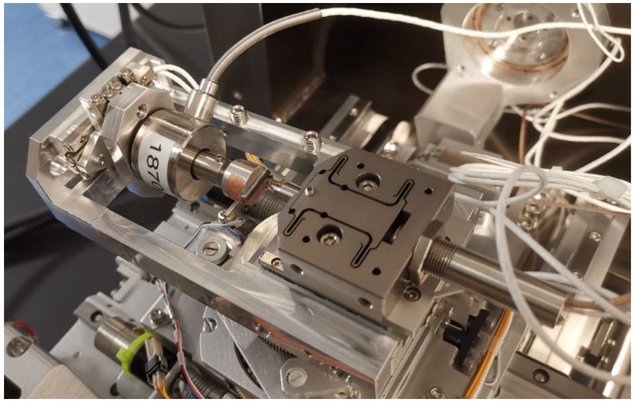

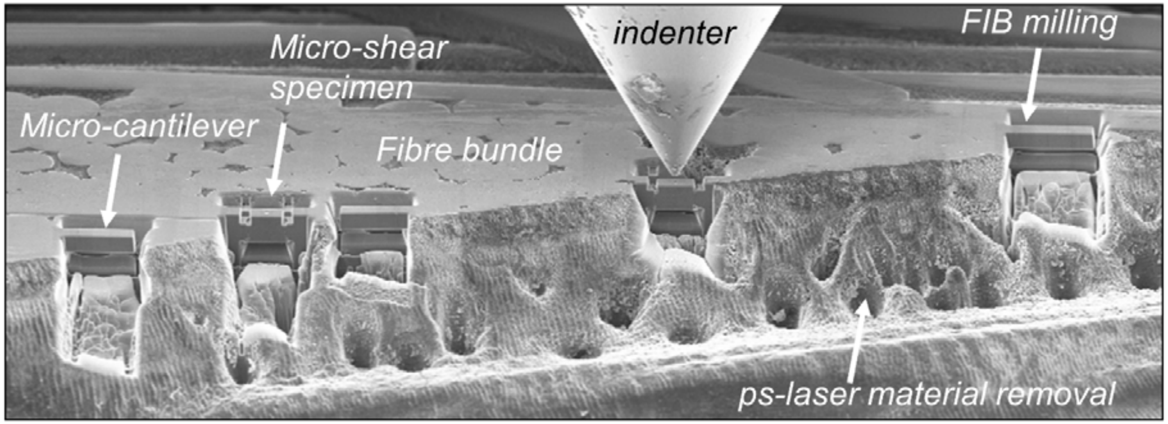

Interfacial fracture toughness – mode I

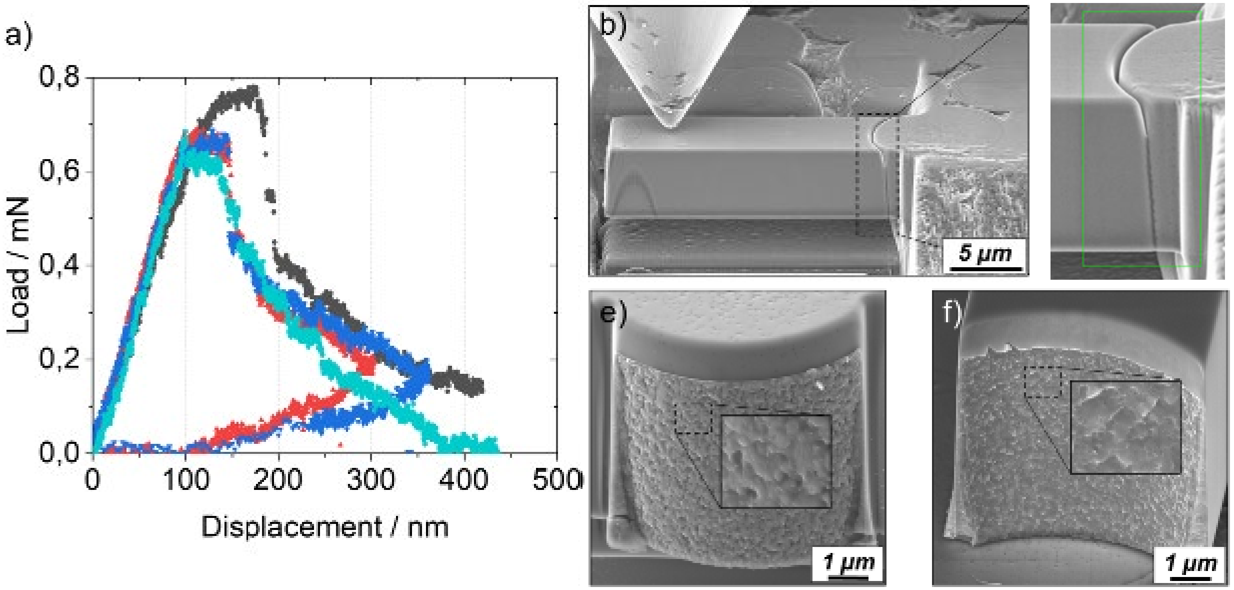

- Consistent fracture loads: K_{IC} of PyC interphase is $0.24 \pm 0.02\ \mathrm{MPa}\sqrt{\mathrm{m}}$
- Fracture surfaces are consistent with fiber-PyC interface failure
- Crack deviates from fibre-PyC interface at free edges due to complex stress state

Interfacial strength – bending

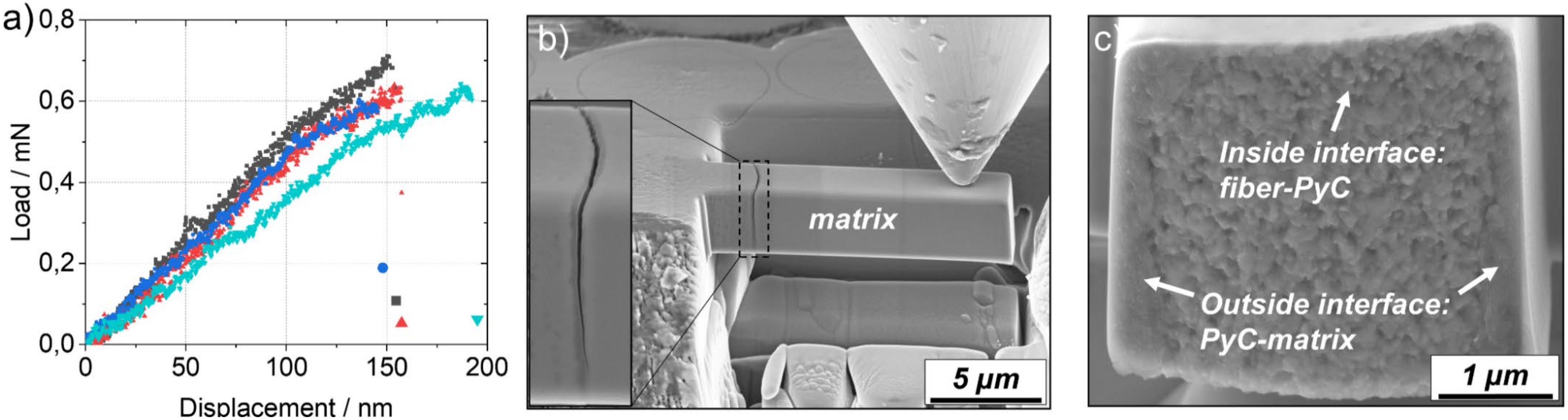

- Loading of unnotched cantilevers allows measuring interfacial strength
- PyC interphase strength in bending: 934 ± 137 MPa
- Failure along the fibre-PyC interface on the inside, crack deviates at free edges

Interfacial fracture toughness – mode II

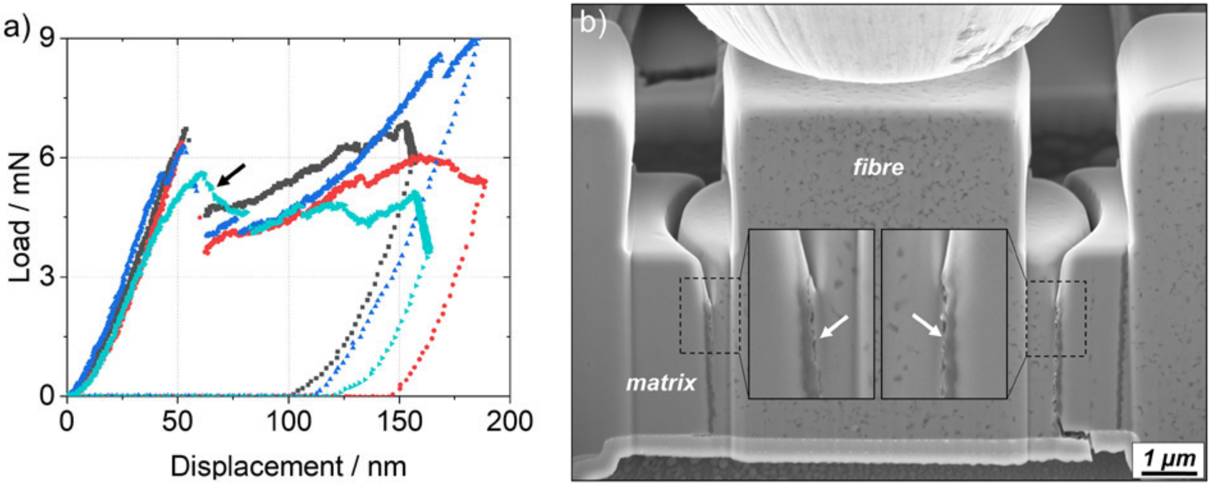

- K_{IIC} of PyC interphase: 0.17±0.06 MPa√m
- Higher variation likely due to small deviations from perfect symmetry
- Crack travels consistently along the fibre-PyC interface

Interfacial strength – shear

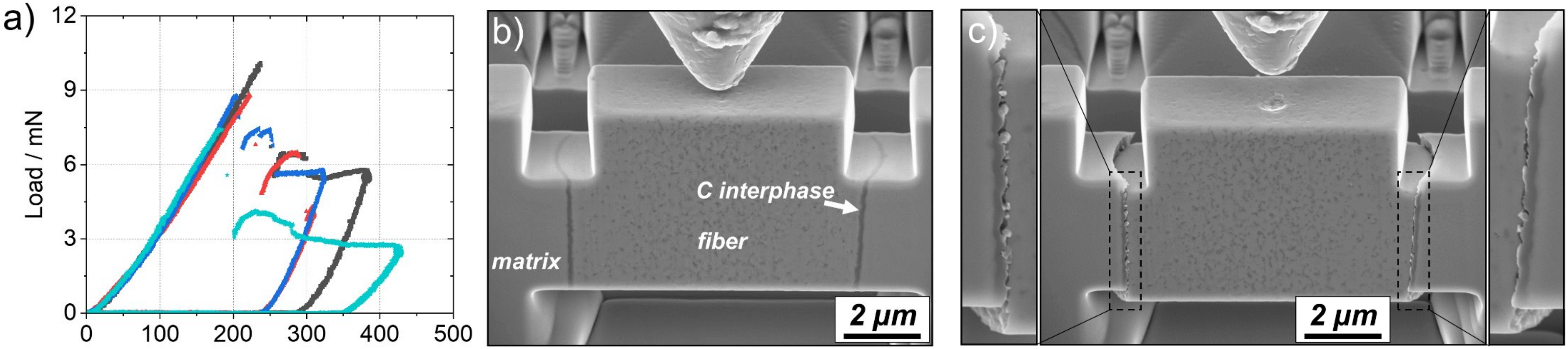

- Loading of unnotched shear specimens allows measuring shear strength
- PyC interphase strength in shear: 418 ± 36 MPa
- Cracking in shear mode along fibre-PyC interface

TEM lamella lift-out at fiber-matrix interface

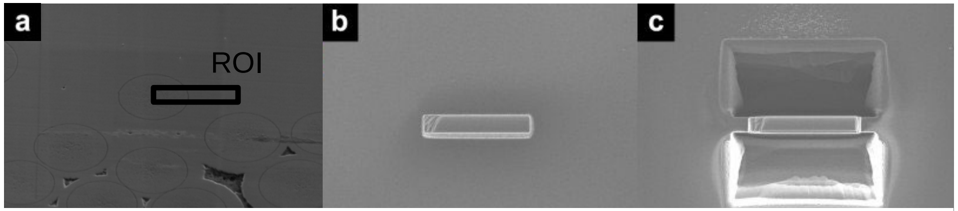

ROI   1. Protection layer   2. Trenches milling

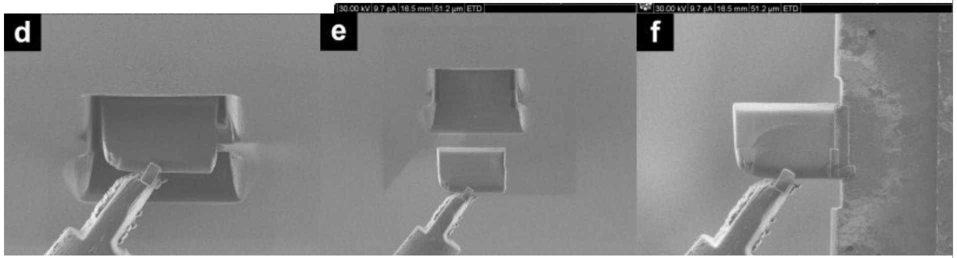

3. Manip. attachment   4. Free lamella   5. Grid attachment

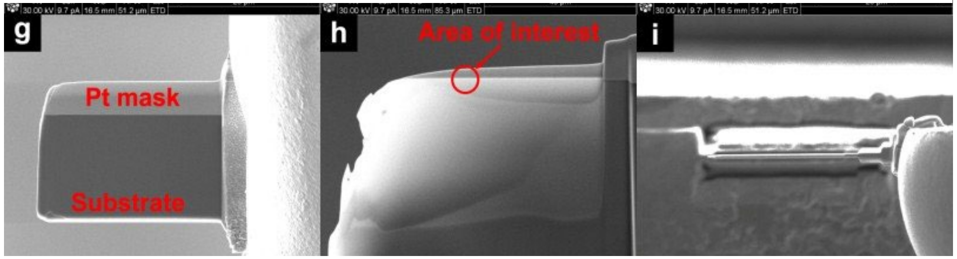

6. Man. detachement   7. Polishing   8. Glancing incidence

Why does the fibre-PyC interface fail?

- TEM lamellae were prepared by a FIB lift-out technique
- TEM highlights different grain structure of fiber and matrix
- Interface between SiC fiber and PyC interphase is rougher compared to the PyC-matrix interface
- Crack in a confined system steers towards the more compliant phase
- Theoretical defect size was computed to be around 20nm-
- Local defects of 20-50nm size can be found at the fiber-PyC interface

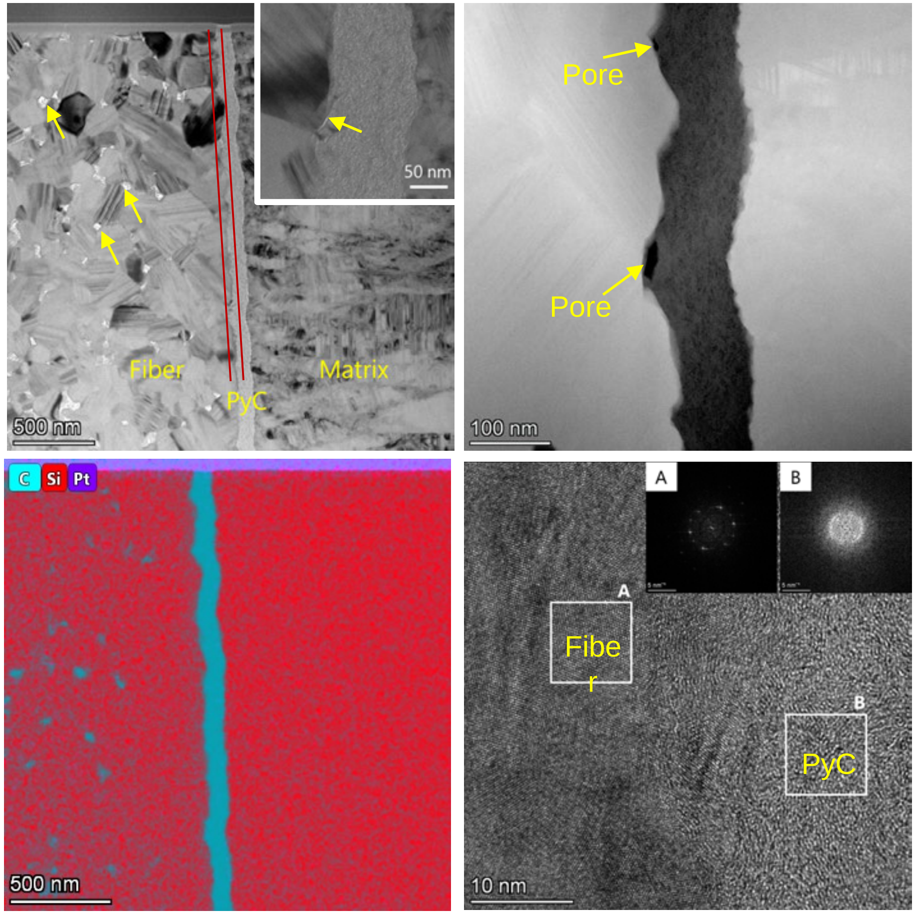

Summary

- Novel FIB-based specimens were developed that allow probing of local mechanical properties of thin interphases
- Mechanical characterization of the specimen geometries by parametric finite element analysis allows interpreting the experiments in a quantitative fashion
- Consistent measurements of fracture toughness and strength under bending and shear loading can be obtained
- PyC interphase is stronger and tougher in bending than shear
- Failure always occurs at the fibre-PyC interface
- Bending strength is consistent with flaw size found in TEM analysis

Micromechanics at extremes

High temperature testing

Motivation for high temperature testing

- Measurement of properties at application relevant temperatures
- Identification of ductile-brittle transition temperatures
- Measurement of mechanical properties at varying temperature allows identifying deformation mechanisms based on thermal activation analysis

Challenges in elevated temperature nanoindentation

$$\text{experimental data} = \text{mechanical deformation} + \underbrace{\text{thermal drift behavior}}_{\text{artifact of measurement due to thermal effects}} + \underbrace{\text{noise}}_{\text{instability of the measurement system}}$$

thermal drift – drift occurs due to thermal expansion of the indenter tip and load frame

system stability - control electronics and sensors must be protected from heat to avoid noise in experimental data

sample and tip oxidation - undesirable for surface property testing. oxidative loss of diamond will damage the indenter tip at high temperatures (>400 degrees C) without high vacuum or high purity inert gas.

frame drift on heating to 200°C

thermal drift

schematic load-displacement curve

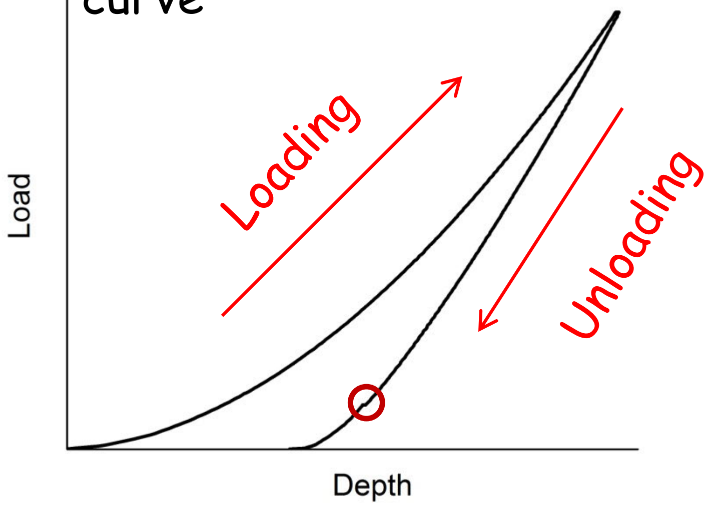

thermal drift data

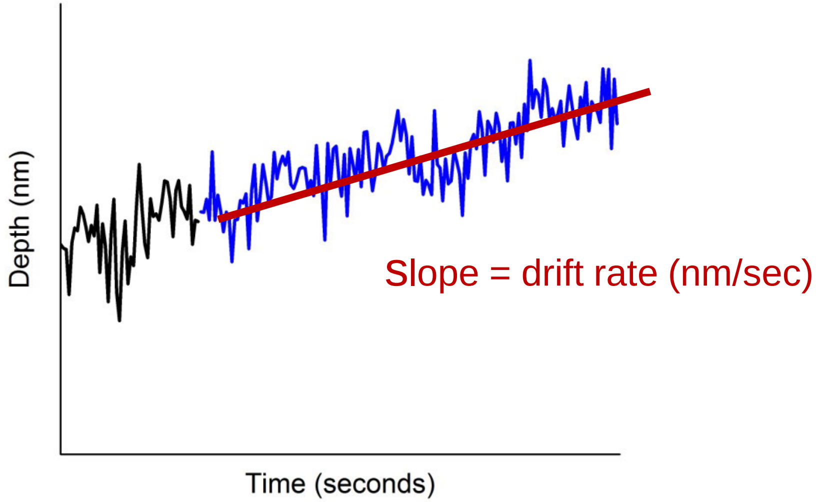

○ thermal drift measured at 10% peak load value during unloading, typically less than 0.05nm/sec at RT

effect of drift rate on hardness

$$H = \frac{F_{max}}{A_c}$$

Let's assume an ideal tip area function for simplicity. $A_c = 24.5\ d^2$

Let maximum depth of penetration be 'd' nm.
Let drift rate be 'r' nm/sec
Let loading time be 't' sec

Let the data unaffected by drift be represented by H_1
Let the data affected by drift be H_2

Therefore, change in hardness due to thermal drift (ΔH) = $(H_2 - H_1)/ H_1$
If we take 5% change in hardness as the tolerance in our experiments:

$$\Delta H = \frac{H_2 - H_1}{H_1} = \frac{\frac{Fmax}{24.5\,(d+rt)^2} - \frac{Fmax}{24.5\,d^2}}{\frac{Fmax}{24.5\,d^2}} = 0.05$$

Rearranging, we obtain:

$$1.05r^2t^2 + 2.1\,drt + 0.05d^2 = 0$$

hardness with 5% error

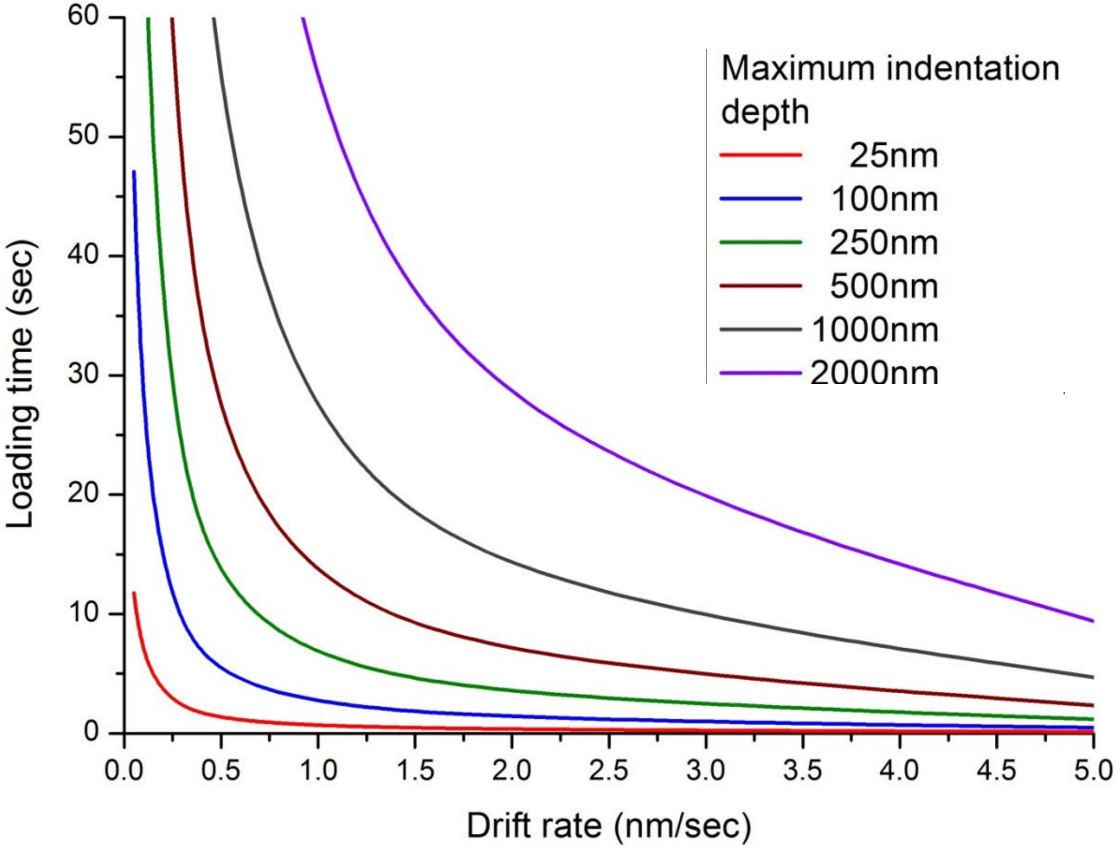

low thermal drift rates essential for accurate property measurement at elevated temperatures and low indentation depths

solutions to overcome thermal drift

frame drift

(a) long stabilization times to heat the tip passively – sample heating

(b) heating both indenter and sample separately - indenter tip heating

(c) active surface referencing – differential displacement measurement

contact drift

(a) tip-sample surface temperature matching - Calibrating and matching the tip temperature with the sample surface temperature in case of sharp tips

(b) use flat punch – constant contact area during indentation/micro-pillar compression

electronic drift

(a) contain heating locally to avoid heat flow back to the sensors/electronics by water cooling

System Thermal Drift

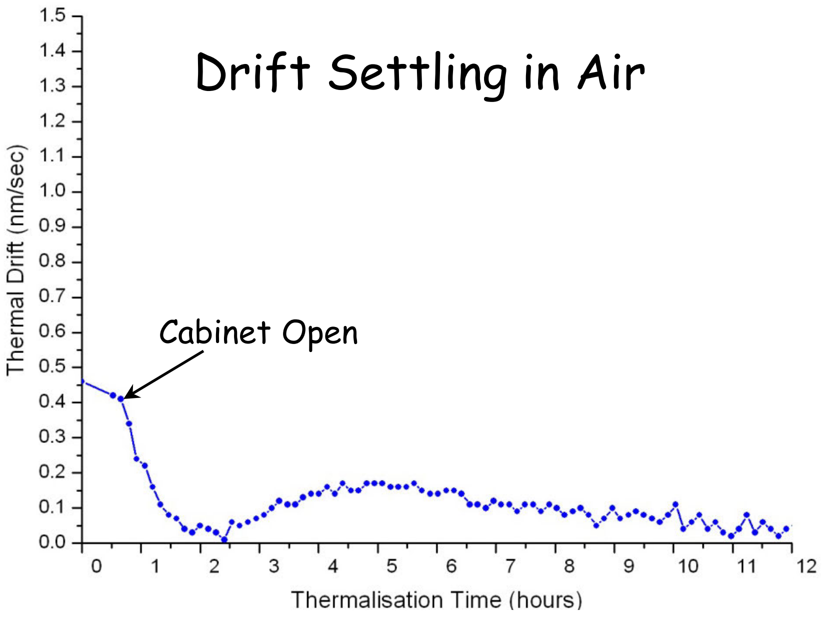
Drift Settling in Air

Cabinet Open

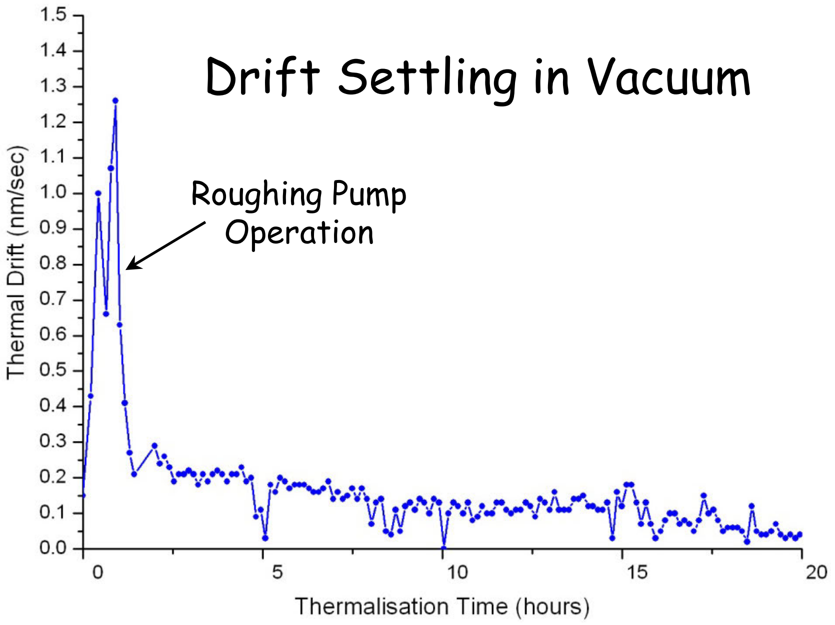
Drift Settling in Vacuum

Roughing Pump Operation

- Air currents from opening cabinet disturb system.
- System temperature achieves uniformity by convection.

- Vacuum pumping disturbs system.
- System temperature reaches uniformity by conduction.

Tip-Sample Heating

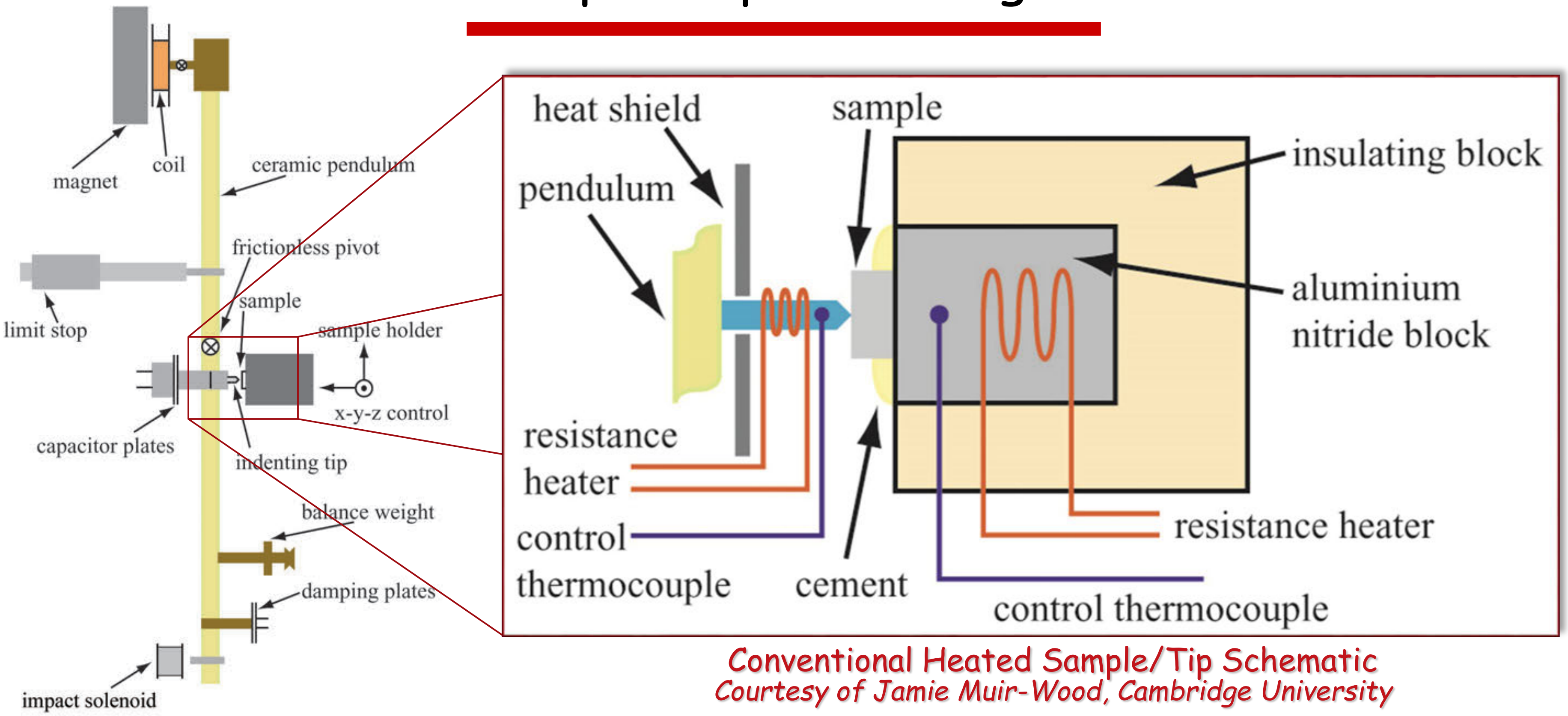

Conventional Heated Sample/Tip Schematic
Courtesy of Jamie Muir-Wood, Cambridge University

- Heater schematic for a MicroMaterials ltd. Nanoindentation system.
- Horizontal indentation plane avoids convective heating problems in atmosphere; vacuum removes convection.
- Tip and Sample heaters/thermocouples on independent feedback loops allow testing to be performed at thermal equilibrium.

Thermal Drift at Elevated Temperature

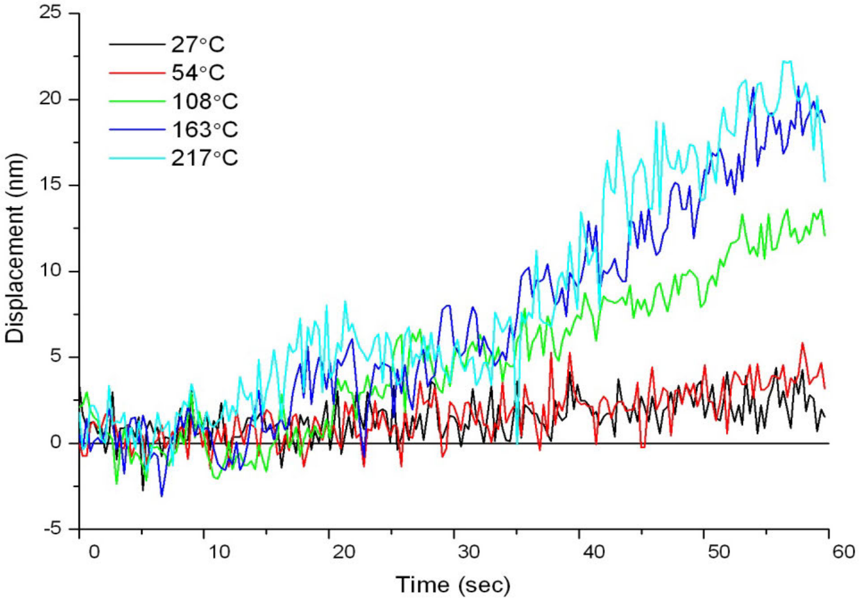

Tip and Sample at Nominal Temperature

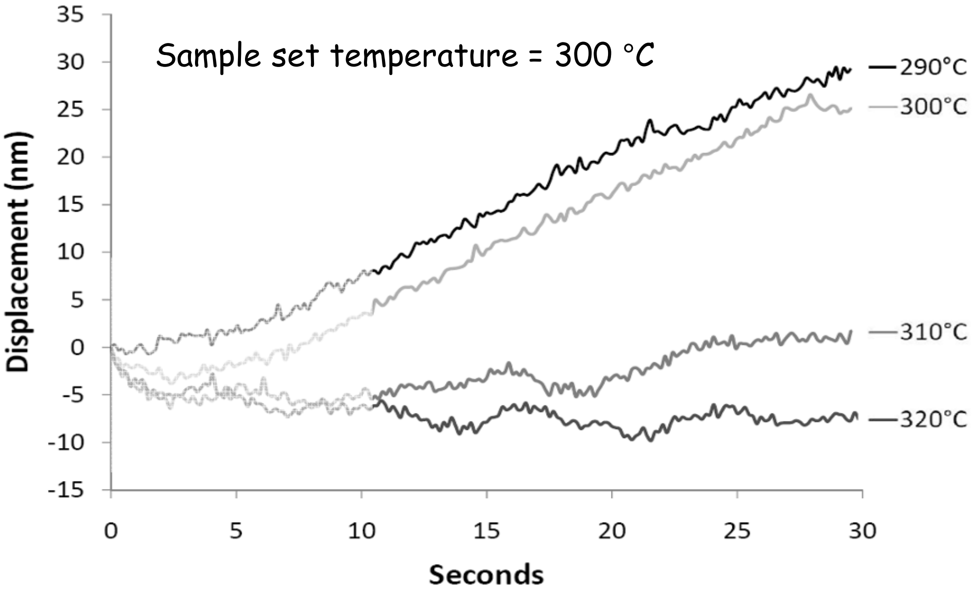

Tip Temperature Tuned

Courtesy of Sandra Korte, Cambridge University

- Heating both the sample and tip is required to achieve thermal equilibrium, but this does not immediately remove issue of drift.
- Thermocouples cannot be placed exactly at the contacting surfaces, so there is a gradient between measured and true temperature.
- True tip temperature can be calibrated, but variation in sample geometry and thermal conductivity prevent simple sample temperature calibration.
- Assuming drift is zero at thermal equilibrium, varying sample temperature until drift drops to zero achieves both zero drift and accurate sample temperature.

Sample Oxidation

- Nearly all metals oxidise.
- Reactive metals such as Samarium can oxidise quickly at room temperature.
- Careful preparation is required to maintain the oxide thickness on a sample does not interfere with indentation measurements.

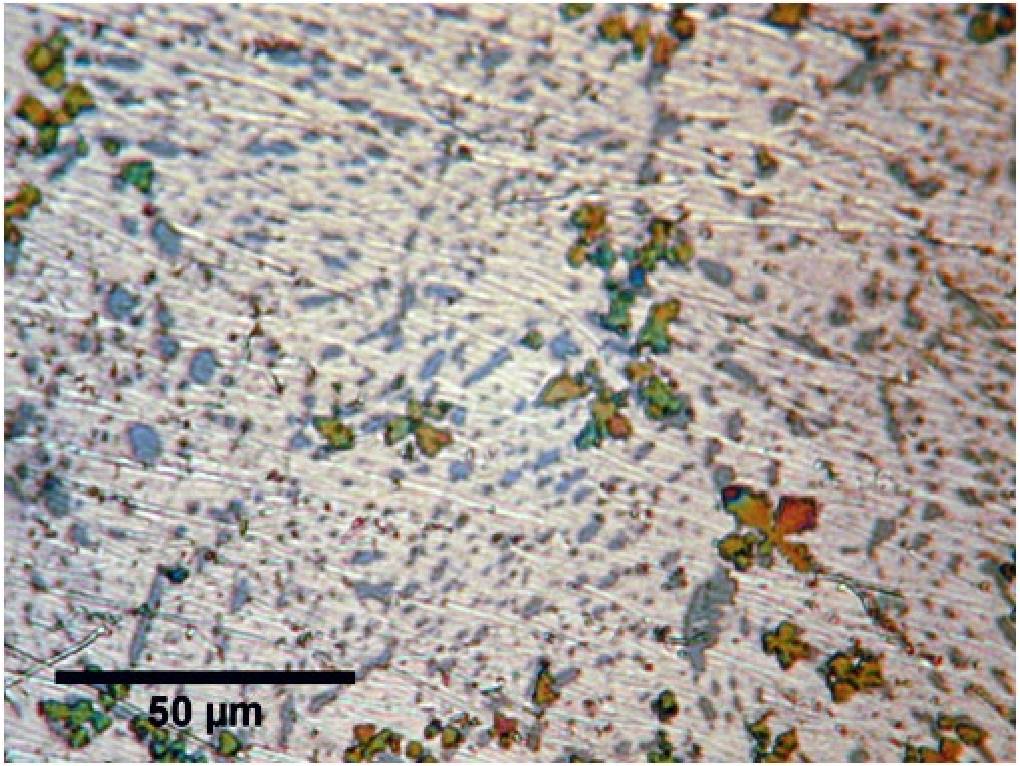

Samarium: 1 hour after polishing in air.

Sample Oxidation: Theory

- At elevated temperatures, oxidation rates increase.

- Nickel Oxide growth rates exhibit parabolic kinetics,

$$x \propto \sqrt{t}$$

- After 1 hour at 750°C, oxide thickness:
  - ☐ ~450nm at 1 bar of O_2
  - ☐ ~30nm at 10^{-6} bar of O_2

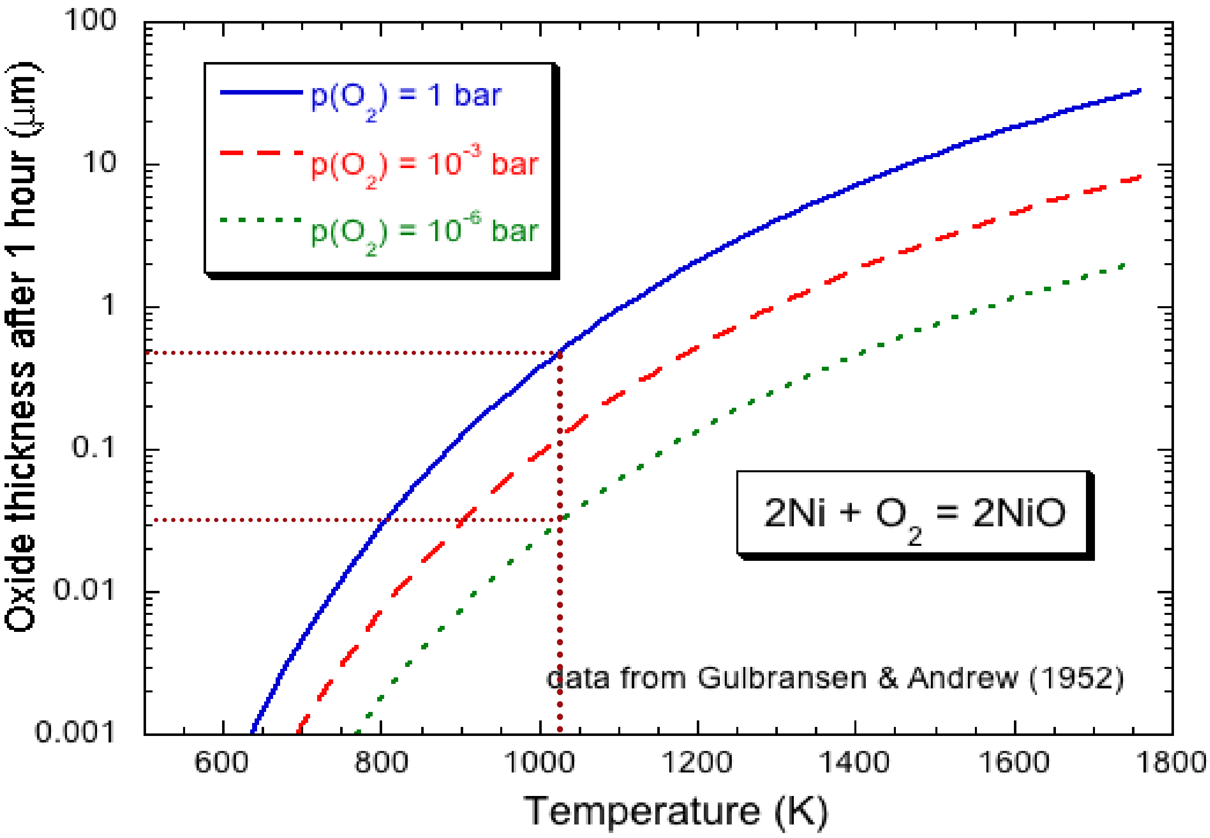

- High vacuum allows nano-micro scale mechanical testing at elevated temperatures with minimal interference from surface oxide layer and prevents oxidative erosion of small features of interest.

Sample Oxidation: Prevention

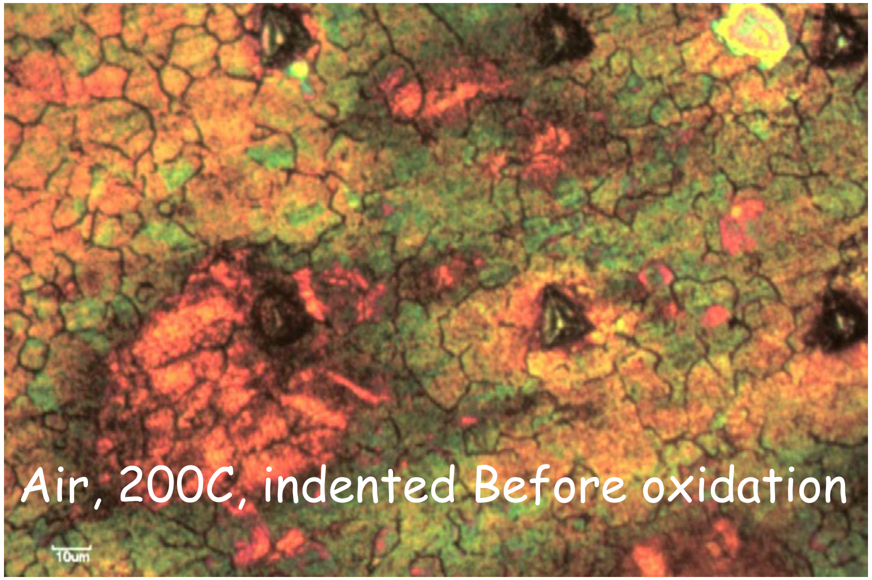
Air, 200C, indented Before oxidation

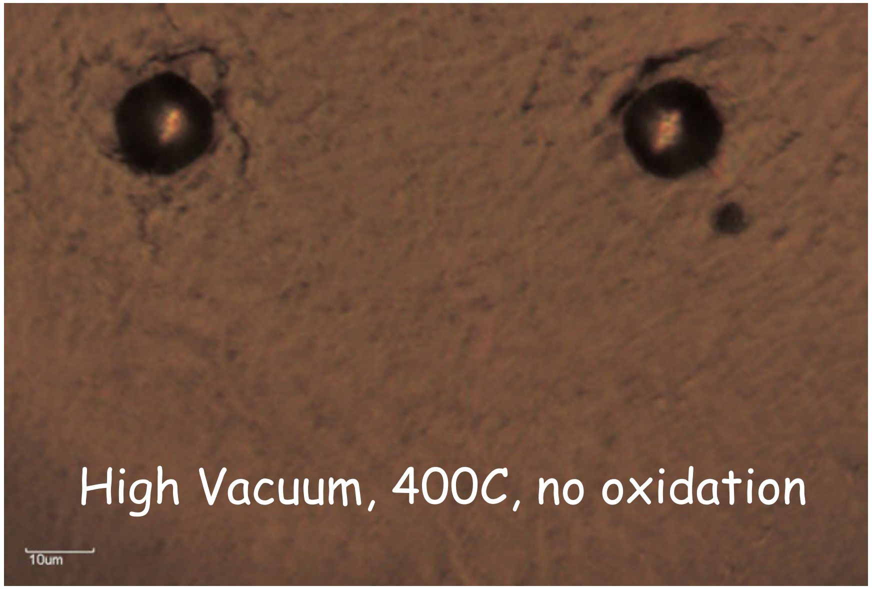
High Vacuum, 400C, no oxidation

- Copper indented in Air at 200C oxidised rapidly within 12 hours.
- Indents made prior to oxidation show some preferential oxidation.
- Indents performed in High Vacuum show no visible evidence of oxidation. Any oxide is too thin for optical inference colors to form.

Tip Oxidation: Theory

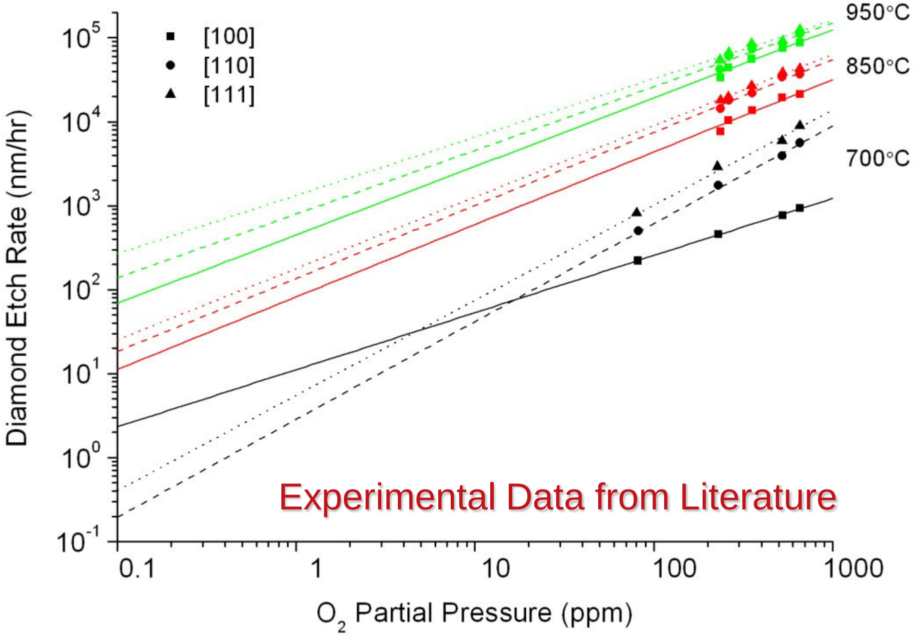

Experimental Data from Literature

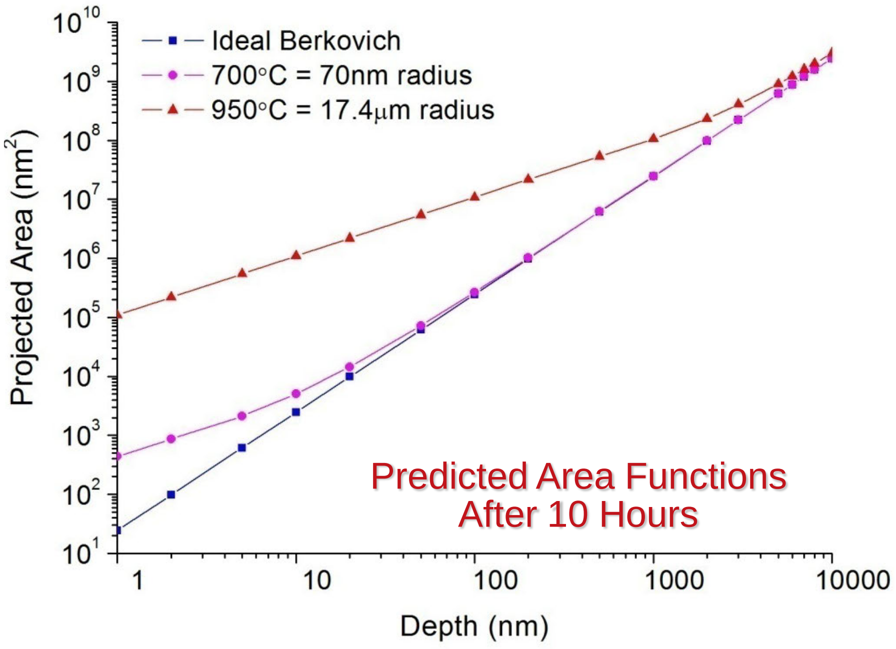

Predicted Area Functions
After 10 Hours

- Literature data (Evans and Phaal, 1962) taken under flowing O_2 at varying pressure and temperature.
- Extrapolated mean diamond etch rates between low angle crystal faces :
  - 0.5nm/hr at 700°C.
  - 150nm/hr at 950 °C.

- Area functions calculated by approximating tip as conospheroid with tip blunted by etch distance.
  - Blunting at 700°C is tolerable or within manufacturing limits.
  - Blunting at 950°C is excessive.

Tip Oxidation – Morphology

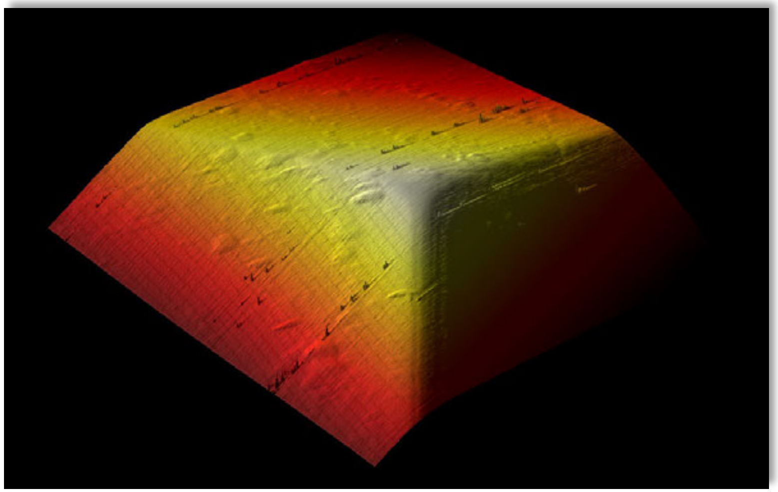

450C in Air for 30 minutes

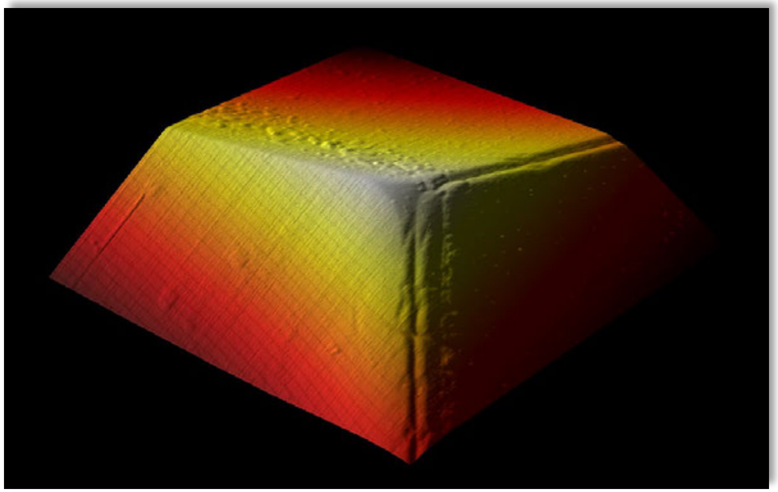

750C in Argon (15ppm O_2) for 90 minutes

- Berkovich tip exposed to three successive atmospheres.
    - 30min in Air at 450°C.
    - 90min in Argon at 750°C.
    - 90min in Argon at 900°C.
- Faces get smoother after exposure below 900°C, though edges blunt.
- Pitting is observed after 900°C exposure.

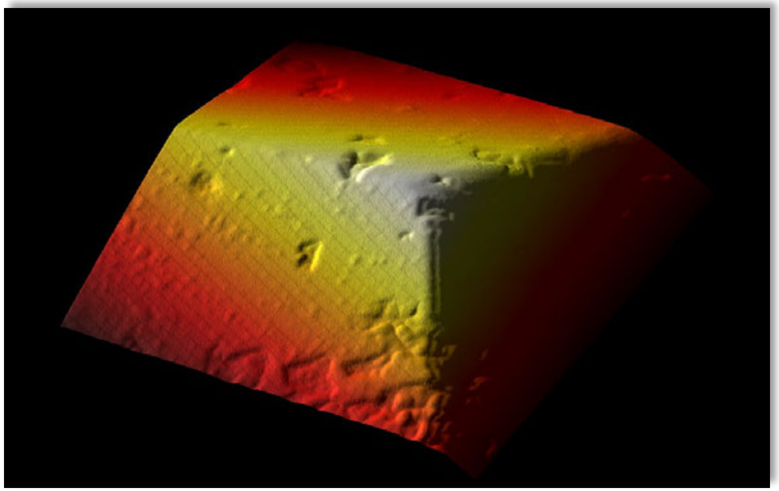

900C in Argon (15ppm O_2) for 90 minutes

Tip Oxidation: Area Functions

- Initial blunting at intermediate temperature appears the worst.
- At elevated temperatures, the tip can appear to become sharper due to edge grooving, but this is not real sharpening.

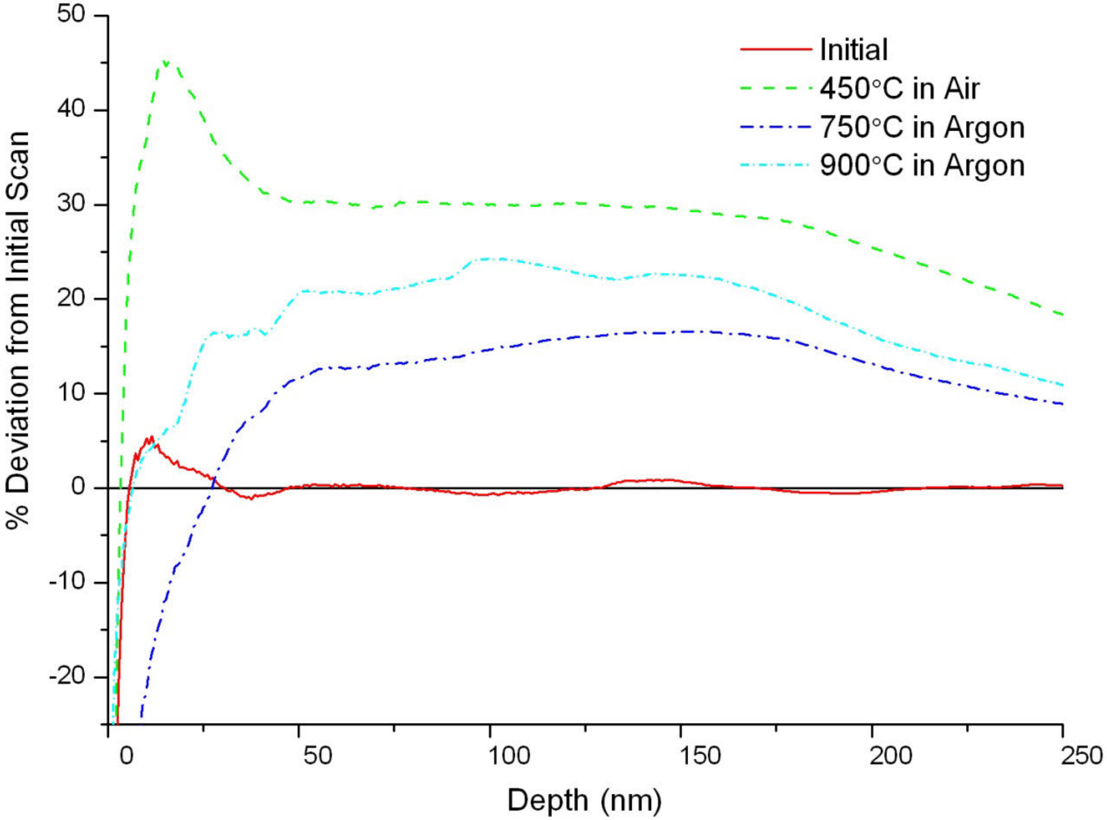

Change in Diamond Area Functions after Oxidation

Tip-Sample Reactions

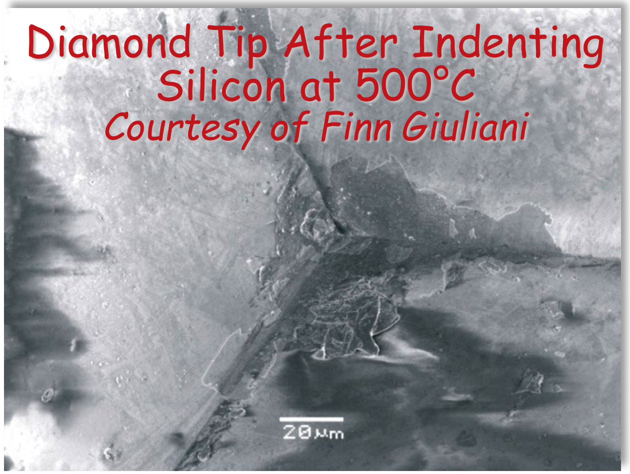
Diamond Tip After Indenting Silicon at 500°C

Courtesy of Finn Giuliani

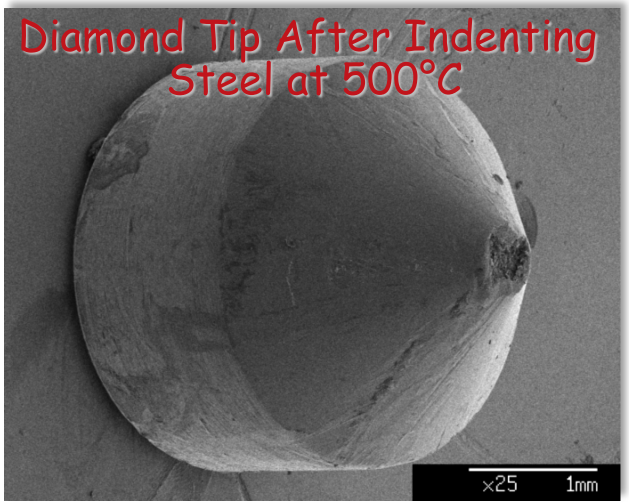
Diamond Tip After Indenting Steel at 500°C

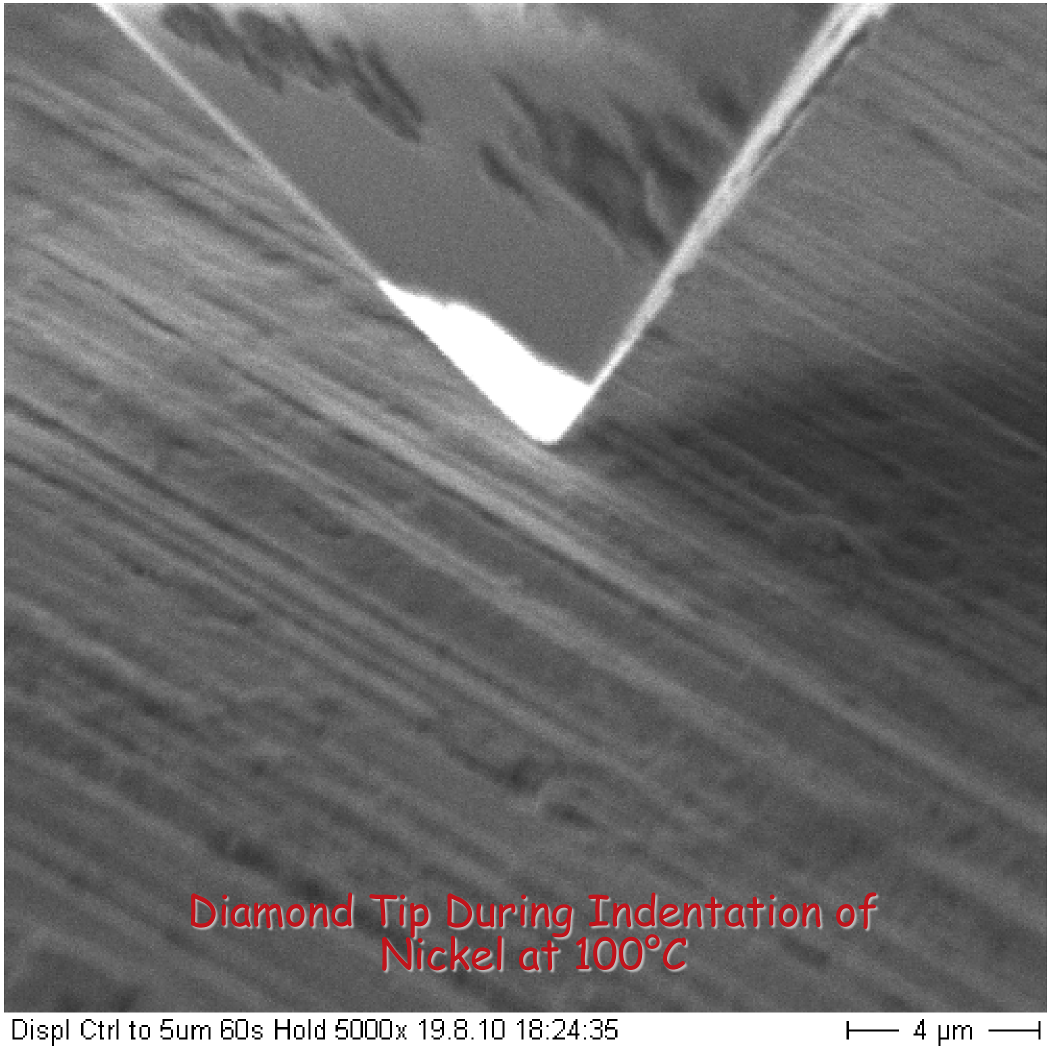
Diamond Tip During Indentation of Nickel at 100°C

in-situ SEM high temperature system

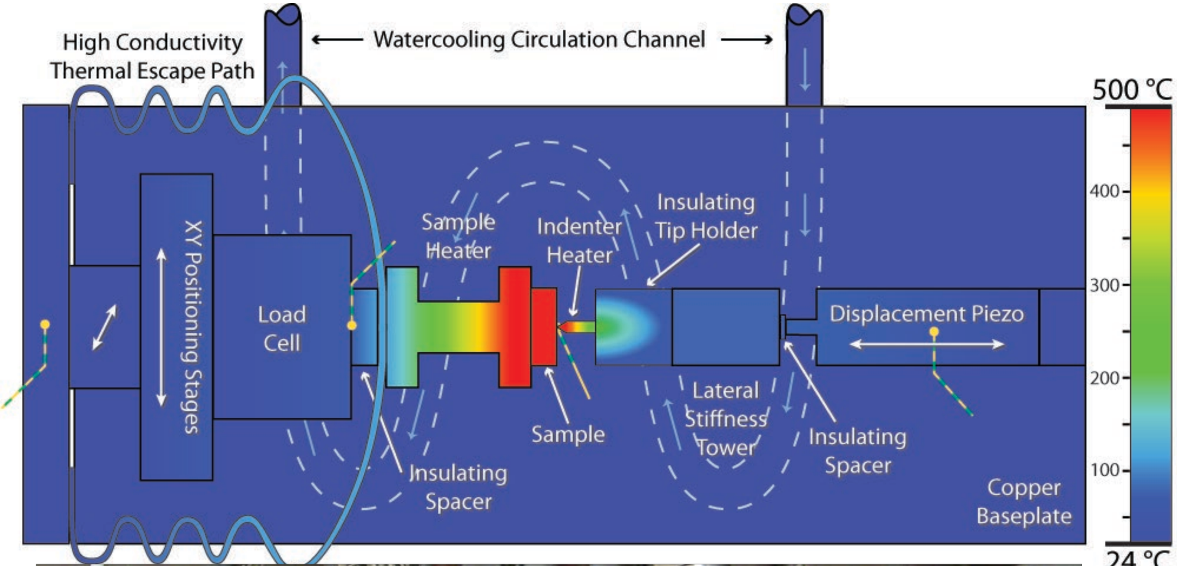

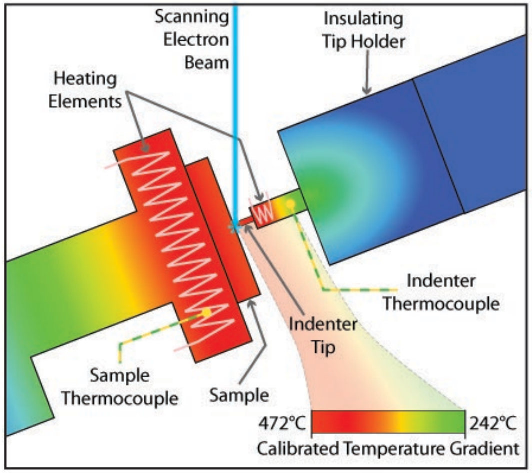

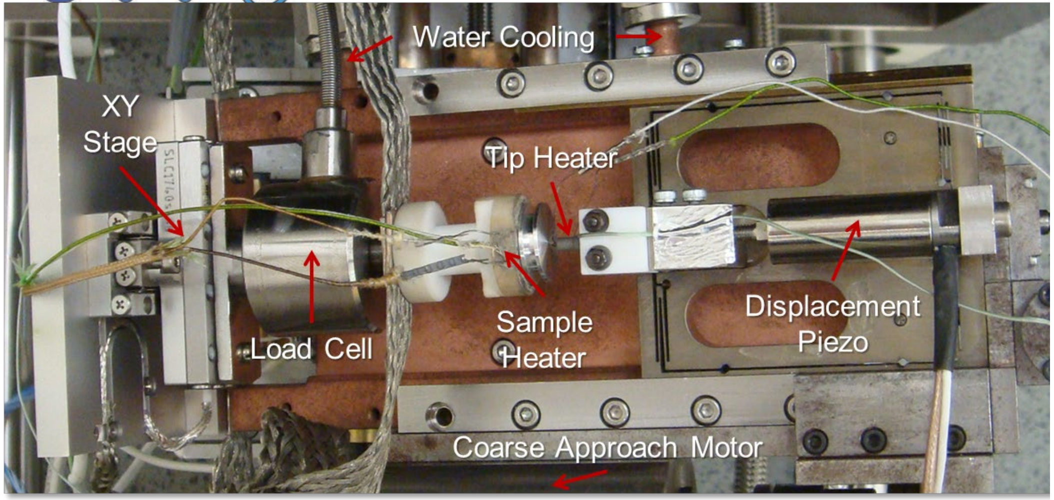

indenter temperature tuning

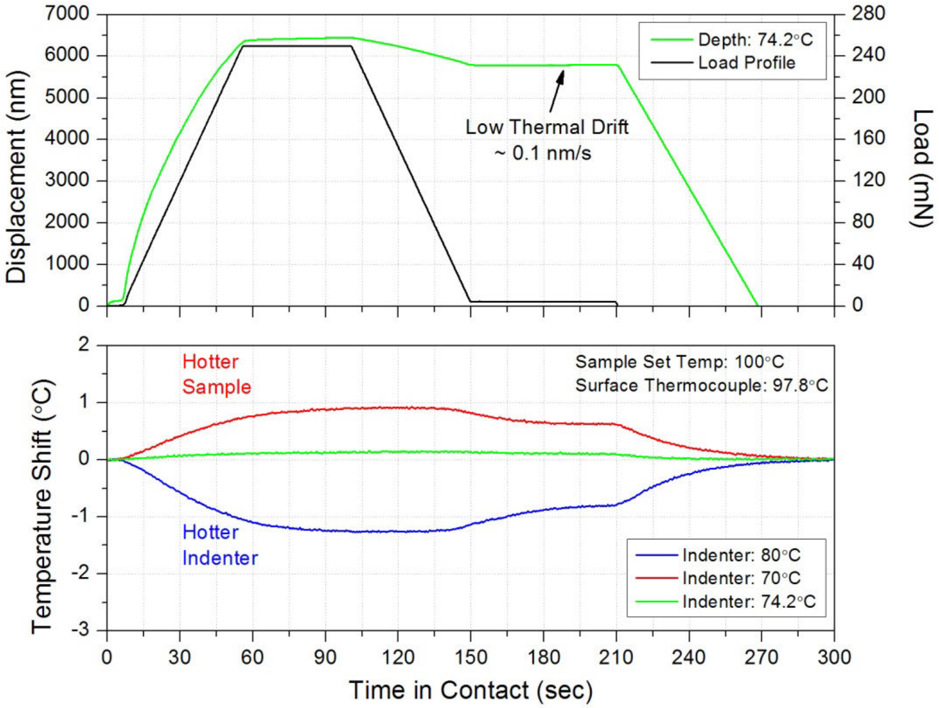

*Displacement vs. Temperature Change

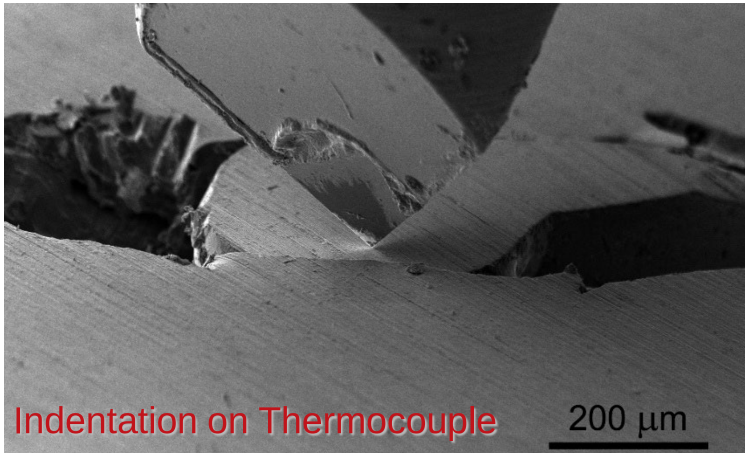

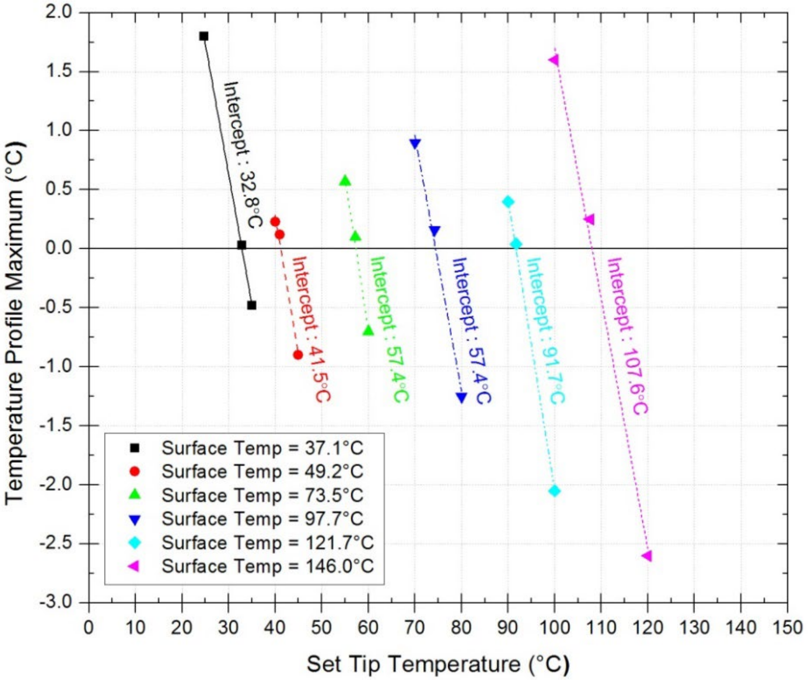

Temperature Shifts at several Surface Temperatures

JM Wheeler, P Brodard & J Michler,
Phil Mag, 92 (2012) 3128-3141.

temperature distribution

Indenter Temperature Calibration Curves

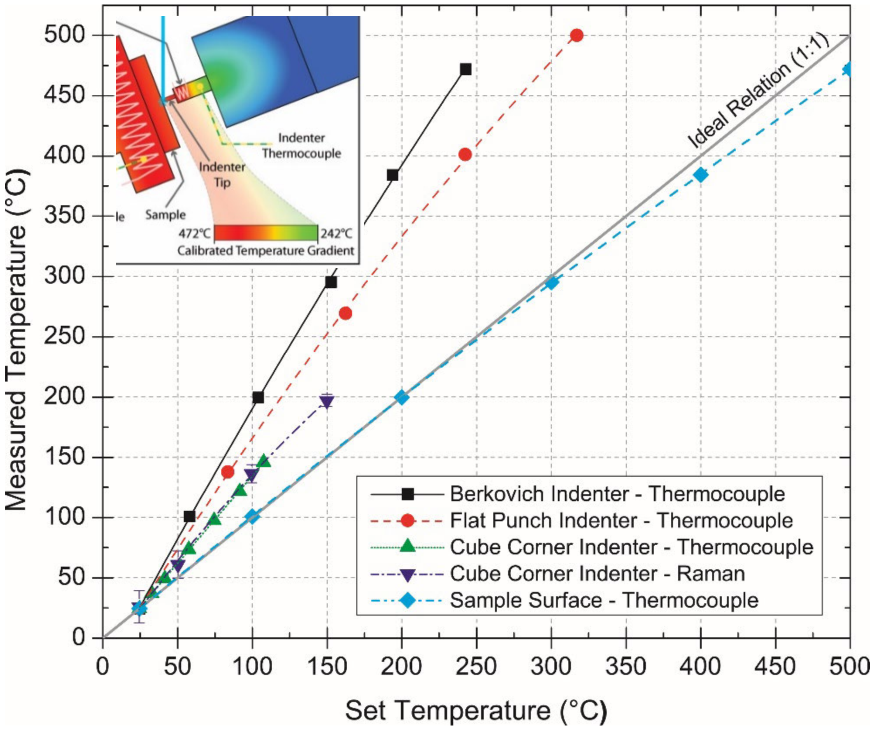

Good agreement between both Raman and thermocouple indentation measurements.

Larger value expected, since heating element is closer to the indenter than the indenter's control thermocouple in this tip design

Allows much greater temperature accuracy in elevated temperature indentation.

nanoindentation of fused silica

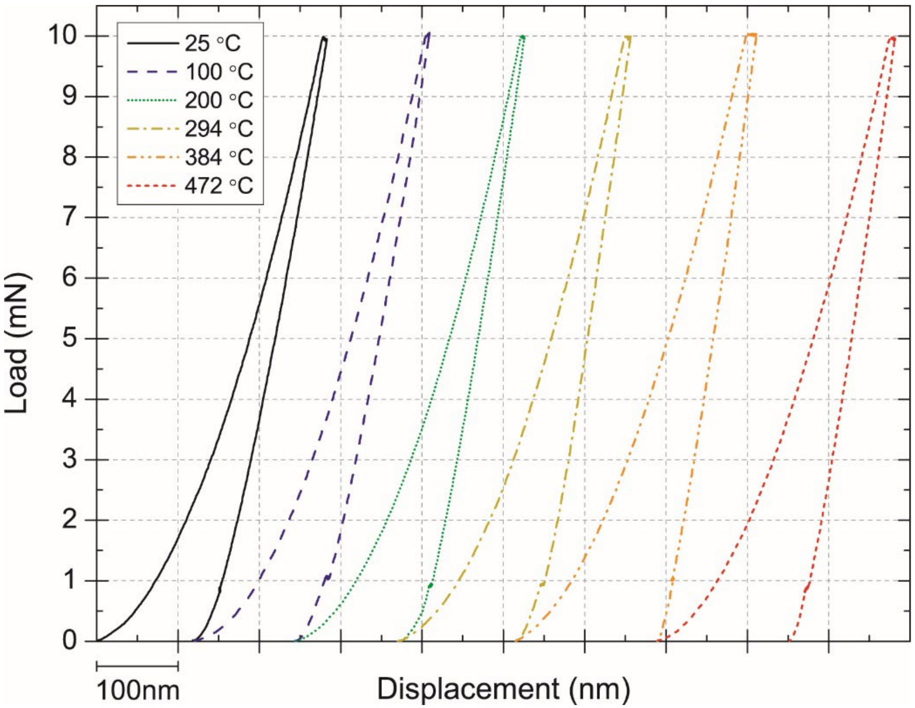

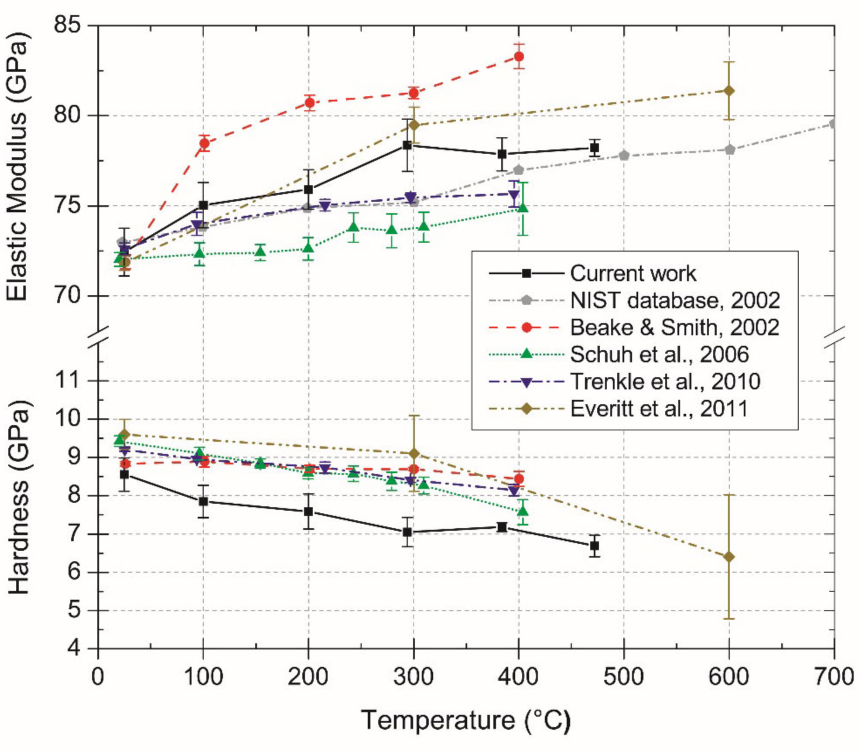

Load-displacement curves are shown uncorrected for drift, with a 60s hold period. All thermal drift is < 0.05 nm/s.

Good agreement is observed between elastic modulus results on fused silica of the current work

Case study: Load bearing Capacity of Hard Coatings: Nitride based ceramic coation on nitrided tool steel surface

How to get a simple materials index for forging, forming and milling operations?

nitride – based PVD coatings

Adding to TiN	hardness	friction	Cold welding	Oxidation resistance	Wear resistance	Wear resistance 600°C
C	++	++	++	– –	+	– –
Al	+	–	–	+(+)	Ø	+
Cr	+	Ø	(+)	+	++	+
Si	++	Ø	(+)	+	+	+

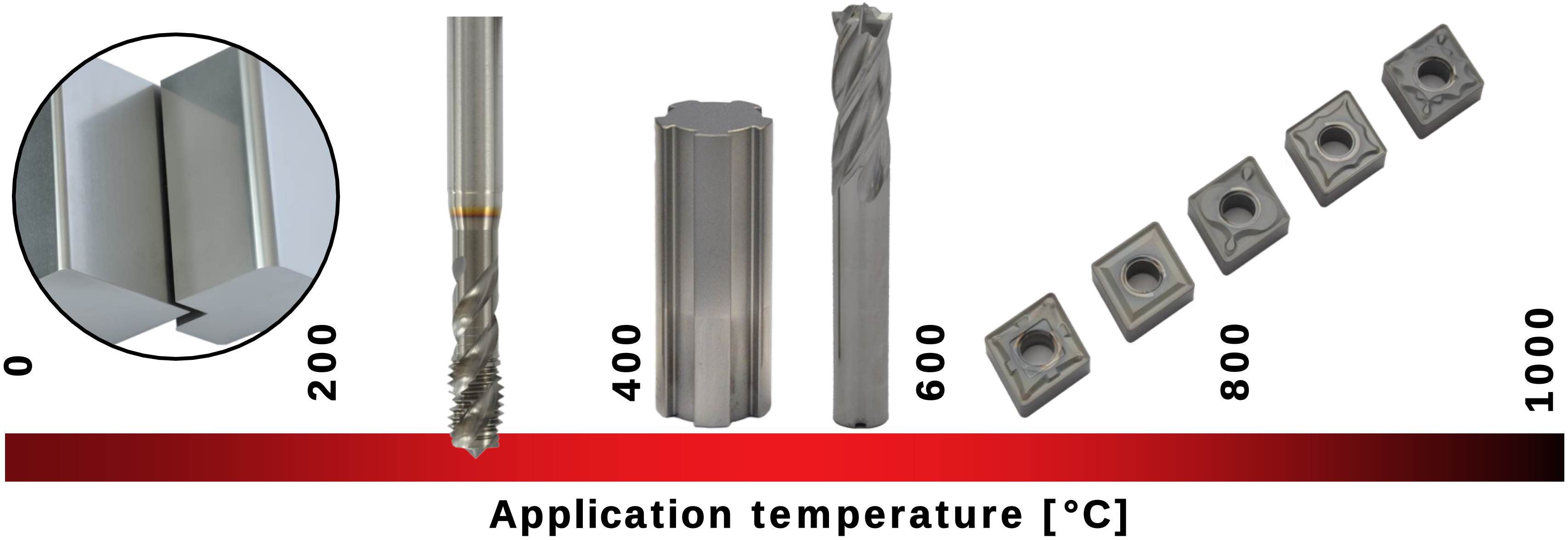

plasma nitrided & coated surface

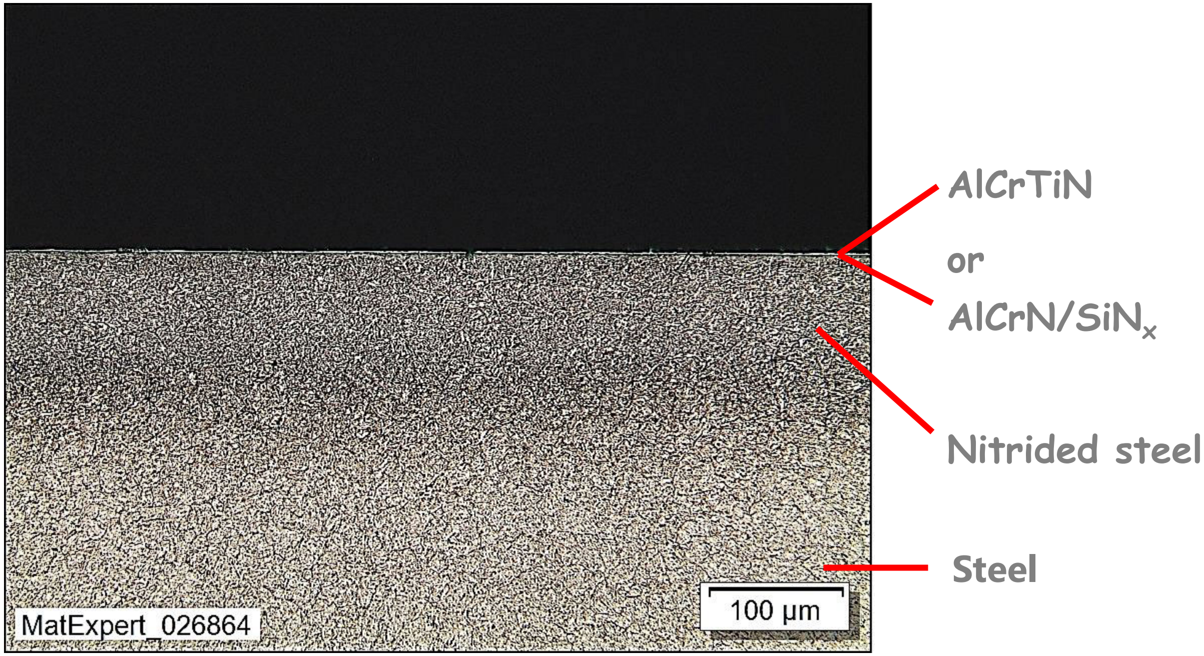

To establish a failure map we need to measure fracture strength of the coatings and the yield strength of the substrates at service temperature!

fracture strength of ceramic coatings

- Representative coatings of all 5 CrN-based coating generations:
  - CrN, AlCrN, AlCrTiN, AlCrSiN, AlCrTiSiN
    N always 50at%, rest mostly Cr & Al, Ti & Si few at%
- Coating Production
  - π411 industrial PVD unit from PLATIT AG
  - Combination of lateral (LARC®) and central (CERC®) cylindrical rotating arc cathodes
  - Process pressure of 3.5 to 4 Pa
  - Bias voltage of –40V
  - Targets: highly pure Cr, Ti, AlCr, Al, and AlSi materials from Plansee AG
  - Coating thickness of approx. 7 µm
- Sectioning and Pillar Preparation
  - Tescan Vela and Lyra dual-beam FIB
  - Cross-sectioning trenches cut using Ga^+ at 30 kV and ~ 6 nA , then fine milled and polished using ~700 pA.
  - Micropillars with an aspect ratio of ~3 were cut using the same parameters

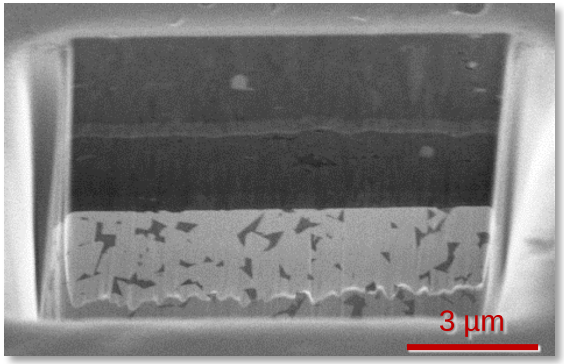

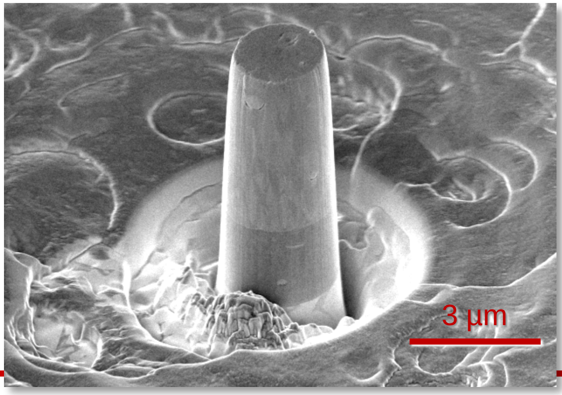

microstructure

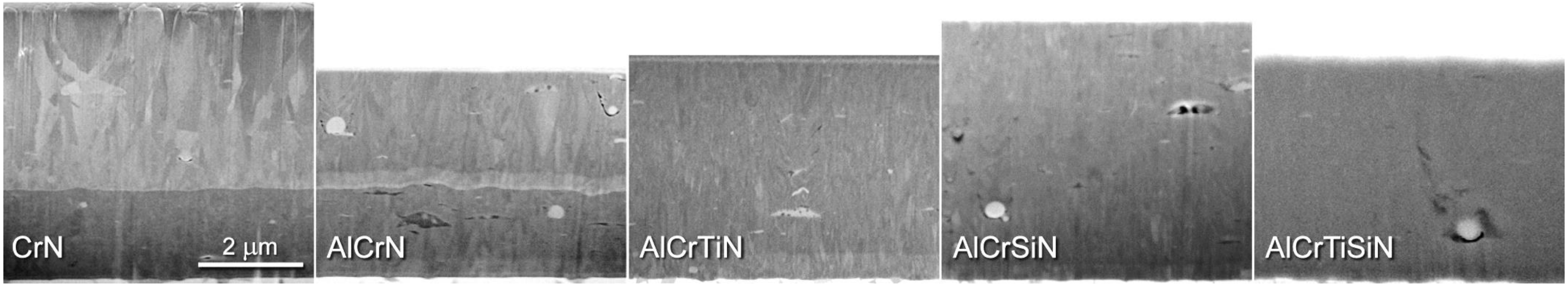

FIB Cross-sections of Coating Microstructures

- Microstructural observations
  - ☐ Adhesion layers present
  - ☐ Micron long columnar grains in CrN
  - ☐ Grain refinement in each series
  - ☐ ~200nm voids and inclusions
- Crystallite size from XRD: ~16nm for CrN and ~11nm for all others.

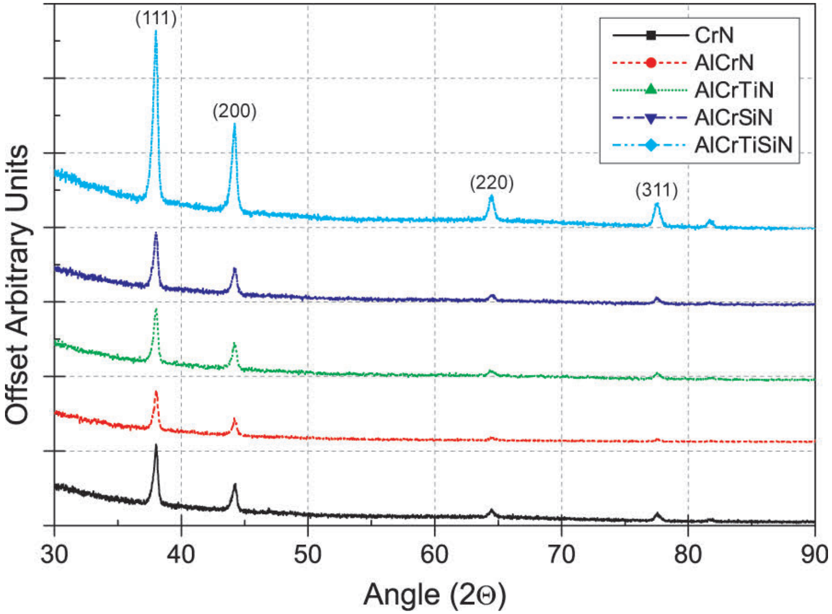

X-ray Diffraction

stress-strain curves of AlCrTiN coating

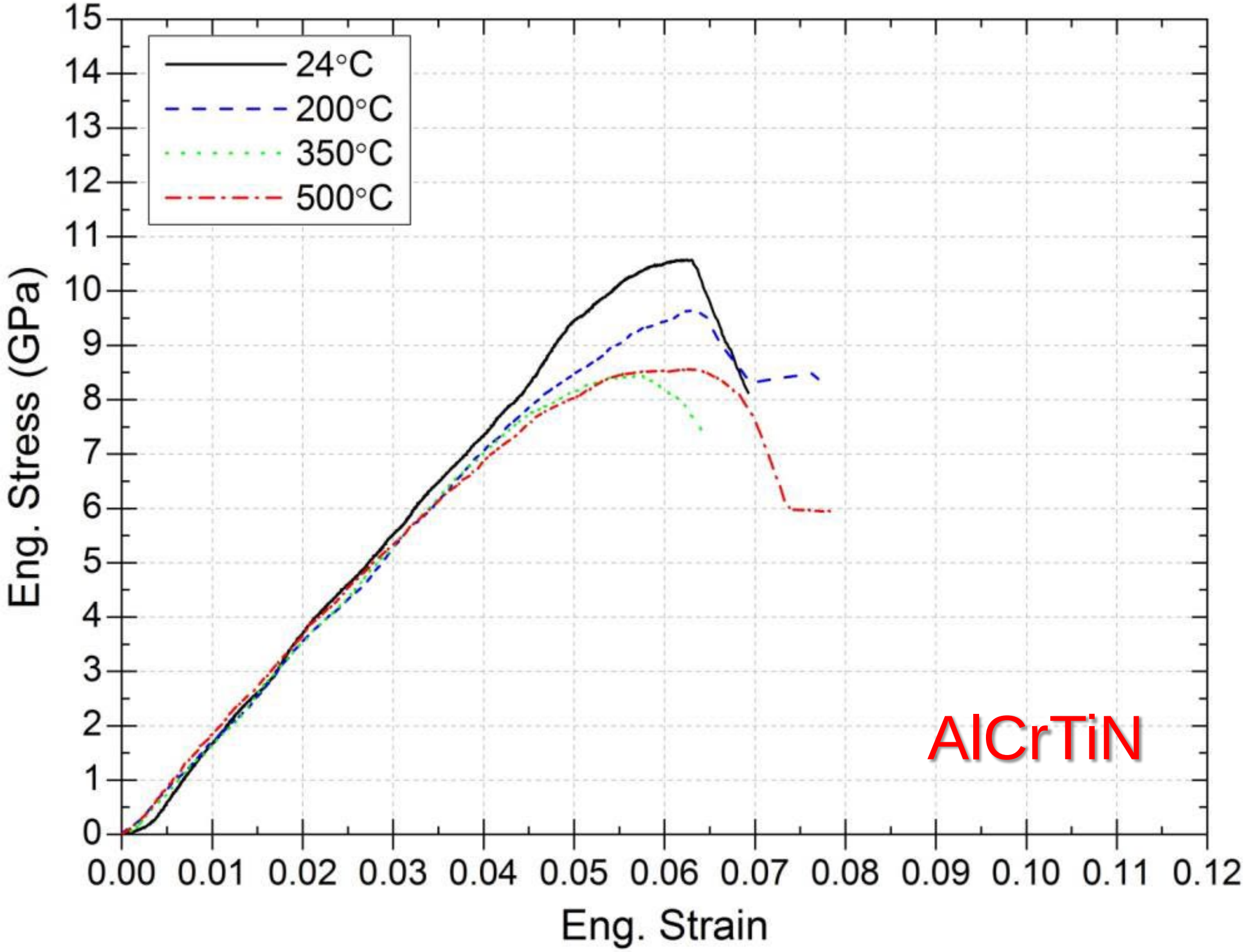

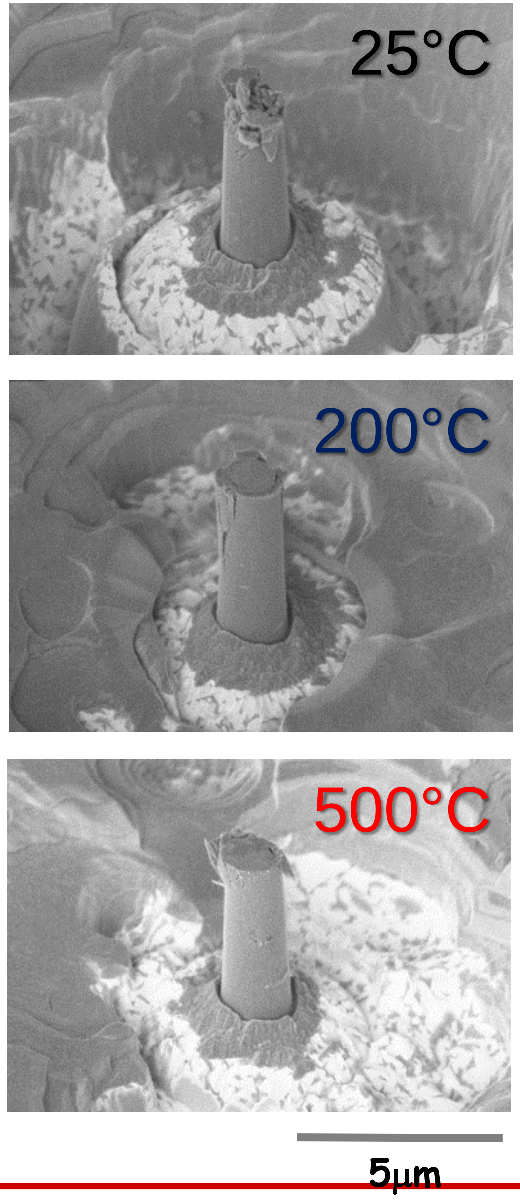

Wheeler et al. *Surf. Coat. Tech.* (2014)

stress strain behavior

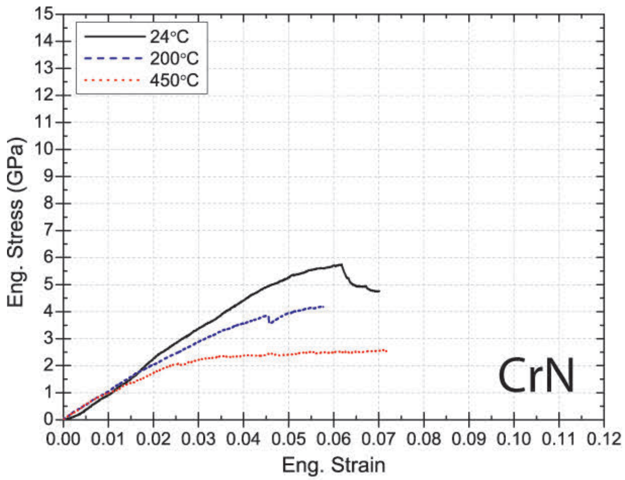

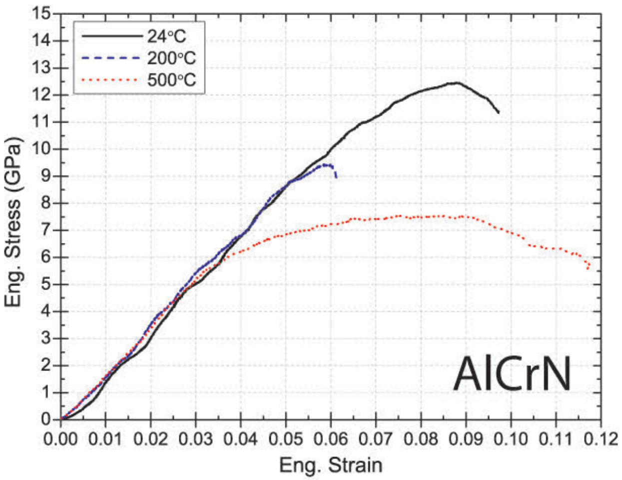

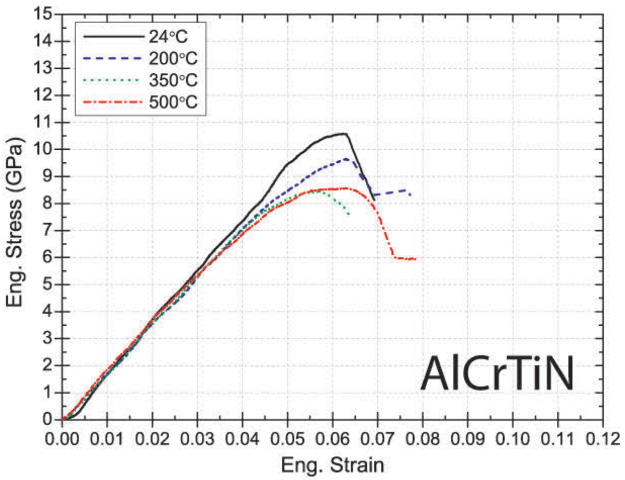

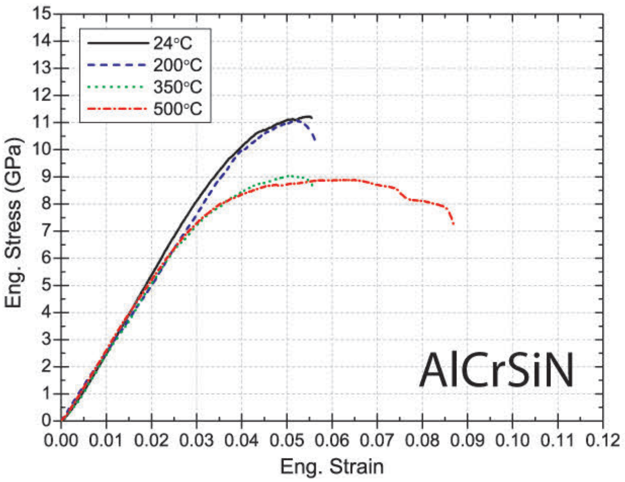

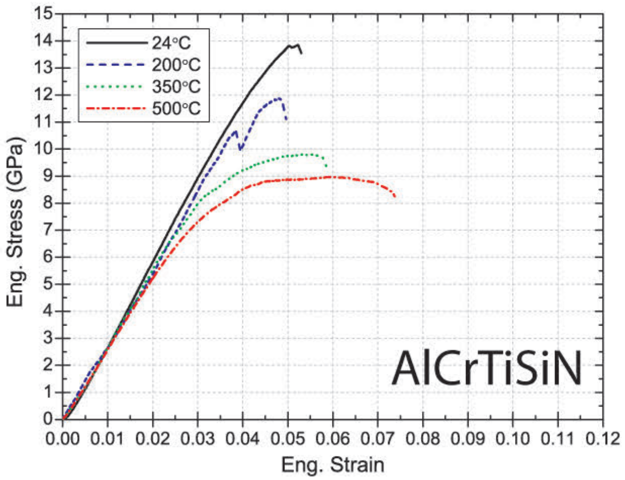

- Stiffness values are lower than expected from Indentation – Adhesion layer/sink-in
- Most coatings do not show catastrophic brittle failure
- Evidence of plasticity-enabled ‘ductility’ or graceful failure at higher temperatures

deformation and failure mechanisms

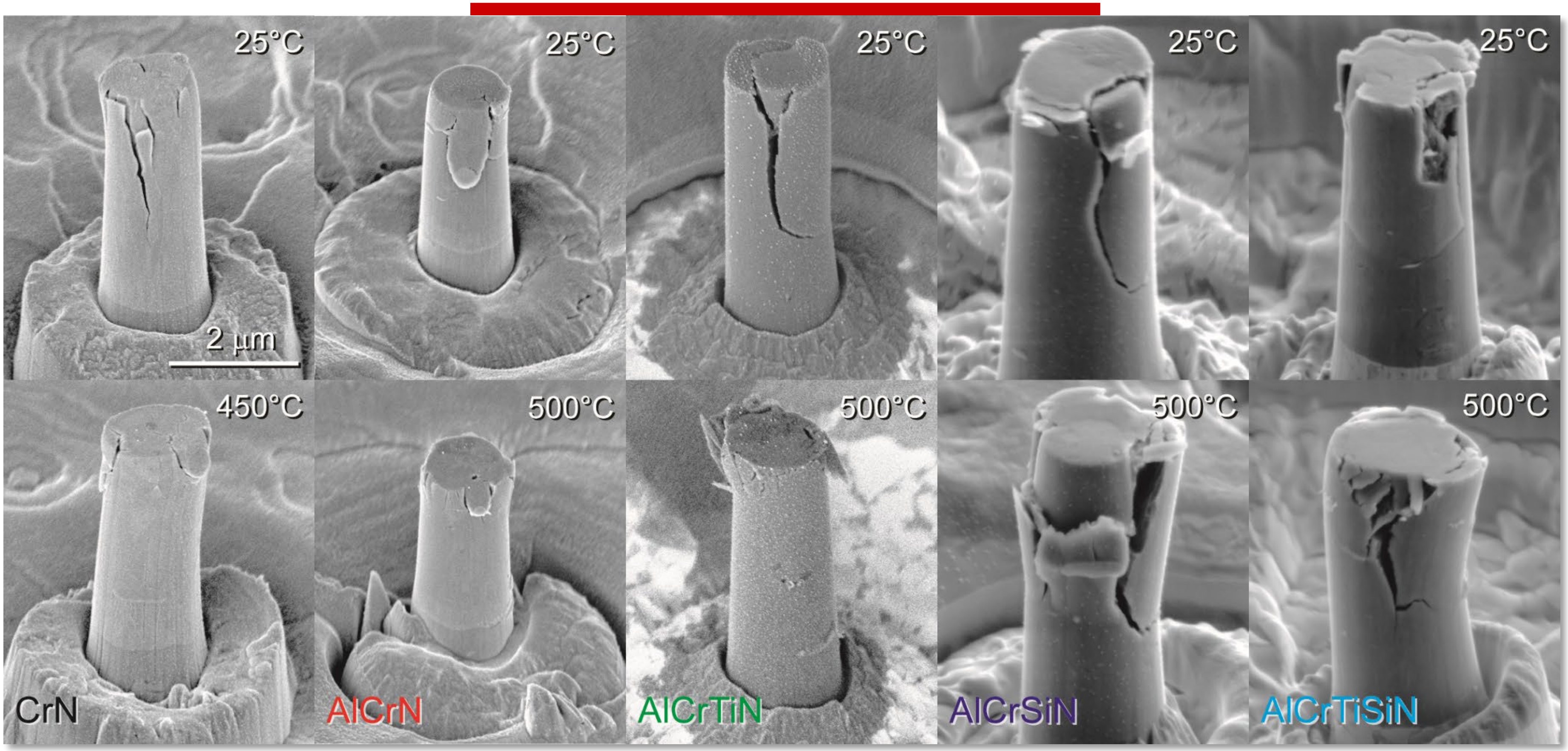

- Pillar failure occurs by fracture, in all cases.
  - ☐ No obvious slip or barreling due to plastic flow.
  - ☐ Failure observed within top coating layer, not substrate or adhesion layer.
- Fracture occurs at defects, such as voids and inclusions, frequently.

trends with temperature

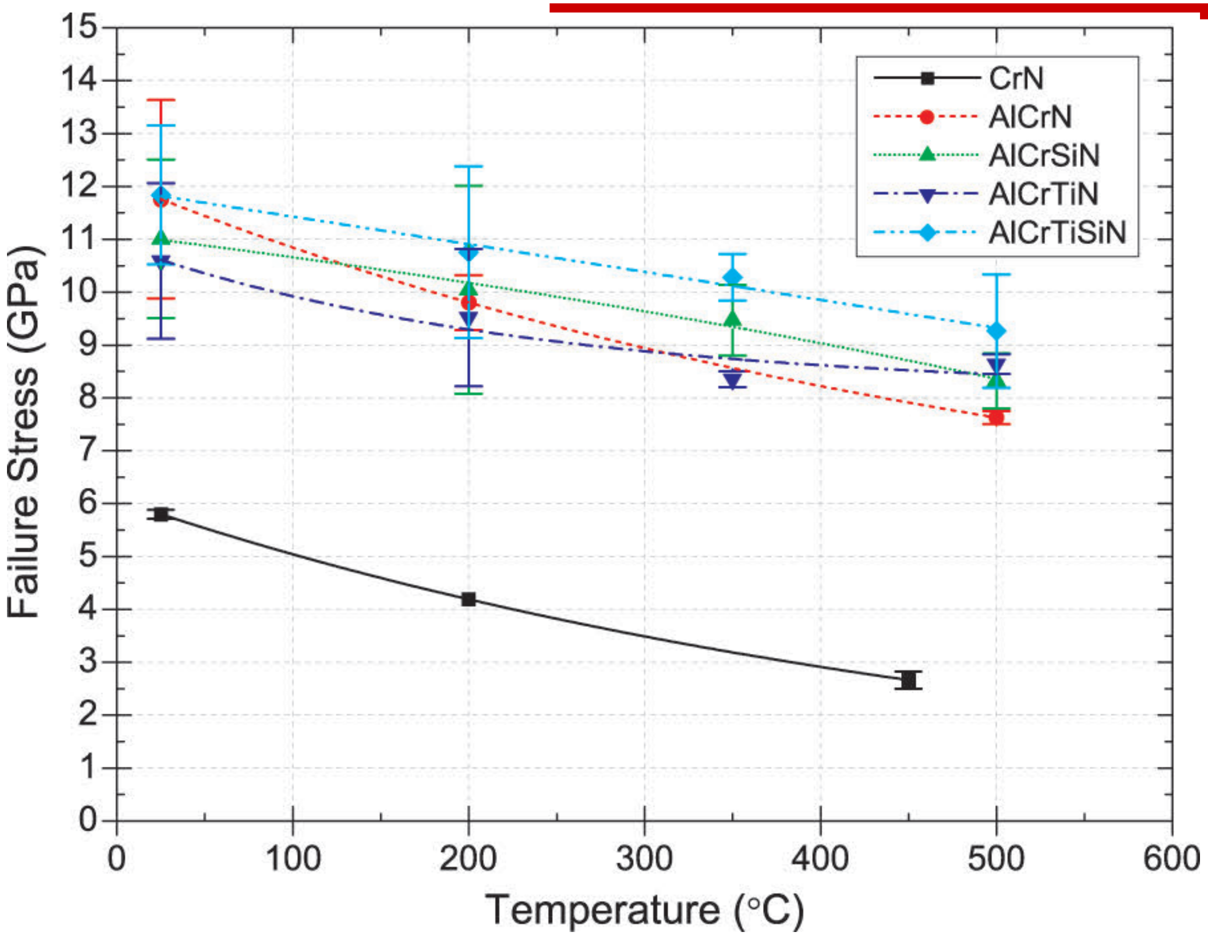

In situ Observation of Failure

- Each new coating generation shows improved high temperature strength.
- Low temperature strength can be misleading about high temperature behavior.
- Addition of Ti or Si to the coatings decreases temperature sensitivity, adding them together achieves the greatest temperature insensitivity.

yield strength of nitrided layer

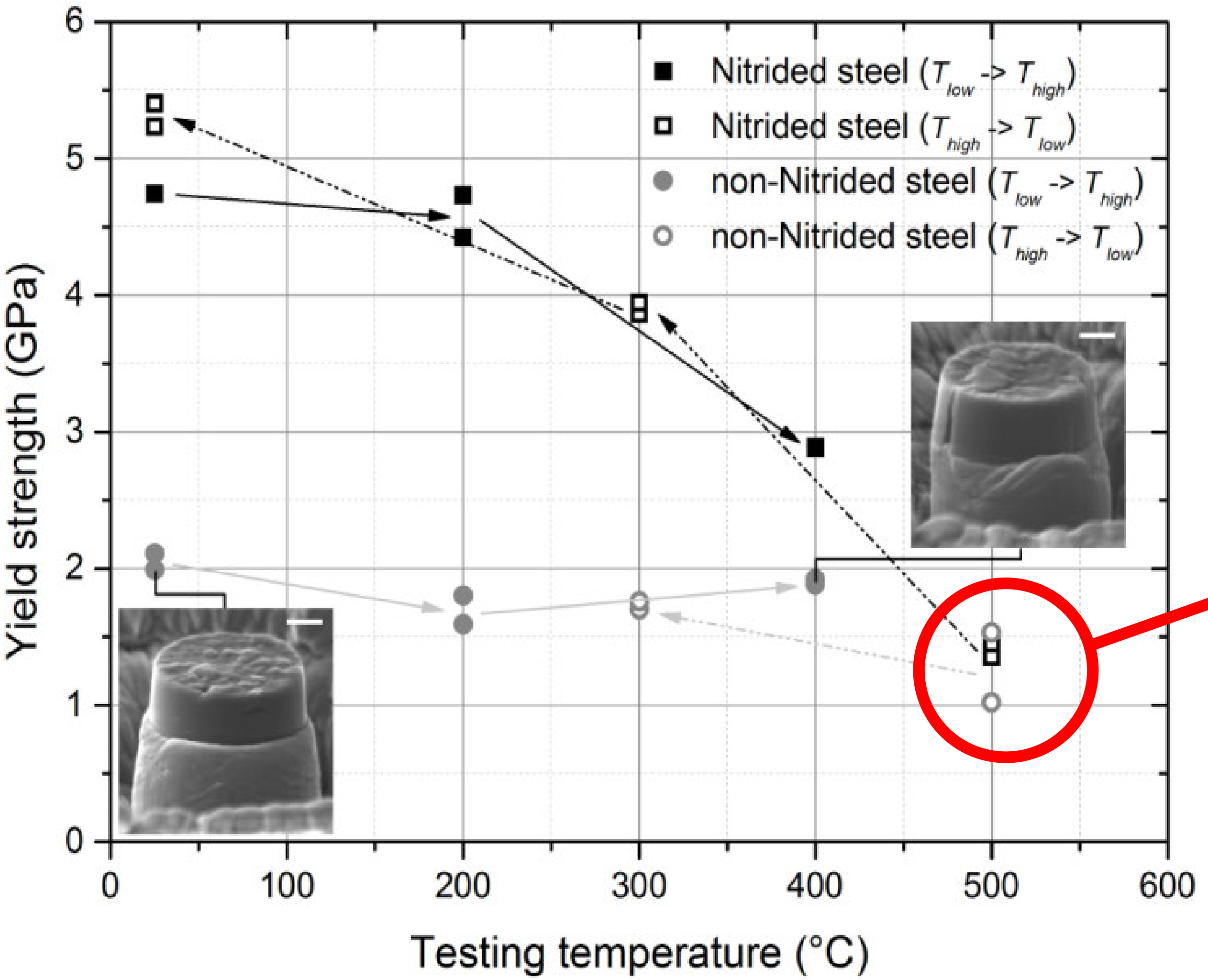

Does plasma nitriding make sense?
Other effects such as residual stress and higher toughness?

plasma nitrided & coated surface

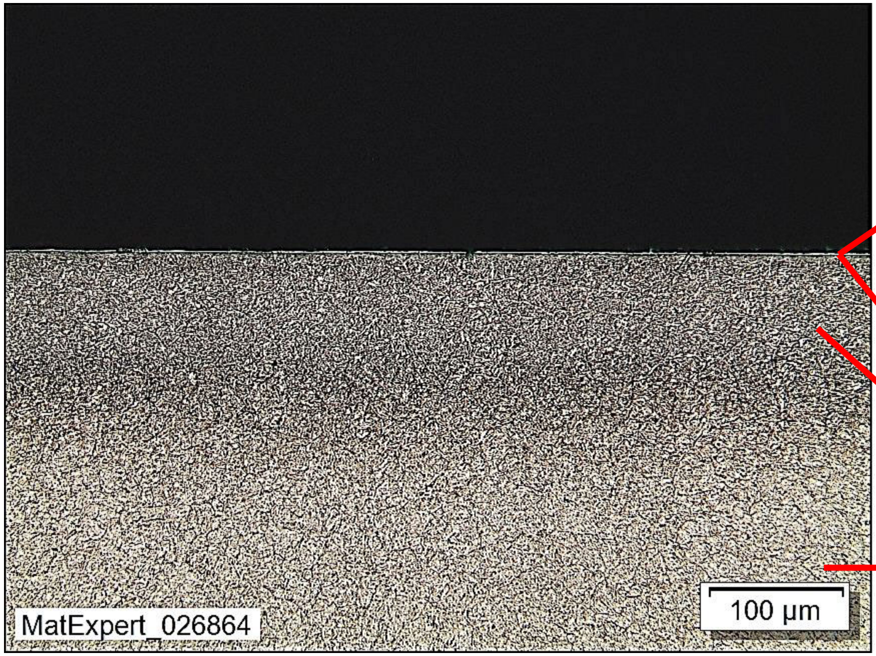

	E (GPa)	σ_y (GPa)	σ_f (GPa)
AlCrTiN	535		10.6 (8.7)
AlCrN/SiN x	524		13.1 (9.3)
Nitrided	306	7.6 (1.4)	-
HT-steel	243	2.2 (1.3)	-

Room Temperature (500°C)

failure mechanism map

Fracture of AlCrTiN
on nitrided steel as substrate

W300= tool steel,
Trademark Böhler, Switzerland
N-W300 = nitrided tool steel

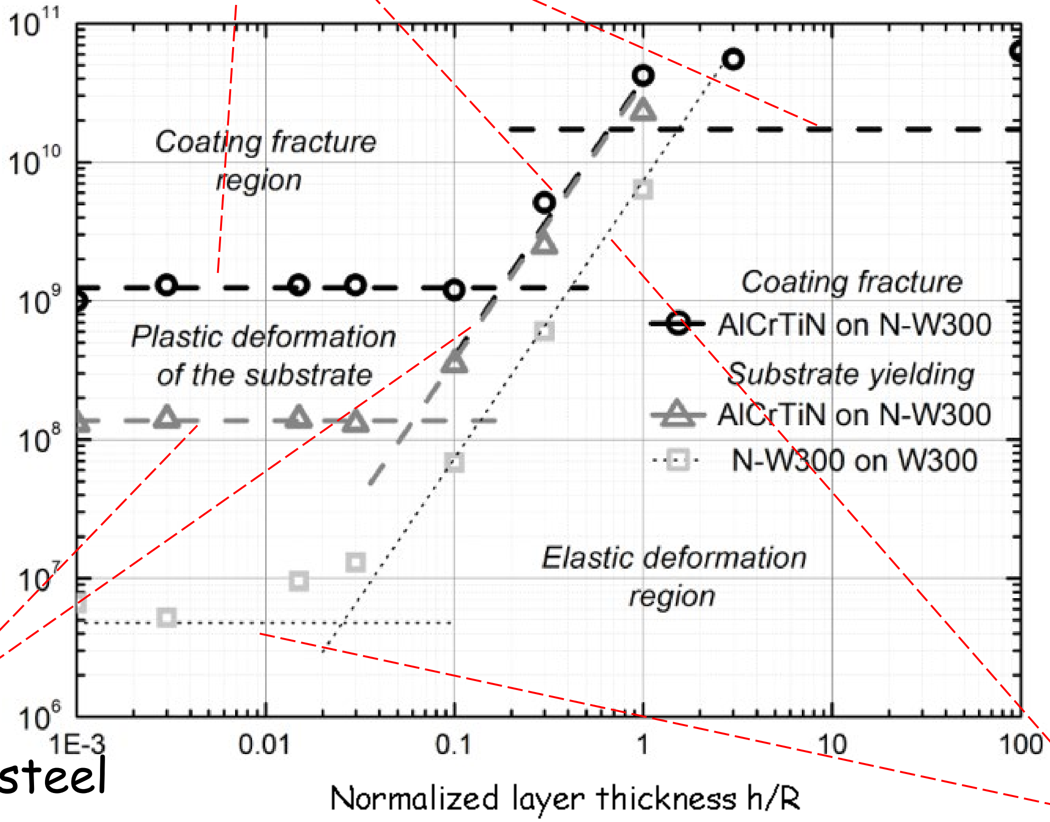

Yield of on nitrided steel
as substrate below
AlCrTiN coating

Yield of steel below nitrided steel
Nitrided steel is treated as coating

Empa
Materials Science and Technology

failure mechanism map

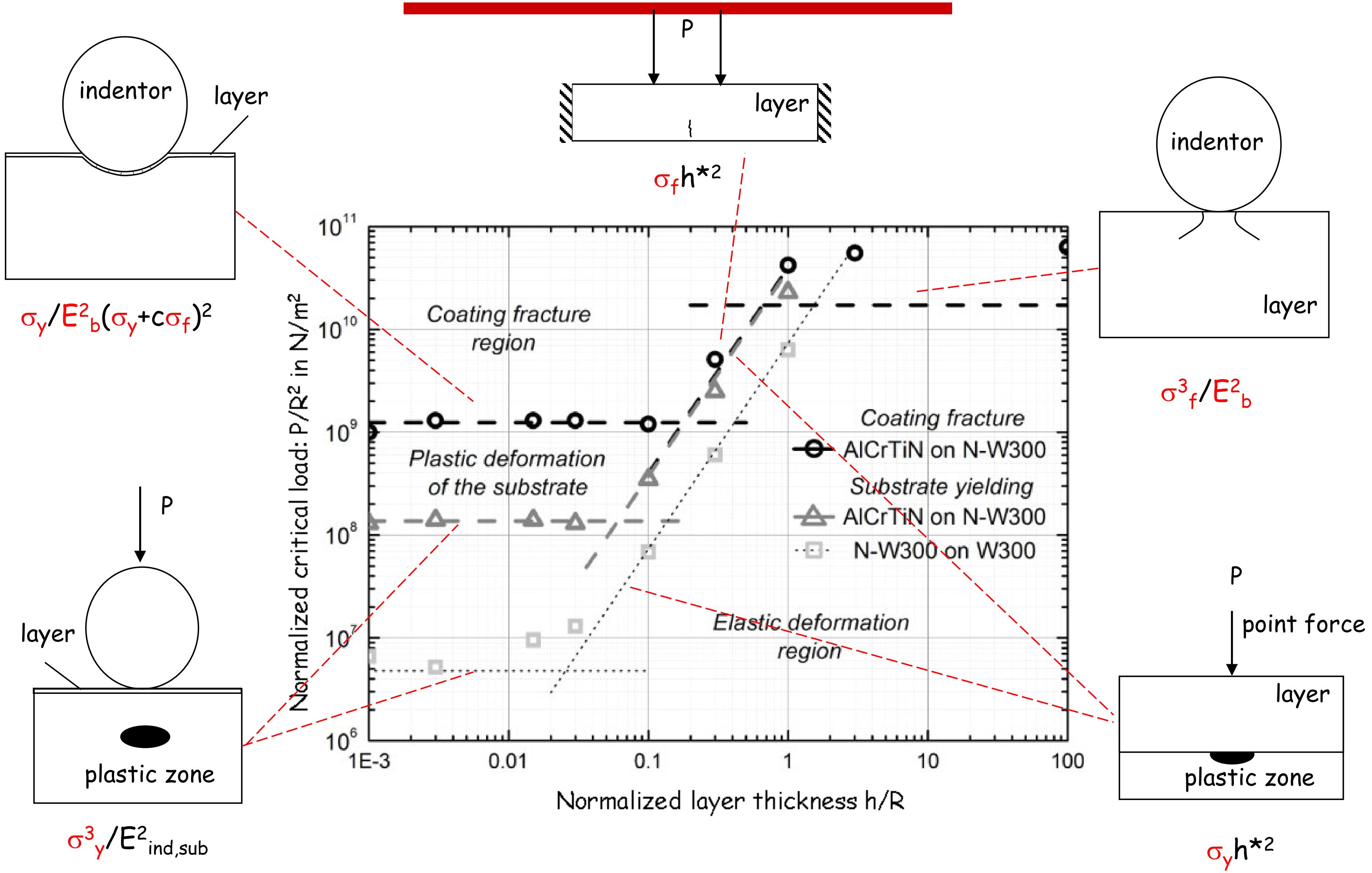

temperature trends AlCrTiN

Fracture strength 10.6 (RT) -> 8.7 (500°C)

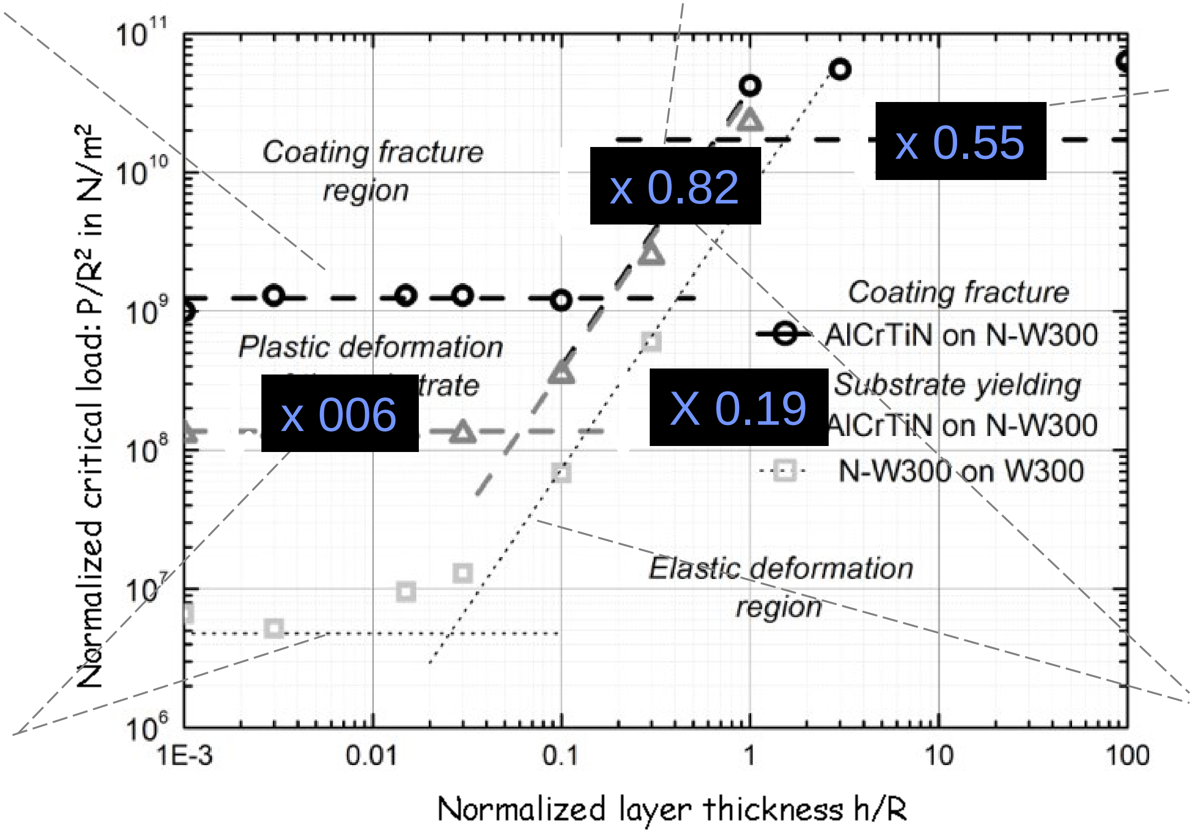

$\sigma_f h^{*2}$

$\sigma_y / E^2_b (\sigma_y + c\sigma_f)^2$

σ^3_f / E^2_b

$\sigma^3_y / E^2_{ind,sub}$

$\sigma_y h^{*2}$

x 0.82

x 0.55

x 006

X 0.19

Yield strength 7.6 GPa (RT) -> 1.4 Gpa (500°C)

scratch testing – can we predict the failure load?

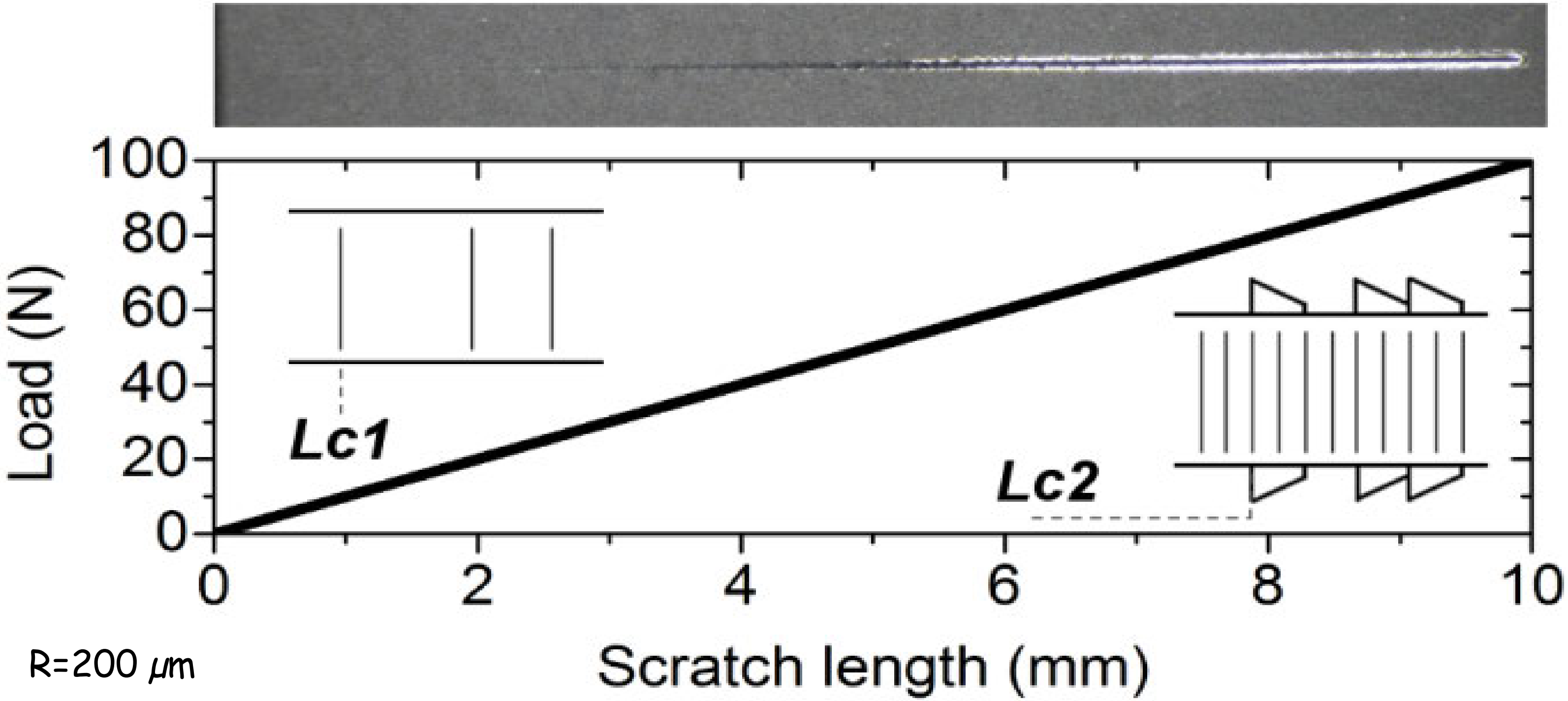

R=200 µm

application of coating failure mechnism maps

R=200 μm

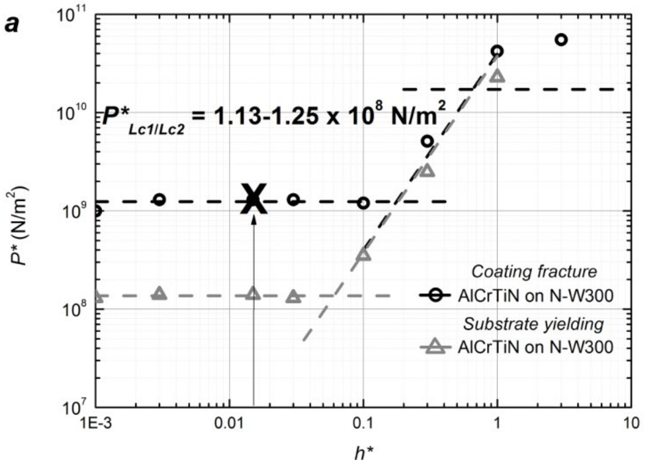

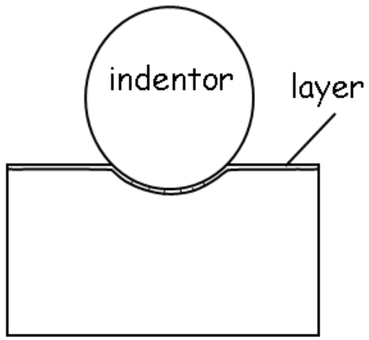

$\sigma_y/E^2_{lay}(\sigma_y+c\sigma_f)^2$

	E (GPa)	σ_y (GPa)	σ_f (GPa)
AlCrTiN	535		10.6 (8.7)
AlCrN/SiN$_x$	524		13.1 (9.3)
Nitrided	306	7.6	-
HT-steel	243	(1.4) 2.2 (1.3)	-

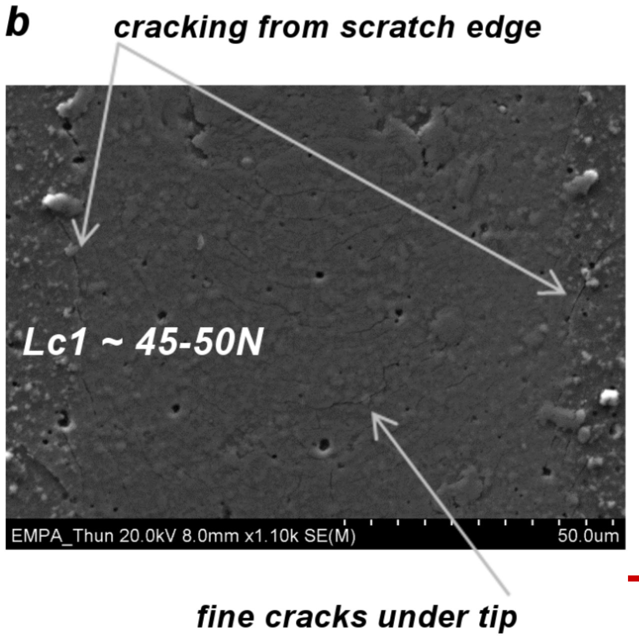

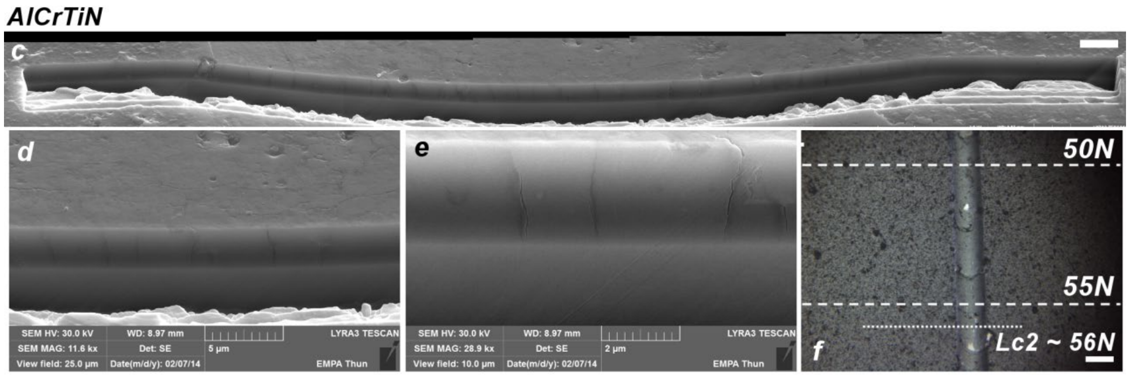

R=200 μm

conclusions

- Micro-pillar compression near service temperature is a useful method for studying fracture and yield strength of hard ceramic coatings and nitrided steel layers, respectively

- Temperature dependence of hard coating decreased by adding Si and Ti. Reversible softening of nitrided steel layer at high temperatures independent of testing geometry

- Failure mechnisms map constructed from simple mechanical analogons allow to estimate failure mode and critical load

Case study: deformation mechanisms of nanocrystalline metals

Need for nanomechanical testing

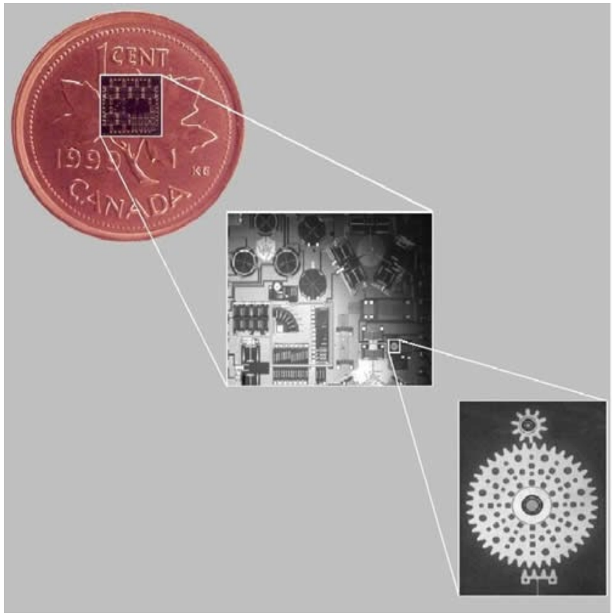

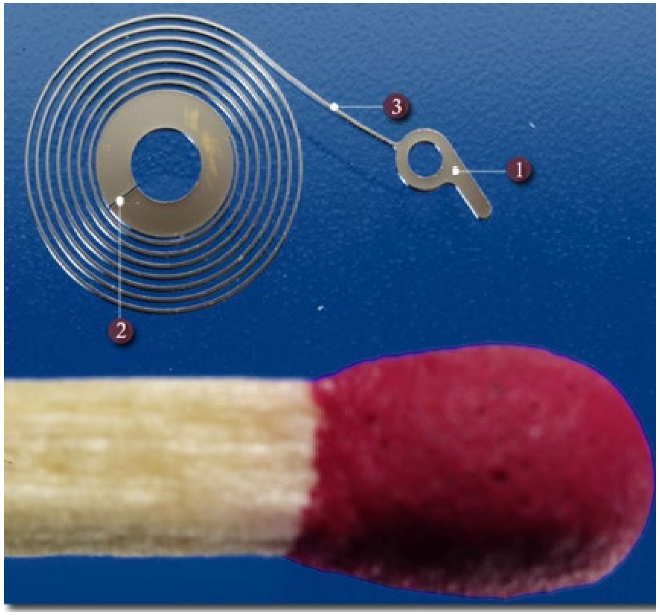

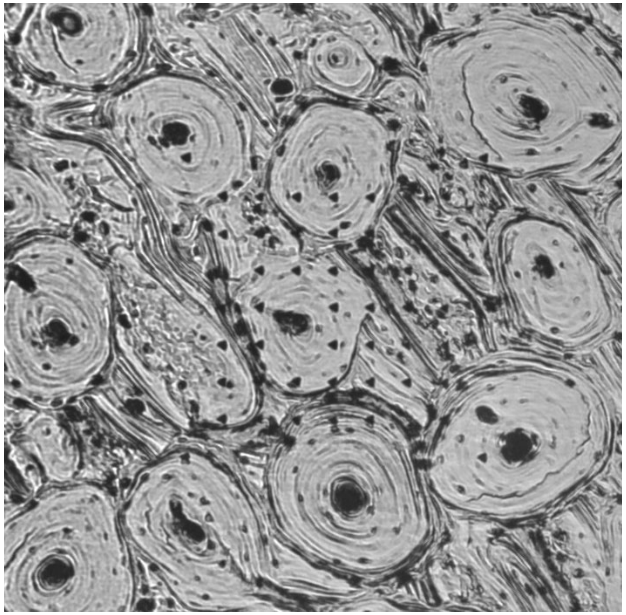

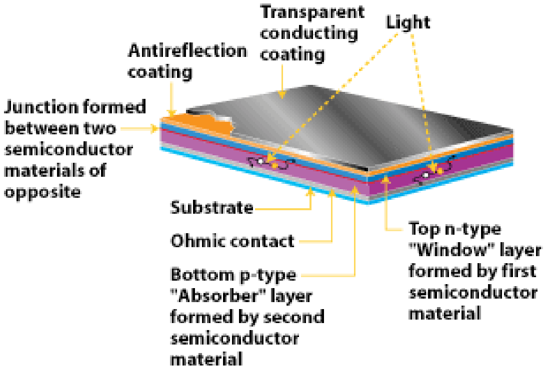

Cases where bulk testing is not possible:

- Thin films
- Microcomponents/MEMS devices

Small length-scale testing

- Individual phases of complex materials
- Size effects

Why low temperature tests – case of the Titanic

The Titanic on the seabed, 3,784 meters deep

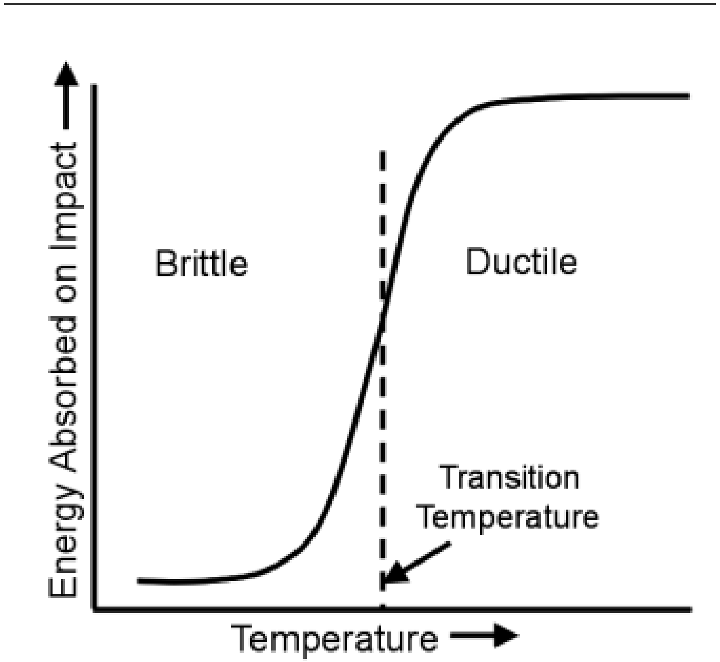

Chapy test results on steel samples at -4°C (the temperature of Atlantic waters when The Titanic sank)

Reference: Robert Gannon, Popular Science, 1995

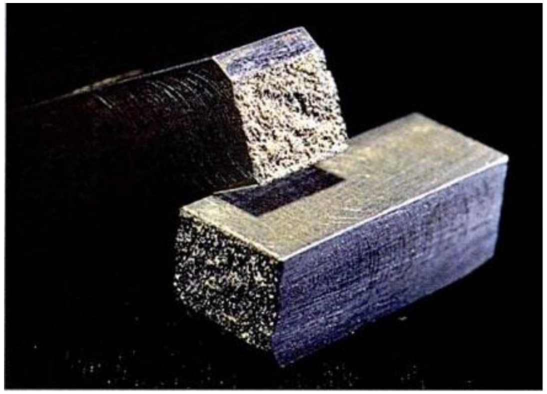

*Steel from Titanic's hull – **Brittle** fracture*

*Modern high quality steel - **Ductile** fracture*

High strain rate micromechanics - Scientific motivation

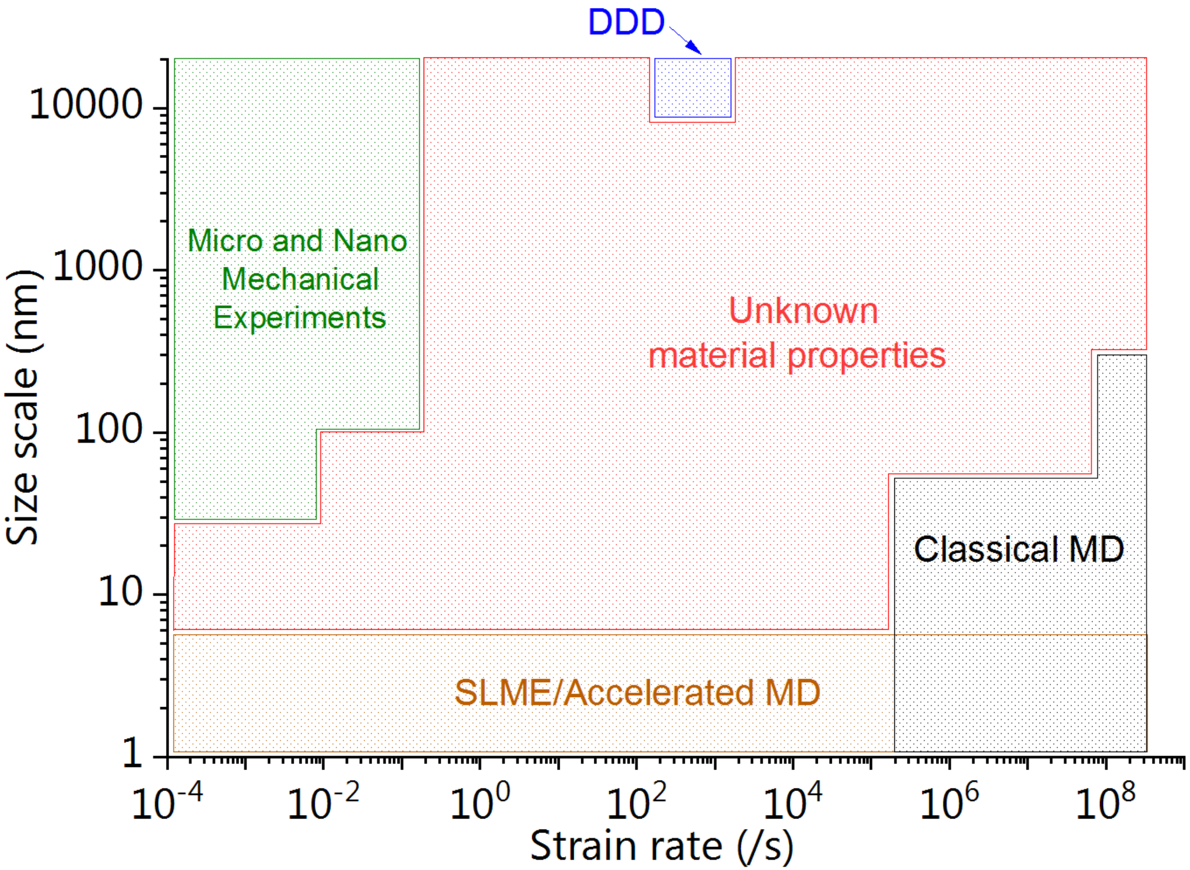

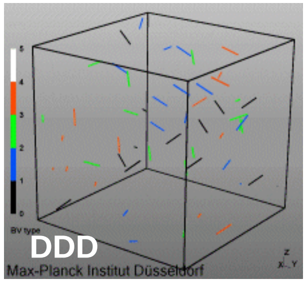

High strain rate experiments help bridge the gap between experiments and simulations

Deformation mechanisms in nc metals

Deformation mechanisms

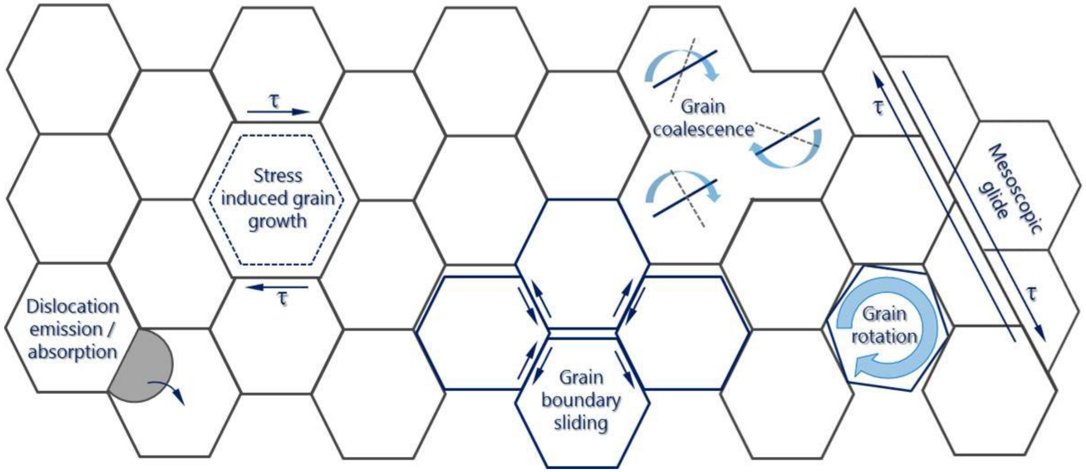

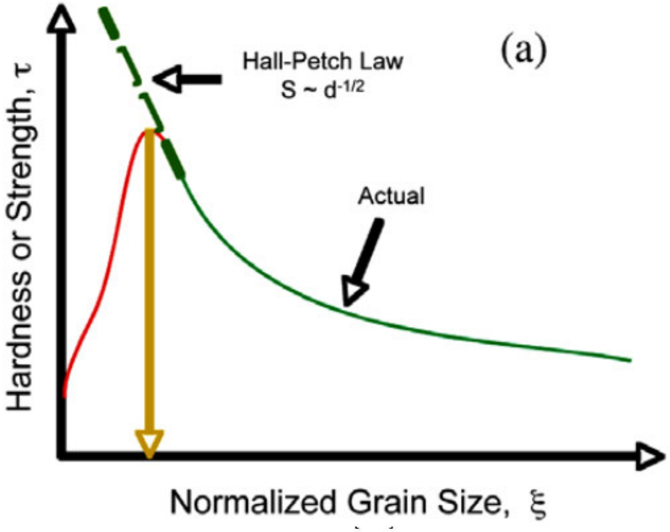

- Mechanical properties are dominated by grain size
- Pronounced time-dependent plastic behaviour
- Grain growth through FIB irradiation and at elevated temperatures
- Electrodeposition into lithography moulds
- Thermal activation analysis at low temperatures and high strain rates

Micropillar array preparation by electrodeposition

Workflow for producing nc metal microstructures

Empa
Materials Science and Technology

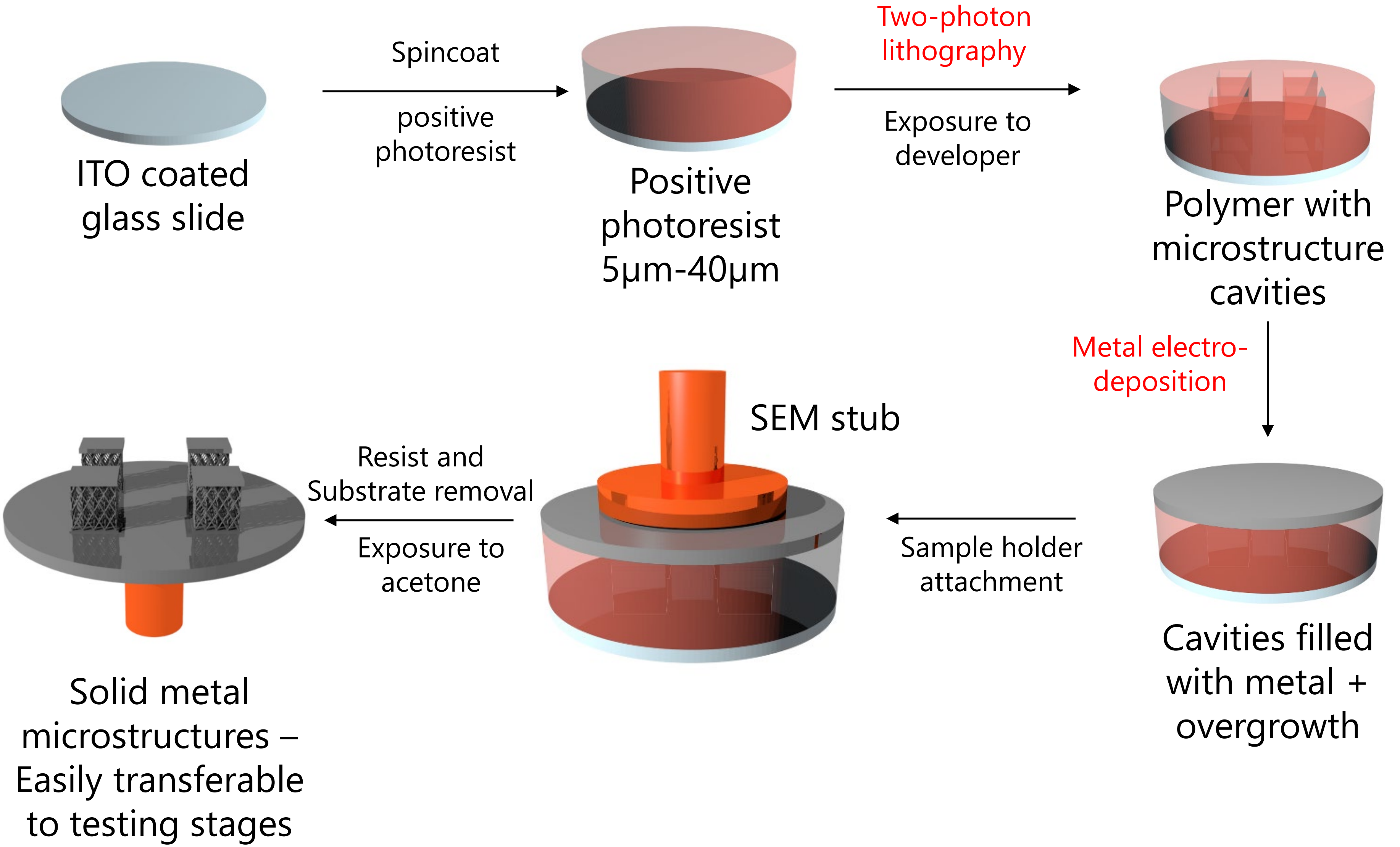

ITO coated glass slide

Spincoat
positive photoresist

Positive photoresist 5µm-40µm

Two-photon lithography
Exposure to developer

Polymer with microstructure cavities

Metal electro-deposition

Cavities filled with metal + overgrowth

Sample holder attachment

SEM stub

Resist and Substrate removal
Exposure to acetone

Solid metal microstructures – Easily transferable to testing stages

Nanocrystalline Ni micropillar array

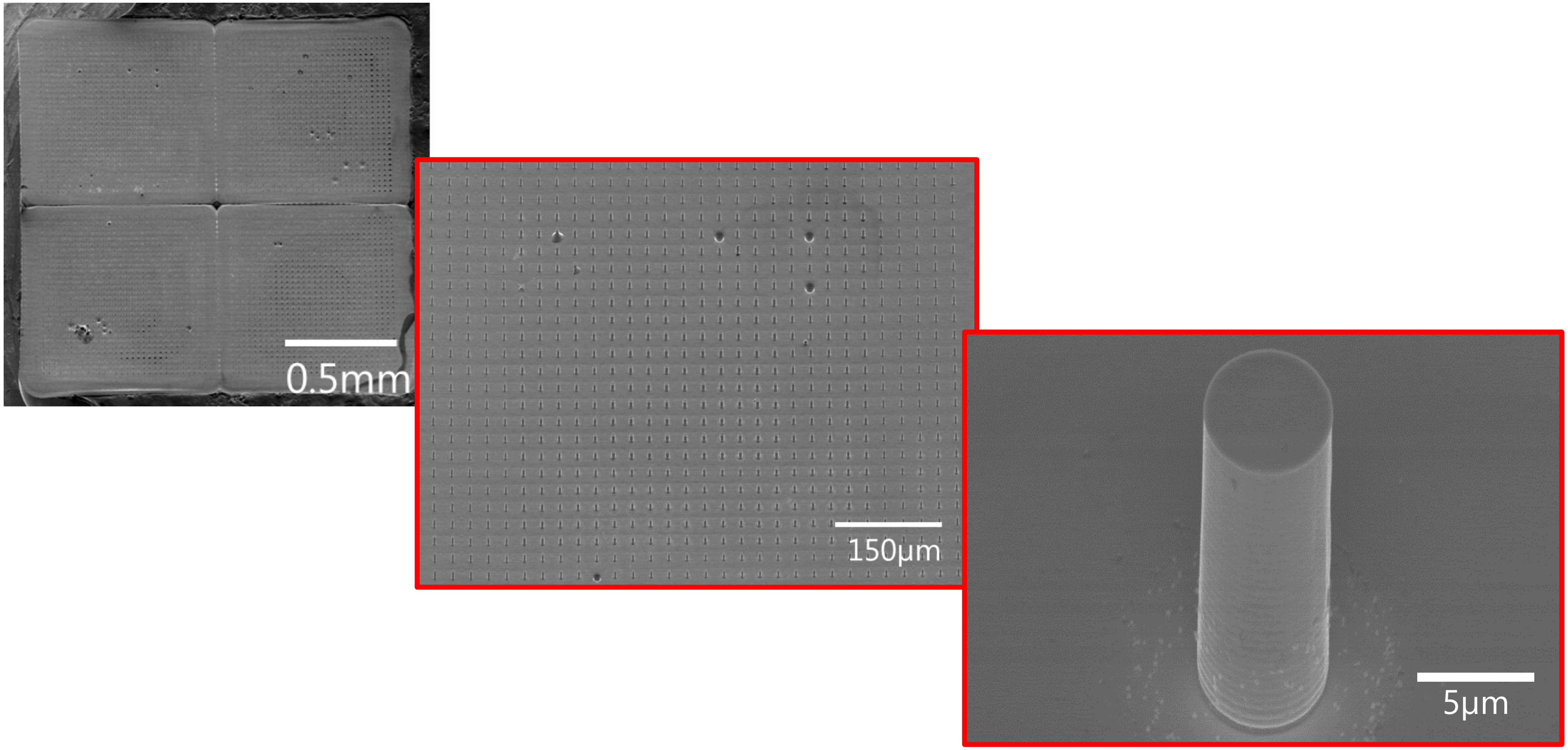

- Array of 4000 electrodeposited nanocrystalline Ni micropillars
- No FIB damage, no FIB-induced grain growth, no taper
- Grain size estimated based on XRD: ~28nm
- Random grain orientation

Thermal activation analysis at subambient temperatures and high strain rates

Challenges in low temperature indentation

- Thermal drift
  - **Frame drift** – displacements due to thermal contraction within the indenter frame components
  - **Contact drift** – displacements due to thermal expansion/contraction in sample and tip due to heat flow from temperature mismatch
  - **Electronics drift** – Change in electronic signals with time or temperature

  - Control electronics and sensors must be protected from cryogenic temperatures

Thermal drift for ΔT of 200K
Courtesy of J.M. Wheeler

- Condensation
  - **Condensation** on the sample surface is undesirable for surface property testing

Thermal management concept

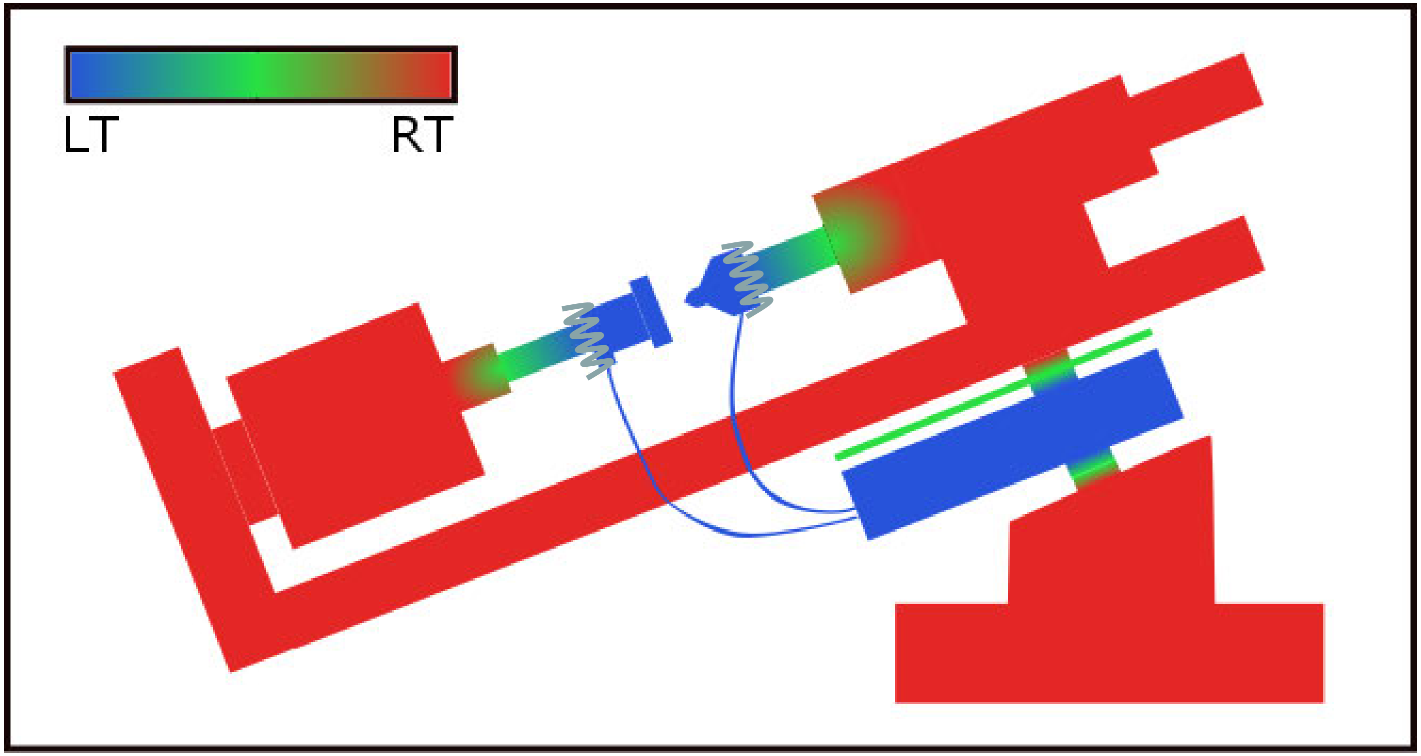

Local cooling of nano-contact:

- Cold finger linked by conductive braids to sample and tip: stable base temperature.
- Miniaturized heaters for sample and indenter for independent temperature tuning.
- Thermal isolation and radiation shielding of the cooled parts to reduce frame drift and protects sensitive electronics.

In situ quasistatic cryoindenter setup

alemnis
engineering your ideas

Empa
Materials Science and Technology

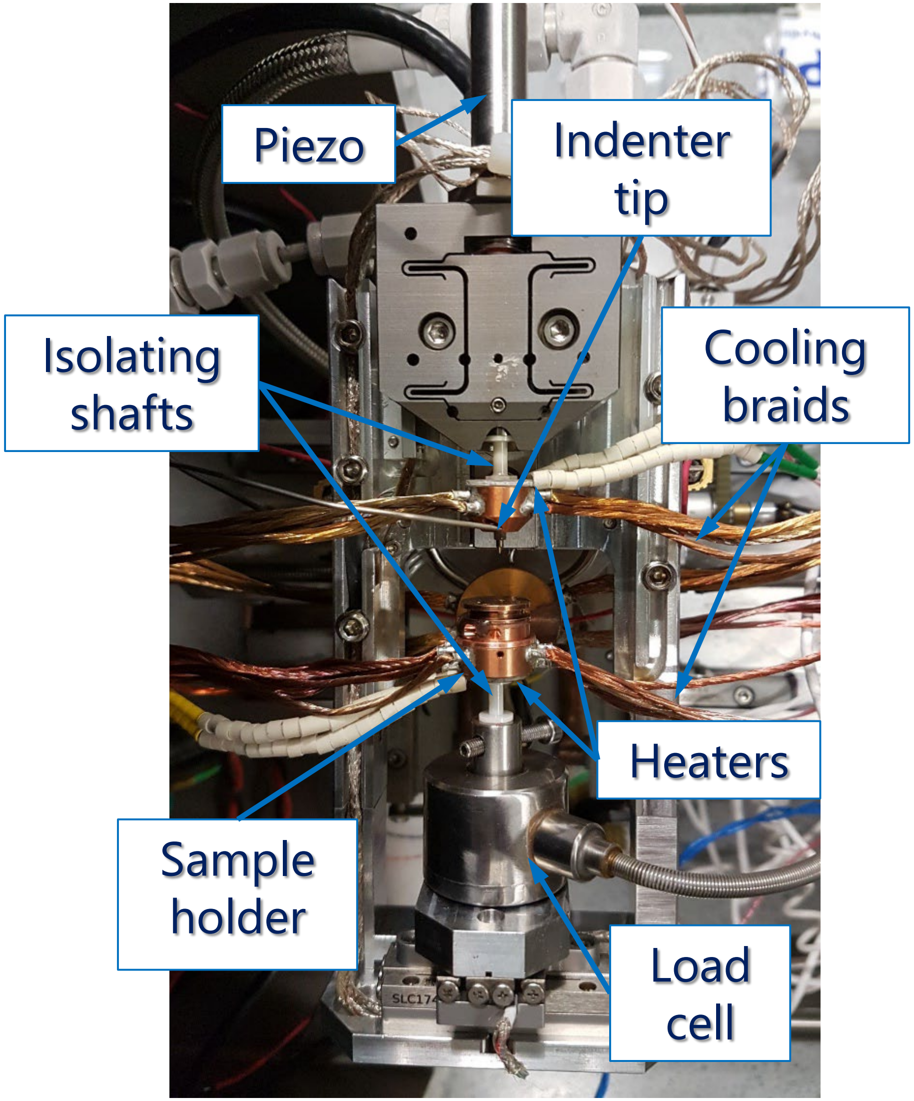

- Temperature range: 120K to 300K
- Strain rate range: 10^{-4} to 10^{-1}s
- Load range: 500mN
- Nitrogen pumped through cold finger cooling indenter tip and sample holder to a base temperature of 120K
- Thermocouples and heaters on tip and sample holders allow indepedent temperature control
- Isolating shafts and heaters in closed loop control keep the frame at constant temperature

Frame compliance measurement

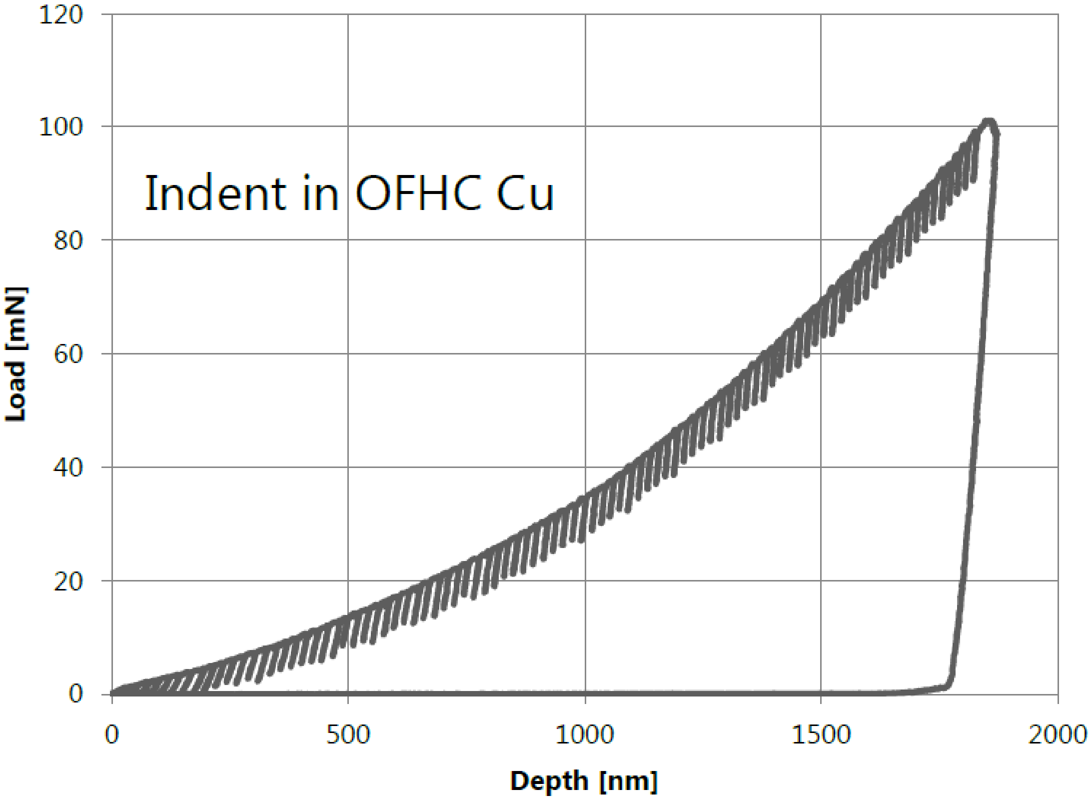

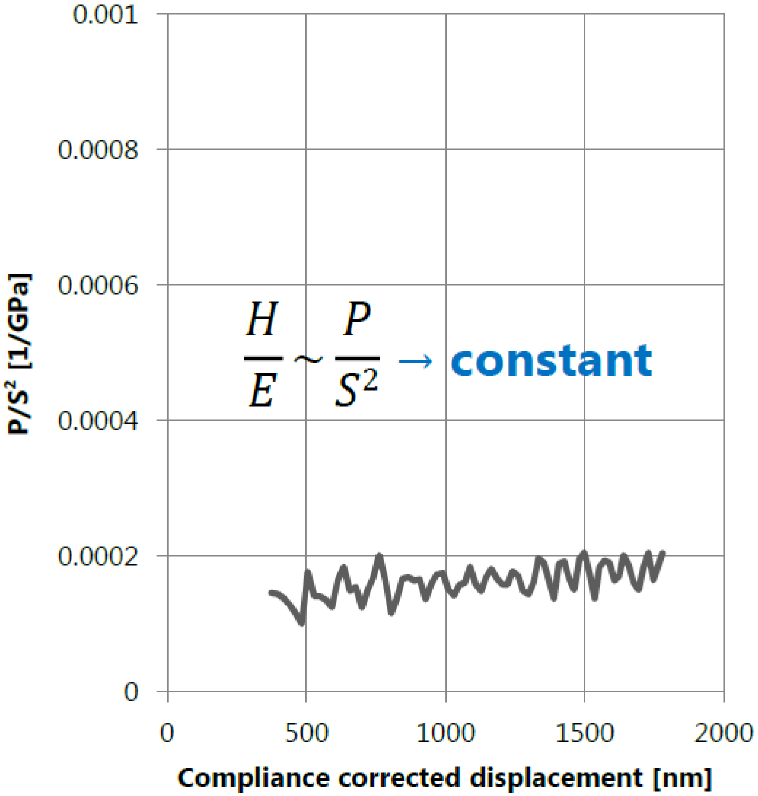

- Room temperature drift < **5 nm/min**
- Frame compliance: 4.85nm/mN (14% increase compared to standard setup)

Hardness: 1.2 GPa
Young's modulus: 115 GPa

} Compares well with literature [Schuh2006]

Thermal drift measurement

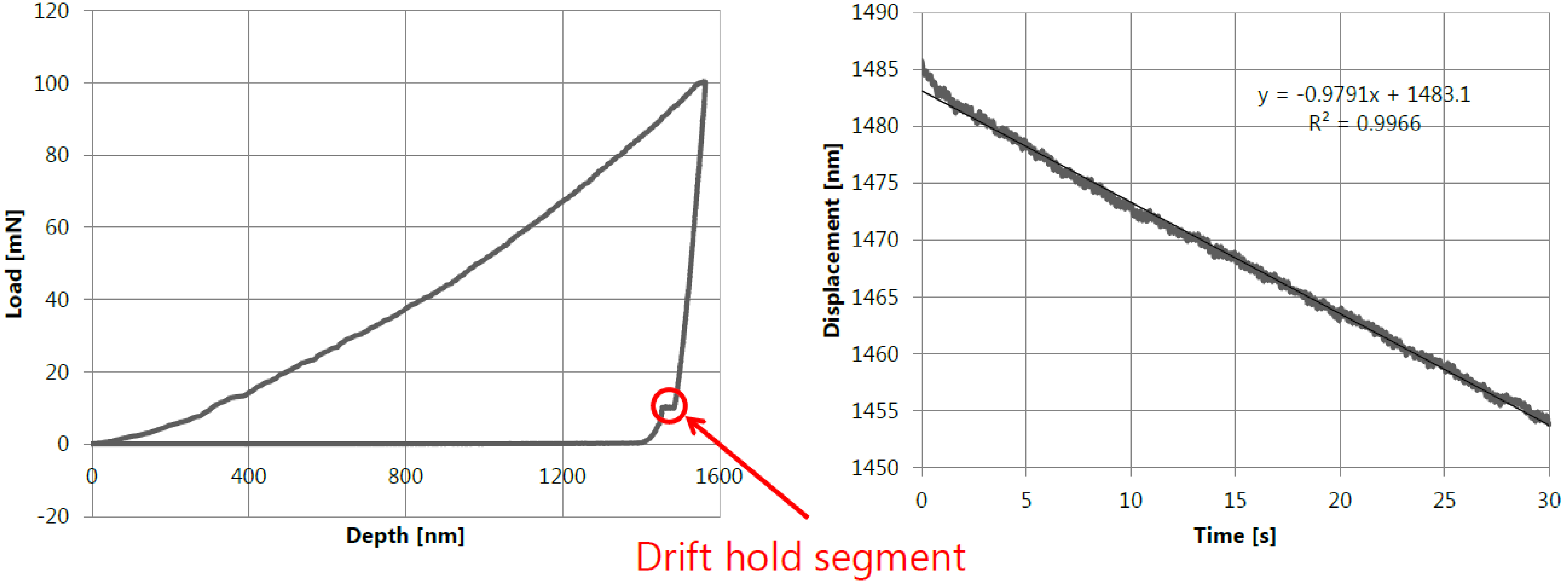

Drift hold segment

- Thermal drift measured experimentally by recording the change in depth with time at 10% of peak load during unloading.
- As the applied load is very low and the material is not expected to creep during unloading, the displacement is assumed to occur due to thermal drift.
- After 3-4 hours of stabilization, a drift of <60nm/min is reached

Drift tuning and correction at -150°C

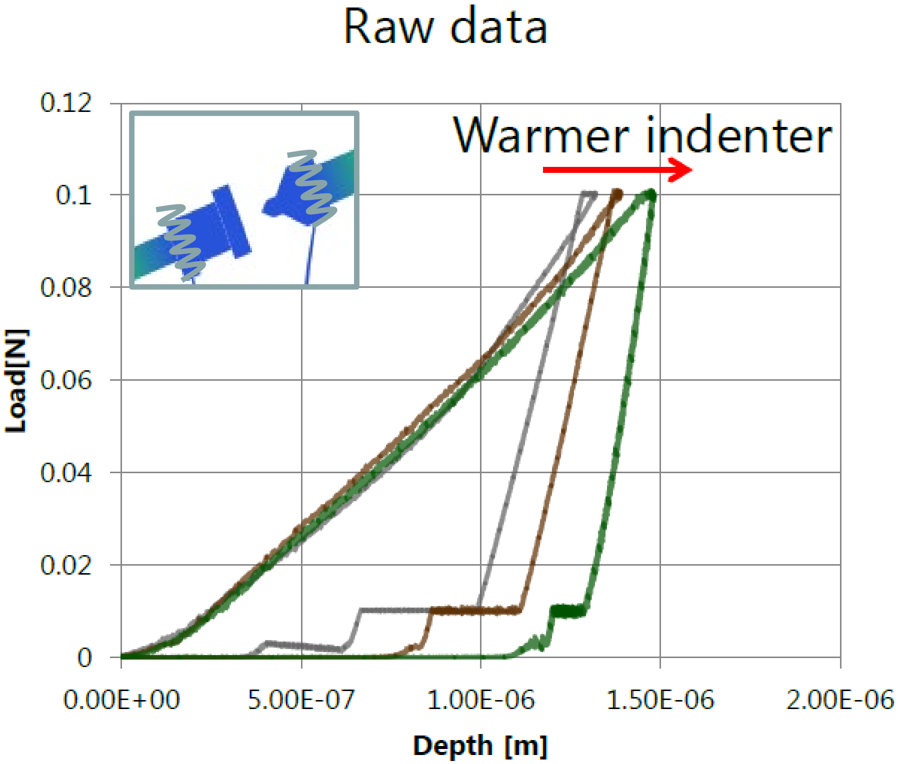

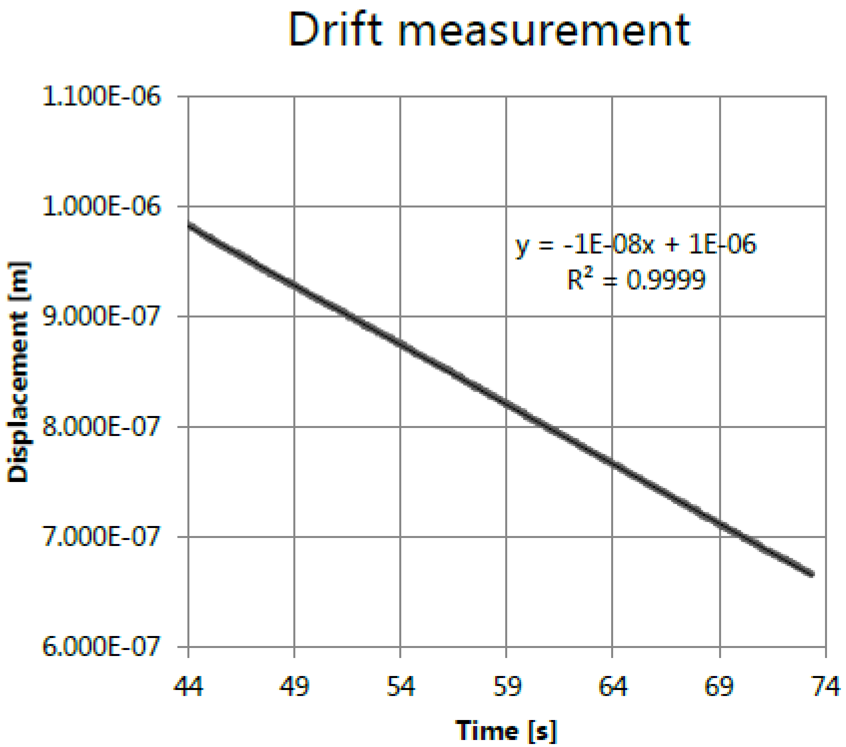

- By changing the indenter or sample temperature, the drift can be tuned
- Linear drift → drift correction possible

Temperature matching for drift minimization

- Indentations are performed with a 2 minute drift measurement at 5% of the maximum load
- Measurements are performed at different ΔT
- Thermal drift as low as 2 nm/min can be reached

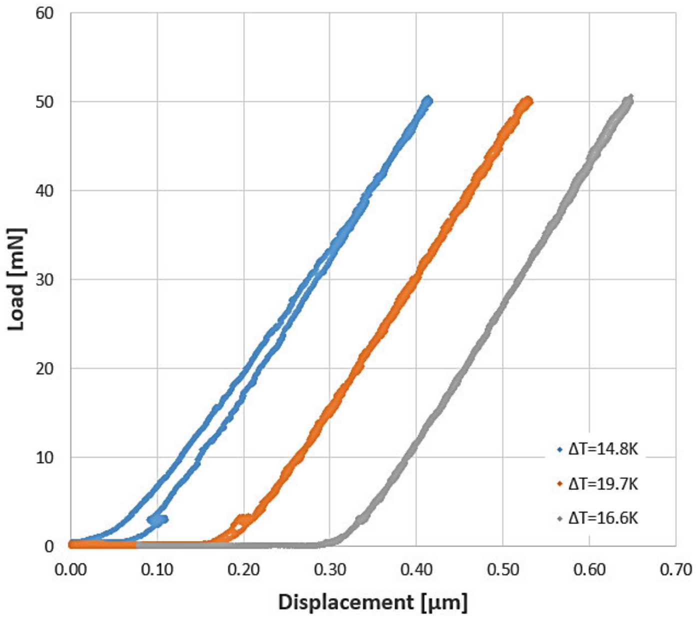

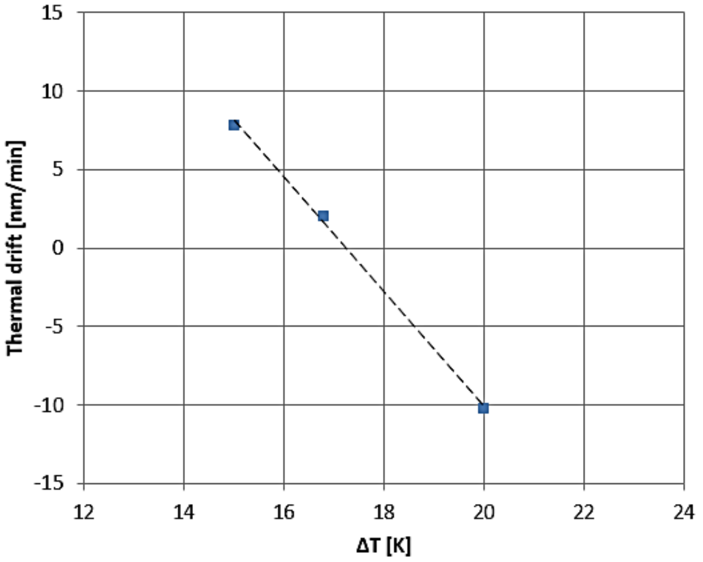

Temperature at the nanocontact

Empa
Materials Science and Technology

- Replaced tip by a thermocouple
- Direct measurement of sample surface temperature
- Determine calibration curve to sample holder temperature
- Plotting the tip temperature for which minimum drift was observed vs. sample surface temperature allows calibrating the tip temperature

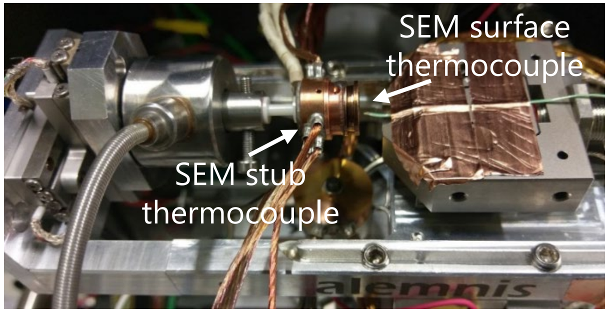

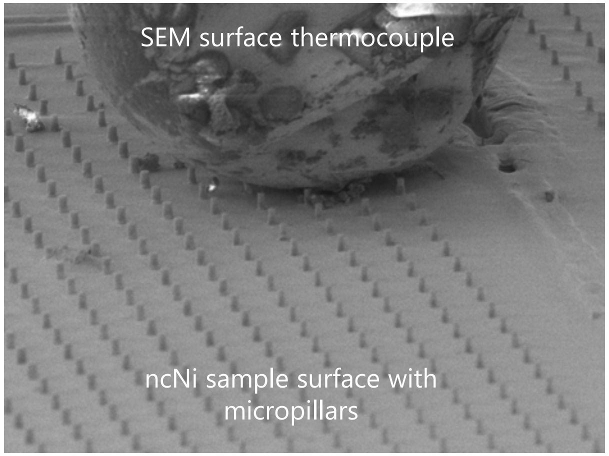

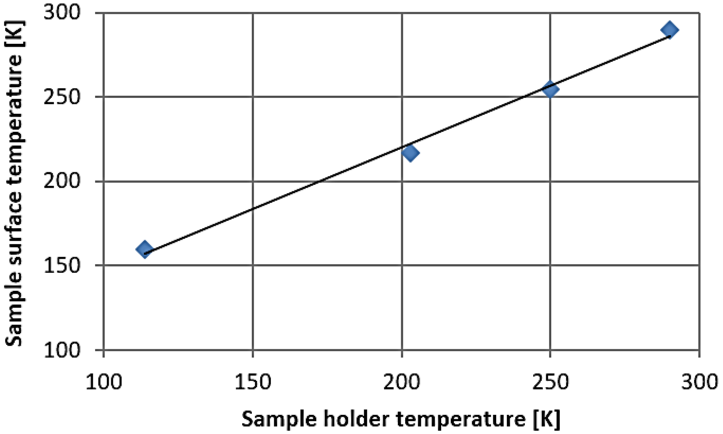

Quasistatic results

Empa
Materials Science and Technology

160K | 224K | 300K

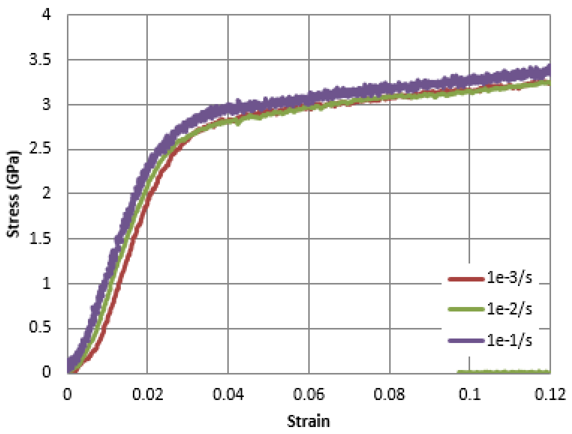

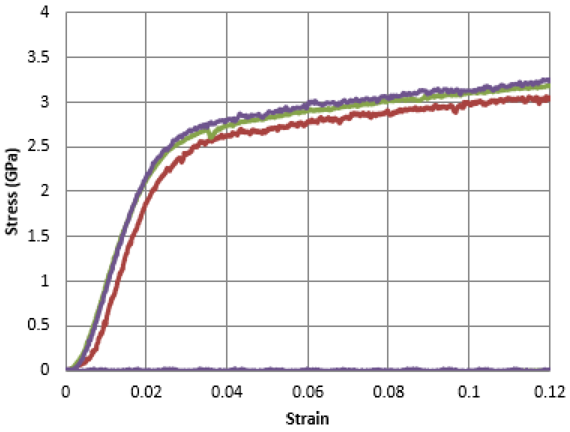

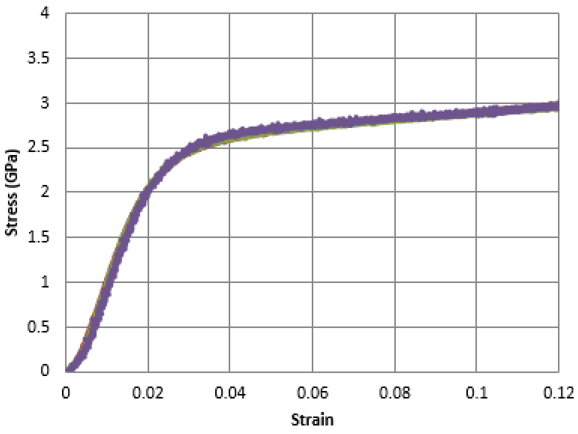

$10^{-3}s^{-1}$

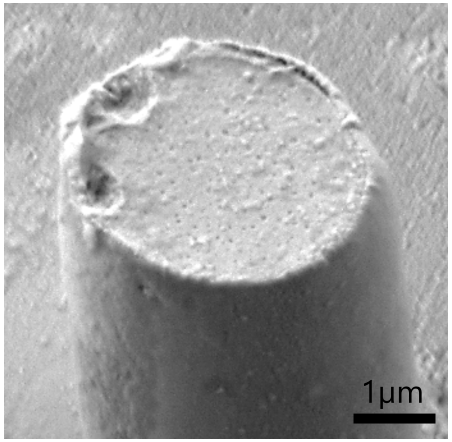

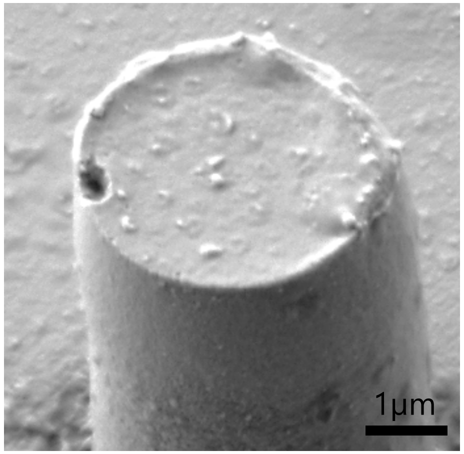

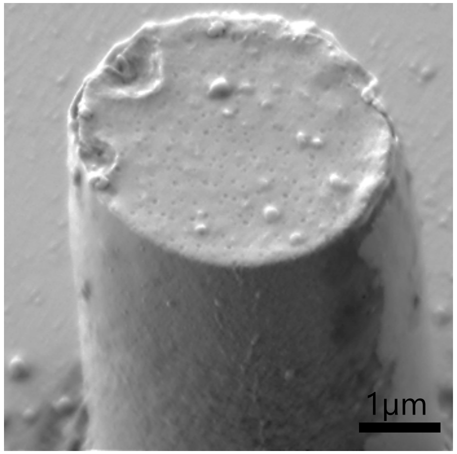

- Homogeneous deformation, barrelling of micropillar
- Weak dependence of yield stress on strain rate, strong dependence on temperature

In situ high strain rate cryoindenter setup

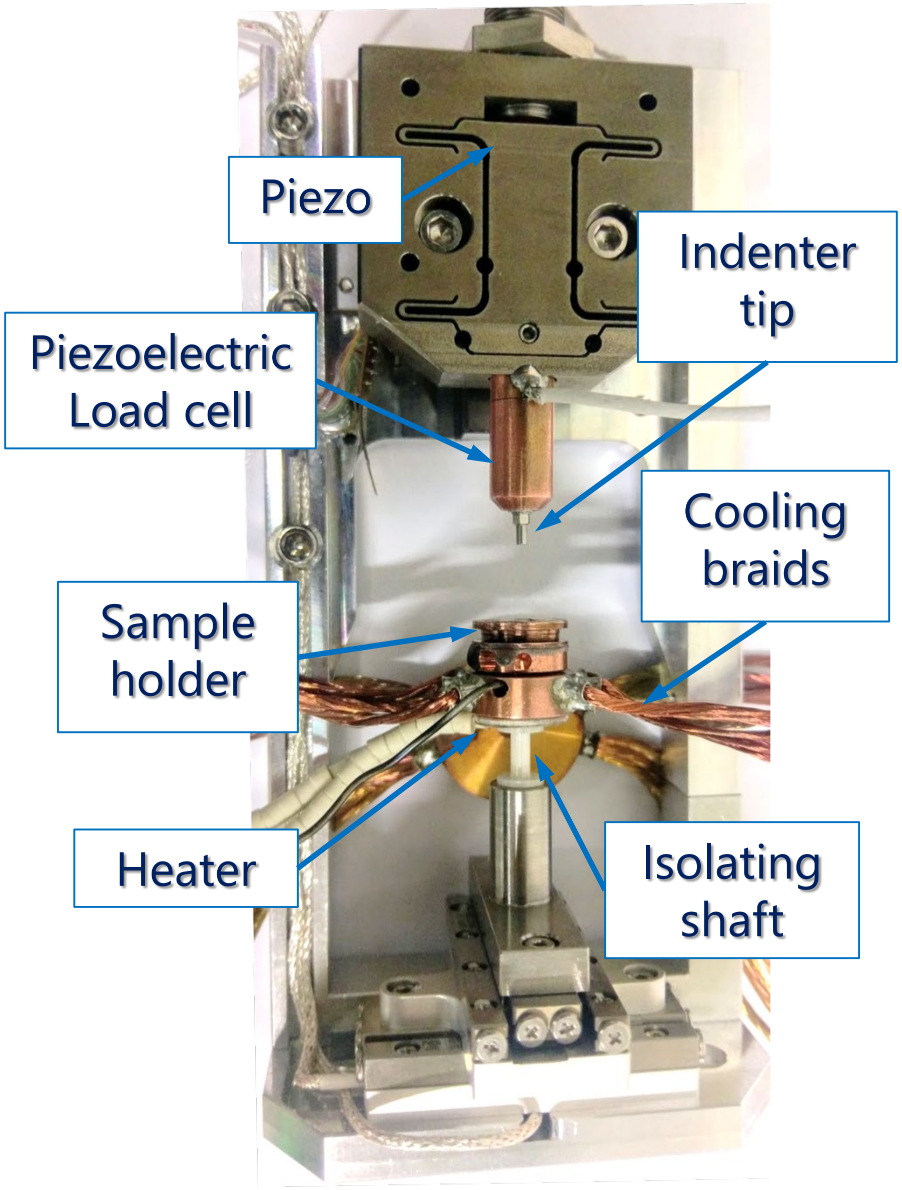

- Temperature range: 120K to 300K
- Strain rate range: 1 to $10^3 s^{-1}$
- Load range: 1N
- Standard load cell is replaced by a piezoelectric load sensor on the indenter tip side
- For measurement duration <50ms, thermal drift remains negligible for an uncooled tip in contact with a cold sample

Instrumentation for high frequencies and strain rates

alemnis
engineering your ideas

Empa
Materials Science and Technology

Maximum actuation speed – *8mm/s*

Strain rate range (gage length ~4µm) – **0.0001/s to 2000/s** – 8 orders of magnitude

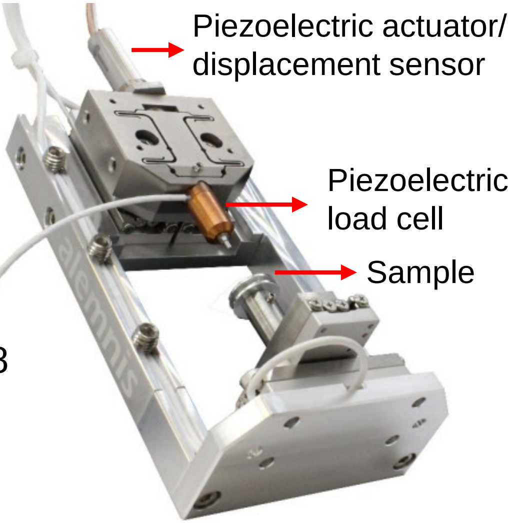

High stiffness load cell

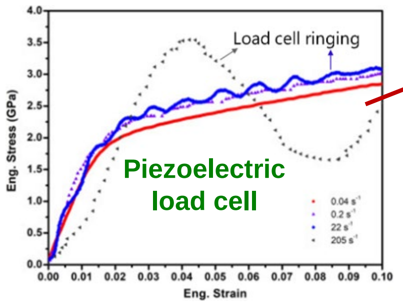

Strain gage load cell

System resonances

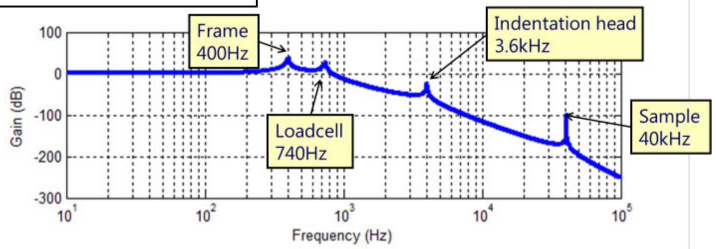

High stiffness frame

High speed actuation with accurate displacement control

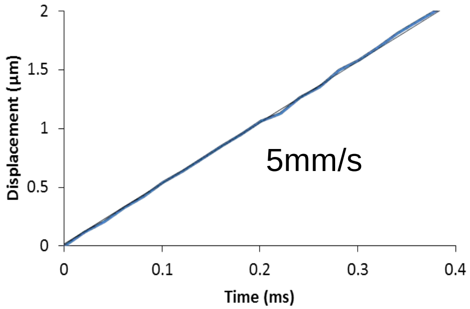

Constant strain rate and accurate strain

High speed electronics for input and output

High bandwidth amplifiers and acquisition systems

Avoiding inertial contributions

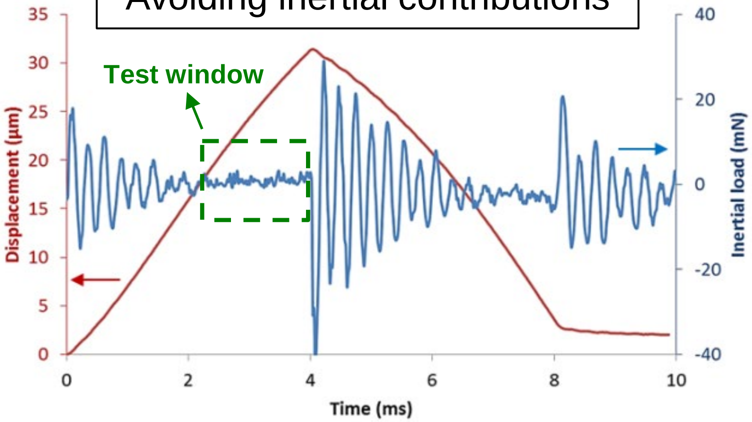

Ramachandramoorthy & Schwiedrzik et al., Nano Letters, 2019

Measurement duration for negligible load drift

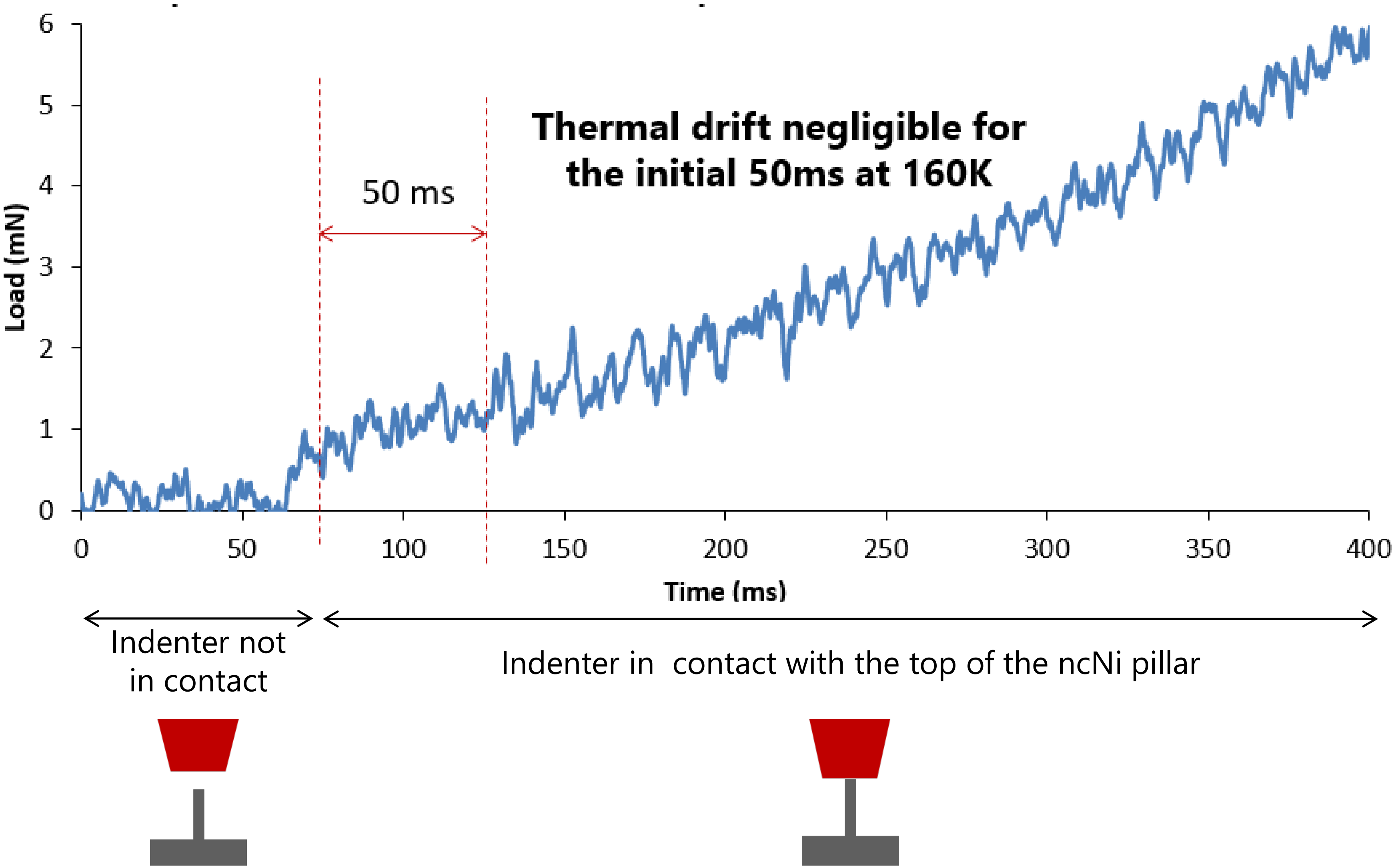

Thermal drift negligible for the initial 50ms at 160K

Indenter not in contact

Indenter in contact with the top of the ncNi pillar

Maximum duration of cryo temperature/high strain rate tests possible – **50 ms**
Translates to a strain rate of ~3/s for a gage length of 8um

High strain rate results

160K

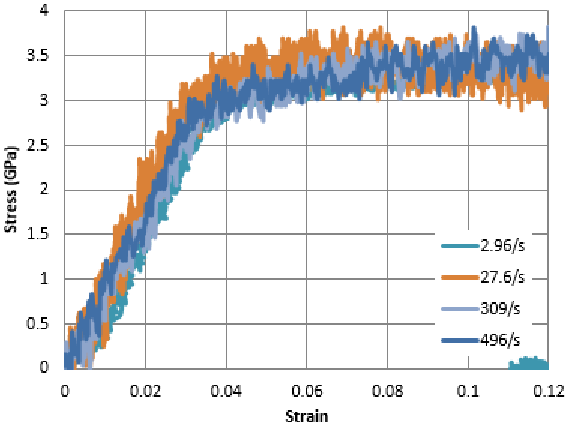

224K

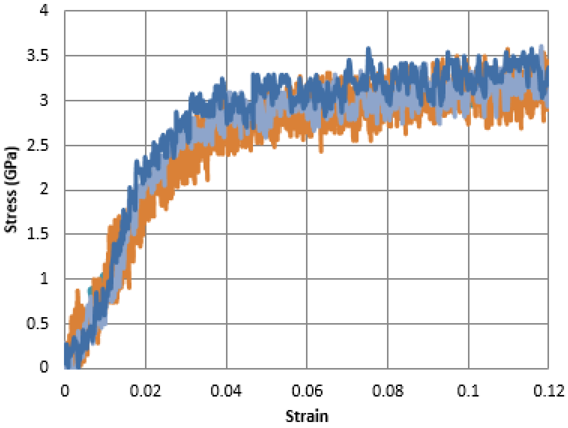

300K

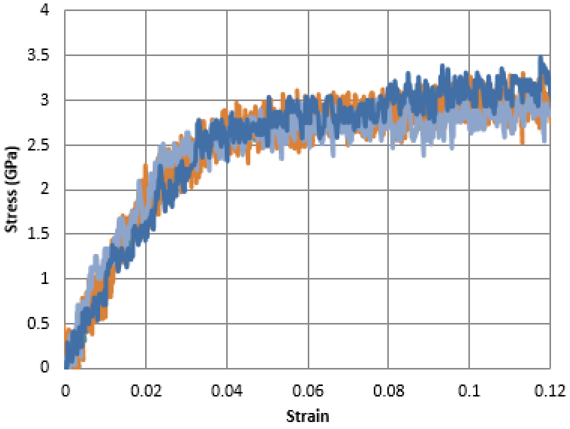

$309s^{-1}$

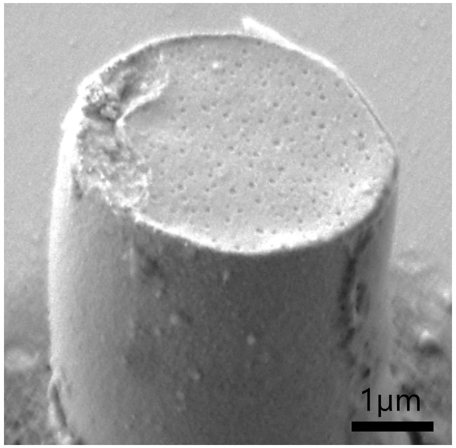

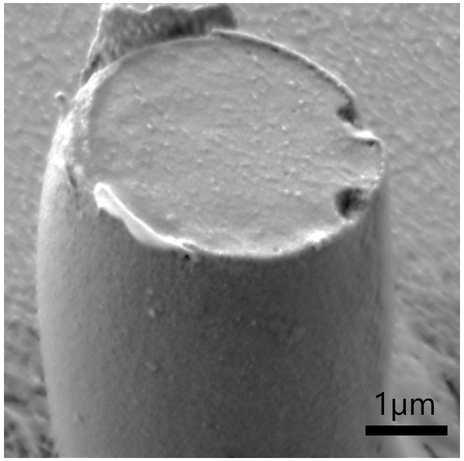

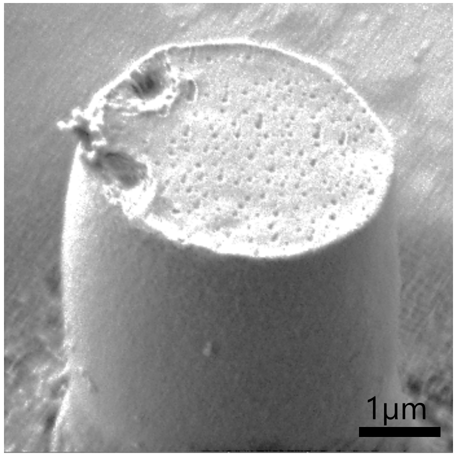

Results consistent with quasistatic experiments:

- Weak dependence of yield stress on strain rate, strong dependence on temperature

Thermal activation analysis

Strain rate sensitivity:

$$m = \frac{dln\sigma}{dln\dot{\varepsilon}}$$

- m is increased at lower temperatures

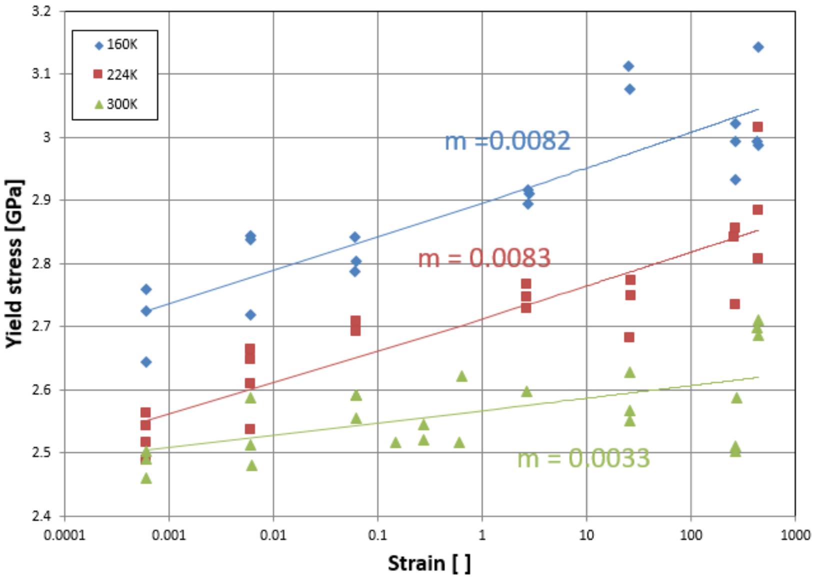

Thermal activation analysis

Strain rate sensitivity:

$$m = \frac{dln\sigma}{dln\dot{\varepsilon}}$$

- m is increased at lower temperatures

Apparent activation energy:

- Extrapolated strain rates for σ_y=2.65GPa
- Q_{app} is approx. 55 kJ/mol (0.58eV)

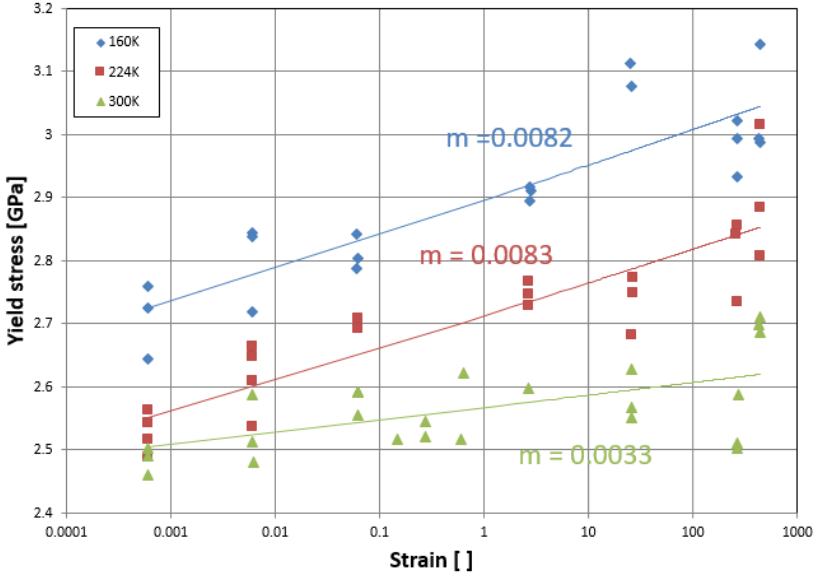

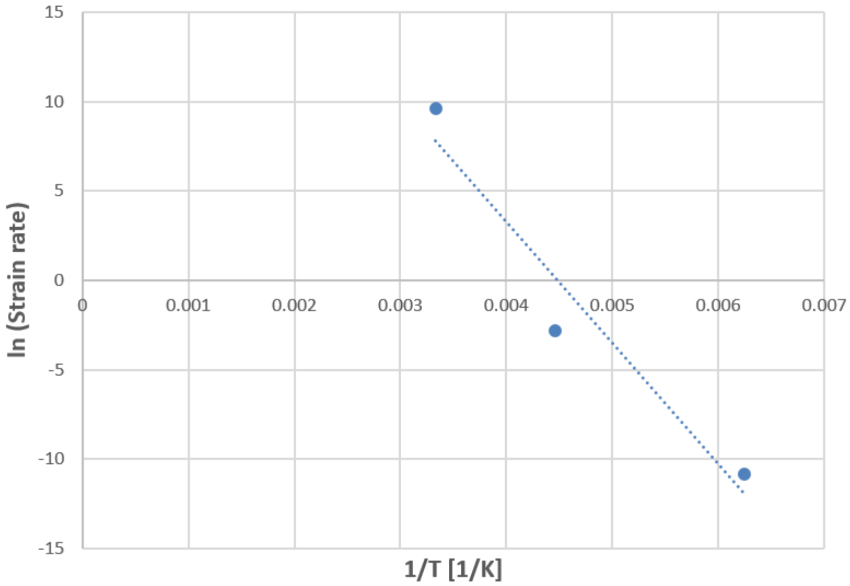

Thermal activation analysis

Strain rate sensitivity:

$$m = \frac{dln\sigma}{dln\dot{\varepsilon}}$$

- m is increased at lower temperatures

Apparent activation energy:

- Extrapolated strain rates for σ_y=2.65GPa
- Q_{app} is approx. 55 kJ/mol (0.58eV)

Apparent activation volume:

$$V_{app} = k_B T \left(\frac{dln\dot{\varepsilon}}{d\sigma} \right)$$

- V_{app} increases with temperature from $5b^3$ at 160 K to $11b^3$ at 300 K

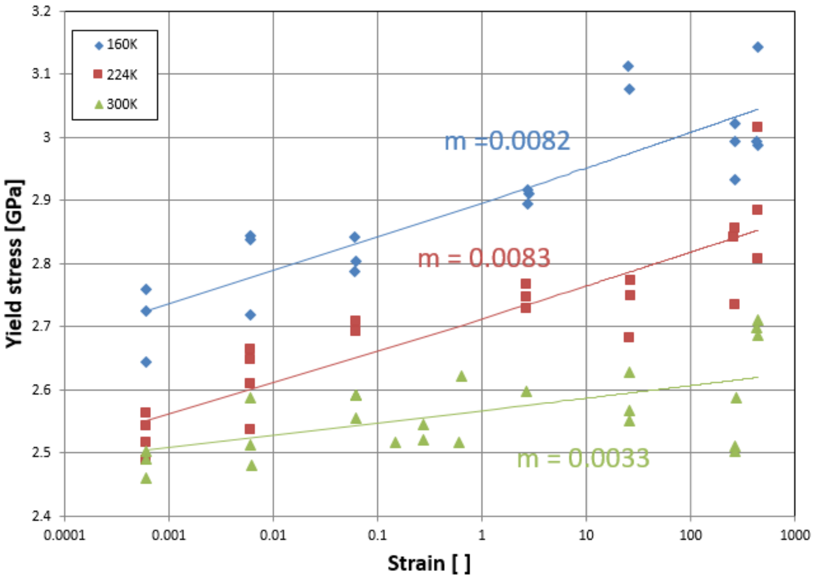

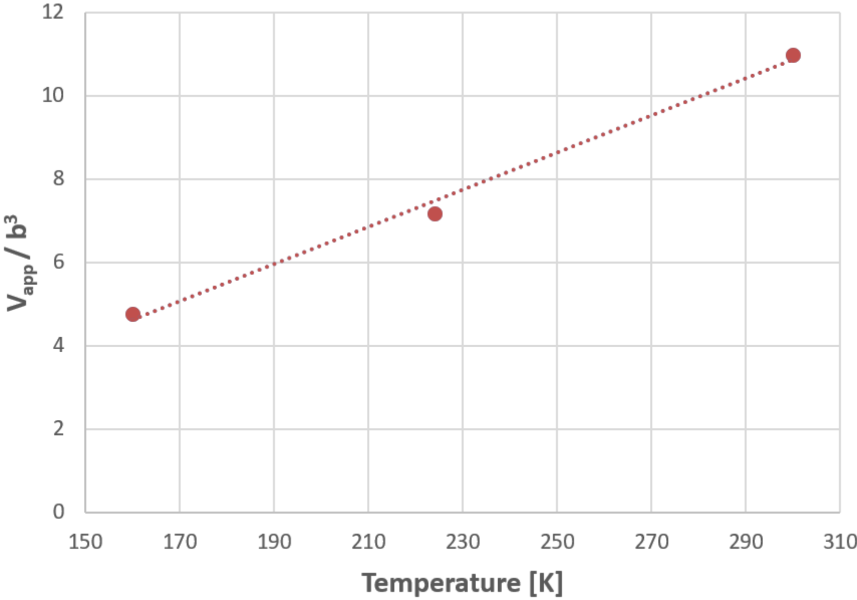

TEM analysis

undeformed

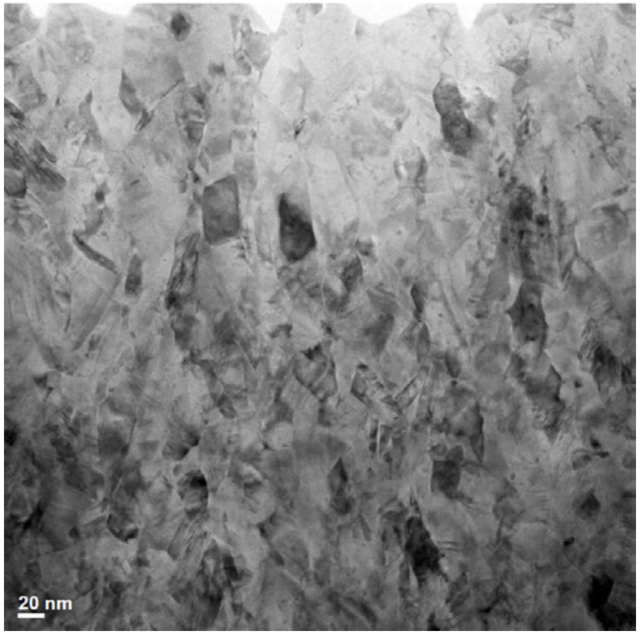

160K, 0.001s^{-1}

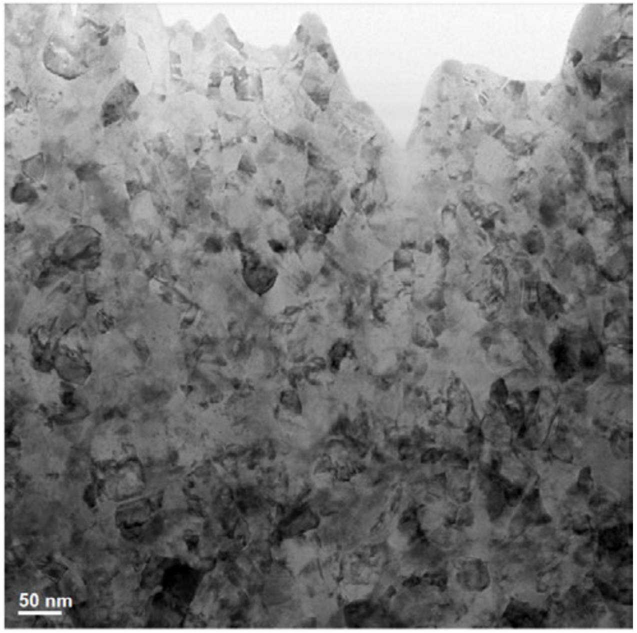

160K, 300s^{-1}

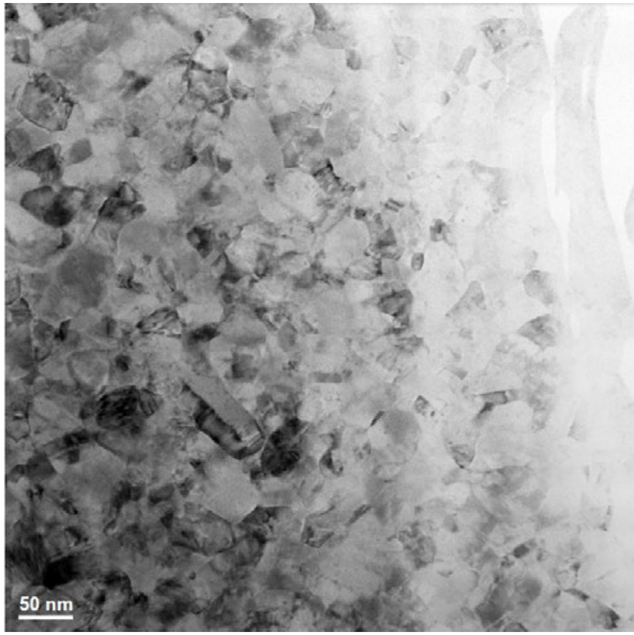

- TEM lamellae have to be extremely thin, preparation and imaging are complicated
- A change in grain shape from elongated in growth direction to oblate is observed in deformed pillars
- Grain size seems more heterogeneous in deformed pillars

TEM analysis

undeformed

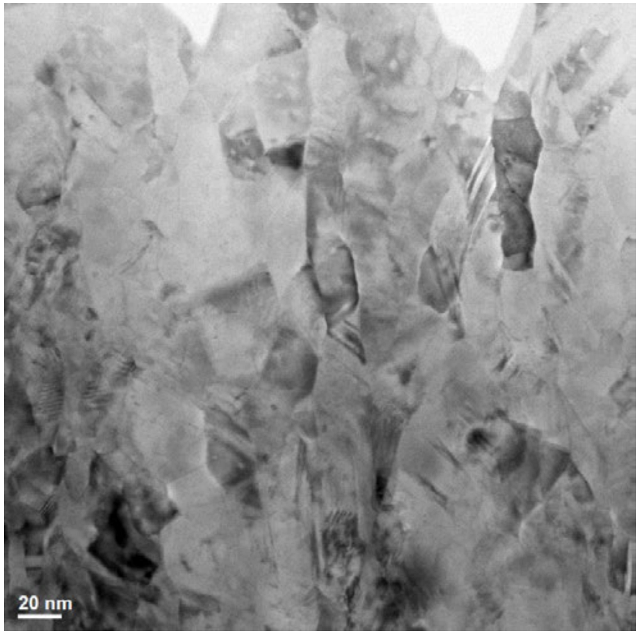

160K, 0.001s^{-1}

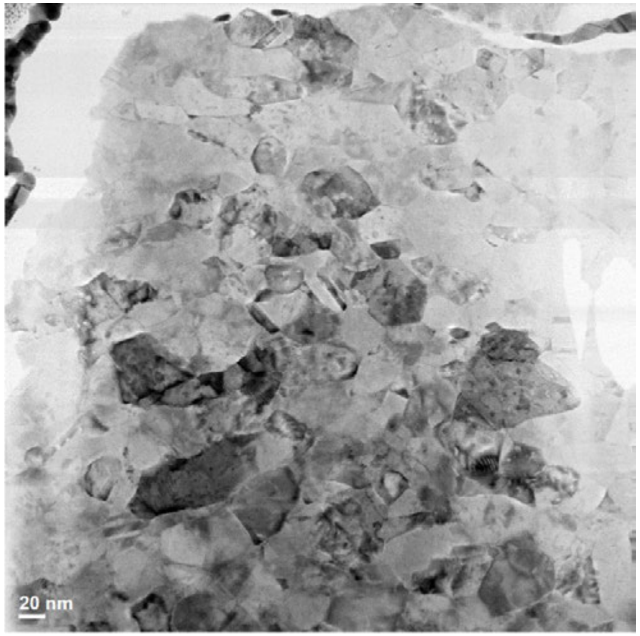

160K, 300s^{-1}

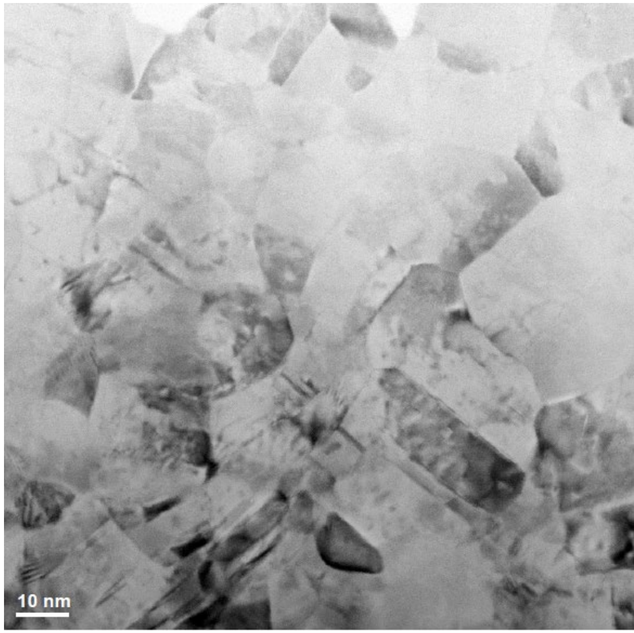

- TEM lamellae have to be extremely thin, preparation and imaging are complicated
- Change in grain shape from elongated in growth direction in undeformed to isotropic/oblate in deformed pillars
- Grain size more heterogeneous in deformed pillars
- Twin density does not increase

Discussion

Electrodeposited micropillar arrays:

- Large number of specimens
- No FIB damage, no taper
- Influence of confined growth on grain structure?
    - Grains elongated in growth direction

Instrument development:

- In situ experiments at low temperatures and in large strain rate range:
    - 120K to 300K
    - Strain rate range: 10^{-4} to $10^{3}s^{-1}$
    - Large strain rate range → even low *m* may be measured

Discussion

Deformation mechanisms in nc Ni:

- Activation volume and energy are consistent with dislocation nucleation, i.e. intragranular plasticity, but also other deformation mechanisms like grain boundary or defect diffusion are likely present
- Temperature dependence of activation volume reflects thermally-dependent interplay of different deformation mechanisms
- Experiments at lower temperature are needed to identify at what point thermal activation is supressed
- Post-test TEM analysis: higher variation in grain size and change in grain shape, needs to be verified
- Next steps: TKD analysis for improved grain size and shape statistics

Micromechanical testing at high strain rates and varying temperatures of 3D-printed polymer structures

Two-Photon Lithography (2PL)

- Two-Photon Lithography Direct Laser Writing allows 3D printing of micron-sized polymer components
- A resolution in the tens of nanometres can be achieved
- Excellent for rapid prototyping, templating or surface modification

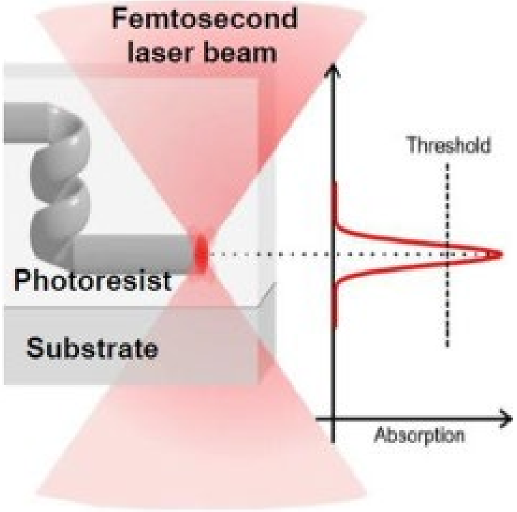

Here:

- Photonic Profession GT (Nanoscribe GmbH)
- Commercially available negative photoresist “IP-Dip” an acrylate-based polymer
- ITO covered glass substrate for improved adhesion

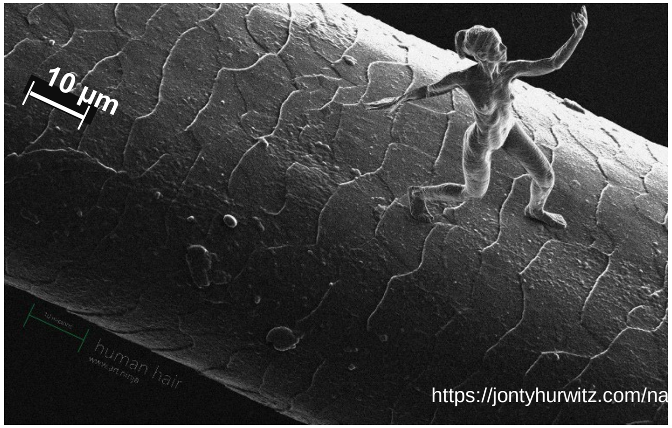

https://jontyhurwitz.com/na

Microlattices and the Fabrication of Metamaterials

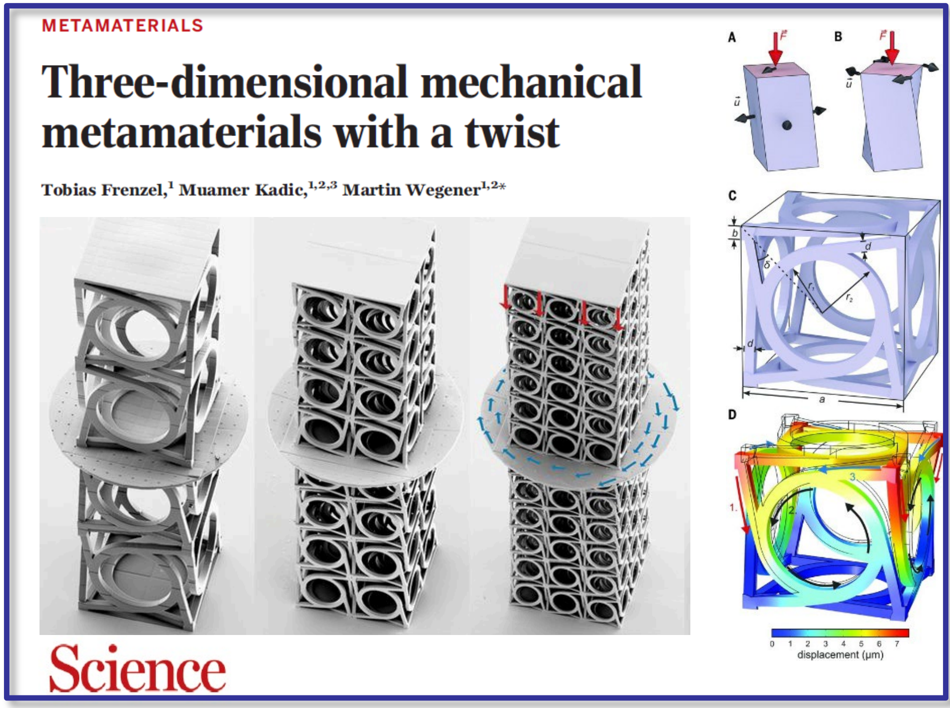

METAMATERIALS

Three-dimensional mechanical metamaterials with a twist

Tobias Frenzel,[1] Muamer Kadic,[1,2,3] Martin Wegener[1,2*]

Science

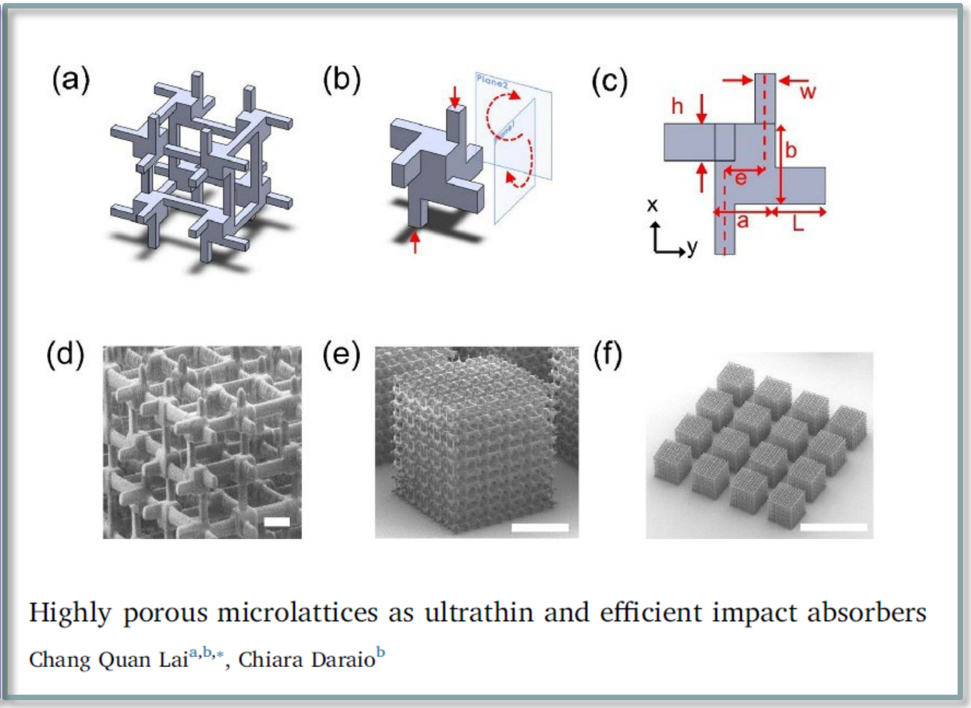

Highly porous microlattices as ultrathin and efficient impact absorbers

Chang Quan Lai[a,b,*], Chiara Daraio[b]

Micromechanical Testing: Experiments

Fabrication	Two-Photon Lithography (IP-Dip, Nanoscribe GmbH)		
Tests	Micropillar Compression	Micro-tensile Test	Nanoindentation
Geometric Dimensions	Pillar d: 6µm; h: 9µm	Dogbone 5^2 µm cross-section	Berkovich tip h_{max}: 700 nm
Conditions	10^{-4} to 10^{2} s^{-1} 25 to 80°C	10^{-4} to 10^{1} s^{-1} ambient	Quasistatic, ambient
Properties	Yield strength, E	Yield strength	Hardness, E

Micropillar compression tests

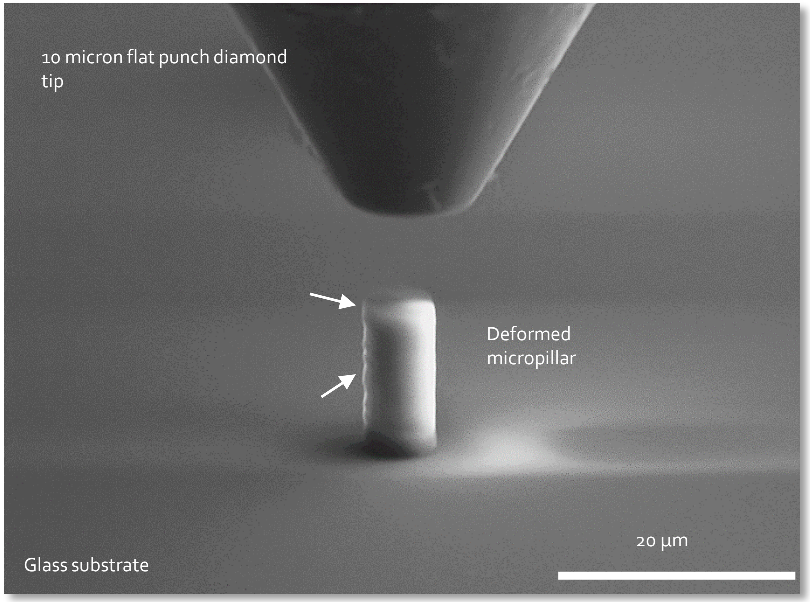

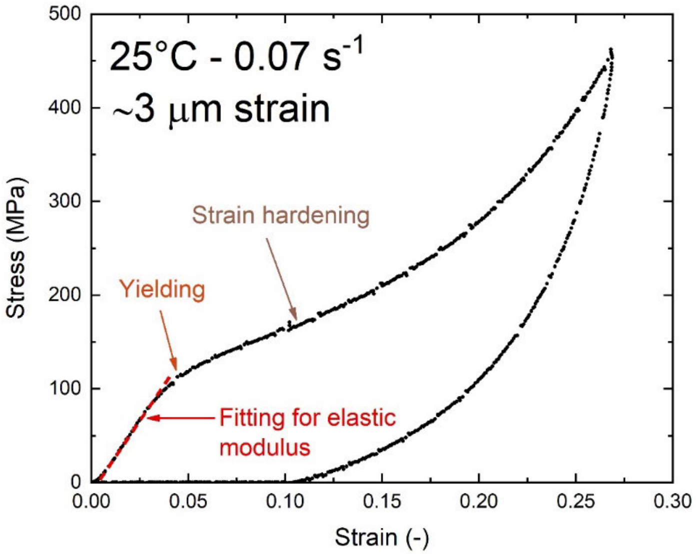

Micropillar compression tests – *Strain rate dependence*

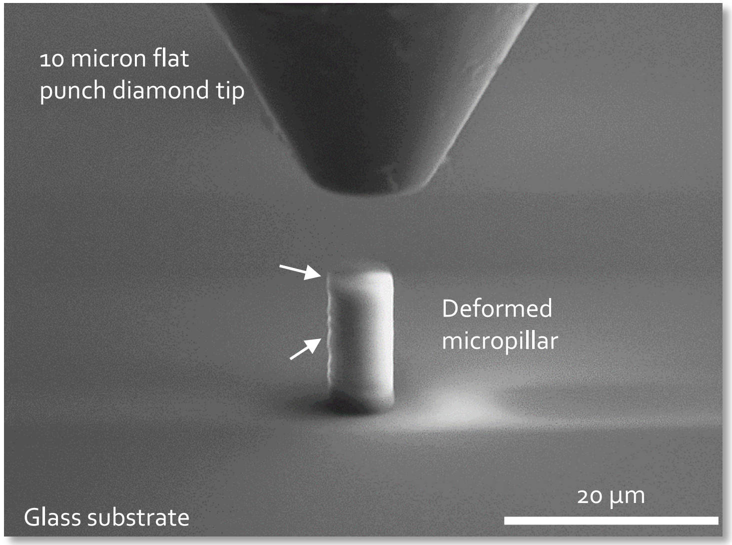

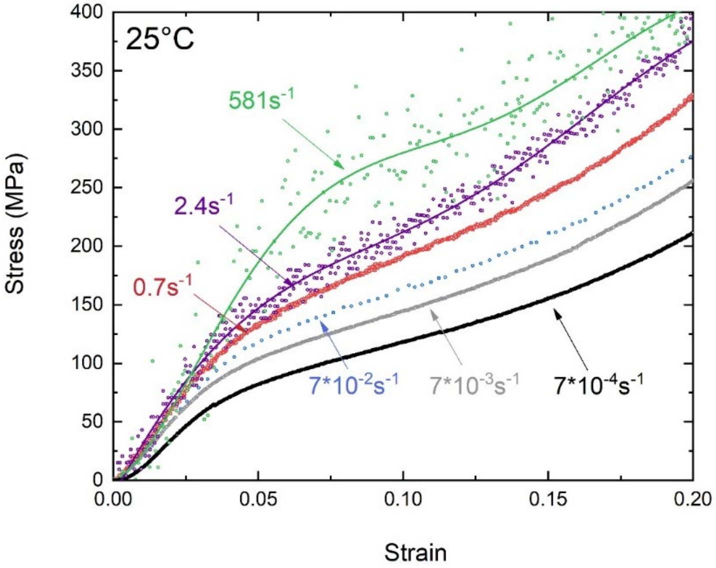

- Strong strain rate dependence in deformation behaviour of polymer pillars
- All pillars were 6 µm in diameter and 9 µm in height
- 3 Pillars were measured for each condition → measurements showed good reproducibility
- Yielding occurred above 2 mN → reliable measurement possible
- Data acquired in the quasistatic regime was corrected for thermal drift

Micropillar compression tests – *Yield Strength*

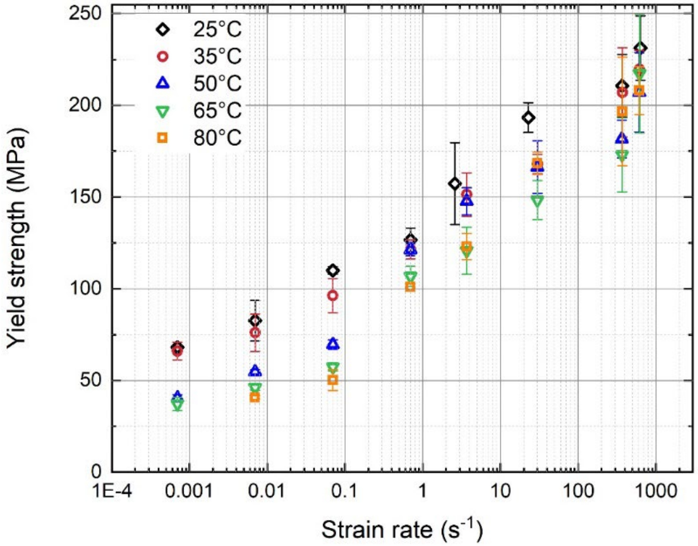

- Yield strength increases strongly with higher strain rates
- Higher temperatures lead to a significant drop in yield strength; this effect is less pronounced at higher strain rates

Micro-tensile test – *Yield strength*

- Yield strength from tensile tests is slightly lower than from compressive tests
- Both tests give a similar strain rate dependence

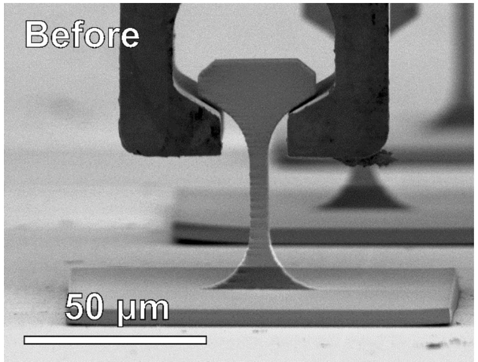

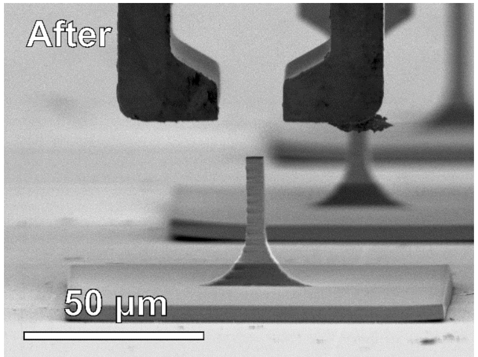

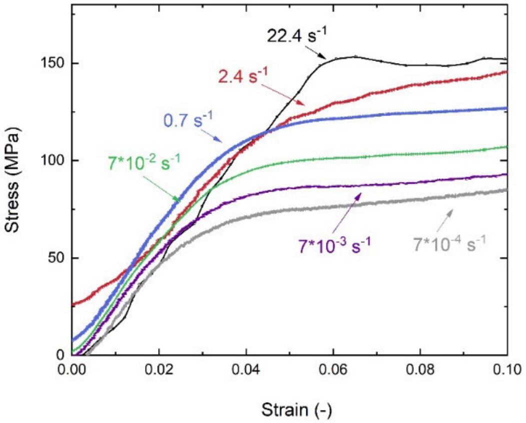

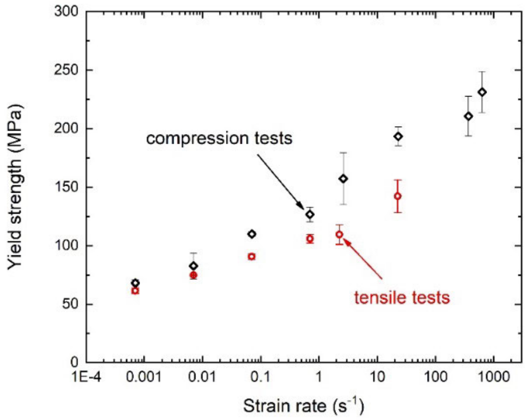

Experimental observations

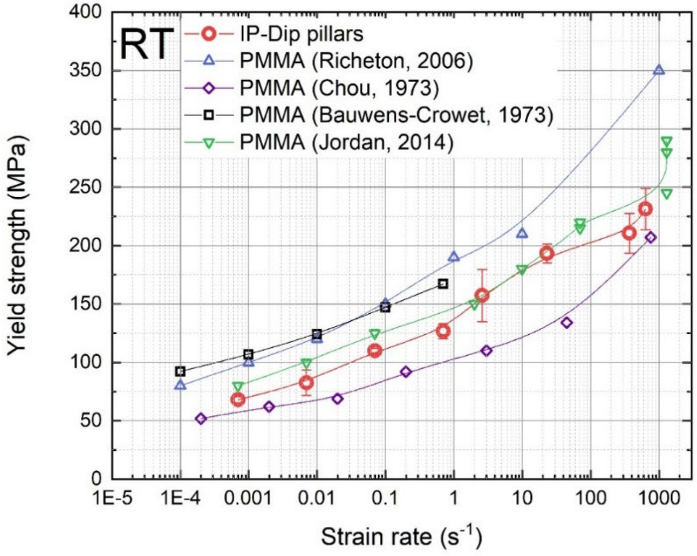

- PMMA closest chemical sibling to IP-Dip
- The strain rate dependency of yield strength in 3D printed polymer micropillars compares well to the data acquired in macroscopic compression tests of PMMA

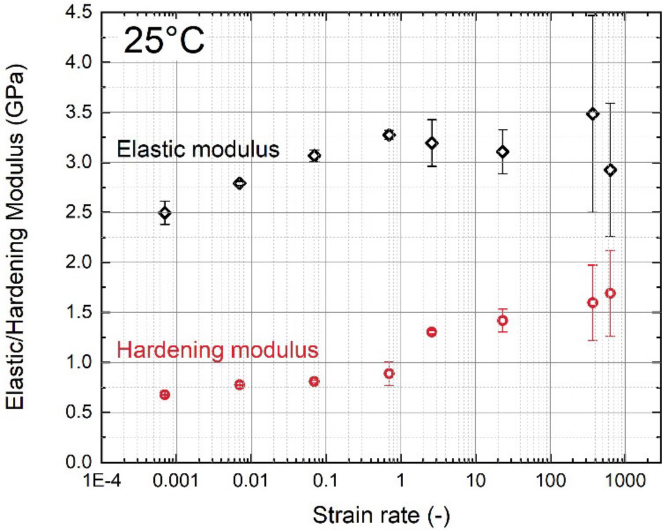

IP Dip: Yielding occurs at higher strains and stresses, slope increases before and after yielding

→ Hardening modulus increases at higher strain rates

Strain rate – Temperature Superposition principle

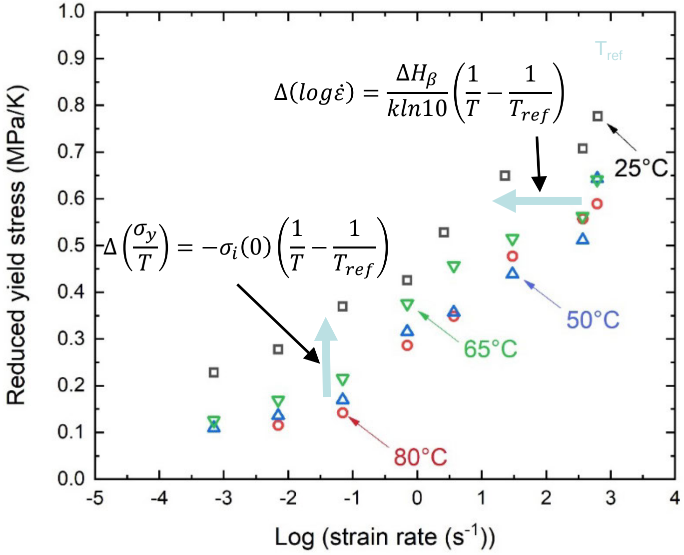

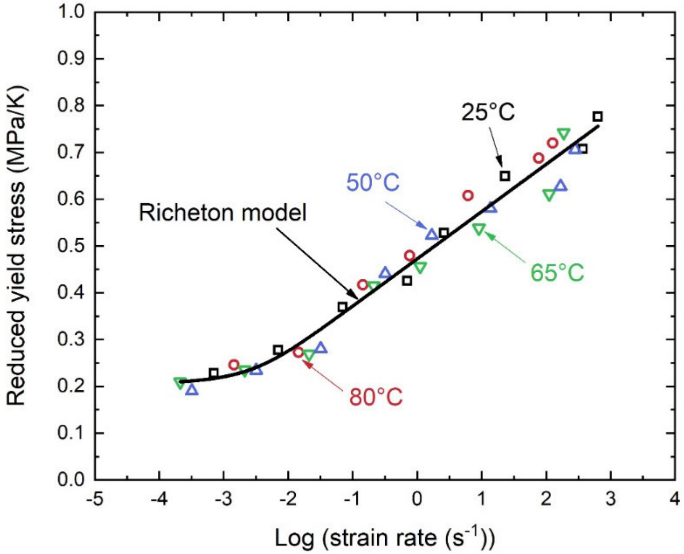

Richeton et al. (2006) propose a formulation for a cooperative model using an Eyring type equation to describe the principle of *Strain rate – Temperature Superposition* for the compressive yield strength in polymers

→ Yield stress increases with decreasing temperature and increasing strain rate

$$\frac{\sigma_y}{T} = \frac{\sigma_i(T_{ref})}{T_{ref}} + \frac{2k}{V}\sinh^{-1}\left(\frac{\dot{\varepsilon}}{\dot{\varepsilon}^*(T_{ref})}\right)^{\frac{1}{n}}$$

Data was fitted with the formula of Richeton model → parameters describing activation of yielding for the specific polymer are extracted

Strain rate – Temperature Superposition principle

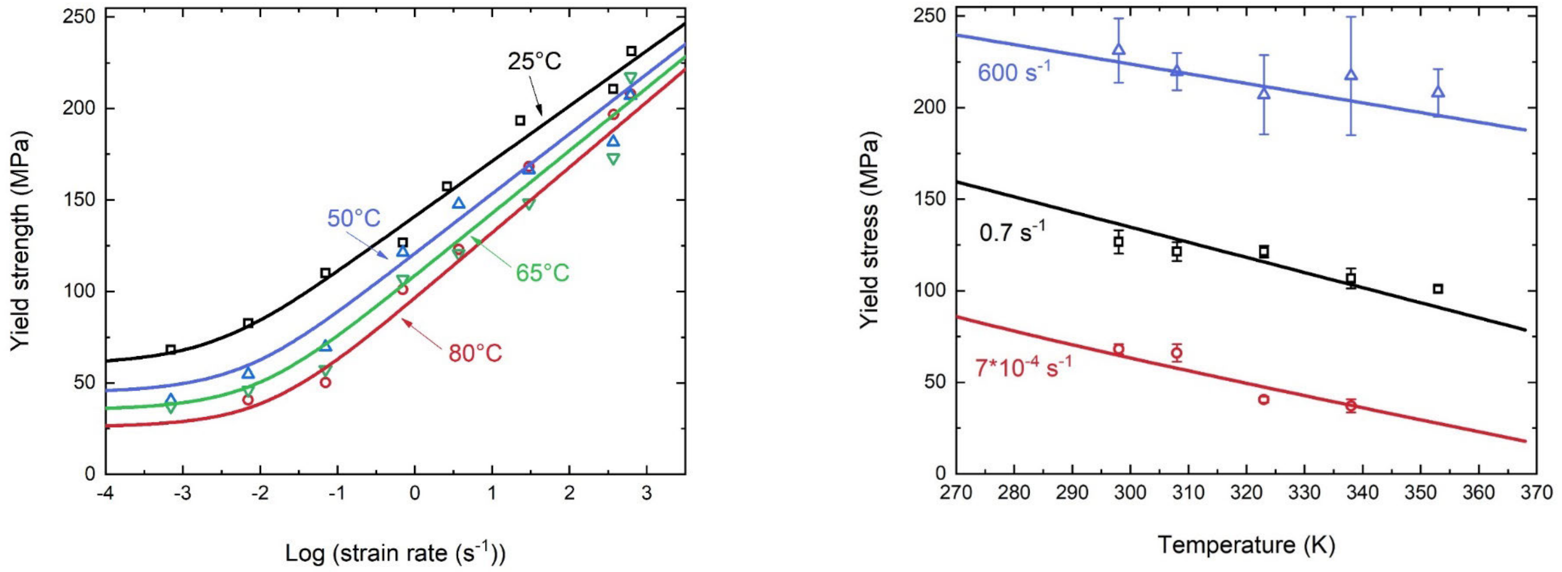

Summary

- This is the first systematic experimental assessment on the micromechanical scale of yield strength and elastic modulus of 3D printed polymer structures investigating the effect of ***higher strain rates*** and ***temperature***.
- It could be shown that such tests can be conducted reliably ranging over 6 orders of magnitude of strain rate showing a strong strain rate dependency of yielding behaviour as well as elastic modulus. Measurements at elevated temperatures showed a strong reduction in mechanical properties of the polymer.
- A model based on the temperature-strain rate superposition principle developed for macroscopic testing was applied to describe the yielding behaviour on the microscopic scale allowing to predict properties beyond the measured scope.
- This work can be continued to more complex (lattice) geometries.

Conclusions and outlook

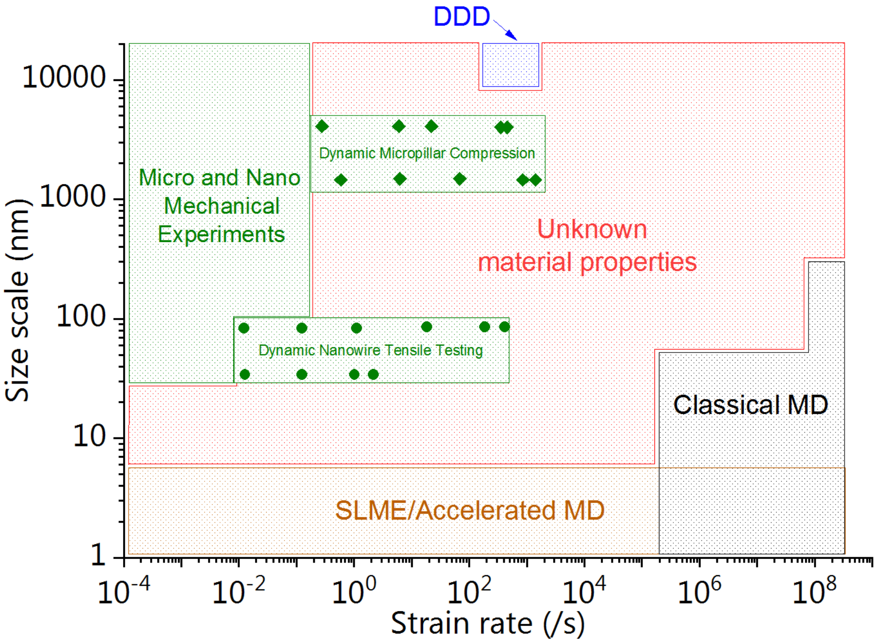

- Micromechanical investigation of deformation and failure under extreme conditions is a new phase space in small scale research
- Open questions on amorphous plasticity
  - Natural extension of dynamic testing to metallic glasses
  - What is effect of strain rate and temperature combination?

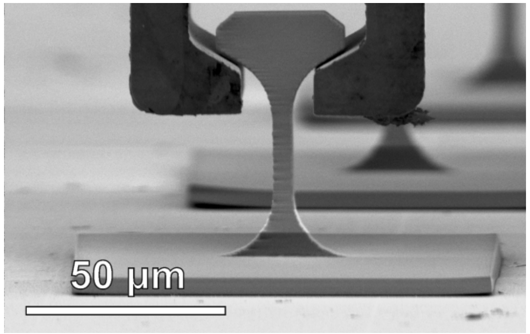

Polymer micropillars – High T + HSR

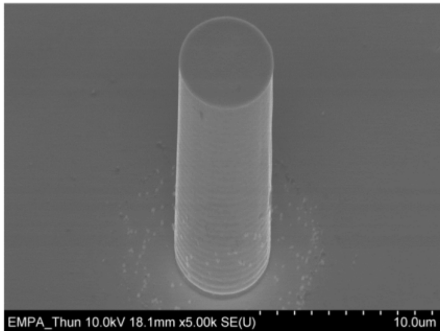

ncNi micropillars – Cryo + HSR

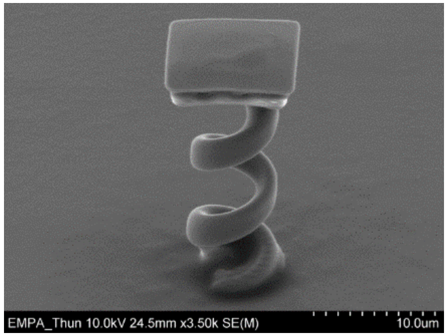

ncNi springs

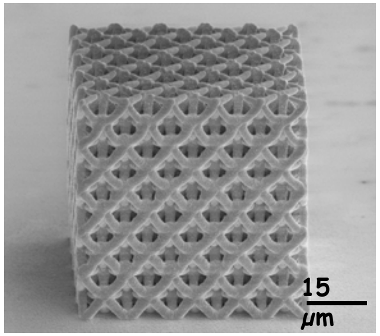

Full metal microlattices

Enhancing strength of micro-architectures

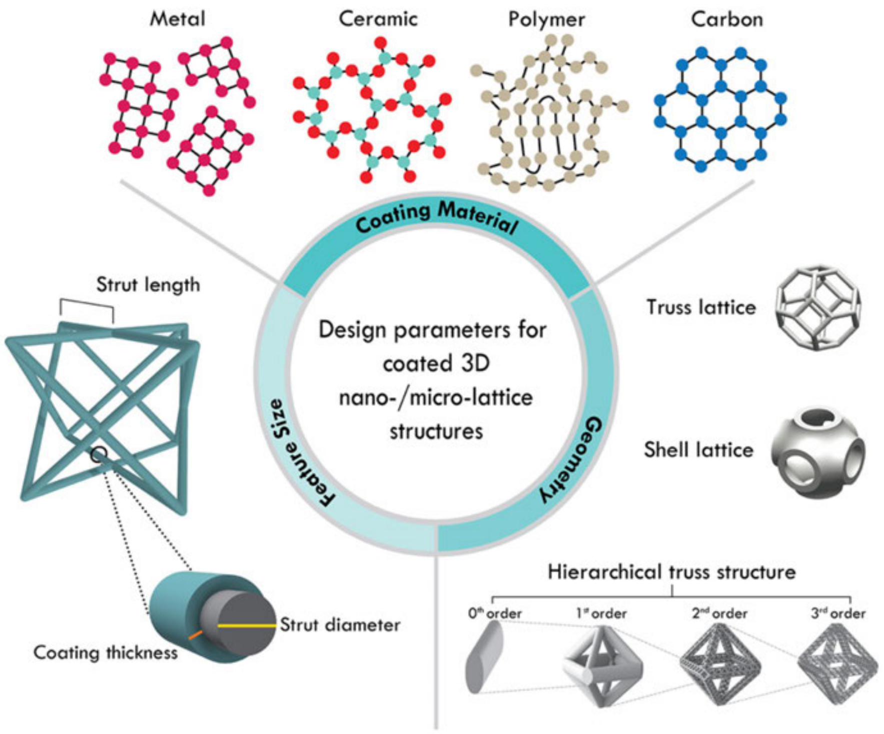

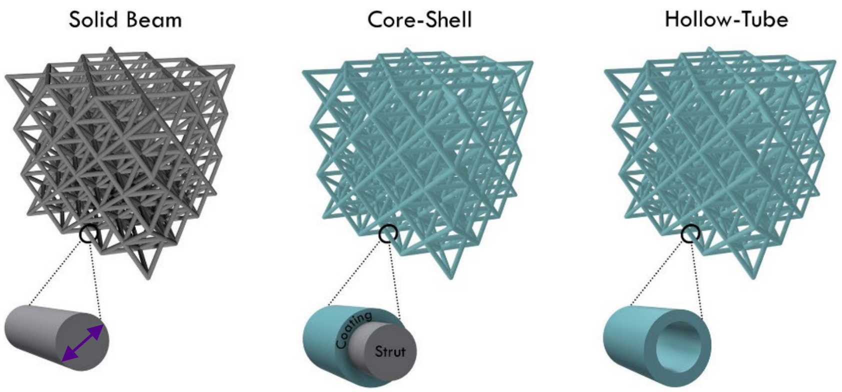

Exploit size effects and coating materials to achieve unique properties!

Adapted from: Garcia-Taormina et al. (2021) *J. Mater Res.*, 36(18), 3607-3627.

Study goals

- Develop additive manufacturing process for hybrid metal-ceramic microscale metamaterials
- Using a combination of synchrotron-based ptychography, SEM, micromechanical testing, and computational models, investigate
  - structure-property relationships and failure mechanisms
  - influence of geometric deviations from the ideal shape and internal defects on mechanical performance

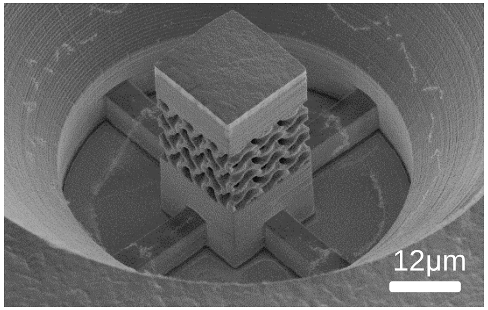

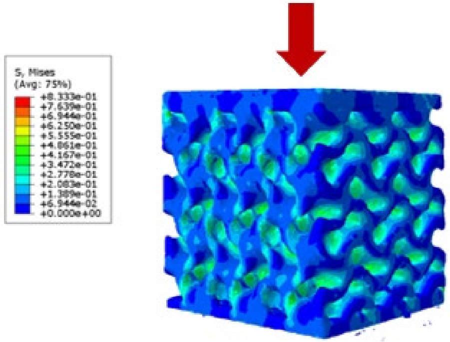

Two photon lithography

- Based on two photon absorption
- 2PP threshold determines voxel size
- Allows 3D printing below diffraction limit

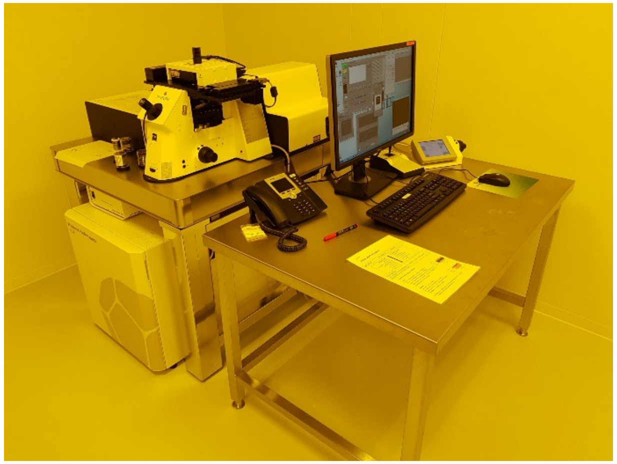

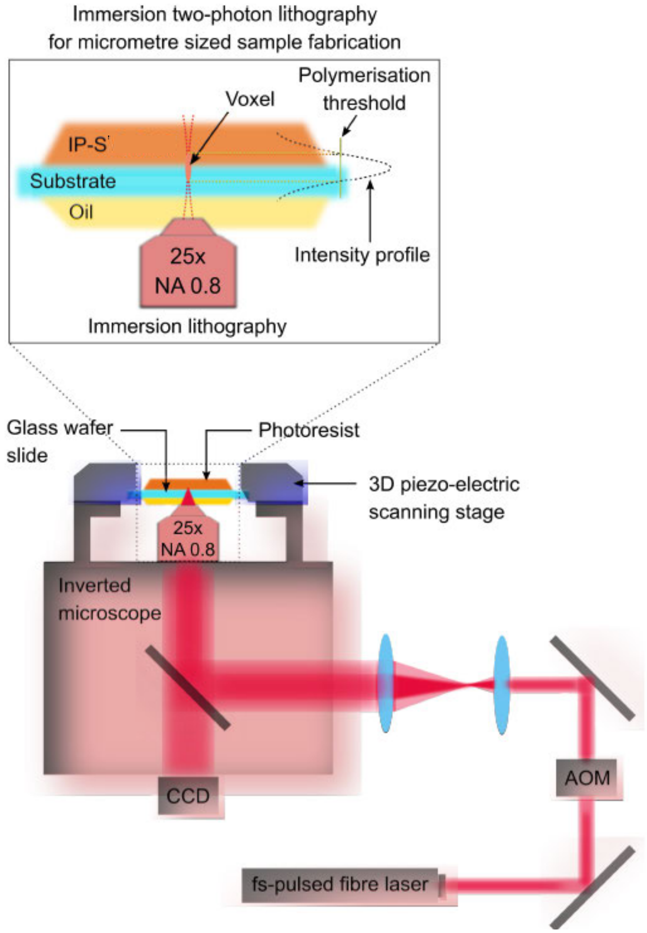

Template assisted electrodeposition

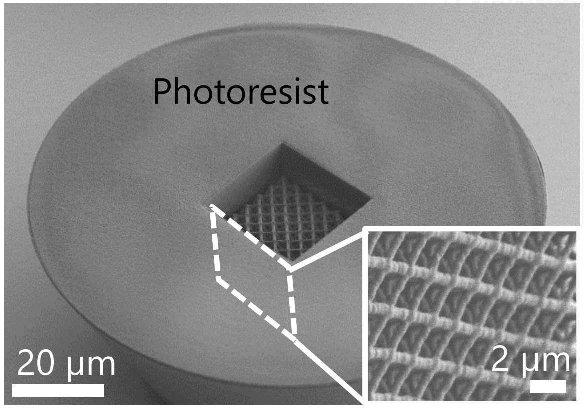

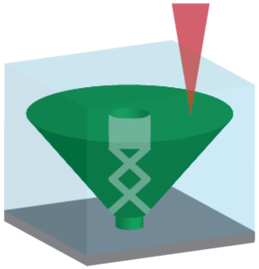

Two-Photon
Lithography

Atomic layer deposition

Atomic layer deposition:

- Self-limiting process
- Sub-nm thickness control
- Conformal coatings

Process conditions:

- Deposition temperature 65°C
- 1000 cycles of
  - Trimethyl aluminum
  - H_2O
- Al_2O_3 film with 134 nm thickness

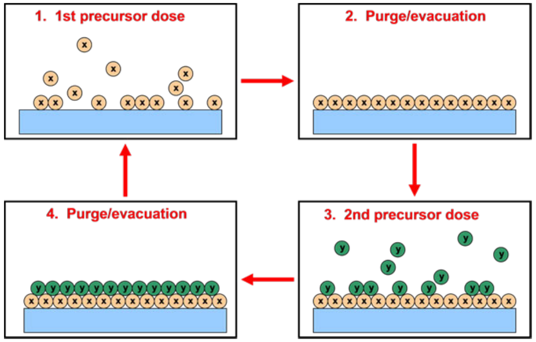

Schematics of the ALD process

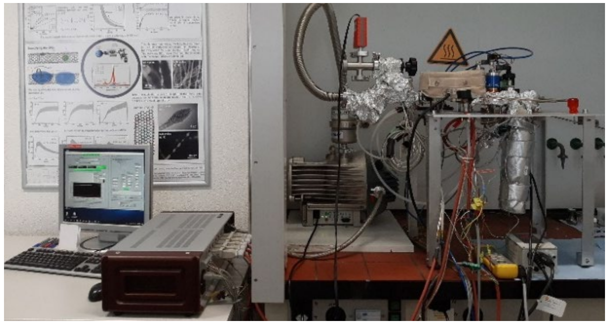

ALD reactor at lab 206

Resulting structures

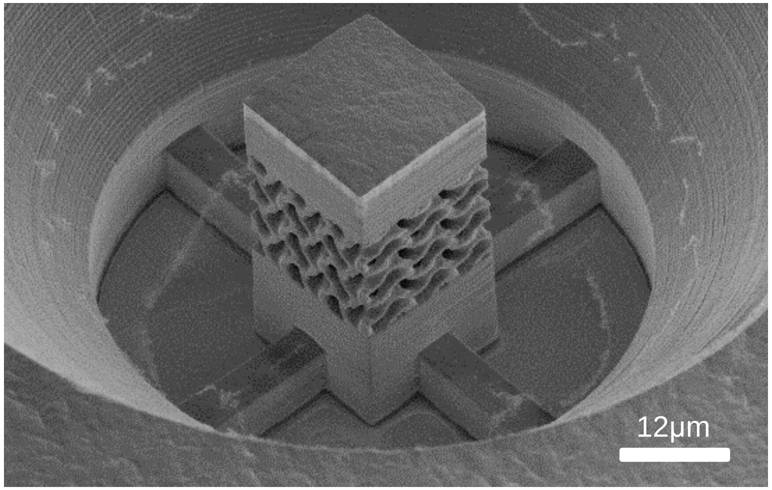

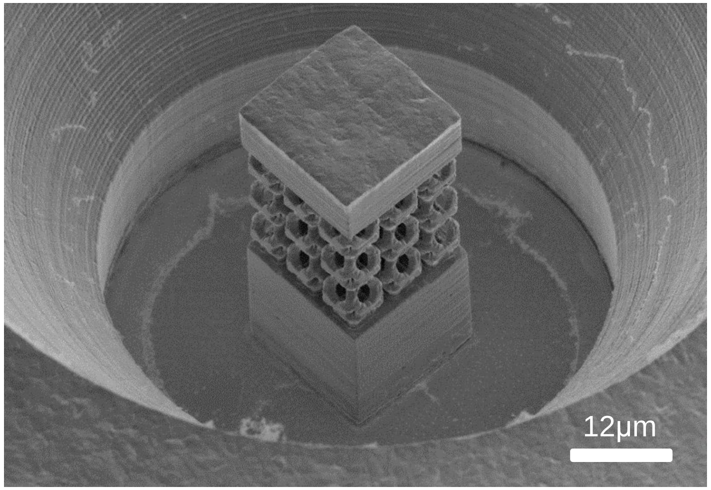

- Template assisted electrodeposition allows synthesizing metal micro-architectures with sub-micron feature sizes
- Process results in high quality, repeatable structures

Microcompression experiments

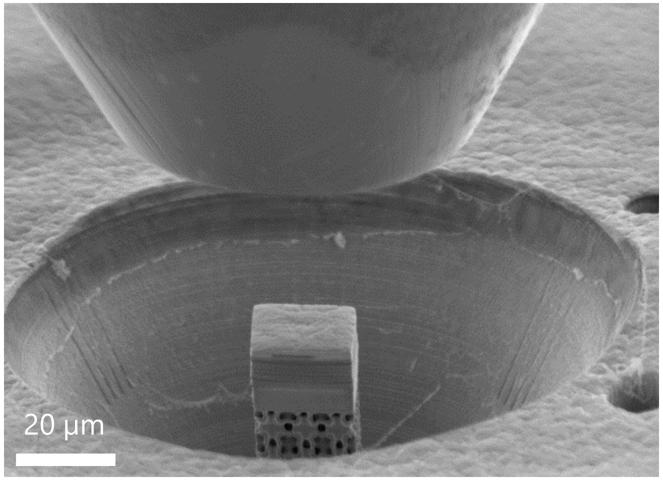

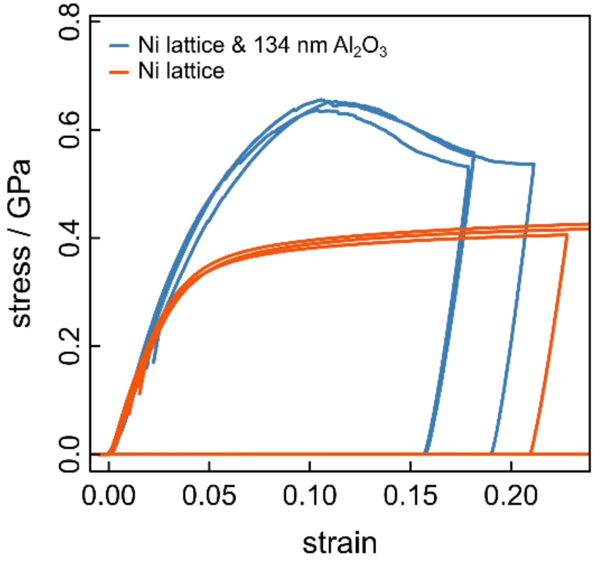

- Quasistatic compression experiments inside a SEM
- Measurement of force and displacement
- Uniaxial deformation allows interpretation as apparent stress-strain behaviour

Micromechanical behaviour

Strut based Ni vs. Ni-Al_2O_3 lattices

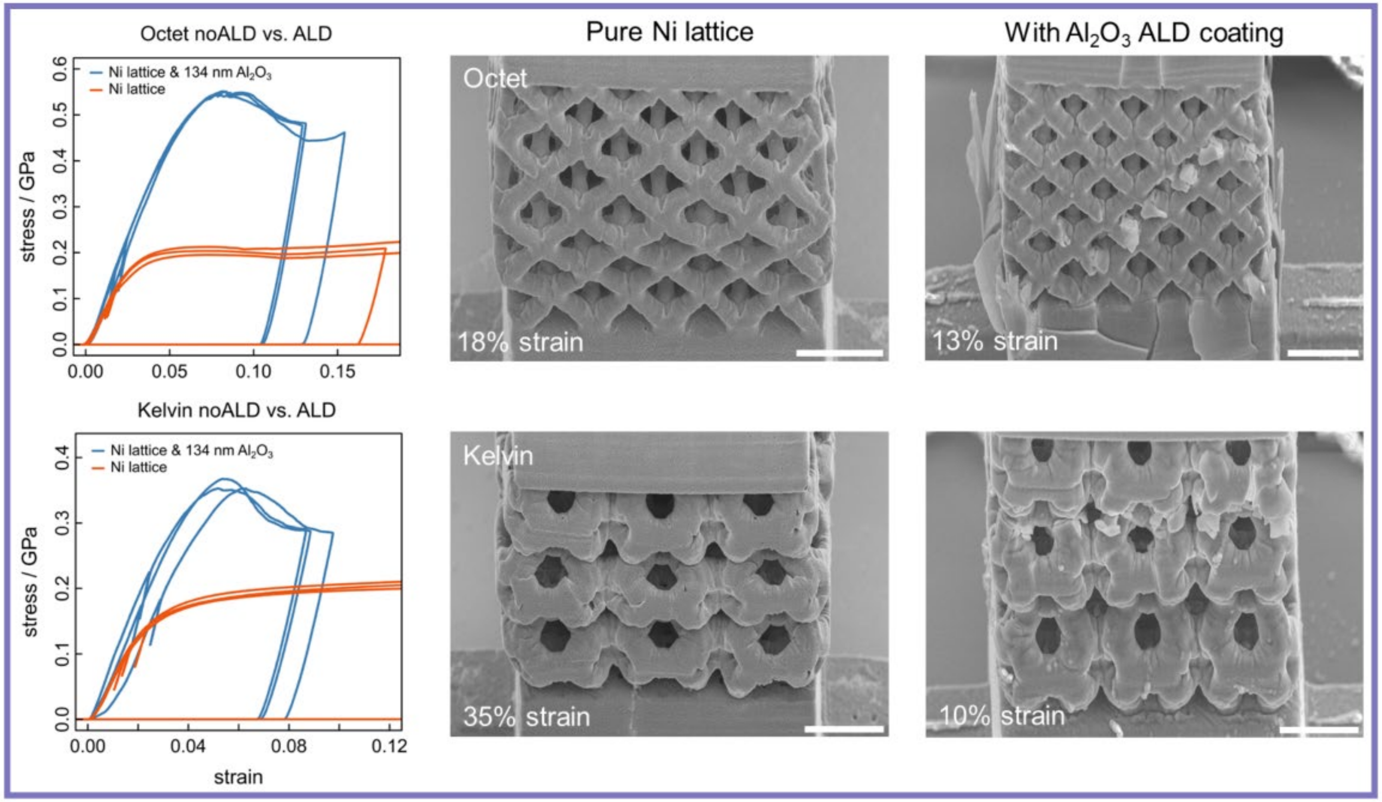

Micromechanical behaviour

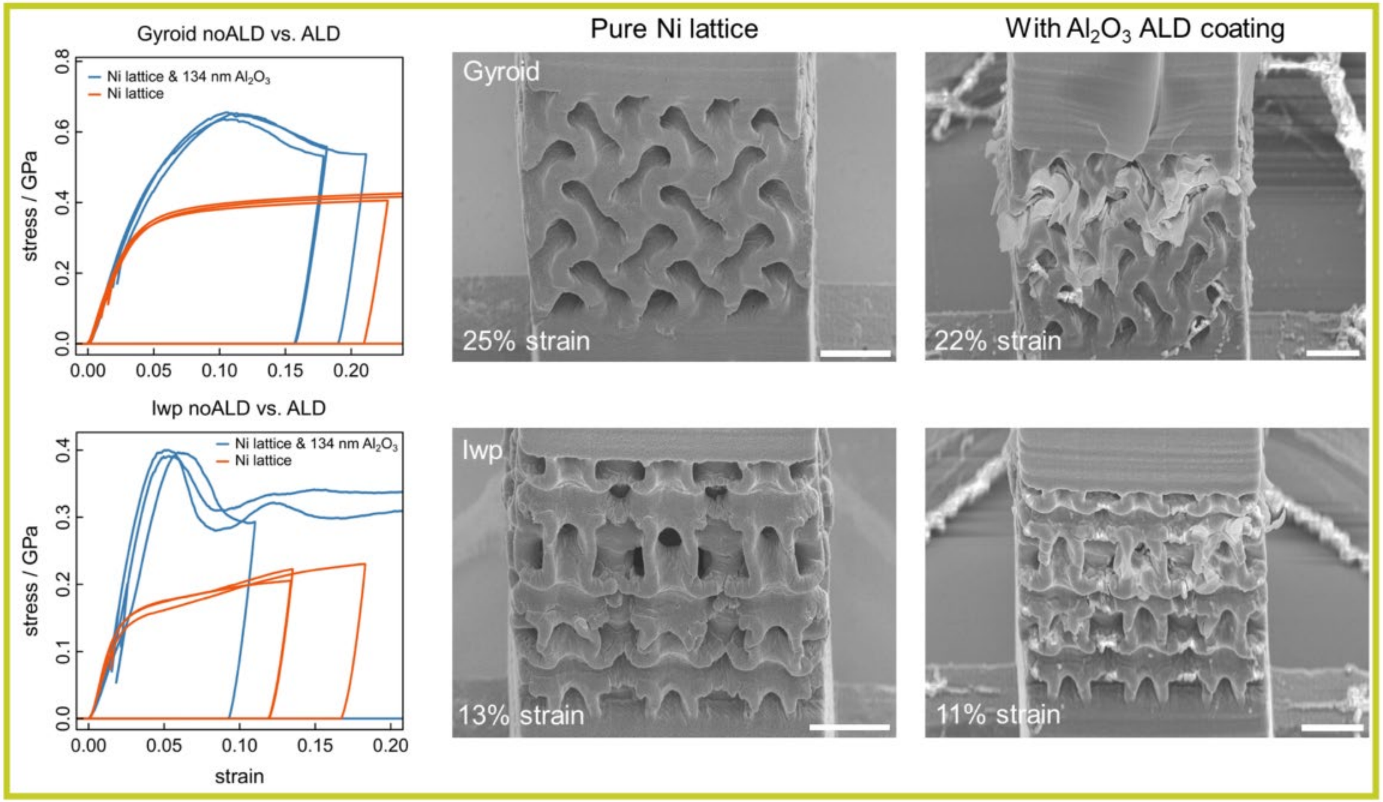

Surface based Ni vs. Ni-Al_2O_3 TPMS metamaterials

Ptychographic X-ray Computed Tomography (PXCT)

- High-resolution tomography down to 16 nm isotropic 3D resolution
- Coherent diffractive imaging that uses multiple diffraction patterns by scanning over specimen
- High phase sensitivity ⇨ high density sensitivity

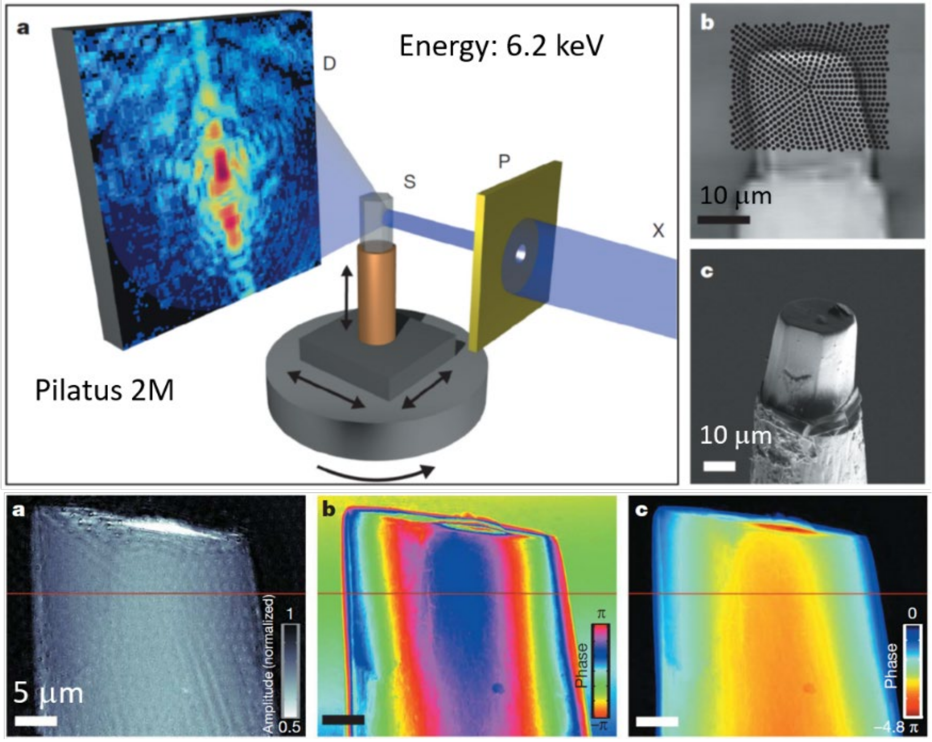

M. Dierolf et al., 2010, *Nature* 467, 436

Lift-outs – Fixation on OMNY pins for PXCT scans

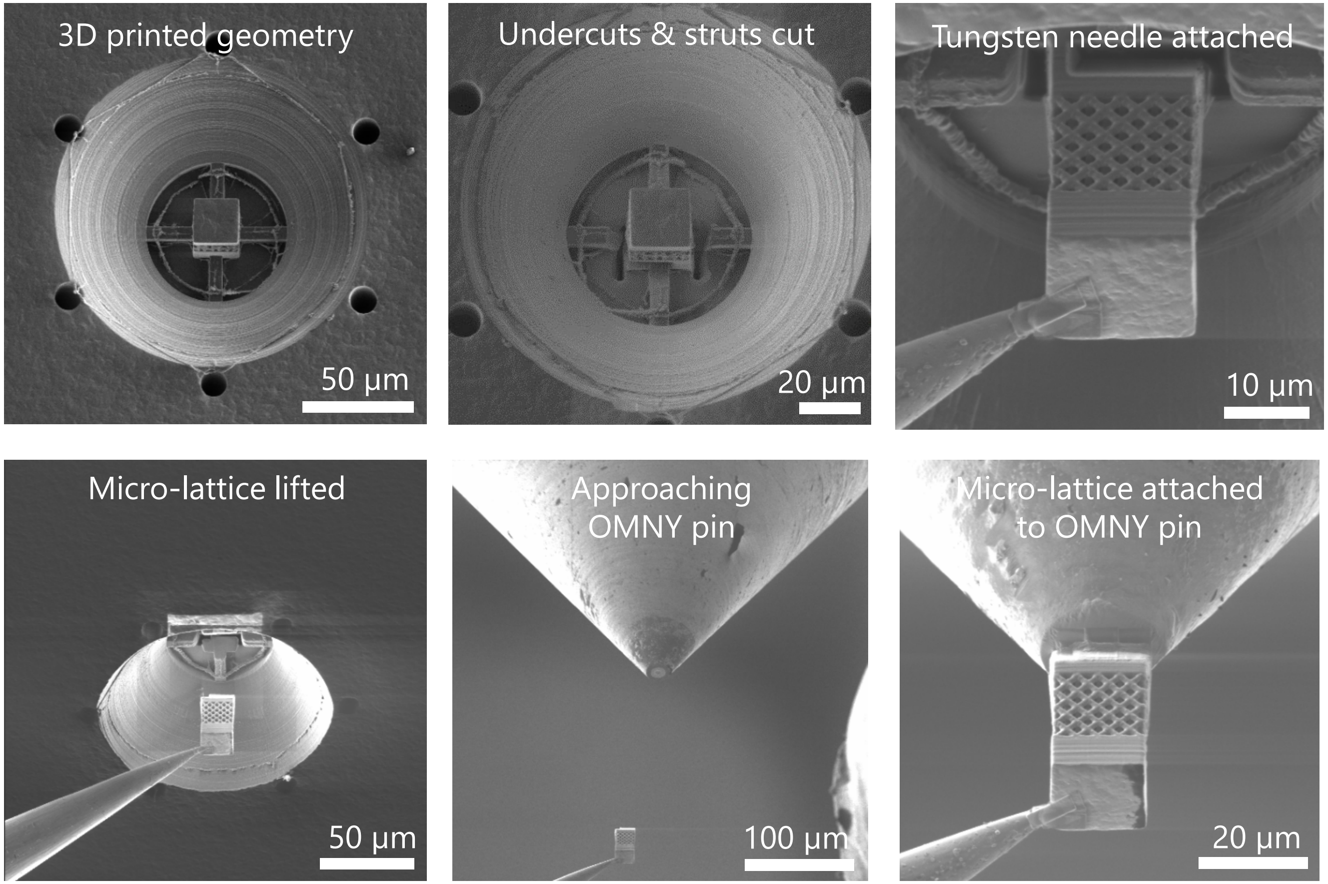

Ptychography for Ni micro-lattices

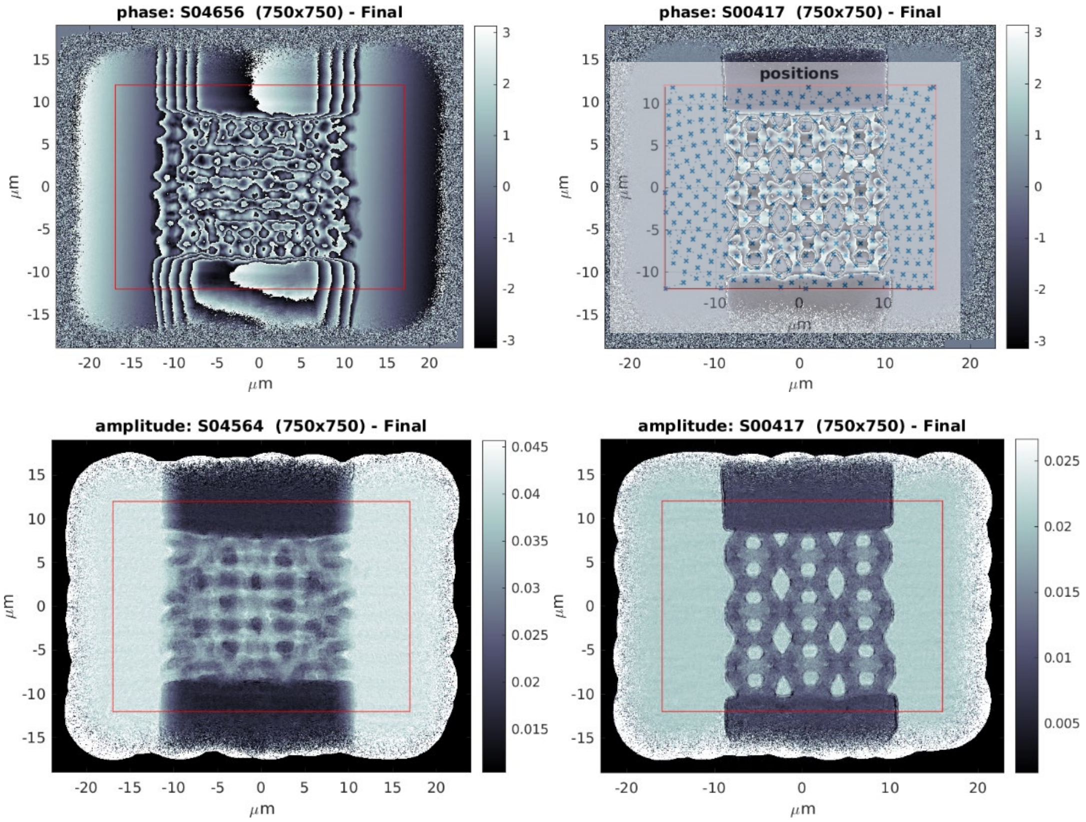

Imaging parameters:

- Photon energy of 6.2 keV
- 850-1000 projections
- 24 μm x 32 μm field of view
- Minimum pixel size: 19 nm
- Achieved resolution: 44 nm
- Scan time: 8-10 hours

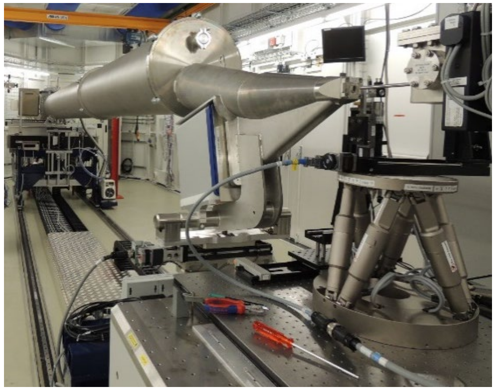

SAXS beamline at PSI

Image processing workflow

Axial reconstructions from beamtime

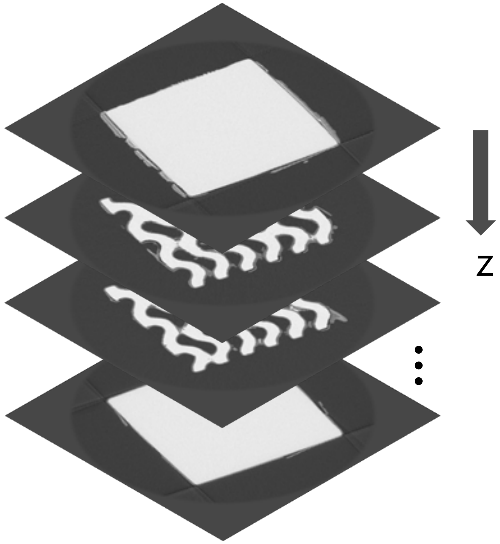

Sagittal reslicing Image sequence videos

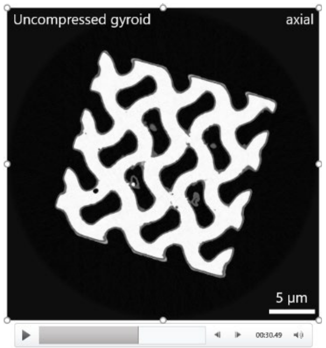

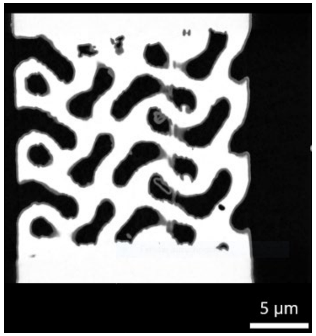

Volume rendering / segmentation based on metaImage files

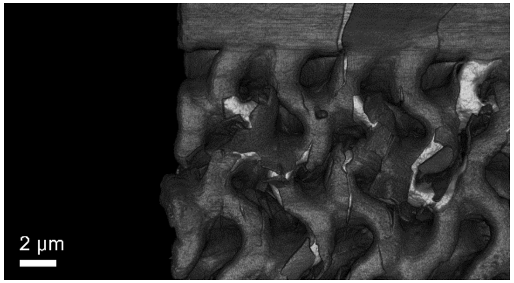

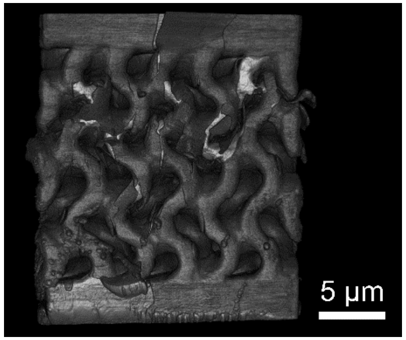

Empa
Materials Science and Technology

Defect distribution and failure mechanisms

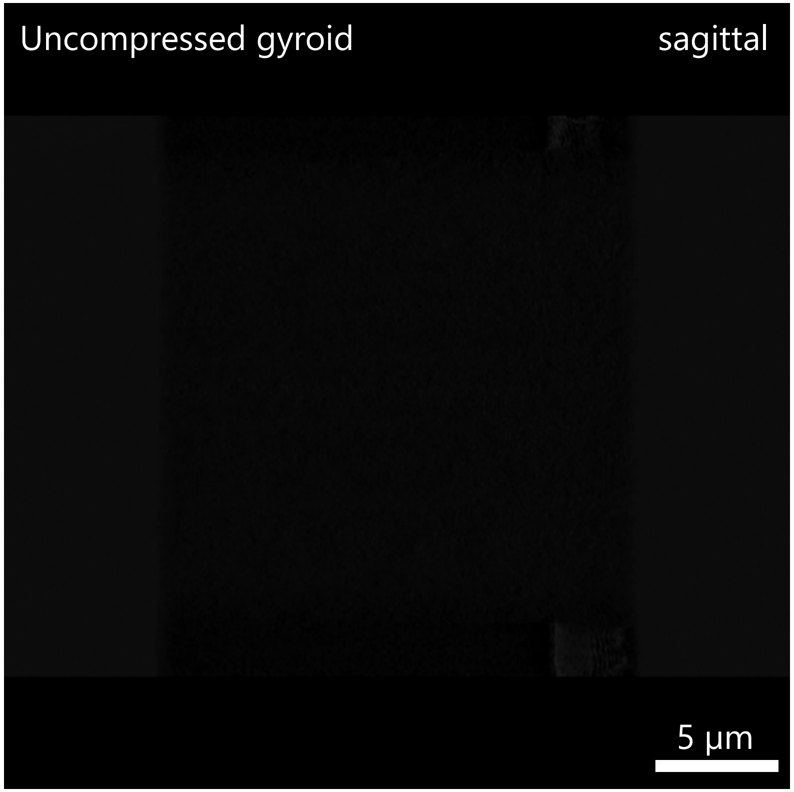

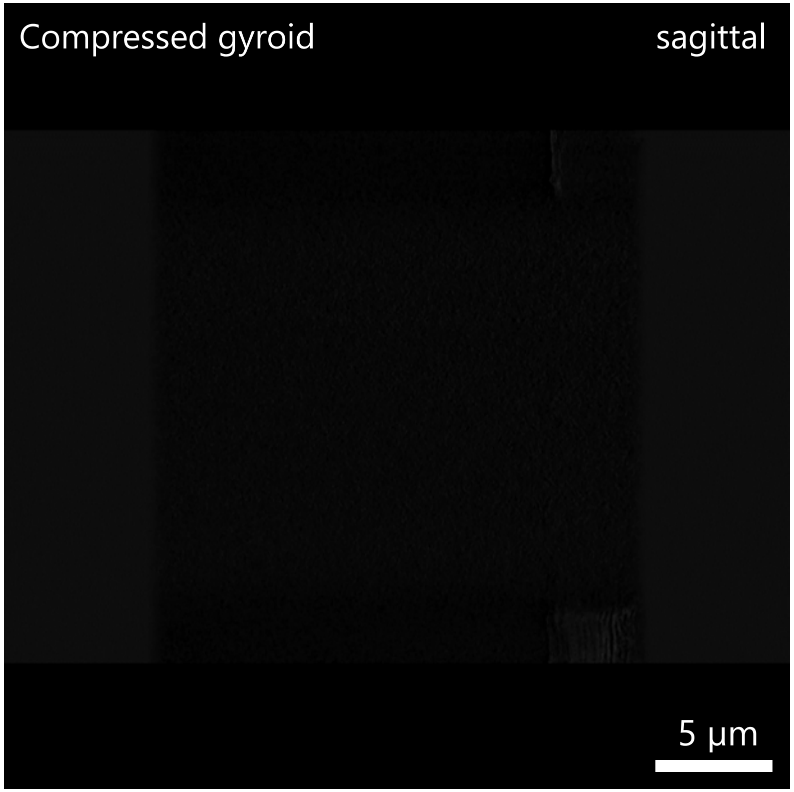

Defect distribution and failure mechanisms

Strut based Ni-Al_2O_3 lattices - PXCT

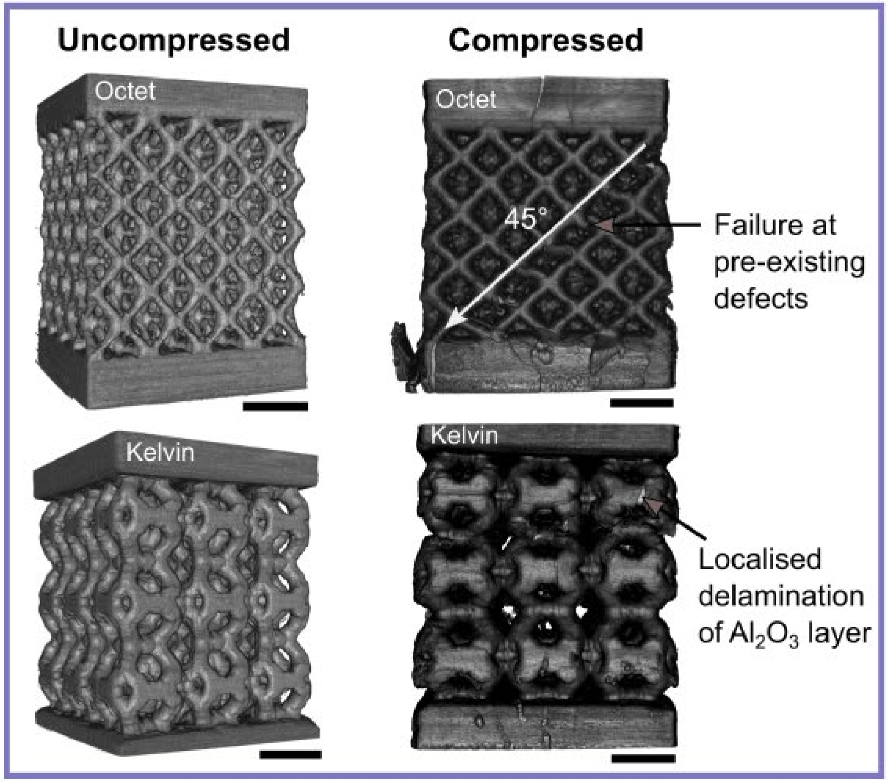

Surface based Ni-Al_2O_3 TPMS metamaterials - PXCT

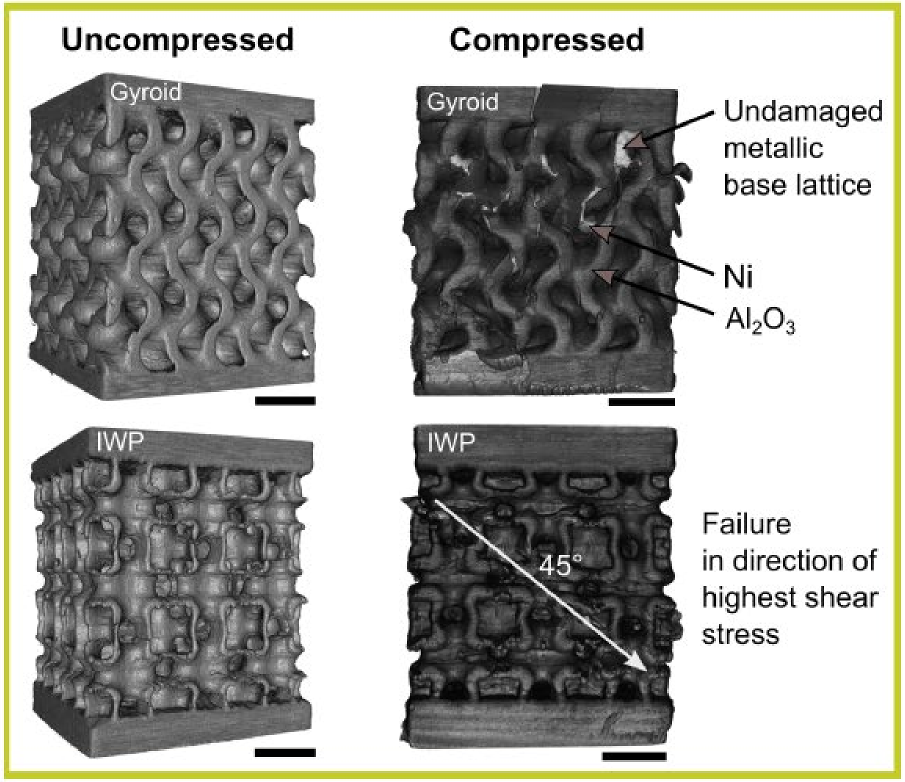

Microstructural analysis by TKD

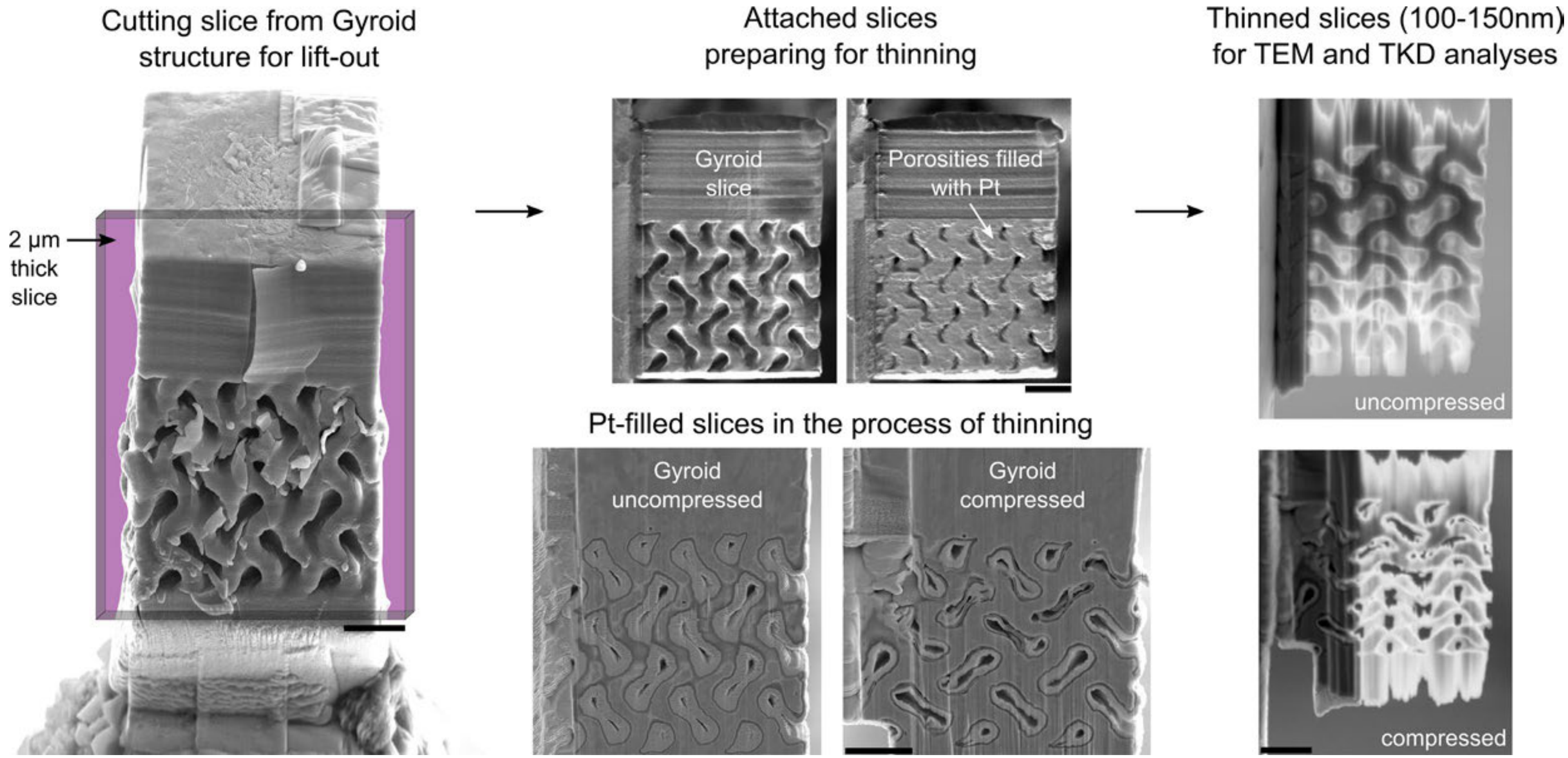

Cutting slice from Gyroid structure for lift-out

Attached slices preparing for thinning

Thinned slices (100-150nm) for TEM and TKD analyses

Pt-filled slices in the process of thinning

Microstructural analysis by TKD

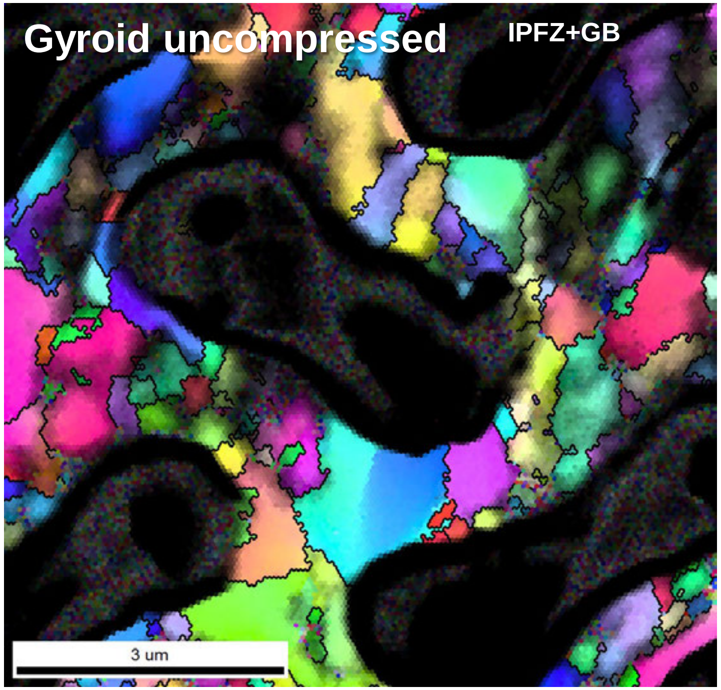

- Heterogeneous grain size between 100nm and 1µm in undeformed structure

Segmentation and meshing pipeline

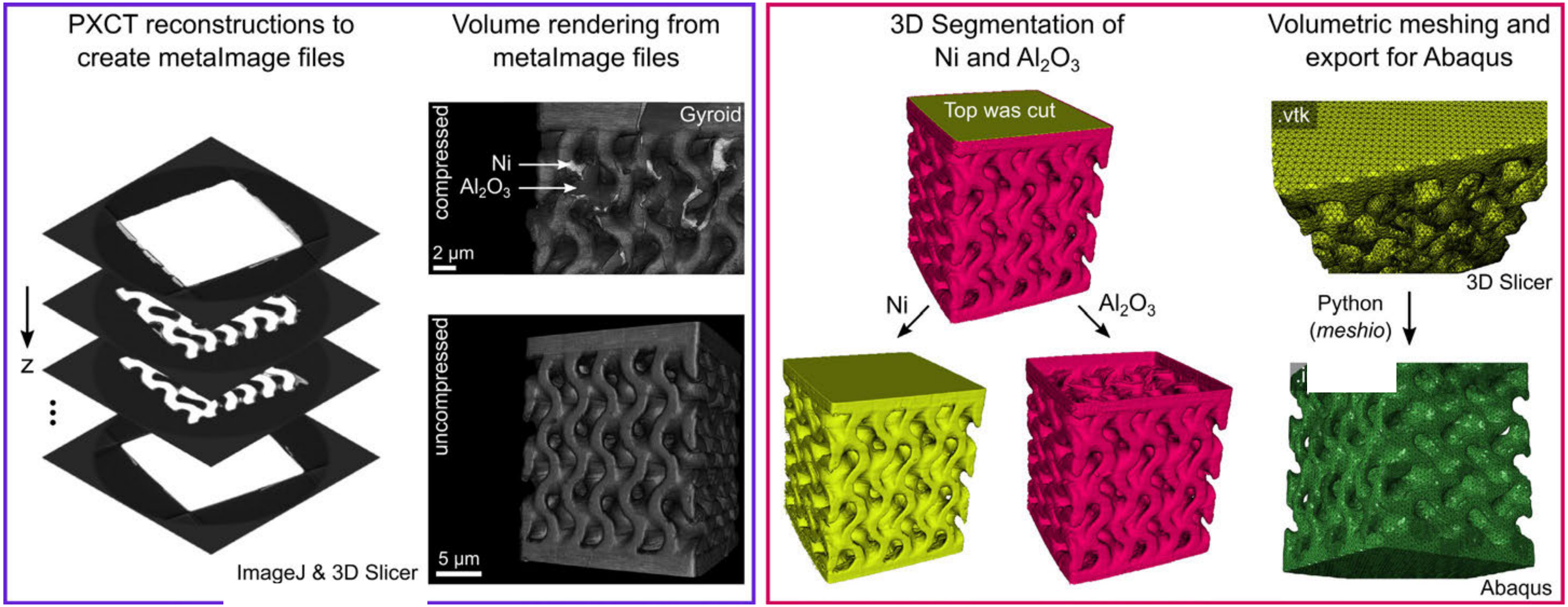

- A workflow was established allowing to segment and mesh the PXCT datasets

Mechanical modeling

- Automatic meshing procedure from segmented ptychography datasets using Python libraries allows simulating realistic geometries
- Comparison of ideal input structures to real 3D printed shapes allows investigating the effect of defects
- Goal: Predictive modeling enabling a simulation-based design approach

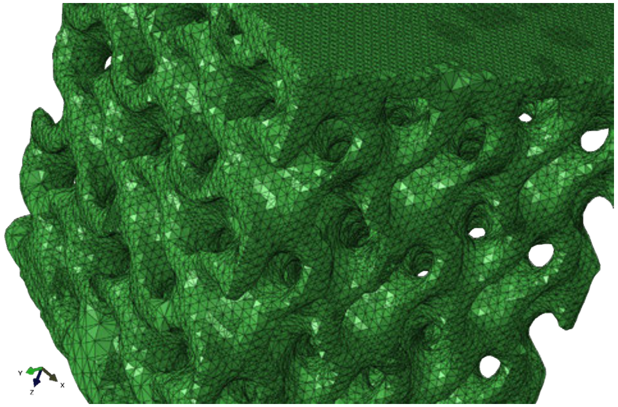

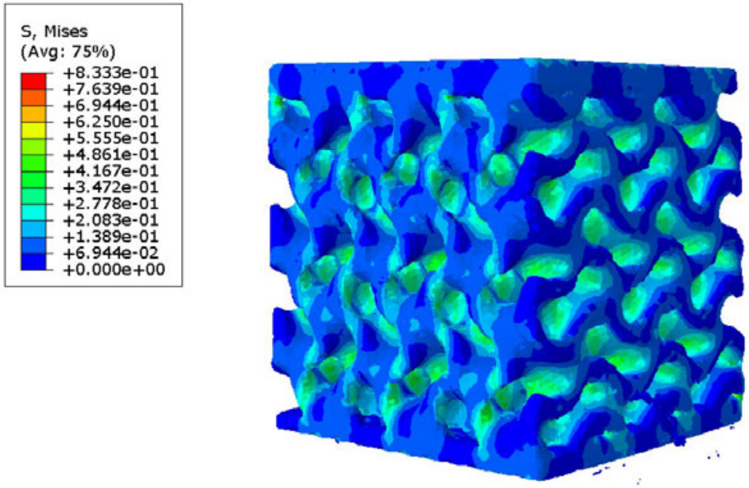

Summary

- Exploiting architecture and size effects in the design of mechanical metamaterials allows reaching unprecedented combinations of
- A novel process was developed for microscale additive manufacturing of hybrid metal-ceramic micro-architectures and lattices
- Under mechanical loading, the ceramic coating enhances the apparent strength, the metal lattice retains its ductility
- PXCT reconstructions used for volume rendering and 3D segmentation to extract Ni base lattice and ceramic coating
- Low adhesion of Nickel oxide layer leads to delamination at the interfaces of the Alumina coating. This enables the ductile behaviour after failure of the ceramic coating
- Automatic mesh generation from PXCT datasets allows studying failure mechanisms as well as the effect of geometric imperfections and defects

Deformation in nanocrystalline gold and 3D gold composites

Content

1203 Mechanics of nanocrystalline gold

1. Metal matrix composites made from electrodeposited gold
    - Fabrication
    - Microcompression tests
        - Varying alumina content
        - High temperatures (up to 100°C)
2. Deformation of nanocrystalline gold
    - Micropillar compression
        - Varying strain rate (10^{-5} to 700 s^{-1})
        - High temperatures (up to 100°C)

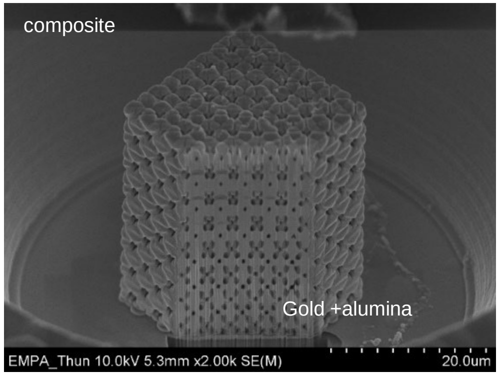

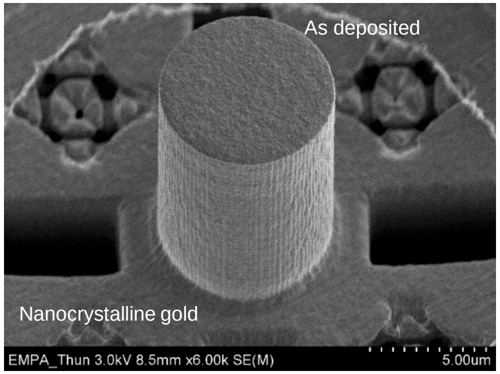

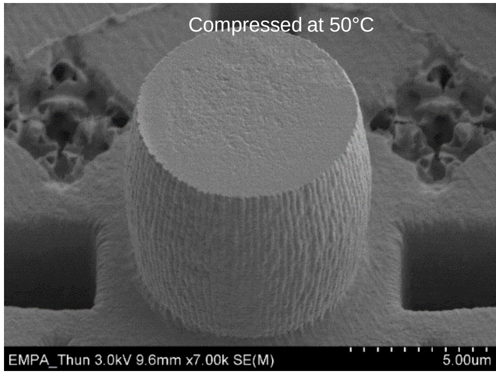

Composite design

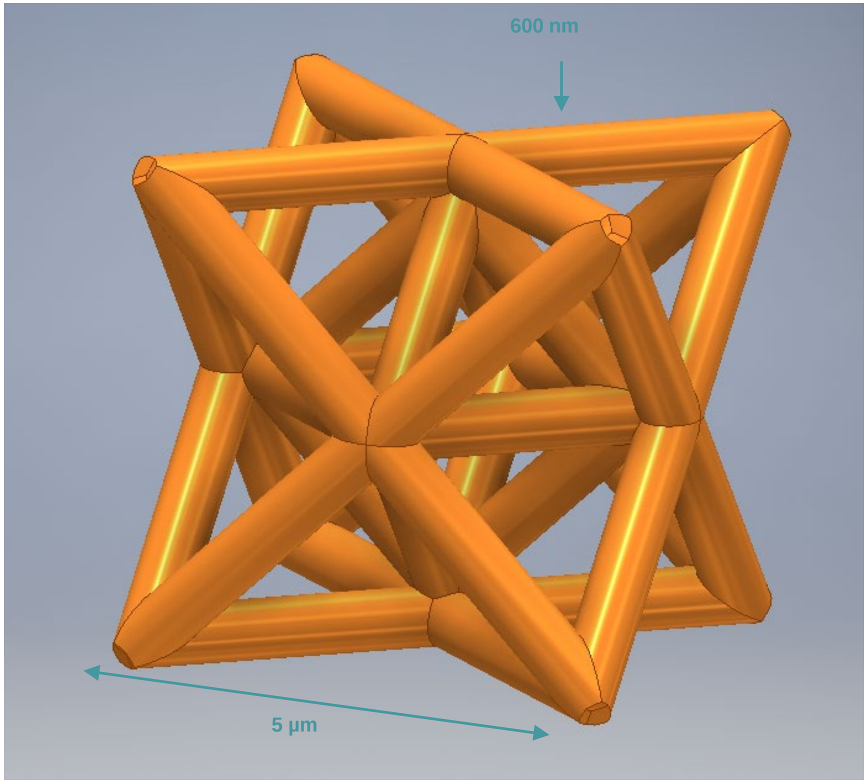

- 3D model of isotropic truss lattice
- Lattice design was selected for high stiffness
- Template printed using Two Photon Lithography with IP-Dip (Nanoscribe GmbH)
- Truss diameter of 600 nm and an overall unit length of 5 μm

Template assisted Electrodeposition

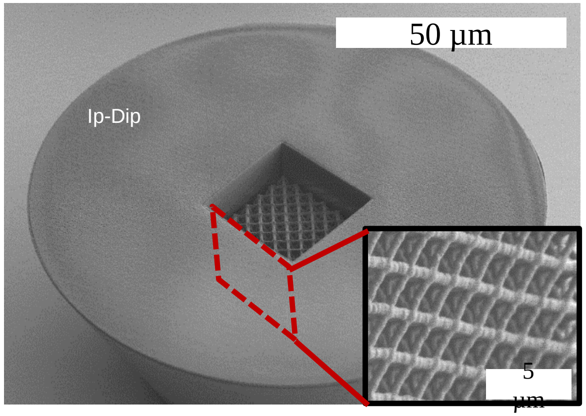

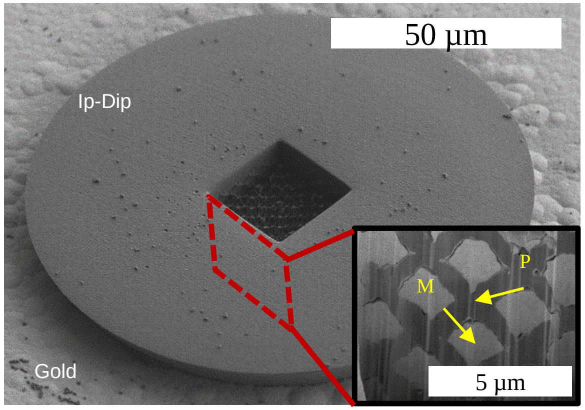

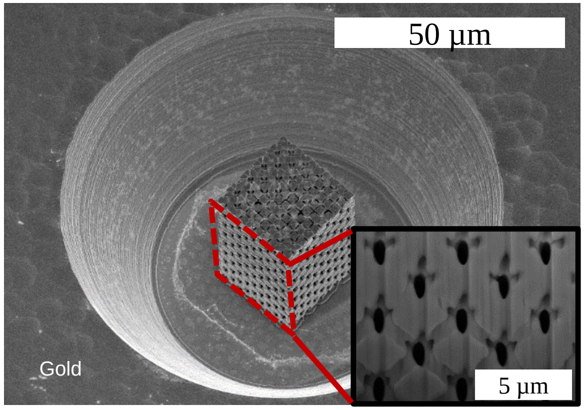

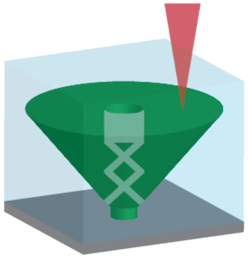

Two-Photon
Lithography

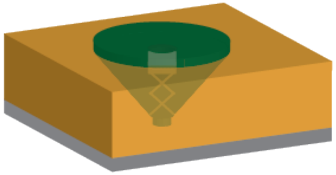

Electrodeposition

Plasma
Etching

Nanoindentation of Gold and Alumina coatings

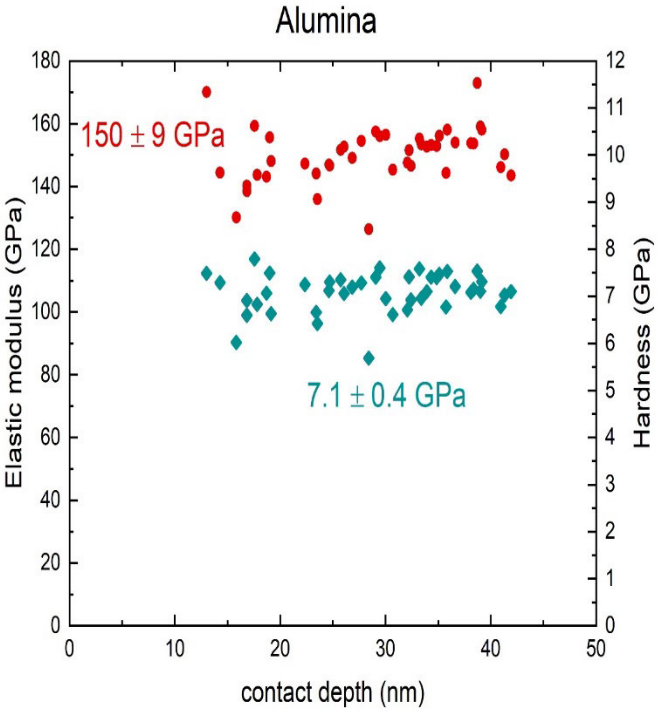

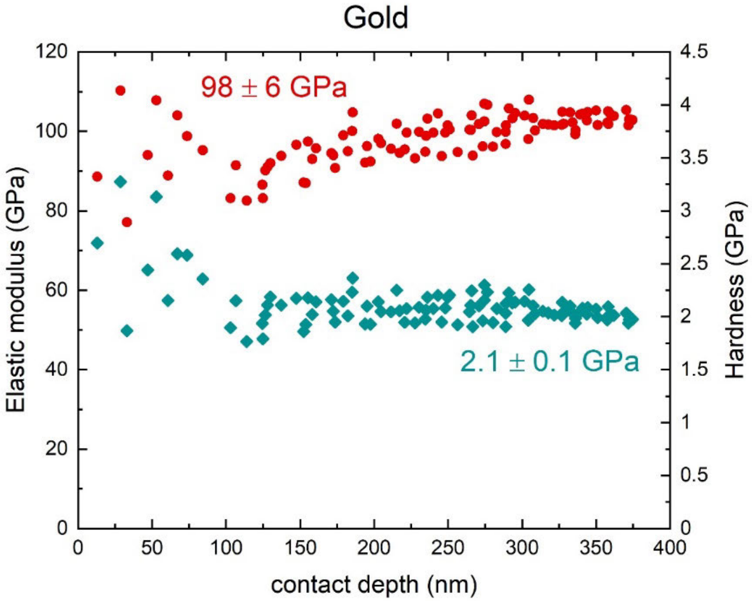

Compression of gold pillars at room temperature

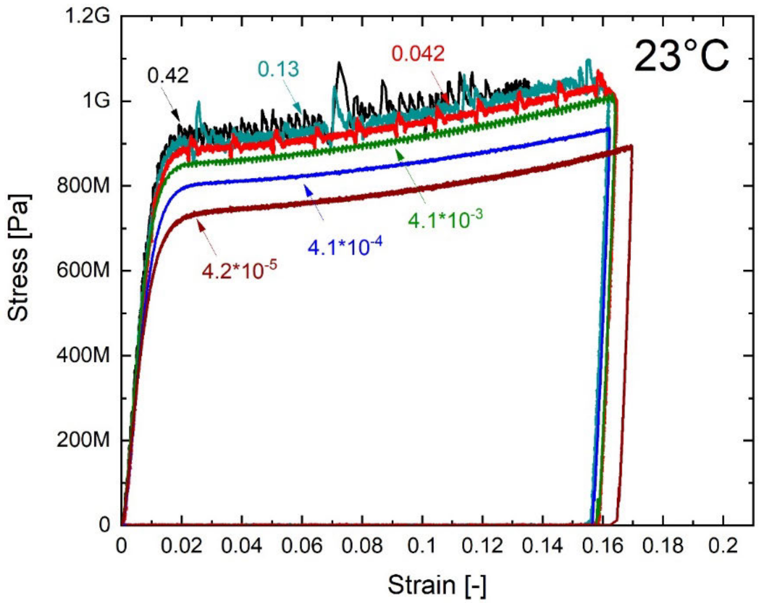

Strain rate (s^{-1})	Yield stress (MPa)
700	
134	996
13	957
0.42	922 ± 3
0.13	903 ± 4
0.042	886 ± 6
$4.1*10^{-3}$	845 ± 5
$4.1*10^{-4}$	792 ± 4
$4.2*10^{-5}$	718 ± 6

EMPA, Thun

Compression of gold pillars at elevated temperatures

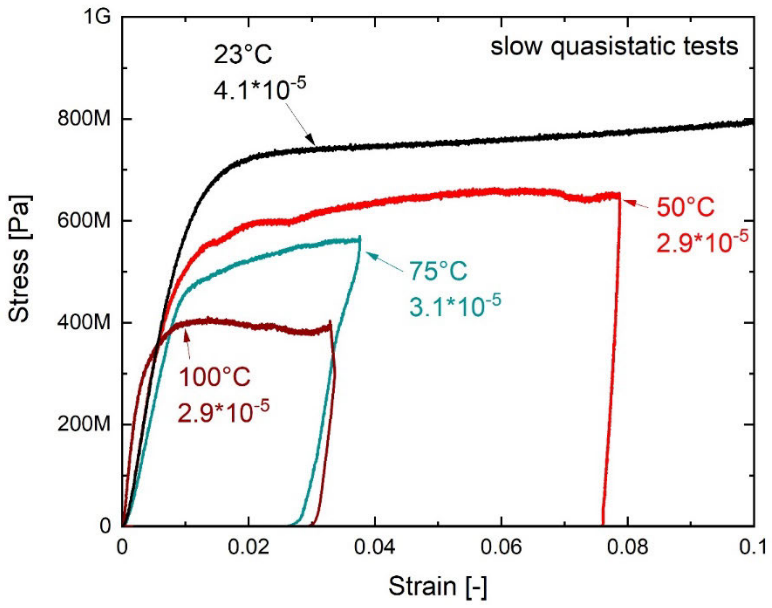

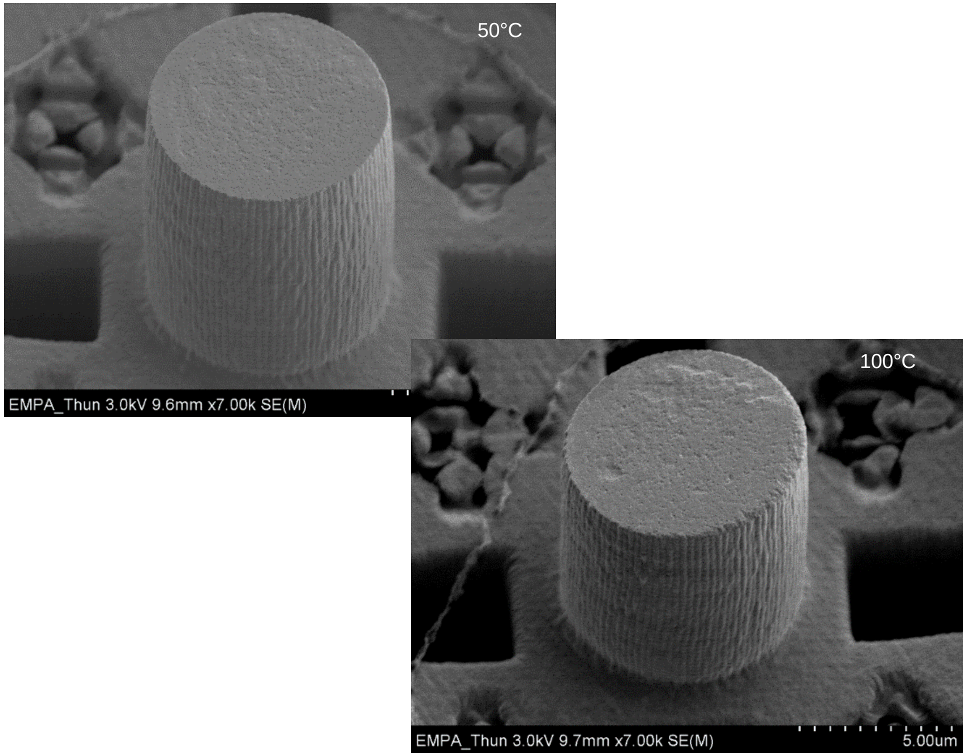

Strain rate sensitivity of nanocrystalline gold

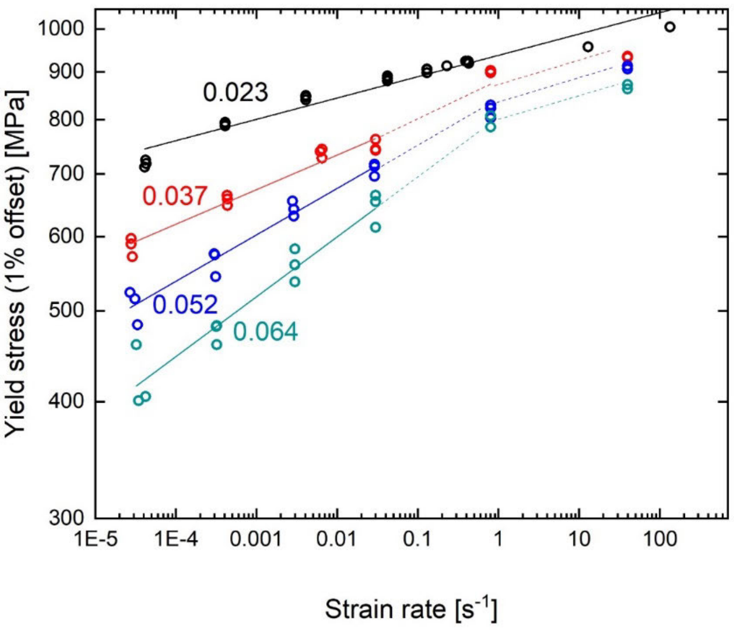

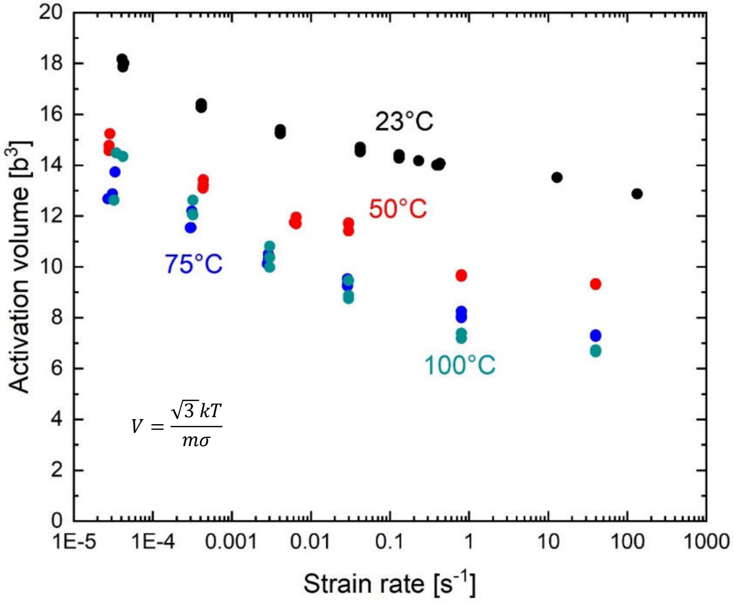

$$V = \frac{\sqrt{3}\,kT}{m\sigma}$$

Summary deformation of nanocrystalline gold

- The micropillars exhibit a higher strength than reported in literature for other nc gold pillars or found in tensile tests of nc thin films
- For the highest strain rate at room temperature the strength is ~1 GPa
- Nanocrystalline gold displays a strong strain rate sensitivity that increases at even slightly elevated temperatures of 50 to 100°C
- It (*probably*) displays a bilinear regime in the High strain rate regime where m is smaller and less temperature-dependent
- The apparent activation volume decreases with increasing temperature (though there does not appear to be a notable change from 75°C to 100°C)
- The apparent activation volume decreases with increasing strain rate
- Overall, for the conditions tested here it is within the range 18 – 8 b^3

Microcompression tests of gold composite structures

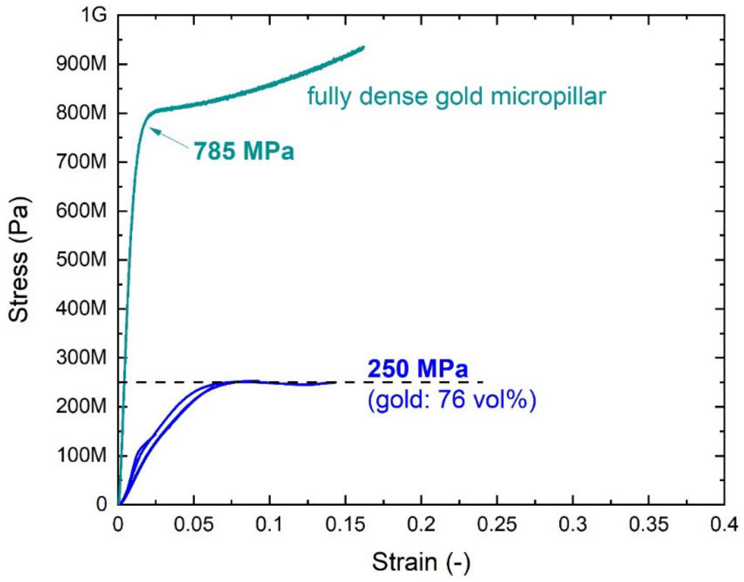

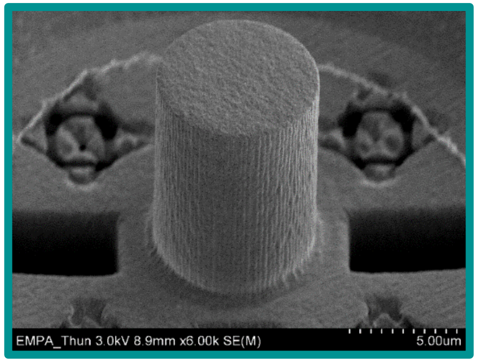

D= 7.46 μm
H= 13.2 μm

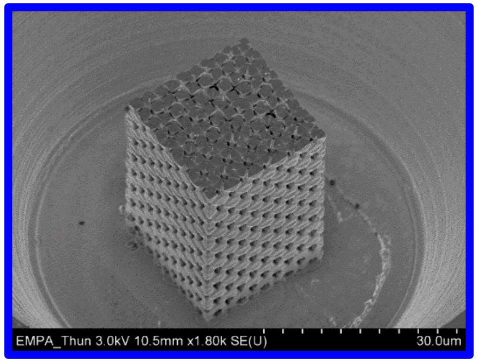

A= 22.3^2 μm^2
H= 35.1 μm

Hollow gold structures

20 µm

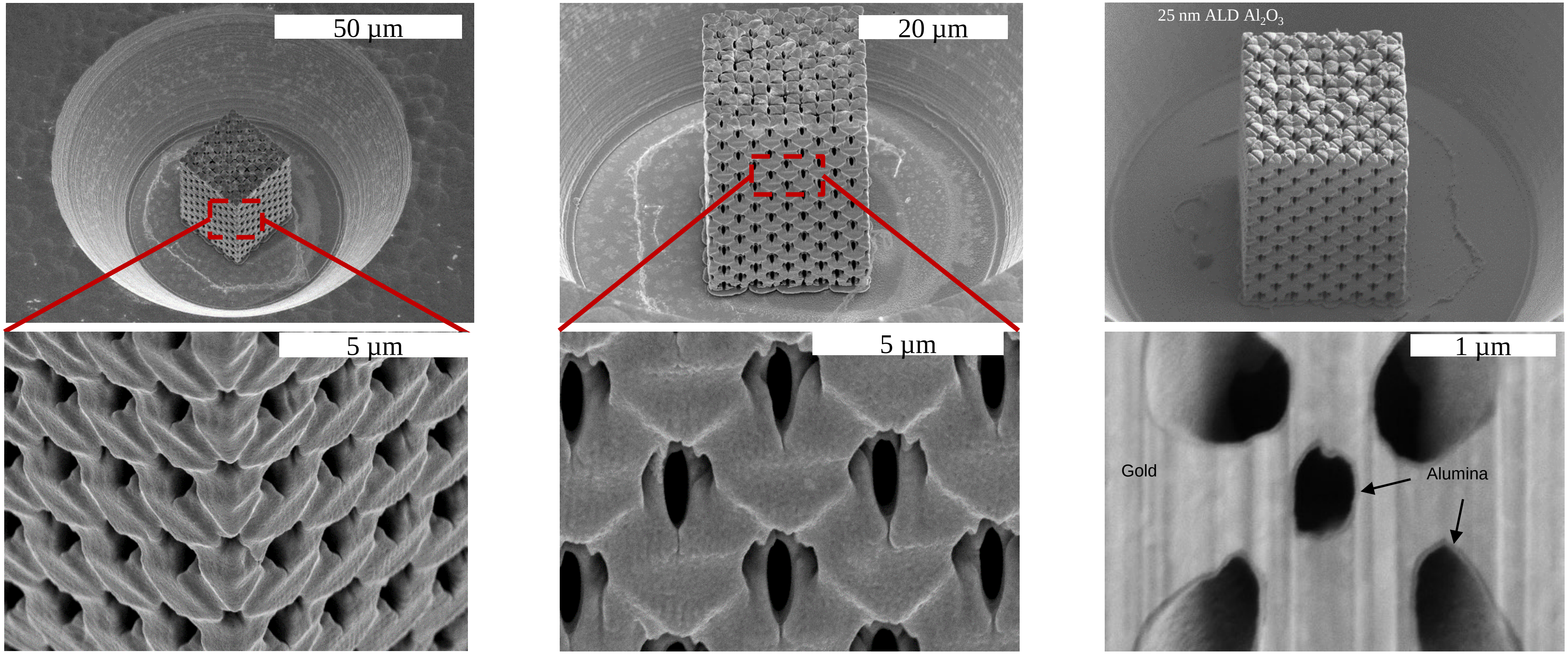

Microcompression tests of gold composite structures

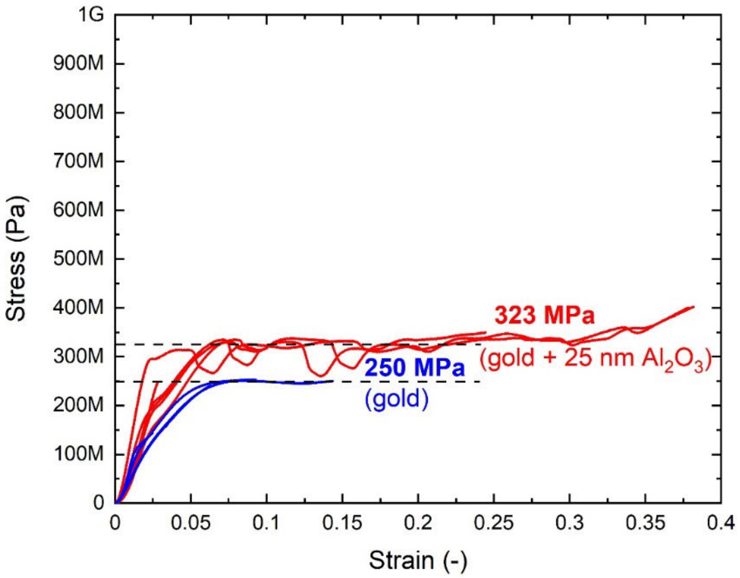

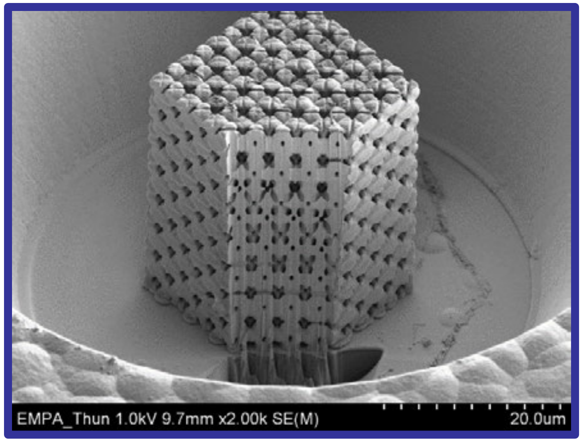

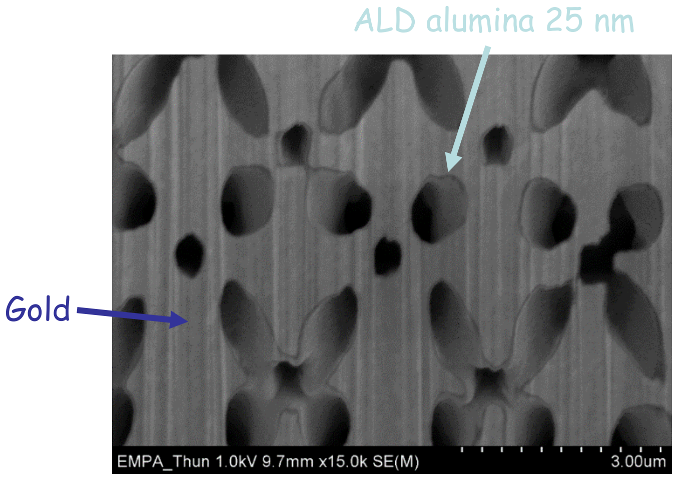

Microcompression tests of gold composite structures

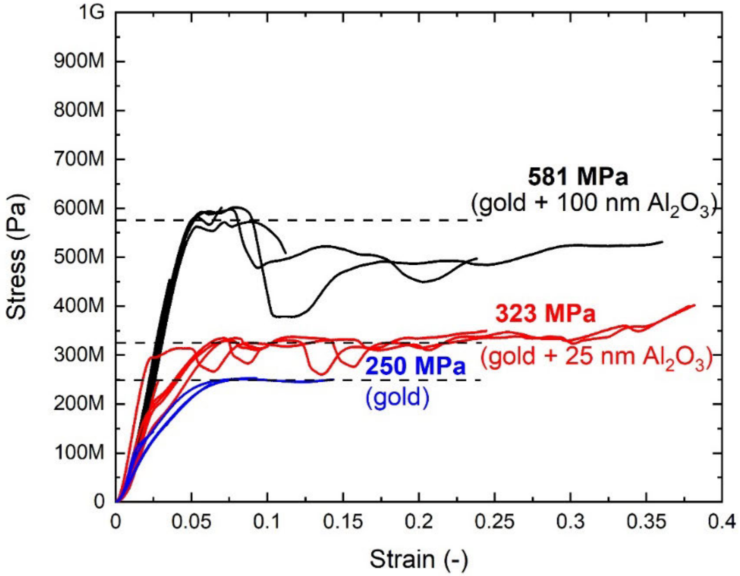

ALD alumina 100 nm

Gold

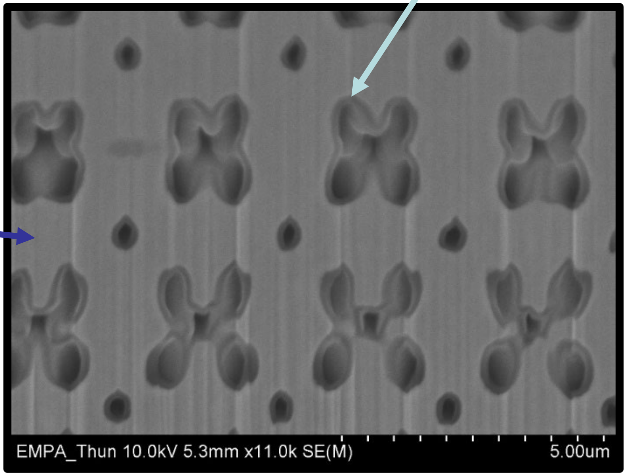

Microcompression tests of gold composite structures

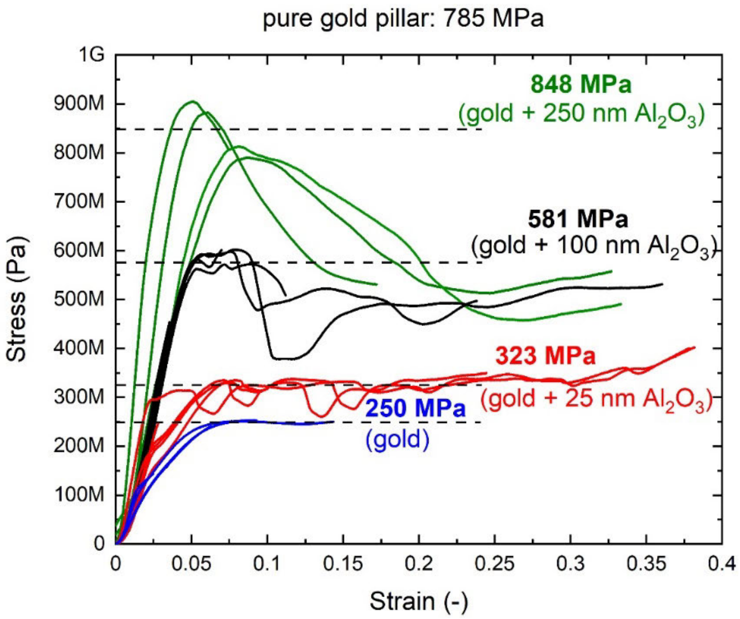

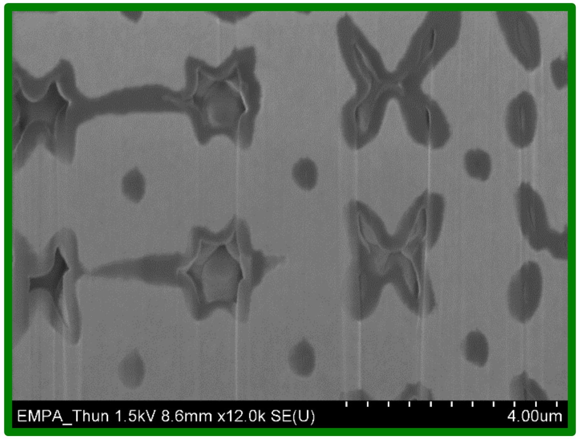

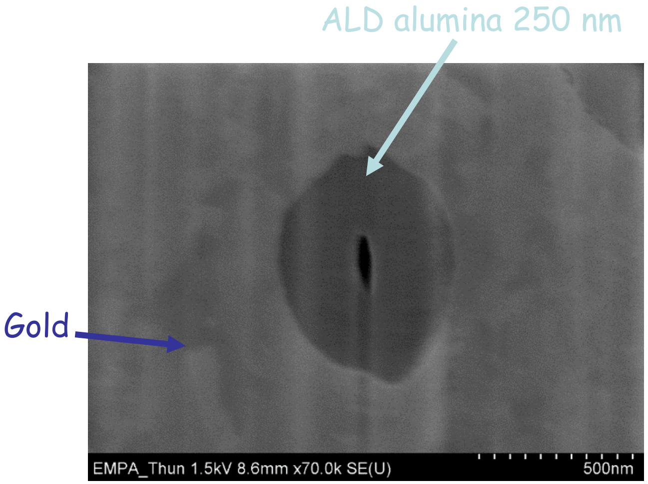

Composition, density and properties of composites

	Gold	Gold-25 nm	Gold-100 nm	Gold-250 nm	Gold pillar
Alumina content	-	3.2%	11.9%		-
Volumetric density	76.1%	79.3%	88%		100%
Density (g/cm³)	14.7				19.3
Yield strength (MPa)	250 ± 2	323 ± 19	581 ± 14	848 ± 58	792 ± 4

Microcompression tests at elevated temperatures

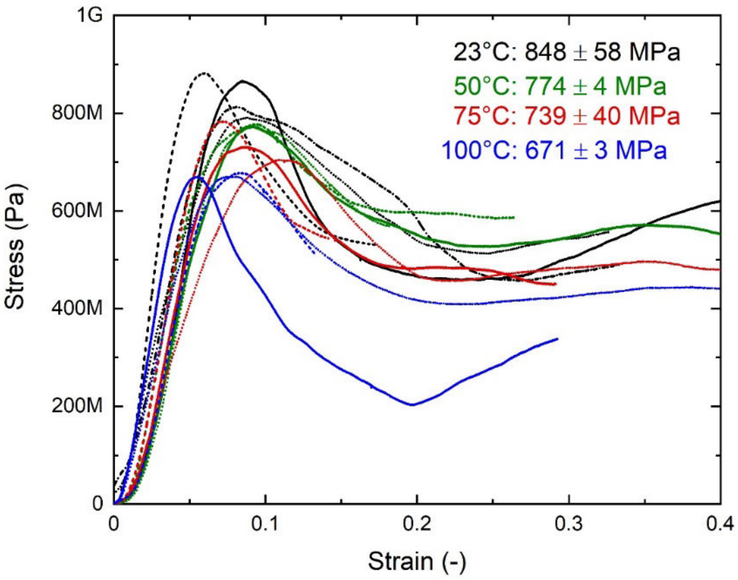

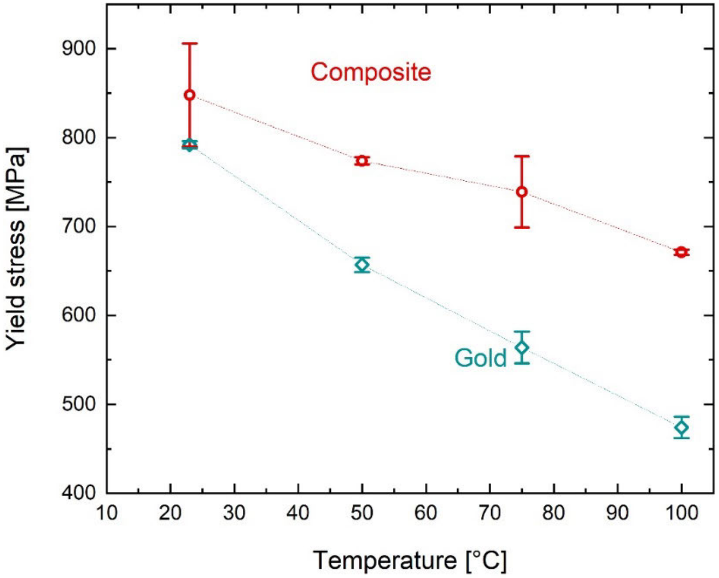

- Both, pure and composites, loose strength with increasing temperature
- In direct comparison, however, the composite retains more strength at increasing temperature

Simulation of the ideal composite behaviour

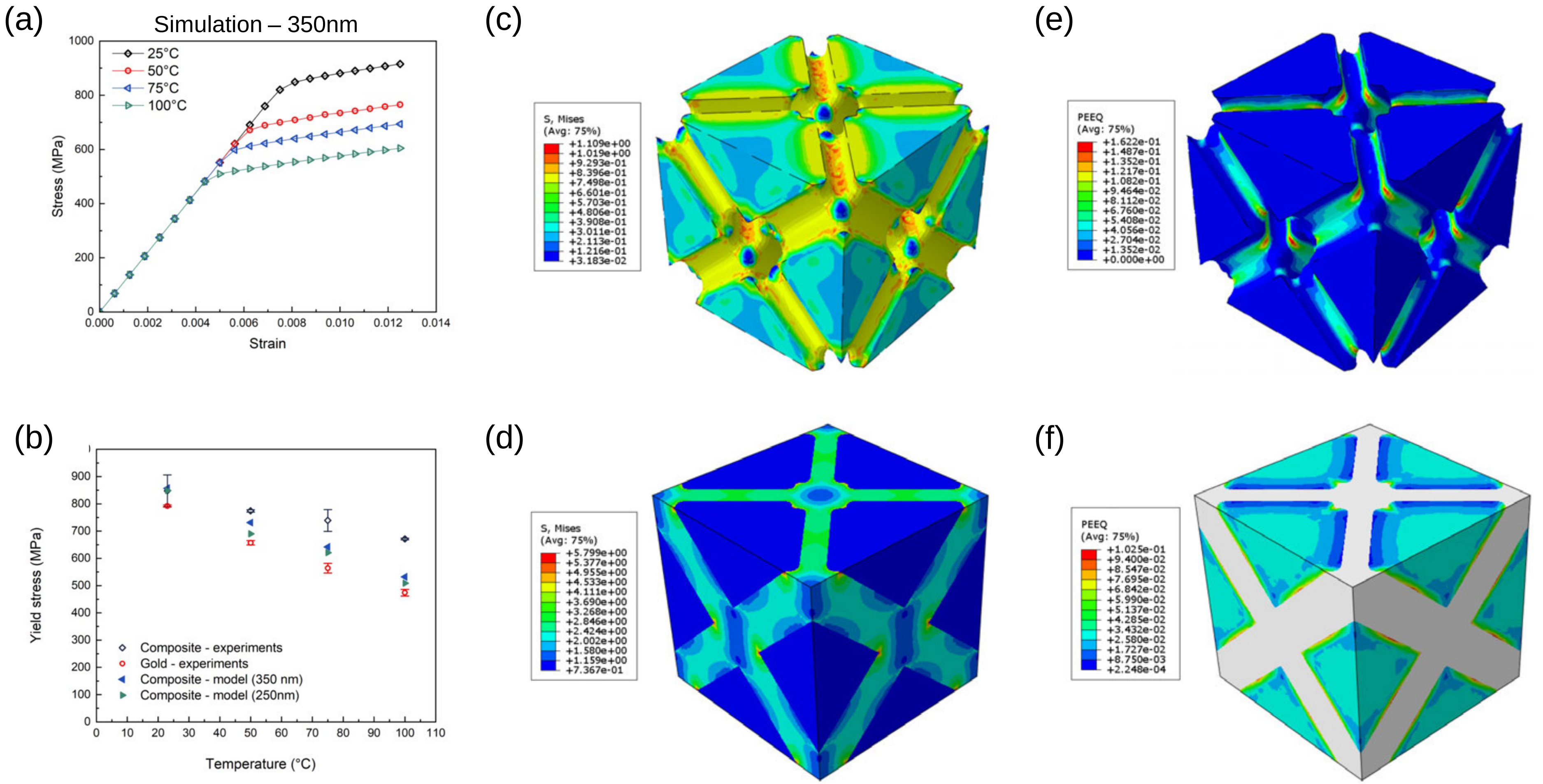

- *Simulation of compressive behaviour of ideal composite by applying periodic BC to a unit cell*
- *Stress concentration and localized plasticity in matrix near the ceramic lattice visible*

Summary

- Novel process to fabricate 3D nanostructured Metal Matrix Composite containing a ceramic reinforcement phase
- Strength and thermal stability of metal matrix are improved by ceramic reinforcement
- Thermal activation analysis reveals a change in deformation mechanism between quasi-static and high strain rate regimes
- Strength can be tuned by varying architecture and wall thickness of hollow reinforcement lattice
- Finite element modelling is able to predict yield strength and point out highly stressed regions